

UNIVERSIDADE DE SÃO PAULO
INSTITUTO DE FÍSICA DE SÃO CARLOS

WILLIAN ANDRIGHETTO TREVIZAN

Nuclear magnetic resonance and digital rock in oil industry: well
logging applications

São Carlos
2017

WILLIAN ANDRIGHETTO TREVIZAN

Nuclear magnetic resonance and digital rock in oil industry: well logging applications

Thesis presented to the Graduate Program in Physics at the Instituto de Física de São Carlos, Universidade de São Paulo to obtain the degree of Doctor of Science.

Concentration area: Basic Physics

Advisor:
Prof. Dr. Tito José Bonagamba

Corrected Version
(Original version available on the Program Unit)

São Carlos
2017

AUTHORIZE THE REPRODUCTION AND DISSEMINATION OF TOTAL OR PARTIAL COPIES OF THIS THESIS, BY CONVENCIONAL OR ELECTRONIC MEDIA FOR STUDY OR RESEARCH PURPOSE, SINCE IT IS REFERENCED.

Cataloguing data reviewed by the Library and Information Service
of the IFSC, with information provided by the author

Trevizan, Willian Andrighetto

Nuclear magnetic resonance and digital rock in
oil industry: well logging applications / Willian
Andrighetto Trevizan; advisor Tito José Bonagamba -
reviewed version -- São Carlos 2017.

175 p.

Thesis (Doctorate - Graduate Program in Basic
Physics) -- Instituto de Física de São Carlos,
Universidade de São Paulo - Brasil , 2017.

1. Nuclear magnetic resonance. 2. Oil/gas
industry. 3. Formation evaluation. 4. Surface
relaxivity. 5. Digital rock. I. Bonagamba, Tito
José, advisor. II. Title.

To those of good will,
who believe and build a much better world
based on truth and knowledge.

ACKNOWLEDGEMENTS

I take the opportunity to express my gratitude to my advisor, Tito José Bonagamba, who so enthusiastically supports not only this work, but the major initiative of bringing Academia closer to Industry daily challenges, generating opportunities for scientists of several fields.

I am thankful for the trust taken by my manager Vinícius de França Machado, who has always been open to the initiatives that put this project in motion, and for the investment made by Petrobras.

I would also like to make a special acknowledgement to Martin Hürlimann and Yi-Qiao Song for the insightful discussions that took place during my stay at Schlumberger-Doll Research Center in Boston, which was possible due to the efforts of Austin Boyd and Andre Souza. Those conversations were of great importance for the development of the ideas presented in Chapter 5.

For the endless discussions on time scales and NMR processes in general, I thank my colleagues Bernardo Coutinho Camilo dos Santos, from Petrobras, and Everton Lucas de Oliveira, Mariane Barsi Andreeta, Rodrigo de Oliveira Silva, Elton Tadeu Montrazi and Arthur Gustavo de Araujo Ferreira, from the LEAR group, IFSC/USP. I also thank the LEAR group, extending to Edson Luiz Gea Vidoto and Aparecido Donizeti Fernandes de Amorim, for enabling the experimental setups.

ABSTRACT

TREVIZAN, W. A. **Nuclear magnetic resonance and digital rock in oil industry:** well logging applications. 2017. 175p. Thesis (Doctor in Science) - Instituto de Física de São Carlos, Universidade de São Paulo, São Carlos, 2017.

This thesis discusses Nuclear Magnetic Resonance (NMR) techniques for formation evaluation in well log analysis for the oil/gas industry. We present the standard ingredients for NMR data processing and interpretation, and develop a methodology that extends the determination of surface relaxivity from the laboratory to the well site. The methodology consists of a processing algorithm for diffusion editing data, which enables surface relaxivity determination for conditions close to those found in well logging (regarding data availability and noise levels). At moderate noise levels, lower relaxivity values (below $10\mu\text{m/s}$) can be determined solely from NMR diffusion data, while higher values ($\sim 30\mu\text{m/s}$) can be separated from intermediate ones. Application for actual logging data still requires some noise reduction techniques such as stationary measurements downhole or data stacking among different depths. However, it provides a way of converting T_2 distributions into actual pore size distributions even for downhole acquisitions, before the samples get to the laboratory for routine analysis. Besides the logging analysis, we also developed a theoretical approximation to the diffusion equation with partial absorptive contour conditions, by calculating appropriate transition rates between cells in an arbitrary grid, allowing a simple methodology for obtaining the NMR data based on pore imaging. Calculated rates can in principle be used for modeling/understanding different diffusion phenomena, such as exchange between pores or relaxation sites.

Keywords: Nuclear magnetic resonance. Oil/gas industry. Formation evaluation. Surface relaxivity. Digital rock.

RESUMO

TREVIZAN, W. A. **Ressonância magnética nuclear e rocha digital na indústria do petróleo:** aplicações em perfilagem de poços. 2017. 175p. Tese (Doutorado em Ciências) - Instituto de Física de São Carlos, Universidade de São Paulo, São Carlos, 2017.

Neste trabalho são discutidas técnicas de Ressonância Magnética Nuclear (RMN) aplicadas à avaliação de formações por meio da perfilagem de poços pela indústria de óleo e gás. São apresentados os conceitos básicos para processamento e interpretação dos dados de RMN, e desenvolvida uma metodologia para determinação da relaxatividade superficial em poço. O método consiste em um algoritmo de processamento de dados de *diffusion editing*, que permite a obtenção da relaxatividade superficial em condições próximas as encontradas na perfilagem de poços de petróleo (em relação à disponibilidade de dados e nível de ruído). Para níveis moderados de ruído, as relaxatividades mais baixas (menores que $10\mu\text{m/s}$) podem ser determinadas através das medidas de difusão por RMN, enquanto valores mais altos ($\sim 30\mu\text{m/s}$) podem ser separados dos intermediários. Aplicações em dados de perfilagem ainda requerem técnicas de redução de ruído como aquisições estacionárias em poço ou empilhamento de dados ao longo de um intervalo de profundidades. Entretanto, o método possibilita uma forma de converter as distribuições de T_2 em distribuições de tamanhos de poros ainda em poço, antes que as amostras sejam enviadas para o laboratório em análises de rotina. Além da perfilagem, foi desenvolvido também uma aproximação para a equação de difusão com condições de contorno absorptivas, através de equações de taxas. A forma das taxas de transição permite o desenvolvimento de metodologias simples para obtenção dos dados de RMN através de imagens dos poros das rochas. As taxas de transição podem ser utilizadas também para a modelagem de outros fenômenos que envolvam difusão, como fenômenos de troca entre poros ou entre sítios com diferentes valores de relaxação.

Palavras-chave: Ressonância magnética nuclear. Indústria de óleo e gás. Avaliação de formações. Relaxatividade superficial. Rocha digital.

LIST OF FIGURES

Figure 2.1 -	Thin section of a well sorted Botucatu Sandstone.	27
Figure 2.2 -	Thin section of a poorly sorted Leopard Sandstone.....	27
Figure 2.3 -	Example of carbonate structure - Indiana Limestone.....	30
Figure 2.4 -	Single peaked pore size distribution	33
Figure 2.5 -	Bimodal pore size distribution	34
Figure 2.6 -	Example of pore throat distribution	35
Figure 2.7 -	Capillary pressure curve.....	36
Figure 2.8 -	Example of a geologic model containing the elements of a petroleum system	38
Figure 2.9 -	Example of seismic image.	39
Figure 2.10 -	Logging results. First track shows gamma ray log in green and the difference between the expected well caliper and measured one in shaded light brown. Second track shows the density log in red, its corresponding porosity in shaded grey, and Neutron porosity in green. Last track shows the NMR transverse relaxation times distributions. Depth increases downwards.	43
Figure 3.1 -	States of a spin $\frac{1}{2}$ particle in a the presence of a static magnetic field ..	47
Figure 3.2 -	Precession of magnetization around a static magnetic field	50
Figure 3.3 -	Precession of magnetization during application of $\mathbf{B1}(t)$, from a) laboratory and b) rotating frames of reference.....	51
Figure 3.4 -	Generating the $\mathbf{B1}$ rf pulse.....	52
Figure 3.5 -	Relaxation to thermal equilibrium. a) Longitudinal magnetization and b) Transverse magnetization.	54
Figure 3.6 -	Free induction decay (FID) signal.....	57
Figure 3.7 -	CPMG pulse sequence	59
Figure 3.8 -	Pulse sequence for a) Inversion Recovery and b) Saturation Recovery	61
Figure 3.9 -	Pulsed Field Gradient acquisition	62
Figure 3.10 -	Molecule's tumbling and diffusion restricted by interface	

	interactions.....	63
Figure 3.11 -	Magnetization profile in a “1D pore” for Slow and Fast diffusion limits.	65
Figure 3.12 -	Example of well log result with NMR standard petrophysical interpretation.....	69
Figure 3.13 -	Fluid fractions in a standard T2 distribution	70
Figure 3.14 -	Erratic motion of a molecule inside a fluid	71
Figure 3.15 -	Two common types of sensitive volumes - a) one sided or b) ring shaped	74
Figure 3.16 -	A simple B1 rf pulse and its corresponding Fourier Transform. Even if the pulse is tuned to a single frequency, its limited duration carries a band of frequencies around the predominant one.	75
Figure 3.17 -	CPMG blocks at several different frequencies (shells) through acquisition time (time increases to the right). Each acquired echotrain can have different waiting times (TW), echo times (TE), number of echoes (NE) and repetition number (Nrep).....	76
Figure 3.18 -	Example of gradient distribution.	78
Figure 3.19 -	Diffusion Editing pulse sequence	79
Figure 4.1 -	Error ϕMSQ as a function of regularization parameter α	89
Figure 4.2 -	Data projection for each eigenvector ui . The red dotted line represents the noise level of the data.	91
Figure 4.3 -	Density (red), neutron (blue), and sonic (pink) logs for well in a sandstone field.	93
Figure 4.4 -	Averaged echotrain from DT2 acquisition	94
Figure 4.5 -	Data projection for each eigenvector ui in a DT2 well data	95
Figure 4.6 -	Error as a function of regularization parameter α in a DT2 well data..	96
Figure 4.7 -	Data fit for a) echotrain as function of time and b) echotrain and noise as function of the position in the data vector d	96
Figure 4.8 -	Diffusion-relaxation distribution for the whole averaged interval shown in Figure 4.3. The dotted reference line corresponds to water diffusion coefficient at room temperature.	97
Figure 4.9 -	Reservoir 1 top zone. a) acquired data and fit as function of time b) normalized data, normalized noise and fit as function of position in data vector c) data projection over data space basis (SVD) d) fit	

	error as function of regularization parameter α . For final inversion there were used 100 singular values and $\alpha = 2$, based on fit curve.	98
Figure 4.10 -	Reservoir 1 bottom zone. a) acquired data and fit as function of time b) normalized data, normalized noise and fit as function of position in data vector c) data projection over data space basis (SVD) d) fit error as function of regularization parameter α . For final inversion there were used 100 singular values and $\alpha = 2$, based on fit curve.	99
Figure 4.11 -	Reservoir 2 top zone. a) acquired data and fit as function of time b) normalized data, normalized noise and fit as function of position in data vector c) data projection over data space basis (SVD) d) fit error as function of regularization parameter α . For final inversion there were used 100 singular values and $\alpha = 2$, based on fit curve.	100
Figure 4.12 -	Reservoir 2 bottom zone. a) acquired data and fit as function of time b) normalized data, normalized noise and fit as function of position in data vector c) data projection over data space basis (SVD) d) fit error as function of regularization parameter α . For final inversion there were used 100 singular values and $\alpha = 2$, based on fit curve.	101
Figure 4.13 -	DT2 distributions for a) reservoir 1 top zone b) reservoir 2 top zone c) reservoir 1 bottom zone d) reservoir 2 bottom zone.	102
Figure 4.14 -	Averaged log data acquired with parametrization of table 2	103
Figure 4.15 -	T2 distribution and data fit for long echotrain.	104
Figure 4.16 -	Error between fit and acquired data for short echotrain, as a function of $R = T1/T2$	105
Figure 4.17 -	Fit for long and short echotrans using $R = 2.1$ and full inversion described by matrix A of equation (4.38).	105
Figure 4.18 -	Comparison between distributions obtained from inversion of long echotrain only, and from complete data.	106
Figure 4.19 -	Data fit for long and short echotrans in a well section.	107
Figure 4.20 -	Comparison with the commercially delivered distribution and T1/T2 curve (black – service company and red – in house processing).	108
Figure 4.21 -	Single sided magnet	109
Figure 4.22 -	Field intensity as a function of the distance from the magnet.	109
Figure 4.23 -	a) CPMGs and b) T2 distributions for solutions with 0.01 , 0.1 and 1M of CuSO4 measured using a single sided magnet.	110
Figure 4.24 -	Echotrans acquired for solution with 0.1M CuSO4 in a diffusion editing experiment.	111

Figure 4.25 -	First echo amplitude as function of <i>TD</i> in diffusion editing sequences, for solutions with different concentrations of <i>CuSO4</i>	111
Figure 4.26 -	Gradient distributions calculated from data acquired with 0.1M concentration sample, using 0.6 and 0.2μs for radiofrequency pulses.	112
Figure 4.27 -	<i>DT2</i> maps for samples with 0.01 , 0.1 and 1M <i>CuSO4</i> concentrations, obtained from diffusion editing acquisition, and incorporating gradient distribution in the inversion.	113
Figure 4.28 -	<i>DT2</i> map for samples with 0.1M <i>CuSO4</i> concentration, obtained from diffusion editing acquisition, and considering a single gradient in the inversion.	114
Figure 5.1 -	<i>DT2</i> map obtained from a PFG experiment on water saturated rock core	116
Figure 5.2 -	Permeability prediction improvement by introducing surface relaxivity ρ in the model. a) standard <i>kSDR</i> model (equation 3 – 51) and b) <i>kρ</i> model (equation 3 – 52), compared with core permeability.	117
Figure 5.3 -	<i>T2</i> distribution for a water saturated reservoir	119
Figure 5.4 -	Modeled restricted diffusion coefficient using function <i>Drest</i>(Δ,<i>T2</i>), with $\rho = 5\mu\text{m/s}$ and $\Delta = 1, 5$ and 10$\mu\text{m/s}$. As diffusion time increases, long pore limit shrinks as more spins are subject to stronger restriction.	120
Figure 5.5 -	Modeled restricted diffusion coefficient using function <i>Drest</i>(Δ,<i>T2</i>), with $\Delta = 5\text{ms}$ and $\rho = 5, 15$ and 30$\mu\text{m/s}$. An increase of ρ makes the restriction for big pores less severe, making it difficult to detect	121
Figure 5.6 -	Modeled well logging diffusion editing data for various reservoir surface relaxivities.	122
Figure 5.7 -	Modeled well logging diffusion editing data for various SNR and $\rho = 5\mu\text{m/s}$	124
Figure 5.8 -	Inversion of diffusion editing data showed in Figure 5.6a. Continuous lines represent restricted diffusion coefficients <i>Drest</i>(<i>TD</i>,<i>T2</i>) , for each one of the diffusion times used in the modeling.	125
Figure 5.9 -	Restricted diffusion coefficient logarithmic mean <i>DLM</i>(<i>T2</i>) (star dots) compared with <i>Drest</i>(ΔRMS,<i>T2</i>) (continuous line).	126
Figure 5.10 -	Fitting results as a function of <i>T2C</i> , for all surface relaxivity simulated data.	127

Figure 5.11 -	a) Average fitted surface relaxivities as function of SNR and b) Average fitted surface relaxivities and standard deviations. Each noise level was repeated 30 times for calculating statistics. Dotted lines correspond to the real values used in the forward modeling.	128
Figure 5.12 -	a) Average fitted surface relaxivities as function of SNR for data modeled from a distributed gradient tool, and b) Average fitted surface relaxivities and standard deviations. Each noise level was repeated 30 times for calculating statistics. Dotted lines correspond to the real values used in the forward modeling.....	129
Figure 5.13 -	a) <i>D0</i> and b) <i>ρ</i> determined at each iteration, for example cases where data was simulated with <i>ρ</i> = 5, 10 and 15 μm/s	132
Figure 5.14 -	Example of data fit (continuous black lines) generated by the non-linear regression algorithm. Data was simulated with <i>ρ</i> = 5 μm/s , and estimated parameters were <i>ρ_{est}</i> = 5.70 μm/s and <i>D0_{est}</i> = 2.25 10 – 9 m²/s	133
Figure 5.15 -	a) Average fitted surface relaxivities (using the non linear regression algorithm) as function of SNR and b) Average fitted surface relaxivities and standard deviations. Each noise level was repeated 30 times for calculating statistics. Dotted lines correspond to the real values used in the forward modeling.	134
Figure 5.16 -	a) Average fitted surface relaxivities (using the non linear regression algorithm) as function of SNR for data modeled from a distributed gradient tool, and b) Average fitted surface relaxivities and standard deviations. Each noise level was repeated 30 times for calculating statistics. Dotted lines correspond to the real values used in the forward modeling.	135
Figure 5.17 -	PFG data for brine saturated carbonate samples, along with corresponding <i>T2</i> distributions.	140
Figure 5.18 -	Relaxivities from non-linear regression as function of expected ones, for several <i>r</i> values.	141
Figure 5.19 -	Relaxivities from non-linear regression as function of expected ones, for <i>r</i> = 0.8	141
Figure 5.20 -	<i>ρ_{estimated}/ρ_{expected}</i> as a function of <i>T2_{max}/T2_c</i> , for all samples.	143
Figure 5.21 -	a) Well logging diffusion editing acquisition and b) corresponding <i>T2</i> distributions.	144
Figure 5.22 -	<i>DT2</i> map for well logging diffusion editing data.	145
Figure 5.23 -	Relaxivity iteration steps for well logging diffusion editing data.	145

Figure 6.1 -	Schematics of a pore system.....	148
Figure 6.2 -	Grid subdivision of a schematic pore system.	149
Figure 6.3 -	Representation of a single cell in the pore system.....	151
Figure 6.4 -	Cubic cell represented along the x axis, located at $x = n\Delta x$	151
Figure 6.5 -	Spherical cell located at $r = n\Delta r$, $\theta = m\Delta\theta$ and $\phi = l\Delta\phi$, focused mainly on the r dimension.	153
Figure 6.6 -	Spherical cell located at $r=n\Delta r$, $\theta=m\Delta\theta$ and $\phi=l\Delta\phi$, focused mainly on the θ dimension.	155
Figure 6.7 -	Example of cell subdivision in a spherical pore.	158
Figure 6.8 -	Comparison between exact solution (black circles) and master equation approach (red star dots) for normal modes and relaxation rates in a sphere of radius $a = 10\mu m$ in the fast diffusion limit, using 4 cells.	160
Figure 6.9 -	Comparison between exact solution (black circles) and master equation approach (red star dots) for normal modes and relaxation rates in a sphere of radius $a = 10\mu m$ in the slow diffusion limit, using 39 cells.	160
Figure 6.10 -	Attempt of cell subdivision in a cubic pore.	161
Figure 6.11 -	Comparison between exact solution (black circles) and master equation approach (red star dots) for normal modes and relaxation rates in a cube of side $a = 10\mu m$ in the a) fast diffusion limit with 10 cells and b) slow diffusion limit with 19 cells.....	162
Figure 6.12 -	Natural shell subdivision for a cubic pore, respecting pore geometry and free diffusion symmetries.	163
Figure 6.13 -	Diffusion-relaxation eigenmode 111 contour plot for a cubic pore.	164
Figure 6.14 -	Diffusion-relaxation eigenmodes a) 113 and b) 115 contour plots for a cubic pore.....	165
Figure 6.15 -	Building symmetrical surfaces for a cubic pore.	166
Figure 6.16 -	Comparison between exact solution (black circles) and master equation approach (red star dots) for normal modes and relaxation rates in a cube of side $a = 10\mu m$ in the slow diffusion limit with 30 cells. The cells were made symmetrical with respect to the pore shape and free diffusion.....	167

LIST OF TABLES

Table 2.1 -	Grain sizes classification	29
Table 3.1 -	<i>T2</i> distribution acquisition scheme	76
Table 3.2 -	<i>T1T2</i> distribution acquisition scheme	77
Table 3.3 -	<i>DT2</i> acquisition scheme	77
Table 4.1 -	Well logging <i>DT2</i> distribution acquisition	94
Table 4.2 -	Well logging <i>T2</i> distribution acquisition	102
Table 5.1 -	Routine core analysis (porosity and permeability) and surface relaxivity, for the core samples studied.	136

LIST OF SYMBOLS

ϕ	Porosity
k	Permeability
S_w	Total water saturation
S_{wirr}	Irreducible water saturation
F	Formation factor. Ratio between saturated rock core resistivity and water resistivity
R_t	Rock core resistivity
R_w	Water resistivity
$\vec{\mu}$	Nucleus magnetic dipole moment
\vec{S}	Nucleus spin operator
\vec{B}_0	Static magnetic field
\vec{M}	Net magnetization
M_z	Longitudinal magnetization
M_T	Transverse magnetization
γ	Gyromagnetic ratio
\hbar	Planck's constant
\vec{I}	Dimensionless spin operator \vec{S}/\hbar
I_q	q component of \vec{I} , with $q = x, y, z$
I	Total spin number
H_0	Zeeman Hamiltonian
$ m\rangle$	Eigenstate for Zeeman Hamiltonian
ω_0	Larmor frequency
$ \psi\rangle$	General quantum mechanical state
M_0	Equilibrium magnetization
\vec{B}_1	Oscillating magnetic field
H_1	Perturbing hamiltonian
\vec{b}	Local magnetic field fluctuation
$\tilde{\sigma}$	Quantum density operator
g_{qq}	Fluctuation self-correlation function
τ_c	Fluctuation self-correlation time
T_1	Longitudinal relaxation time

T_2	Transverse relaxation time
J_{qq}	Self-correlation spectrum
\vec{m}	Magnetization density
m_z	Longitudinal magnetization density
m_T	Transverse magnetization density
D_0	Bulk diffusion coefficient
\vec{G}	Magnetic field gradient
T_E	Time between echoes
T_I	Acquisition time values for Inversion Recovery
T_S	Acquisition time values for Saturation Recovery
δ	Gradient pulse duration
Δ	Time between gradient pulses. Diffusion time
T_{1B}	Bulk longitudinal relaxation time
T_{2B}	Bulk transverse relaxation time
ψ_n	n-th diffusional eigenmode for Bloch-Torrey's equation
ρ_1	Longitudinal surface relaxivity
ρ_2	Transverse surface relaxivity
ρ	Surface relaxivity
S/V	Surface per volume ratio
f	Distribution function
D_∞	Restricted diffusion coefficient for long diffusion times
g	Gradient distribution
T_D	Time between first and second echoes in diffusion editing acquisition
\mathbf{d}	General data vector
\mathbf{A}	General model matrix
\mathbf{f}	General distribution vector
p_n	Number of particles in cell n
λ_{nm}	Transition rate from cells n to m
λ_n^S	Absorption rate in cell n through surface S
ΔV_n	Volume of cell n
\bar{A}_n	Mean surface area of cell n

CONTENTS

1	INTRODUCTION AND OBJECTIVES.....	23
2	BASIC PETROPHYSICS AND OIL/GAS EXPLORATION.....	25
2.1	Sedimentary rocks – origins and properties	25
2.2	Petrophysics and petrophysical properties	30
2.3	The Petroleum System and Well Logging.....	37
3	NUCLEAR MAGNETIC RESONANCE THEORY AND LOGGING APPLICATIONS	45
3.1	Basic NMR theory	45
3.2	Laboratory acquisition techniques.....	58
3.3	NMR in porous media – Petrophysical Interpretations	62
3.4	NMR Well logging: general tool's characteristics and acquisition protocols	73
4	DATA PROCESSING	81
4.1	Determining model matrix A	82
4.2	Ill posed nature of the inversion problem	86
4.3	Inversion algorithm description.....	90
4.4	Application for DT2 well logging acquisition: fluid typing.....	92
4.5	One dimensional T2 distributions and T1/T2 ratio estimation	102
4.6	Determining gradient distribution for inhomogeneous magnetic fields.....	108
5	SURFACE RELAXIVITY FOR WELL LOGGING.....	115
5.1	Laboratory determination of surface relaxivity and challenges for well logging.....	115
5.2	Developing ρ logging method – forward simulations and DT2inversions.....	118
5.3	ρ logging method – raw data non-linear regression	130
5.4	Laboratory Experimental Results	136
5.5	Well Logging Experimental Results.....	143
6	ANALYTICAL APPROXIMATIONS FOR DIFFUSION IN POROUS MEDIA – DIGITAL ROCK.....	147
6.1	Rate equations and transition rates	149
6.2	Comparison with exact solutions.....	157
6.3	Generating diffusional and geometrical symmetric cells for an arbitrary pore.....	165
7	CONCLUSION AND PERSPECTIVES	169
	REFERENCES	171

1 INTRODUCTION AND OBJECTIVES

Nuclear Magnetic Resonance (NMR) comprehends a vast number of techniques based on few phenomena arising from the interaction between magnetic fields and the magnetic nuclear dipoles of the atoms. All these different measurement styles and techniques are nowadays applied in several fields of investigation such as:

- Physics and chemistry characterization: Materials, molecular spectroscopy
- Health, medicine, neuroscience: Magnetic Resonance Imaging (MRI)
- Quantum information
- Fluid quantification and materials characterization for several industry branches: food, oil and gas, construction engineering
- Subsurface exploration for searching mining sites and oil and gas reservoirs

We will focus specifically on NMR techniques used in the oil and gas industry for reservoir petrophysical characterization. In a standard exploration program, several physical properties of potential reservoirs are measured in the well site, including NMR relaxation times for saturating fluids and possibly their diffusion coefficients. Under certain assumptions, diffusion coefficients and relaxation times correlate with the rock pores geometry and specifically pore sizes. Therefore, these techniques are widely used for rock porosity determination and permeability prediction.

Specifically, transverse magnetization relaxation rates can be proportional to rock pore sizes under certain circumstances, the proportionality constant being called surface relaxivity. Surface relaxivities can be determined in the laboratory by combining NMR diffusion measurements and electrical conductivity data. However, downhole NMR data are much noisier than lab measurements, and well logging electrical data are usually not robust enough to allow such calculations for complex reservoirs. Indeed, electrical conductivity values for carbonate reservoirs are usually close to or beyond the tolerable tool limits. Also, NMR acquisition schemes for well logging require adaptations of the available methods for obtaining relaxivities. Therefore, the main objective of this work is the development of a method capable of overcoming these challenges in obtaining surface relaxivities for well logging data. The results can then in principle be used to obtain pore size distributions downhole, improving permeability predictions and reservoirs' evaluation.

As a secondary objective, we analyze the diffusion equation with partial absorptive contour conditions (which models NMR relaxation and diffusion measurements) in terms of simple rate equations. The resulting transition rates between different sites depend on the

geometry of the cells, and can be used for modeling other processes based on diffusion, such as exchange measurements and diffusional coupling.

These objectives and contents are distributed in the thesis in the following way.

In Chapter 2 we contextualize the topic of formation evaluation and petrophysics, giving a brief description of the petroleum exploration chain, and the process of well drilling and logging. Chapter 3 is dedicated to the introduction and development of NMR theory and basic measurement schemes, including discussion of well site conditions, and behavior of relaxation times and diffusion coefficients for fluids trapped inside a porous medium. In Chapter 4 we describe a general processing workflow for NMR data inversion, applicable for different kinds of data generated downhole. Chapter 5 discusses a way of adapting existing methods for determining surface relaxivity via downhole measurements, providing laboratory and well logging examples.

Finally, in Chapter 6 we develop a way of understanding the diffusion of magnetization inside a rock pore, based on pore imaging. The method provides analytic approximations for the solution of the diffusion equation subject to absorptive contour condition for, in principle, an arbitrary shaped pore. The diffusion problem is formulated in terms of rate equations, where transition rates are calculated from surface areas and volumes of the pore.

2 BASIC PETROPHYSICS AND OIL/GAS EXPLORATION

Fossil fuels such as petroleum and coal still constitute the main (nonrenewable) energy sources in our global matrix energy. Petroleum, specifically, is a complex mixture of hydrocarbons that is stored in the subsurface as a result of millions of years of natural processing of organic matter, through exposition to high pressures and temperature. This organic matter is the remainder of once living beings (mostly phytoplankton and algae) that accumulate in ancient oceans, lakes or riverbeds through geologic time. Oil and gas are then found between the pores of reservoir rocks, most of the time sharing this space with water. (1)

The process of finding new petroleum fields depends firstly on gathering the most information available on the geologic history and subsurface structure that result in probable reservoir sites, and then, once those plays are identified, on answering with the best precision mainly two important questions: how much oil and/or gas are available in such reservoir, and how easy it is to get them out. These two questions, on **storage capability** and **fluid transport**, constitute some of the **petrophysical** assessments one should be interested in.

Petrophysics can be defined as the study of physical properties of rocks, as well as their interaction with fluids contained in them. (2) These properties are mainly controlled by the geologic history of formation and development of the rocks. Therefore in this chapter, we will describe how sedimentary rocks are formed and some important factors that control their petrophysical properties. We then define the geological components of a petroleum play, as well as the ways petrophysics is usually assessed downhole in an oil/gas well.

2.1 Sedimentary rocks – origins and properties

There are three general rock types occurring in nature: igneous, metamorphic and sedimentary. Igneous rocks result from solidification of magma from cooling either at Earth's surface or subsurface. Metamorphic rocks result from physical and chemical transformations occurring in pre-existent ones due to compression, high temperatures and reactions with fluids in subsurface. Although in principle any kind rock can hold oil and gas and therefore constitute a legitimate petroleum reservoir, we will focus on the third kind, sedimentary, which constitute the majority of Earth's known reservoirs. (3)

Sedimentary rocks are formed from pieces of preexistent ones or dissolved minerals that under certain conditions of burial, compression and or chemical

precipitation/transformation, aggregate into new rocks. The origin of such rocks can be understood in terms of the following simplified stages:

Weathering and Erosion

Processes by which rocks are fragmented or dissolved, due to the action of weather and chemical reactions, and are mobilized to other locations. Due to mechanical weathering, fragmentation can occur because of successive expansions and contractions of the materials due to temperature variations, friction with abrasive materials carried by water or wind currents as well as with rain water, for example. Weathering can also have chemical origins, as contact with water can promote rock dissolution. The sediments are therefore rock fragments (or clasts), remains of living beings (bioclasts such as shells) or dissolved materials. It is important to notice that the analysis of types of sediments which constitute a certain formation can give clues to the type of environment in which those clasts or minerals were formed.

Transport and deposition

Sediments can be carried away mainly by water and air currents to be deposited in locations that can be different than those of the source rocks. The intensity of the currents determine the size of the sediments that are carried away. Strong water currents of rivers or sea waves can carry larger clasts, while calmer waters of less steep streams or deep oceans tend to allow deposition of much finer grains. Winds are also usually able to carry only lighter grains, and friction between these grains tend to give them rounder shapes. These examples show that the types of transport also reflect on the grain size distribution of sedimentary rocks. Those resulted from grains carried by the wind, for example, have a sharp size distribution and are called well sorted rocks. Figure 2.1 shows an example of a well sorted sandstone, where one can see the grains have approximately the same sizes.

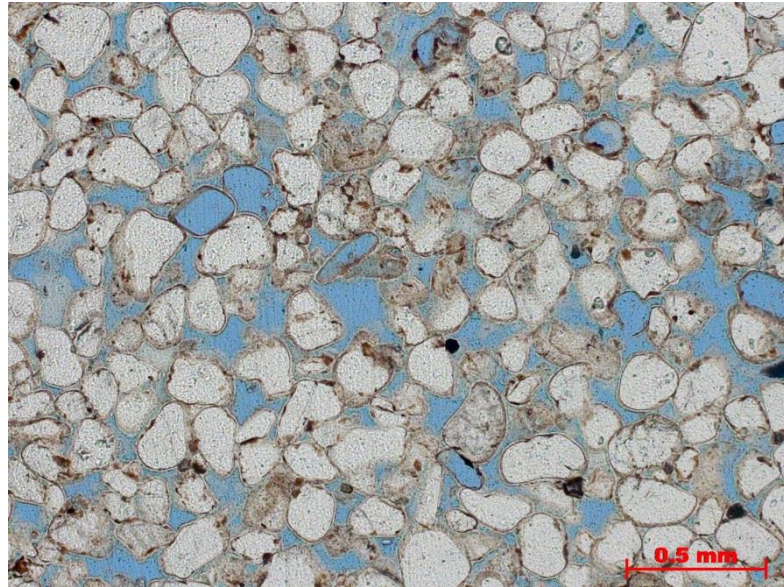


Figure 2.1 - Thin section of a well sorted Botucatu Sandstone.
Source: By the author.

On the other hand in Figure 2.2 one can see a sandstone with a broader grain size distribution. That could come from sediments carried and deposited by higher energy currents, able to transport larger clasts.

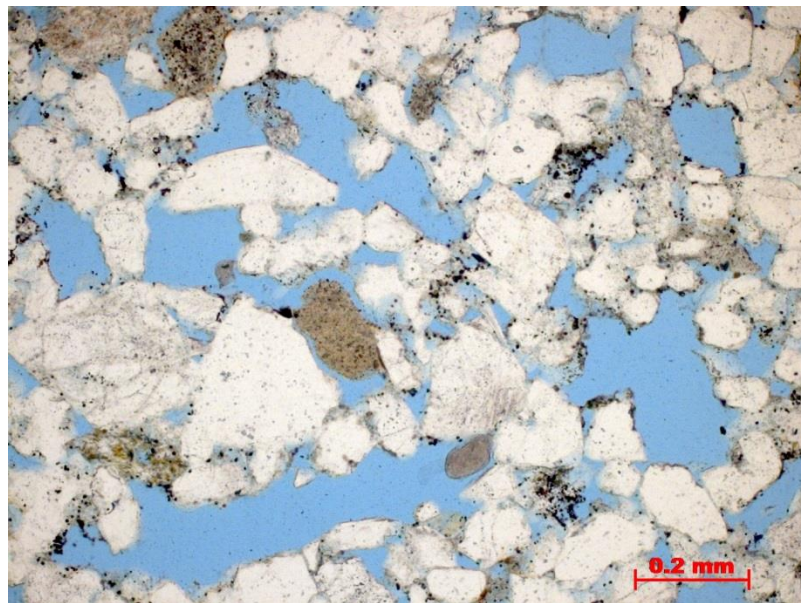


Figure 2.2 - Thin section of a poorly sorted Leopard Sandstone.
Source: By the author.

Deposition can also occur through precipitation of dissolved minerals, through favorable chemical reactions of that specific environment. Shallow salt lakes, for example, can favor precipitation of salt, creating evaporitic rocks. The action of living organisms can also favor the deposition of biochemical sediments.

Once again, these examples show that analysis of textural characteristics of the grains composing a sedimentary rock can tell the story of all these transport possibilities, therefore giving clues about the entire environment that existed by that time.

Diagenesis

After deposition, the sediments can be solidified through physical and chemical processes, creating the actual sedimentary rocks. Burial increases the pressure over the sediments giving rise to a compaction process, which associated with an increase in temperature can glue the clasts together. Other diagenetic processes can be produced by chemical reactions, as the precipitation of minerals forming cement between the grains (cementation process that decreases the space between grains). Chemical reactions can also produce the substitution of minerals by others, increasing or decreasing the space between grains, or by dissolution of minerals due to contact with water, increasing the space between grains. The action of living organisms can also alter the original depositional distribution of grains and minerals, via mechanical or chemical processes.

In this work, we will deal specifically with two classes of sedimentary rocks that are described below: clastic or siliciclastic rocks and carbonates.

Siliciclastic rocks

Frequently called simply as sandstones, they are rocks formed from the aggregation of clasts and fragments (usually silicates such as quartz) of other rocks, by the processes described before. They can be formed far from the rocks that originated these fragments because of the transport processes (water currents, gravity flows), therefore being deposited in several environments ranging from riverbeds to deep ocean. They have in general a simple pore structure, governed primarily by the grain sizes distribution.

The grain sizes are usually classified accordingly with Table 2.1 below (intermediate grain sizes are called sands, and finer sizes are silts and clays).

Table 2.1 - Grain sizes classification

Particle size (mm)	Sediment classification
> 256	Boulder
64 – 256	Cobble
2 – 64	Gravel
0.062 – 2	Sand
0.0039 – 0.062	Silt
< 0.0039	Clay

Source: Adapted from PRESS et al. (3)

Clastic rocks formed predominantly of sand sized grains are called sandstones, those formed of grains with silt size are siltstones. Another important clastic rock type is the one formed by a fine mix of silts and clay sized grains, called shale rocks.

Carbonate rocks

Sedimentary rocks formed by precipitation of dissolved components by chemical reactions. Because of the chemical nature of the sediments the depositions are made not too far from the original rocks, and therefore are limited to fewer depositional environments, such as calm lakes with biological activity, and sea coasts not too deep (within the carbonate compensation depth, where the deposition of carbonates is favorable).

They are mainly limestones, which are formed of calcium carbonates (CaCO_3), and dolomites ($\text{CaMg}(\text{CO}_3)_2$), formed by substitution processes.

Since carbonate formation is mainly governed by chemical reactions, they are much more subject to diagenetic process, and can have pore structures that are way more complex than those of sandstones. Carbonates pore spaces can be intergrain, like clastic ones, but can also be extremely impacted by dissolution forming either empty spaces of order of milimeters to centimeters (vugs), or microporosity spaces within the grains. On the other hand, cementation can close the pore spaces almost completely. Unlike sandstones, carbonate pore throats have little to do with the original clasts size distributions.

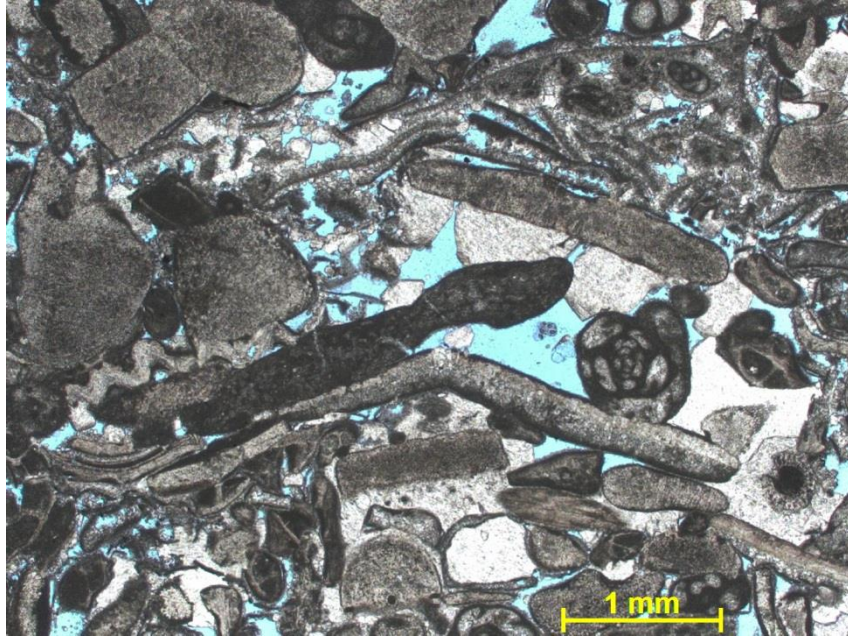


Figure 2.3 - Example of carbonate structure - Indiana Limestone.
Source: By the author.

In the following section we define the main petrophysical properties of rocks, and how they are related with the formation of sedimentary rocks discussed above.

2.2 Petrophysics and petrophysical properties

The history of a sedimentary rock, specially deposition and diagenetic processes, determines its petrophysics properties. As defined in the introduction of this chapter, Petrophysics comprises the study of physical properties of rocks, as well as their interactions with saturating fluids. We list in this section the main petrophysical parameters one is interested in an Exploration or Production program, how they are measured and how they relate with the origins of the rock. (2)

Porosity (ϕ)

It is the ratio between the total empty volume (pore volume V_p) and the bulk rock volume V_b (comprising empty space plus rock matrix), therefore being an indicator of the rock's fluid storage capacity:

$$\phi = \frac{V_p}{V_b} \quad (2.1)$$

Primary porosity is the pore space fraction at the time of deposition and secondary porosity is developed from diagenetic processes such as dissolution (increasing porosity) or cementation (decreasing porosity).

For sandstones, porosity is generally mostly primary, with pore sizes proportional to grain sizes. For well sorted grains porosity is maximum, depending only on the grain packing configuration. For poorly sorted sandstones, smaller grains tend to occupy spaces inaccessible by bigger ones, hence decreasing porosity. Other important factors can decrease porosity in clastic rocks such as cementation and the presence of clay minerals that obstruct the pore throats.

Carbonate rocks are much more amenable to chemical reactions, therefore having porosities mainly controlled by secondary processes. Porosity is then much governed by dissolution, yielding to microporous spaces within grains, or by cementation, sometimes closing pore spaces completely. Substitution of minerals are much more present, and can either increase or decrease porosity. Presence of clay minerals is much less frequent than in sandstones. These factors combine to generate a much more complex pore space structure in carbonates than in sandstones, which can affect the flux properties of fluids dramatically.

Porosity is usually measured in the laboratory by saturating the core with gas such as nitrogen or helium, inside a chamber of known volume V_1 . The chamber is then coupled with a second one (volume V_2 , originally evacuated) and pressure values are taken in the initial and final condition (P_1 and P_2 respectively). If the temperature is held fixed, Boyle's Pressure and Volume Law for Ideal Gases can be used to determine empty pore space as:

$$V_b - V_p = V_1 - V_2 \left(\frac{P_2}{P_1 - P_2} \right) \quad (2.2)$$

Pore space can also be measured using other fluids. For instance, one could saturate the rock with water and obtain porosity by measuring weights differences between initial and final conditions. The advantage of using gases instead of liquids is that they are less affected by capillary forces and are able to access the whole interconnected pore space, not being necessary the application of high confinement pressures.

It is worth pointing out that these methods measure only effective porosity, which is interconnected pore space. Isolated pores are not accounted by these measurements. Typical reservoir porosities range from 5 to 15% for carbonates and from 10 to 20% for sandstones.

Absolute permeability (k)

As important as being able to determine the rock's storage capacity, is the quantification of the ability of a fluid to go through the porous medium. Permeability is governed by the amount of interconnections between the pores through pore throats, and also by the pore throats sizes. Smaller throats for instance will oppose to fluid motion due to increasing capillary forces.

Henry Darcy experimentally studied fluid flow through porous media, and obtained a well known relation between flow rate q of a fluid passing through a core of length L , and the pressure drop ΔP . Darcy's Law stands as the definition of permeability k :

$$q = -\frac{kA}{\mu} \frac{\Delta P}{L} \quad (2.3)$$

In equation (2.3) μ is the fluid viscosity and A is the cross sectional area of the plug.

In clean sandstones (with no presence of clay minerals), permeability tend to have high values for well sorted big grains, as the pore throat sizes correlate with grain sizes. For small, but still well sorted grains, although porosity won't change, permeability will diminish because of decreasing throat sizes. For poorly sorted rocks smaller grains will tend to obstruct the pore throats, also decreasing permeability.

Complex carbonate structure will give rise to more complicated permeability behavior. Big pore sizes are not determinant of good flow rates because connections are highly affected by diagenetic processes, and do not correlate in general with pore sizes.

Permeability is measured in the Laboratory by flowing gas such as nitrogen or helium through a confined rock plug, and by measuring the pressure drop. Knowledge of the core's dimensions and fluid viscosity allows the use of equation (2.3) to determine k .

Typical values of k range from below 1mD for bad permeabilities to tenths or hundreds of mD for intermediate to good values. $1\text{Darcy} = 9.869 \cdot 10^{-13} \text{m}^2$, which is an extremely high permeability value.

A simple model for determining permeability from first principles was developed by Kozeny and Carman (2,4) in which they considered a porous medium of length L being made as a network of tortuous pipes or capillaries of lengths $L_c \geq L$ and radius r . Poiseuille's law for flow rate through cylindrical capillaries gives:

$$q = \frac{\pi r^4}{8\mu} \frac{\Delta P}{L_c} \quad (2.4)$$

Comparing with Darcy's Law, permeability is given by:

$$k = \frac{\phi r^2}{8(L/L_c)^2} \quad (2.5)$$

The ratio (L_c/L) is a measure of how “tortuous” the porous medium is. The petrophysical parameter tortuosity is defined as:

$$\tau = \left(\frac{L_c}{L}\right)^2 \quad (2.6)$$

It is important to notice that equation (2.5) relates permeability with the square of a characteristic size of the pore/throat, and also with porosity. This observation is the key for the development of permeability models from NMR data, which will be discussed further on (Chapter 3).

Pore Size Distribution

As a result of the ways sedimentary rocks are formed, one should not expect that these porous media would be formed of pores with only one well defined pore size. In fact, rocks have a distribution of pore sizes, depending on the quality of grain sorting and intensity of diagenetic action.

Well sorted clean sandstones tend to have a narrow single peaked pore size distribution such as the one showed in Figure 2.4. A carbonate with high primary porosity but with grains highly affected by dissolution could have instead a bimodal pore size distribution such as Figure 2.5.

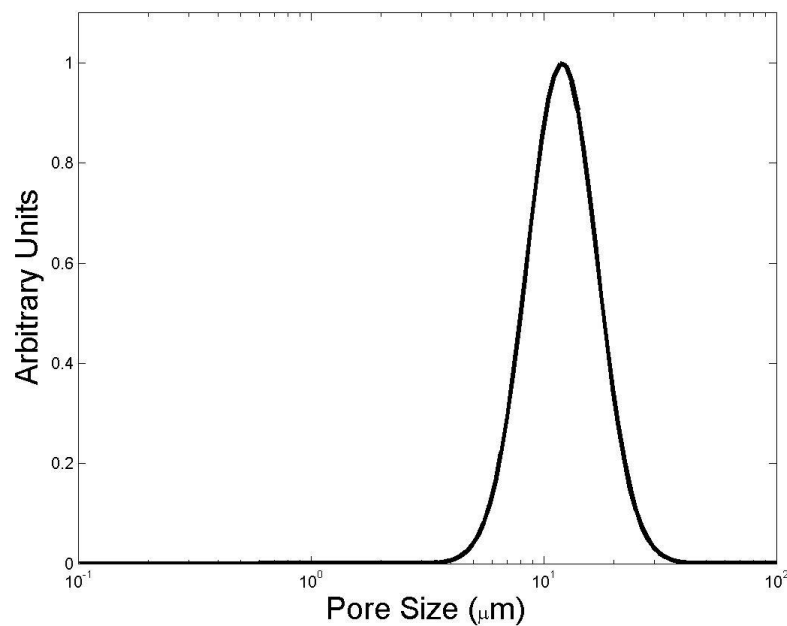


Figure 2.4 - Single peaked pore size distribution.
Source: By the author.

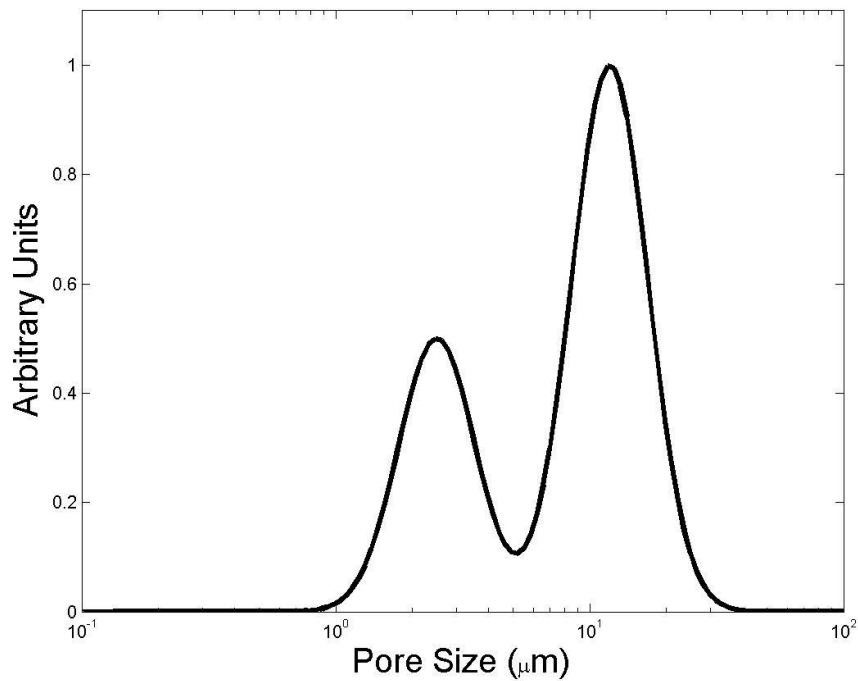


Figure 2.5 - Bimodal pore size distribution.
Source: By the author.

Measuring pore size distribution is not a trivial task. One useful technique is rock core imaging using x-ray tomography. The drawbacks of this method are resolution, that is usually not smaller than a few microns, and the difficulty (shared with all other methods) of giving an unique mathematical/geometrical definition of pore size.

An indirect method is to measure the Pore Throats Size Distribution instead, using the Mercury Injection Capillary Pressure (HgCP) technique. In this technique the core is confined and immersed in liquid mercury, which is submitted to increasing pressures. As the pressure increases, mercury becomes able to overcome capillary pressure from smaller throats and to invade more of the pore space. The amount of Hg absorbed by the rock at each pressure step correlates with the amount of pore throats having a specific radius.

By converting the pressure axis into pore throat radii through a capillary force model, and by changing the y-axis from cumulative to incremental volume, one can get the throat sizes distribution as in Figure 2.6.

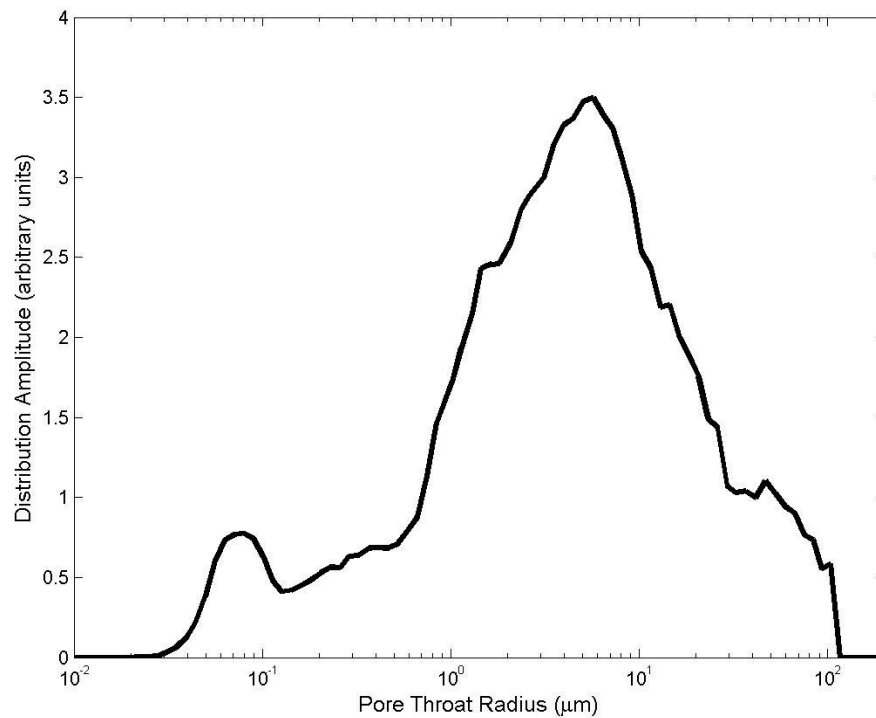


Figure 2.6 - Example of pore throat distribution.
Source: By the author.

In sandstones, where pore throats are in general proportional to pore sizes, the pore throats distribution can be used as a representation of pore sizes distribution. For more complex carbonates this is not the case.

Another extremely useful technique (as it is the only one that can be used downhole) for determining pore size distributions is through the measurement of NMR relaxation times distributions. As will be seen in Chapter 3, NMR relaxation times of fluids saturating rocks correlate under certain conditions with the volume to surface ratio of a pore (hence pore size), and can be used to estimate pore structure properties such as permeability. We will leave this discussion to Chapter 3.

Fluid saturation

In an actual oil or gas reservoir, the pore space is filled with more than one fluid. Water is always present because sediments are deposited in water environments such as rivers, lakes or oceans, and hydrocarbons tend to occupy the pore space after organic matter is processed in the subsurface. The fraction of a certain fluid with respect with the whole pore volume is that fluid saturation.

Because of capillary forces between water and the pore walls, a residual water saturation is always expected to remain inside a rock core even after the draining of that plug after application of high pressures. Figure 2.7 shows a capillary pressure curve relating applied pressure through a rock core as function of remainder water saturation S_w .

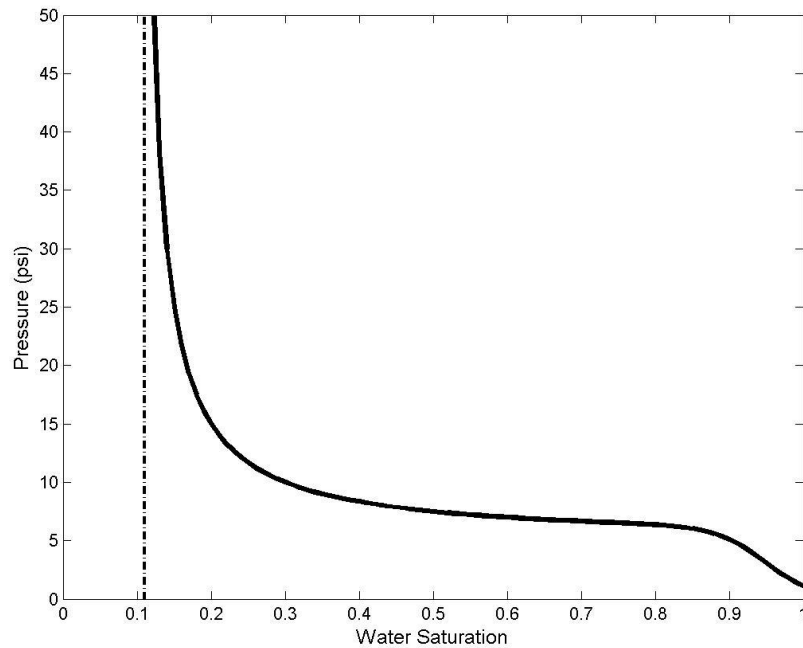


Figure 2.7 - Capillary pressure curve.
Source: By the author.

It can be seen in Figure 2.7 that as the water saturation diminishes, a great increase of pressure tends to expel lesser amounts of water. The limit at which an increase of pressure expels no water at all defines the irreducible water saturation S_{wirr} . This is the water trapped inside the reservoir by capillary forces. We can therefore define the following important parameters (2,5):

BVC (Bound Volume Capillary) – Water or oil volume trapped in pores that are too small or are connected through small throats so that capillary forces are too strong to allow flow.

CBW (Clay Bound Water) – Water trapped by clay minerals

BVI (Bound Fluid Irreducible) – CBW + BVC, that is the total amount of fluid that cannot flow.

FF (Free Fluid) – Amount of water or oil inside pores that are big enough or connected through larger throats that allow flow.

With these definitions, we can see that effective porosity defined before comprises the fluid portions FF and BVI, while total porosity comprises all the volumes.

The amount of free oil available in a reservoir depends on these parameters, and irreducible water also affects its flow capability. We will discuss further on how these parameters are estimated downhole.

Wettability

Wettability is the affinity a certain fluid has with the pore walls. During the formation of a sedimentary rock, clasts or precipitates are aggregated in a water environment, therefore making the pore walls water wet. However when hydrocarbons percolate through the reservoir, depending on the pore walls mineralogy, the rock can experience a wettability inversion. Sandstones tend to remain water wet, as carbonates are more amenable to become oil wet or with mixed wettability.

Knowing which fluid is touching the pore walls is important for oil recovery strategies, once it is easier to flow free oil through a water wet environment, because of less capillary interaction with pore throat.

2.3 The Petroleum System and Well Logging

As briefly described in previous sections, the history of sedimentary and other kinds of rocks might be a really complex one, specially when put in context with broader movements of Earth and its environments. Consider for instance Plate Tectonics Theory. Relative motion between major pieces of Earth crust generating a myriad of environments, ranging from the largest mountains, to several different basins and finally the deepest seas. During millions of years, these environments change, favoring from time to time exposure to intensive weathering, vast deposition and sedimentary processes, exposure to action of living organisms, or large periods of deep silence. Each of these processes creates different rock formations, organized in complex layers in the subsurface, each one with its particular petrophysical properties. For a petroleum system to be able to form in a given sedimentary basin, all these processes must converge to the following elements of an conventional oil/gas play (1):

Source rocks: These are sedimentary rocks which were deposited with a great amount of organic matter. When subject to enough burial, therefore ideal pressure and temperature, a series of chemical reactions occur transforming organic matter in oil and/or gas, depending on the composition of the original matter, the amount of pressure and temperature, and the duration of the reactions. Petroleum is then expelled from generating rocks in a process called

primary migration. Generating rocks are usually shales, that in spite of having a great range of porosities, are really little permeable.

Reservoir rocks: Permeable and porous rocks (mostly generated by the sedimentary processes already discussed) that will store petroleum. In conventional fields they can be made of sandstones or carbonates. After primary migration, oil and gas must find a permeable and porous path to move upwards due to buoyancy forces (these fluids are less dense than water), against opposing capillary forces. This process that can also take millions of years and is called **secondary migration**, and goes on until the fluids hit a **trap** made by a much less permeable rock, a **seal rock**. Sealing rocks can be usually shales or salt.

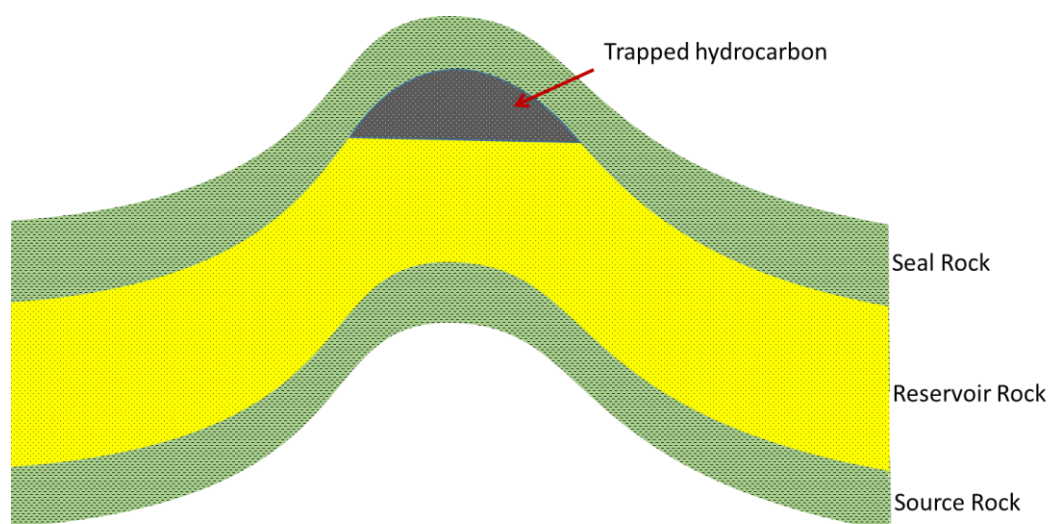


Figure 2.8 - Example of a geologic model containing the elements of a petroleum system.
Source: By the author.

The last key element is the timing between these events. If a seal forms after secondary migration, or if everything is in its correct place but generating rocks had never hit a mature stage of pressure and temperature, no oil field will be formed.

In an Exploration Process, those elements are contextualized in the major low frequency history of the basin, and a geologic model of how subsurface should look like is developed. For this matter, knowledge of drilled nearby wells and other input data can be used. Subsurface can be sounded using seismic, gravitational or electromagnetic methods. In seismic exploration, for example, large sources of energy such as explosives or air cannons (in marine acquisitions) excite sound waves that propagate downward. As these waves are reflected and scattered by the layers of rock formations, their returning times are recorded by a large grid of detectors at the surface. These times are processed generating an image of the

major structures that exist below the surface, as the one showed in Figure 2.9 (made available by Stewart (6) at Virtual Seismic Atlas website).

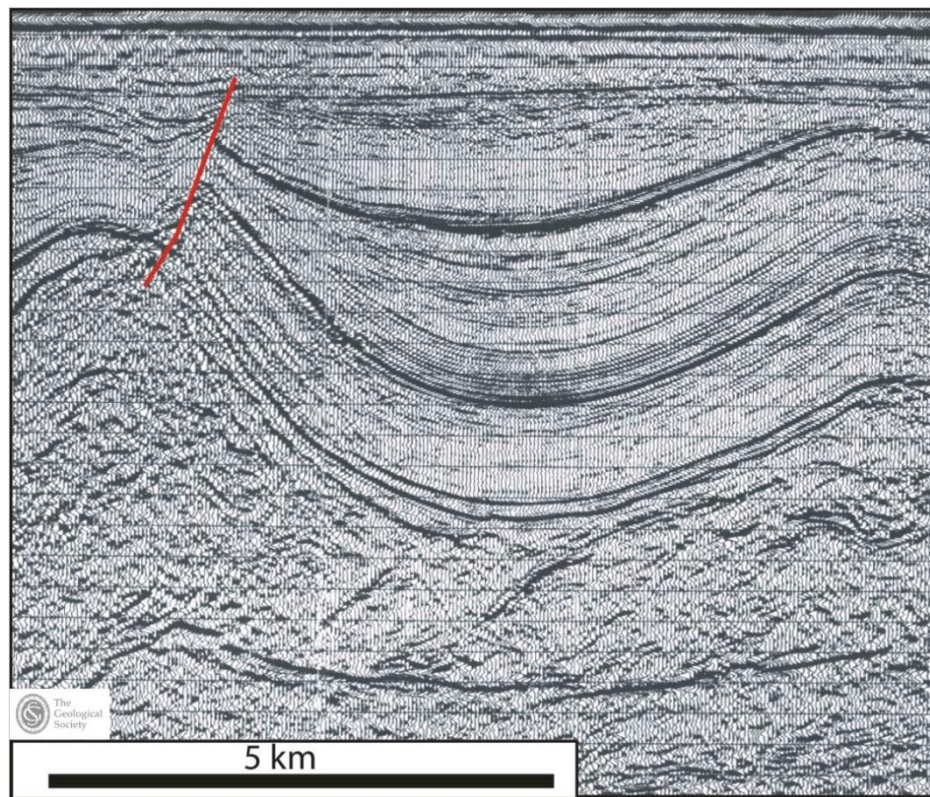


Figure 2.9 - Example of seismic image.
Source: Adapted from STEWART. (6)

Based on such images and geological knowledge, a drilling site is chosen for searching petroleum accumulations. During well drilling several pieces of information are obtained such as a general description of rock types at each depth (sandstones, carbonates, shales, salt...), and indicators of oil and gas presence. Once a drilling section of the well is completed, a more complete set of petrophysical information is obtained from the exposed well walls, in a process known as logging and formation evaluation.

Logging tools are put inside the well bore and measure a set of physical parameters that will be interpreted and converted into petrophysical data for the rock formations. At this point, the objective is to find the reservoirs, estimate their porosities and permeabilities, the amounts of fluids contained in them, the intervals that are oil/gas filled, among other petrophysical parameters. The most common well logging measurements are described below.
(2,5)

Gamma Ray Log

Measures the natural gamma radiation emitted by elements that compose the formation, mostly Uranium, Thorium and Potassium. As these radioactive elements tend to sediment with fine sized grains like silt or clays, gamma ray log is usually an indicator of shale content in a formation.

Density, Neutron and Sonic logs

Density tools use a radioactive source to send gamma ray photons to the rock formation, which are scattered by formation electrons through Compton Effect. As a consequence, these photons have different energy and frequency, which enables their detection by an appropriate sensor in the tool. The measured amount of scattered energy converts into counting of electron density, which can then be translated in bulk formation density ρ_b . If assumptions are made for rock matrix density ρ_m (sandstones have density around $2.65g/cm^3$ and carbonates about $2.71g/cm^3$) (2-3), and for fluid density ρ_f , porosity can be estimated with:

$$\phi = \frac{\rho_m - \rho_b}{\rho_m - \rho_f} \quad (2.7)$$

Neutron logs are also used for porosity estimation. The tool uses a high energy neutron source which emits neutrons that are scattered in the formation. In this case, scattering is more efficient in the interaction with Hydrogen, which slow down the neutrons. Low energy scattered neutrons are counted by sensors in the tool, and this measurement is converted in total amount of Hydrogen count (or Hydrogen Index). As most of H atoms are found in the fluids saturating the formation (water or hydrocarbons), this is finally a measurement of space occupied by fluid, hence porosity.

Sonic tools' transmitter send a mechanical wave that travels through the bore walls, and are detected by the tools' receivers. The basic measurement is the transit time of the wave, hence velocity. Several properties can be calculated from such measurements. For instance, assuming a known transit time for rock matrix and fluid, one can estimate porosity in a similar way as done with density logs (equation (2.7)).

Wave velocity can also relate to mechanical properties of rocks, like compressional coefficient for example. There are also models for rock permeability that are based on the excitation of compressional, sheering and surface waves.

Porosity logs (density, neutron and sometimes sonic) can be combined for determining other petrophysics properties. By analyzing the differences between density and neutron

porosity, one can detect packs of sandstone reservoir for example. Comparison between neutron and sonic porosities can identify zones with vuggy porosity.

Resistivity logs

These tools measure bulk resistivity (or conductivity) of rock formations, which can be done by applying a potential difference between two detectors or by inductive methods.

By measuring resistivity of hundreds of rock cores, Archie (7) found empirically a relation between bulk resistivity R_t , water resistivity R_w and porosity (for water saturated rocks):

$$F \equiv \frac{R_t}{R_w} = \frac{a}{\phi^m} \quad (2.8)$$

Coefficient m is the cementation coefficient, with gives a measure of how much the porous media deviates from a set of parallel straight tubes. In fact, the Formation Factor $F = R_t/R_w$, is also related to tortuosity defined in equation (2.6), as it measures in some sense the distance that an electric current has to run inside a porous medium.

In a rock saturated with water and oil, Archie found out the following relation that includes water saturation S_w and saturation exponent n :

$$R_t = a \frac{R_w}{\phi^m S_w^n} \quad (2.9)$$

Resistivity logs are then extremely important as resistivity contrasts allow the determination not only of oil zones, but also a quantification of water/oil saturation using equation (2.9).

These logs can as well be used to investigate invasion profiles. While drilling, some of the drilling mud filtrate used in perforation can invade the formation, creating a rock layer that includes fluids that are not original from the formation. By changing the frequency of resistivity tools or distance between detector, one can vary the depth of investigation and check the invasion depth.

Nuclear Magnetic Resonance Logs

NMR logs are extremely important because they can be used to determine total porosity, irreducible water saturation, fluid identification and permeability estimation. (5,8) We will leave the details of measurements and petrophysical interpretations to Chapter 3. Briefly, NMR logs measure the amount of Hydrogen in saturating fluids (hence porosity) through detection of a net magnetization induced by an external magnetic field. The technique

also measures at each depth a distribution of magnetization relaxation times to an equilibrium condition, which correlates with a pore size distribution. Relaxation times distributions are used to estimate absolute permeability.

NMR diffusion techniques can also be used to determine saturating fluid properties, and pore geometry characteristics.

Figure 2.10 shows an example of the logging results in an oil reservoir.

In the following Chapter we develop the theory behind NMR relaxation and diffusion techniques, as well as discuss their relation to petrophysics, and specific well site and tools conditions.

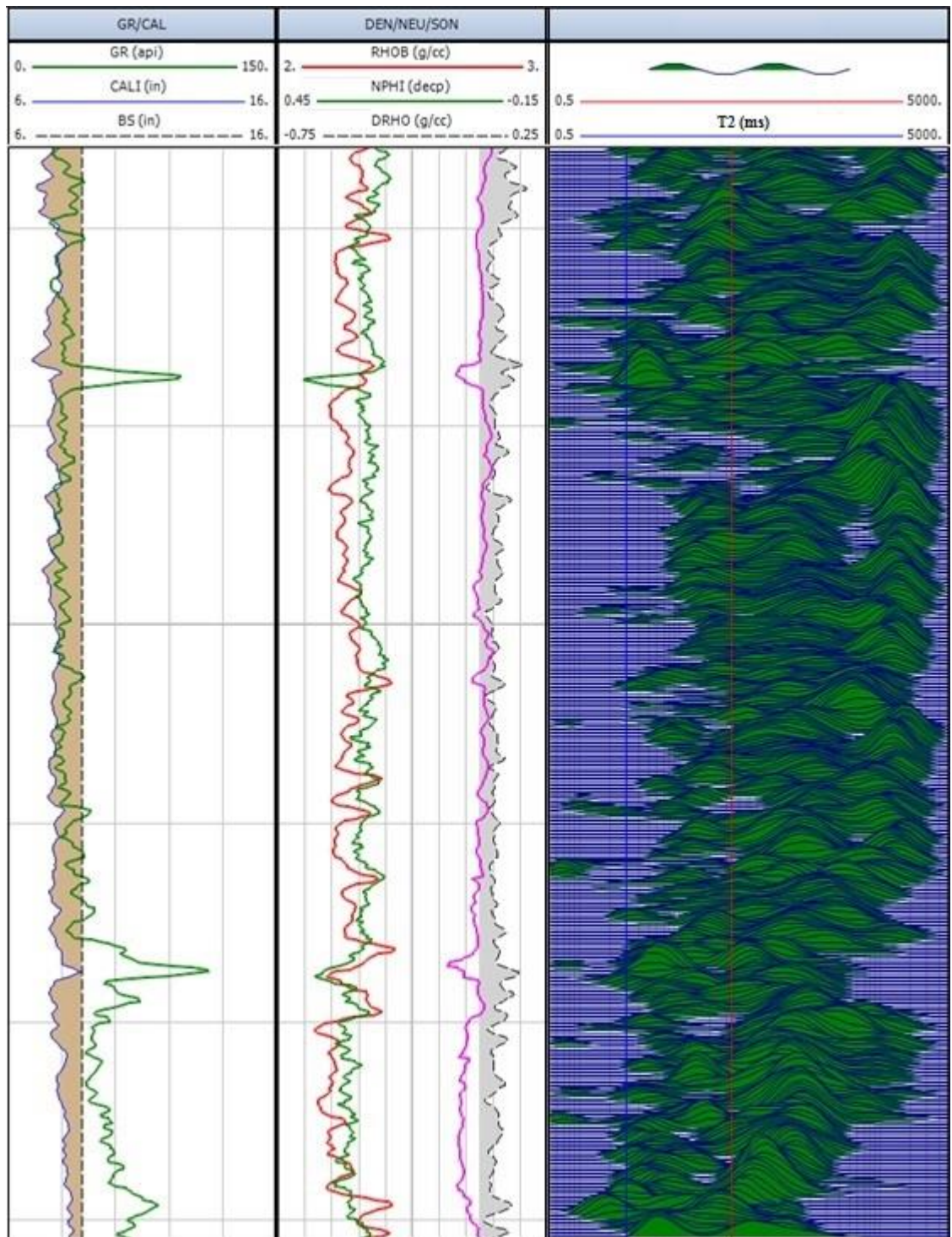


Figure 2.10 - Logging results. First track shows gamma ray log in green and the difference between the expected well caliper and measured one in shaded light brown. Second track shows the density log in red, its corresponding porosity in shaded grey, and Neutron porosity in green. Last track shows the NMR transverse relaxation times distributions. Depth increases downwards.

Source: Provided by Petrobras.

3 NUCLEAR MAGNETIC RESONANCE THEORY AND LOGGING APPLICATIONS

In this chapter we will introduce the theoretical fundamentals of Nuclear Magnetic Resonance (NMR) techniques, with emphasis on relaxation and diffusion, which are the main topics for oil and gas industry and petrophysical applications. Then we discuss how these concepts apply to fluid saturated rocks.

Certain nuclei in nature, those with odd mass number like the proton in the Hydrogen nucleus, have an intrinsic magnetic dipole moment ($\vec{\mu}$) which arises from the nucleus natural angular momentum \vec{S} , or Spin. Although this magnet dipole moment resembles (regarding its mathematical structure) the one that would arise from a charged rotating particle, the Spin has no classical analogue, and should be seen as a purely quantum effect and an intrinsic property of particles, instead of an actual rotation. Nevertheless, whatever origin the magnetic dipole has, its existence allows nuclei be manipulated by applied magnetic fields.

In NMR techniques, the sample is submitted to a static magnetic field \vec{B}_0 , which causes the intrinsic magnetic moments $\vec{\mu}$ to ‘align’ in some sense along the applied field, resulting in a sample net magnetization \vec{M} . Magnetization direction can be manipulated with intermittent radio frequency (rf) fields, and the observation of its return to equilibrium gives important information about the sample and its environment. For oil and gas applications, the sample is a fluid (either water, hydrocarbon, or both) saturating rock pores, and the nucleus of interest is the Hydrogen proton.

We will first introduce the basic ingredients for an NMR measurement, which are: equilibrium magnetization establishment in a static field, magnetization manipulation through rf fields, relaxation to equilibrium and self-diffusion effects. These elements are combined and summarized in equation (3.26), Bloch-Torrey’s equation for transverse magnetization evolution. We then apply the solutions of this equation to describe the most common designed laboratory measurements of magnetization. Finally, Petrophysical applications and well logging considerations are presented.

3.1 Basic NMR theory

The intrinsic magnetic dipole moment $\vec{\mu}$ is related to the nucleus Spin angular momentum through the relation (9):

$$\vec{\mu} = \gamma \vec{S} \quad (3.1)$$

γ is the gyromagnetic ratio, a physical constant tabled for each nucleus, with value of $267.513 \cdot 10^6 \text{ rad s}^{-1} \text{ T}^{-1}$ (or $2\pi \cdot 42.576 \text{ MHz/T}$) for Hydrogen.

Angular momentum can be written as $\vec{S} = \hbar \vec{I}$, where \hbar is Planck's constant and \vec{I} is the quantum mechanical angular momentum operator that respects the following rules (10):

$$[I_x, I_y] = iI_z, \text{ and cyclic permutations} \quad (3.2)$$

$$I^2|m\rangle = I(I+1)|m\rangle \quad (3.3)$$

$$I_z|m\rangle = m|m\rangle, m = -I, -I+1, \dots, I \quad (3.4)$$

Equation (3.2) implies the Heisenberg Uncertainty Principle, which in this context means that one is unable to determine simultaneously the value of two or more components of a nucleus angular momentum. Therefore, a complete description of a nucleus (regarding its angular momentum) can only take into account one of its components. Let's say that all the possible states for the z component are labeled as $|m\rangle$. Then equation (3.4) says that if one were able to measure the Spin's z component, the only possible outcome for this measurement would be one of the $m\hbar$. The other components would remain undetermined and the modulus of \vec{S} would always be equal to $\hbar\sqrt{I(I+1)}$. I is a positive integer or semi integer constant for each nucleus. For protons $I = 1/2$, which is why we say that Hydrogen nuclei have Spin $1/2$.

The z component of Hydrogen nuclei's angular momentum can then only have the values $\hbar/2$ (its associated magnetic dipole moment is pointing upwards in the z direction) or $-\hbar/2$ (pointing downwards). For Spin $1/2$ particles the states and angular operators can be represented as:

$$|\frac{1}{2}\rangle = \begin{pmatrix} 1 \\ 0 \end{pmatrix}, |-\frac{1}{2}\rangle = \begin{pmatrix} 0 \\ 1 \end{pmatrix}, I_z = \frac{1}{2} \begin{pmatrix} 1 & 0 \\ 0 & -1 \end{pmatrix}, I_x = \frac{1}{2} \begin{pmatrix} 0 & 1 \\ 1 & 0 \end{pmatrix}, I_y = \frac{i}{2} \begin{pmatrix} 0 & -1 \\ 1 & 0 \end{pmatrix} \quad (3.5)$$

Suppose we place a sample (water for example) in a static magnet field which we will assume is pointing in the z direction, such as $\vec{B}_0 = B_0 \hat{z}$. The energy operator (Hamiltonian), that is, the interaction between one nucleus' magnetic dipole $\vec{\mu}$ and the static field, is:

$$H_0 = -\gamma \hbar B_0 I_z \quad (3.6)$$

From equation (3.4) follows:

$$H_0|m\rangle = E_m|m\rangle, \quad E_m = -m\gamma \hbar B_0 \quad (3.7)$$

The meaning of this is similar to that of equation (3.4): each nucleus may be found in the presence of \vec{B}_0 at one specific value of energy, given by one of the $E_m = -m\gamma \hbar B_0$. Spin $1/2$ particles for example have two possible states: one of lower energy $E_{1/2} = -\frac{\gamma \hbar B_0}{2}$, where $\vec{\mu}$ is pointing in the positive z direction along with \vec{B}_0 , and one of higher energy $E_{-1/2} = \frac{\gamma \hbar B_0}{2}$,

pointing in the opposite direction, as depicted in Figure 3.1. It is worth noticing that regardless the particle's Spin number, the difference between two consecutive energies is always $\hbar\gamma B_0$, suggesting that an electromagnetic interaction in the frequency $\omega_0 = \gamma B_0$ might induce transitions between these states. This is the Larmor frequency and, as will be seen in the following sections, an electromagnetic pulse oscillating at this frequency can alter the states' populations and coherences, therefore, magnetization.

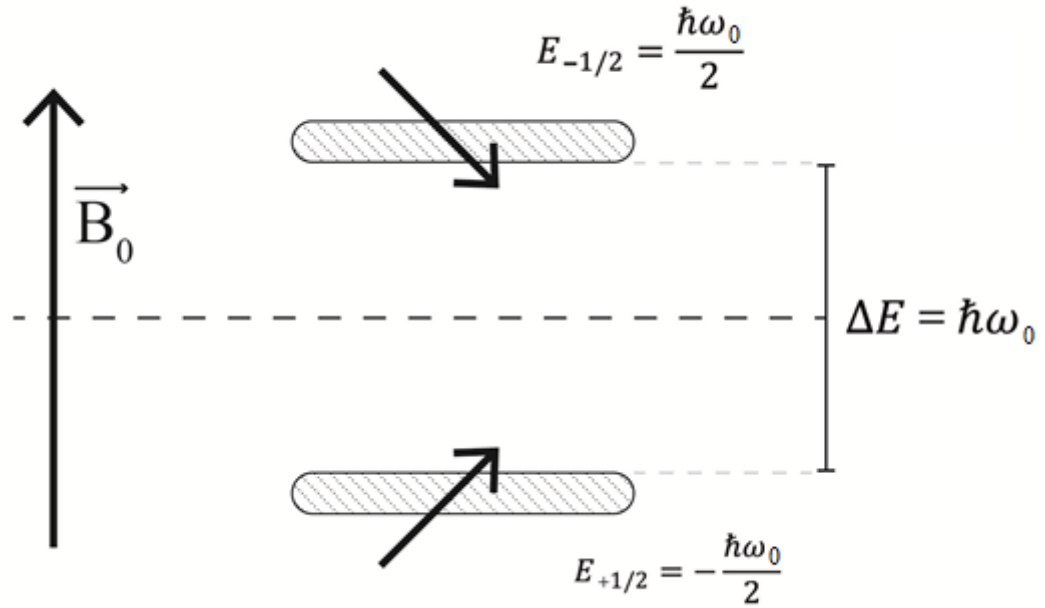


Figure 3-1 - States of a spin $\frac{1}{2}$ particle in the presence of a static magnetic field.
Source: By the author.

The evolution of the system comprising all the Spins in the sample, for example all the Hydrogen nuclei in water, can be determined by solving Schrodinger's equation:

$$i\hbar \frac{d|\Psi\rangle}{dt} = H|\Psi\rangle \quad (3.8)$$

Depending on the system one is willing to solve, the Hamiltonian might be just H_0 or might take into account the interactions between all the Spins and \vec{B}_0 , among themselves and even with external sources. The general solution for one nucleus may be written as:

$$|\Psi(t)\rangle = \sum_m c_m(t) e^{-im\omega_0 t} |m\rangle \quad (3.9)$$

The amplitudes $c_m(t)$ evolve in time accordingly to H , and have the property that $P_m(t) = |c_m(t)|^2$ is equal to the probability that at time t the nucleus is measured at state $|m\rangle$. However, regardless the specific details of H , one should expect that a macroscopic sample submitted to \vec{B}_0 might reach at some point a thermal equilibrium state, in which the

probabilities $P_m(t)$ are stationary, that is, don't vary in time anymore. Each state will then be populated with a number of nuclei that depends on the competition between the magnetic energy E_m , and the available thermal energy kT , k being the Boltzmann constant and T the absolute temperature. If we assume that equilibrium is well described by Boltzmann statistics (and $E_m \ll kT$), then $P_m \propto \exp\left(-\frac{E_m}{kT}\right)$, yielding (9,11):

$$M_0 = \frac{N\gamma^2\hbar^2 I(I+1)B_0}{3KT} \quad (3.10)$$

For typical total number of nuclei ($N \sim 10^{23}$), and at room temperatures, equilibrium magnetization will be $M_0 \sim 10^{-6} B_0$.

Therefore, at thermal equilibrium, a resulting net magnetization is established aligned with the external field, with an intensity of about 6 orders of magnitude smaller than B_0 . For an experiment to be able to detect such a small magnetization, rf pulses are used to drive \vec{M} away of equilibrium, where it can be measured.

Manipulation through rf fields

Before considering how the interaction between \vec{M} and oscillating magnetic fields proceeds, it is worth analyzing magnetization's behavior in the presence of \vec{B}_0 , when it is initially not aligned with the external field. The evolution of the mean dipole magnetic moment of a single nucleus $\langle \vec{\mu} \rangle = \langle \Psi | \gamma \hbar \vec{I} | \Psi \rangle$ with respect of H_0 can be derived from Schrodinger's equation (through Ehrenfest's theorem (10)), yielding:

$$\frac{d\langle \vec{\mu} \rangle}{dt} = \gamma \langle \vec{\mu} \rangle \times \vec{B}_0 \quad (3.11)$$

Equation (3.11) has the following interpretation: if one were able to measure at an instant t one of the components (say z , for example) of a nucleus' magnetic dipole $\vec{\mu}$, they would obtain one of the $m\gamma\hbar$ possible values as result. If the system was lead to the same initial state, and a similar measurement were made after an interval t , again one of the discrete values would be obtained. If this process was repeated several times, the mean value of the results would then be governed by equation (3.11). Therefore, although seemingly classic, equation (3.11) is strictly valid in quantum realm, whenever the correct interpretation is given for $\langle \vec{\mu} \rangle$. We might then commit some language abuse by saying 'magnetization of one nucleus' or 'orientation of the Spin', but keeping in mind that these expressions can be made precise if we understand them as referring to the mean value of a quantum measurement.

Total magnetization follows from (3.11):

$$\frac{d\vec{M}}{dt} = \gamma \vec{M} \times \vec{B}_0 \quad (3.12)$$

Equation (3.12) has as direct consequences:

$$\begin{cases} \frac{d|\vec{M}|^2}{dt} = -2\gamma B_0 \vec{M} \cdot (\hat{z} \times \vec{M}) = 0 \\ \frac{dM_z}{dt} = -\gamma B_0 \hat{z} \cdot (\hat{z} \times \vec{M}) = 0 \\ \left| \frac{d\vec{M}}{dt} \right| = (\gamma B_0) \sqrt{M_x^2 + M_y^2} \end{cases} \quad (3.13)$$

The first and second of (3.13) show that either magnetization modulus as its longitudinal component remain constant in time. That means that the magnetization vector moves confined to a cone with angle dictated by the initial orientation of \vec{M} and the z axis, and its projection in the transversal plane is restricted to a circumference. The third of (3.13) shows that the tip of magnetization vector's linear velocity is proportional to the radius of the circumference by a factor $\omega_0 = \gamma B_0$, the Larmor frequency. Hence, when in the presence of a static magnetic field, a nucleus' spin or the total magnetization will execute a precession movement around \vec{B}_0 at the Larmor frequency in the clockwise direction ($\vec{\omega}_0 = -\gamma B_0 \hat{z}$). Equation (3.14) shows the formal solution and Figure 3.2 illustrates this movement.

$$\vec{M}(t) = M_{z0} \hat{z} + M_{T0} \cos(\omega_0 t + \phi) \hat{x} - M_{T0} \sin(\omega_0 t + \phi) \hat{y} \quad (3.14)$$

$M_{z0} = M_z(0)$ is the initial z component of \vec{M} , and $M_{T0} = \sqrt{M_x(0)^2 + M_y(0)^2}$ is its initial transverse component. Phase angle ϕ defines the initial orientation of \vec{M} in the transversal plane.

It will be worth pointing out that in terms of quantum amplitudes $c_m(t)$, solution (3.14) writes, for a spin 1/2 particle:

$$\begin{cases} \langle I_z \rangle = \frac{1}{2} (|c_{1/2}|^2 - |c_{-1/2}|^2) \\ \langle I_x \rangle = \frac{1}{2} (c_{1/2} c_{-1/2}^* e^{i\gamma B_0 t} + c_{1/2}^* c_{-1/2} e^{-i\gamma B_0 t}) \\ \langle I_y \rangle = \frac{i}{2} (c_{1/2} c_{-1/2}^* e^{i\gamma B_0 t} - c_{1/2}^* c_{-1/2} e^{-i\gamma B_0 t}) \end{cases} \quad (3.15)$$

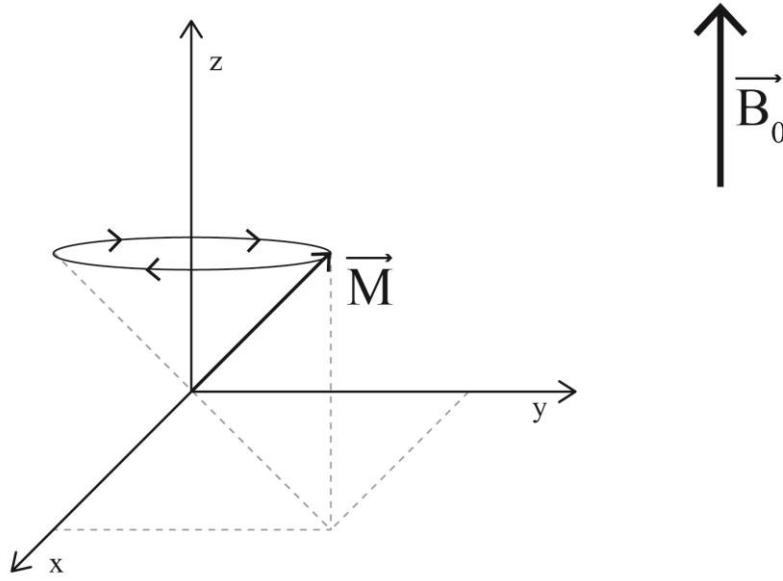


Figure 3.2 - Precession of magnetization around a static magnetic field.
Source: By the author.

Consider now that, besides the original static magnetic field \vec{B}_0 , one could expose the sample to an additional time changing field $\vec{B}_1(t)$, with the particular characteristic that it is confined to the transversal plane, and it also rotates in the clockwise direction at the Larmor frequency, executing precession around the z axis along with the magnetization. In other words, if we consider a new frame of reference x', y', z' (the rotating frame of reference) with the property that $z' = z$, and x' and y' rotating around z with $\vec{\omega} = -\omega_0 \hat{z}$, then $\vec{B}_1(t) = B_1 \hat{x}'$. In the rotating frame of reference, $\vec{B}_1(t)$ is a static magnetic field. Indeed, with the new reference system equation (3.12) becomes simply,

$$\frac{d\vec{M}}{dt} = \gamma \vec{M} \times \vec{B}_1 \quad (3.16)$$

Which is formally identical to equation (3.12). Therefore, in the rotating frame of reference, \vec{M} will execute precession around \vec{B}_1 with angular frequency $\omega_1 = \gamma B_1$, and will tilt away from the z direction. Figure 3.3 illustrates the movement of magnetization under the application of $\vec{B}_0 + \vec{B}_1(t)$ in both frames of reference.

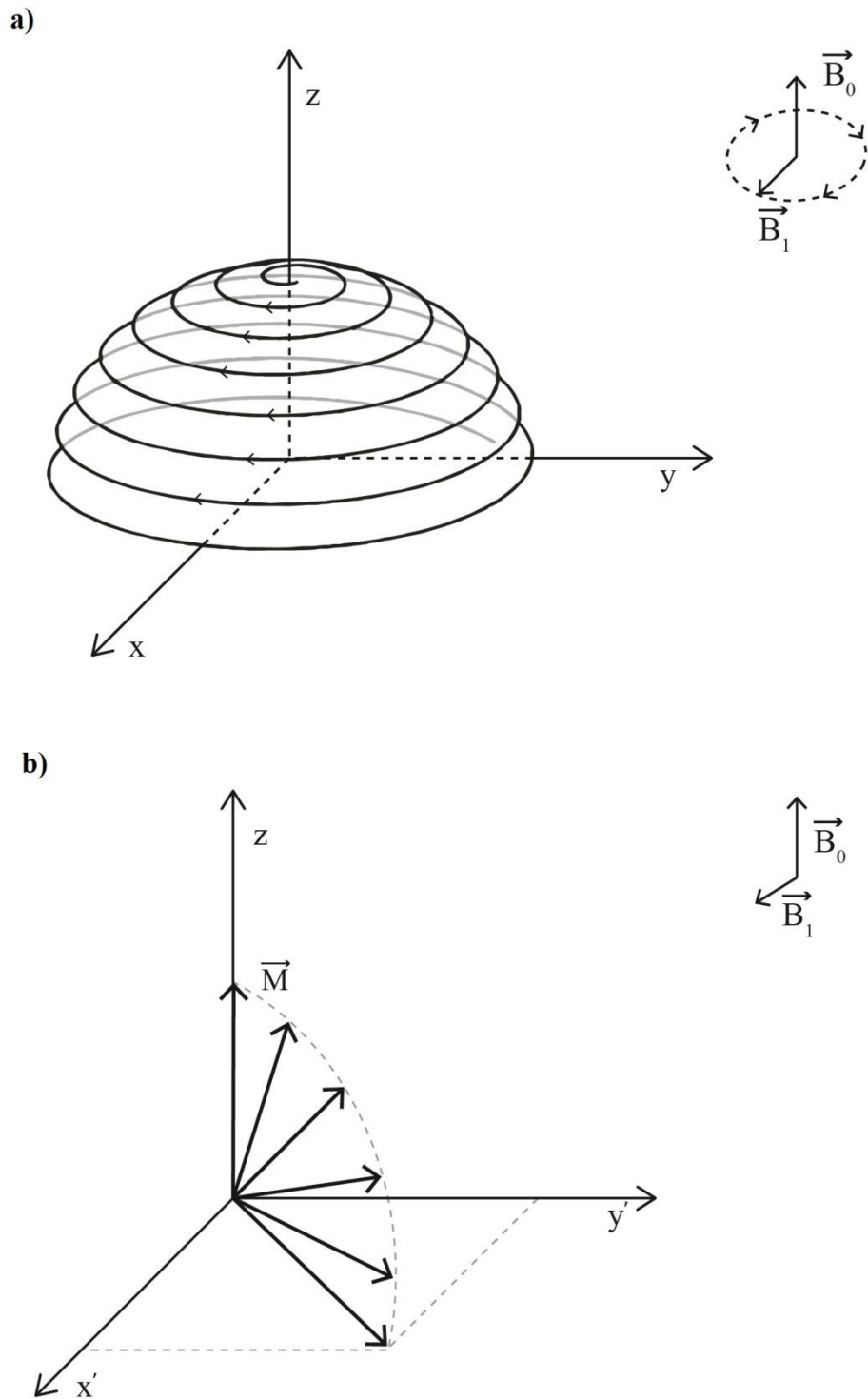


Figure 3.3 - Precession of magnetization during application of $\vec{B}_1(t)$, from a) laboratory and b) rotating frames of reference.

Source: By the author.

Magnetization tilting will only be effective if \vec{B}_1 's rotating frequency matches or is close to the Larmor frequency of the nucleus in \vec{B}_0 . For well logging applications and laboratory relaxometry in oil industry, the static field is generally around 500 Gauss , which

yields Larmor frequencies of about 2MHz for Hydrogen nuclei. Therefore, \vec{B}_1 is generally in the spectrum of radio frequencies (rf), hence being called a rf pulse. By adjusting the duration t_p and intensity of the pulse, one can control the tilting angle for magnetization:

$$\Delta\theta = \frac{\gamma B_1}{2\pi} t_p \quad (3.17)$$

If $\Delta\theta = \pi/2$ we call the rf a $\pi/2$ pulse, and so on for other tilting angles, like the π pulse for example.

In practical laboratory measurements the rf pulse can be generated by flowing an electric current through a coil oriented along the transverse plane, as illustrated in Figure 3.4.

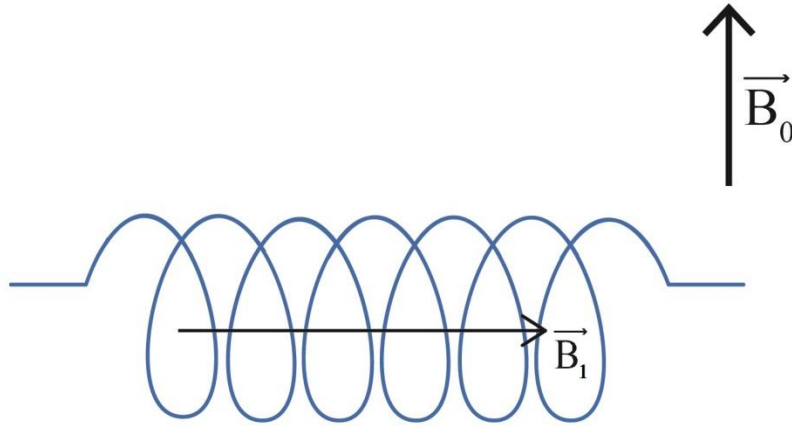


Figure 3.4 - Generating the \vec{B}_1 rf pulse.
Source: By the author.

If $\vec{B}_1(t) = 2B_1 \cos(\omega_0 t) \hat{x}$, then it can be expressed in the rotating frame as:

$$\vec{B}_1(t) = B_1 \hat{x}' + B_1 (\cos(2\omega_0 t) \hat{x}' + \sin(2\omega_0 t) \hat{y}') \quad (3.18)$$

The first term of equation (3.18) is just the static field we have been discussing, that is able to change the direction of \vec{M} . The other term represents a field that oscillates at twice the Larmor frequency, far of resonance, hence not been able to promote alterations in the magnetization.

To sum up, as the sample is submitted to a static magnetic field, magnetization will execute precession around that field at the Larmor frequency $\omega_0 = \gamma B_0$. Any time changing field oscillating at the Larmor frequency (or close), transverse to \vec{B}_0 , is able to deflect the total magnetization. As the magnetic energy equals $-M_z B_0$, tilting implies in energy transference between the alternating field and the sample, happening at the Larmor frequency, therefore changes in populations between the energy levels of the quantum system.

Relaxation

Besides the interaction with the static field or rf pulses, each nucleus in the sample is always interacting with all the environment around it. The environment can be composed by other nuclei that are constantly moving closer and away due to thermal agitation, or to minerals present at the pore walls in the case of fluid saturating a rock sample. Therefore, each nucleus will ‘feel’ at each instant a local magnetic field varying almost randomly in time, that can be represented by $\vec{B}_{Local}(t) = \vec{B}_0 + \vec{b}(t)$, where $\vec{b}(t)$ is a random fluctuating function. These interactions will be responsible for forcing the system back to thermal equilibrium described in the first section, with a total net magnetization along the z direction (longitudinal, parallel to the static field), and no transverse magnetization. This process is called relaxation to equilibrium.

From the discussion in the previous section, any component of $\vec{b}(t)$ that is transverse to \vec{B}_0 and oscillates at the Larmor frequency will be able to change the mean magnetic dipole orientation of that nucleus, therefore contributing to relaxation both in longitudinal and transverse directions. These interactions will be responsible for dissipating energy of the system until thermal equilibrium. However, any component of $\vec{b}(t)$ that is longitudinal to \vec{B}_0 will change the local Larmor frequency for each nucleus, generating a dephasing process between nuclei’s transverse magnetization. This process can hence affect total transverse magnetization while leaving the longitudinal one unchanged (it does not change the energy of the system, but only induces losses in coherence). Therefore, transverse relaxation always occur faster than, or at most at the same pace as, longitudinal relaxation. Bloch (12) found out empirically that in liquids relaxation can be described as (in the rotating frame of reference):

$$\begin{cases} \frac{dM_z}{dt} = \frac{M_0 - M_z}{T_1} \\ \frac{dM_{x'}}{dt} = -\frac{M_{x'}}{T_2} \\ \frac{dM_{y'}}{dt} = -\frac{M_{y'}}{T_2} \end{cases} \quad (3.19)$$

The solutions to the Bloch equations follow below, and are illustrated in Figure 3.5.

$$\begin{cases} M_z(t) = M_0 - (M_0 - M_{z0})e^{-\frac{t}{T_1}} \\ M_{x'}(t) = M_{0x'}e^{-\frac{t}{T_2}} \\ M_{y'}(t) = M_{0y'}e^{-\frac{t}{T_2}} \end{cases} \quad (3.20)$$

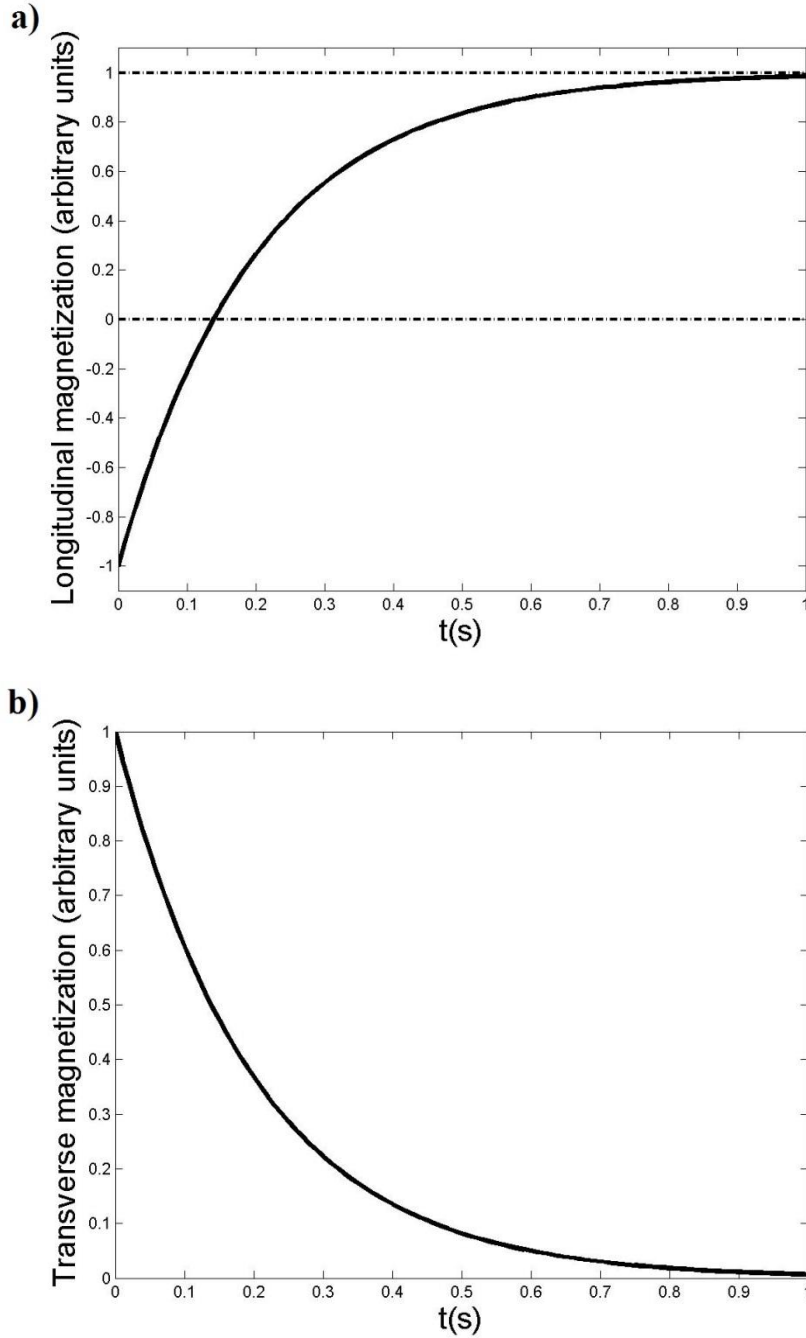


Figure 3.5 - Relaxation to thermal equilibrium. a) Longitudinal magnetization and b) Transverse magnetization.
Source: By the author.

Both processes are described by exponentials with characteristic times T_1 , for longitudinal relaxation, and T_2 for transverse relaxation, with $T_1 \geq T_2$. As T_1 refers to the establishment of longitudinal magnetization, it is also called polarization time.

Bloembergen et al. (13) developed an insightful approach (BPP model) for deriving Bloch equations and understanding relaxation, by considering the additional random classical local field $\vec{b}(t)$ as a small perturbation in the system's Hamiltonian in such a way that $H = H_0 + H_1(t)$, with $H_1(t) = -\gamma\hbar(b_x(t)I_x + b_y(t)I_y + b_z(t)I_z)$. Recording equation

(3.15), magnetization components are expressed in terms of products of type $\sigma_{nm} = c_n^* c_m$. By applying perturbation theory to Schrodinger's Equation one gets (in the rotating frame of reference):

$$\frac{d\tilde{\sigma}}{dt} = -\frac{1}{\hbar^2} \int_0^t d\tau \left[\tilde{H}_1(t), \overline{[\tilde{H}_1(t+\tau), \tilde{\sigma}(t)]} \right] \quad (3.21)$$

The tilde means that the quantities are expressed in the rotating frame of reference, and the trace $\overline{}$ stands for ensemble average. Equation (3.21) shows that magnetization evolves depending on terms like $g_{qq}(\tau) = \overline{b_q(t)b_q(t+\tau)}$, ($q = x, y, z$), which have the following interpretation. If τ is big enough (say much bigger than a characteristic correlation time τ_c) and $b_q(t)$ is random with zero mean, one would expect that the value of the field at a time $t + \tau$ has nothing more to do with its value at t , yielding $g_{qq}(\tau) = 0$. On the other hand, for small values of τ , $g_{qq}(\tau) \neq 0$. $g_{qq}(\tau)$ is the self-correlation function and τ_c measures in some sense the extent of the random function's memory of its previous values. What causes the fluctuations in the local field is mainly translation and rotation of the molecules in the fluid. Correlation time τ_c depends then on the translational and rotational diffusion coefficients of the fluid and, at the end of the day, on temperature and fluid's viscosity. As the molecules 'freedom' increases (higher temperatures and diffusion coefficients, smaller viscosities), more random are fluctuations of local fields and smaller is τ_c , which will slow relaxation. On the other end, greater τ_c will increase relaxation processes

If each component of the local field can be treated as independent and in a random walk fashion, then the correlation function has the form $g_{qq}(\tau) = \left(\frac{\overline{b^2}}{3}\right) e^{-|\tau|/\tau_c}$. By continuing the calculation of equation (3.21) and comparing with Bloch's equations one gets (11):

$$\begin{cases} \frac{1}{T_1} = \frac{\gamma^2}{2} (J_{xx}(\omega_0) + J_{yy}(\omega_0)) \\ \frac{1}{T_2} = \frac{\gamma^2}{2} (J_{xx}(\omega_0) + J_{zz}(0)) \end{cases} \quad (3.22)$$

Where $J_{qq}(\omega)$ is the Fourier transform of $g_{qq}(\tau)$.

Expression (3.22) describes mathematically what we intuitively pointed out in the beginning of this section. Both relaxation times depend on magnetization flipping induced by transverse oscillating fields at the Larmor frequency. However, transverse relaxation depends also on the static component of the fluctuation at the z direction, which induces losses in coherence between spins. For an exponential self correlation function, relaxation times are:

$$\begin{cases} \frac{1}{T_1} = \frac{2}{3} \gamma^2 \overline{b^2} \frac{\tau_c}{1 + \omega_0^2 \tau_c^2} \\ \frac{1}{T_2} = \frac{1}{3} \gamma^2 \overline{b^2} \left(\tau_c + \frac{\tau_c}{1 + \omega_0^2 \tau_c^2} \right) \end{cases} \quad (3.23)$$

These equations show that $T_1 \geq T_2$, for all τ_c , and that as the correlation time becomes really small compared with the inverse of Larmor frequency, $T_1 \cong T_2$. In the BPP model, local field is modeled as a completely classic magnetic field. If one had explicitly written out the perturbing Hamiltonian as the dipolar interaction between spins (which is dominant for liquids), one would also get terms depending on twice the Larmor frequency for relaxation rates. Nevertheless, the general conclusions remain.

Finally, we choose to write Bloch's Equations in the following way (in the rotating frame of reference):

$$\begin{cases} \frac{\partial m_z}{\partial t} = \frac{m_0 - m_z}{T_1} \\ \frac{\partial m_T}{\partial t} = -i\gamma \Delta B_0(\vec{r}, t) m_T - \frac{m_T}{T_2} \end{cases} \quad (3.24)$$

In the rotating frame of reference there are no effects of \vec{B}_0 , as in this system of coordinates magnetization executes no precession. However, any additional local field $\Delta B_0(\vec{r}, t)$ still appears in that frame of reference. We consider as additional field anyone that has not been taken into account as a fluctuating random function leading to T_1 or T_2 relaxation. For the same (yet subtle) reason, we treat ΔB_0 as a scalar, meaning that those are differences only in the longitudinal component of local fields. We do so because, as already pointed out, if any additional transverse fields are not too big compared to \vec{B}_0 , they will only affect longitudinal magnetization if they fluctuate at the Larmor Frequency, which will not be the case. We will then consider only spatial or time field changes that are able to affect transverse magnetization. As x and y magnetization behavior are essentially the same, we chose to define transverse magnetization as $M_T = M_{x'} + iM_{y'}$, i being the imaginary unit such as $i^2 = -1$. Also, as we will allow spatial variations in the local fields, we will work with local magnetization densities $\vec{m}(\vec{r}, t)$, which relate to total magnetization by $\vec{M}(t) = \int_V m(\vec{r}, t) dV$.

Inhomogeneous static field and diffusion effects

Consider the simplest NMR relaxation measurement, in which the initial magnetization of a fluid sample $\vec{M} = M_0 \hat{z}$ (in thermal equilibrium with \vec{B}_0) is excited by a

$\pi/2$ pulse, tilting it to the transversal plane. If the system is then let to evolve, transverse magnetization will execute precession around z direction at the Larmor frequency, while relaxing exponentially. The resulting oscillating transverse field induces in the same exciting coil (through Faraday's Law) an oscillating and decaying electric tension, which is proportional to transverse magnetization. The result is represented in Figure 3.6.

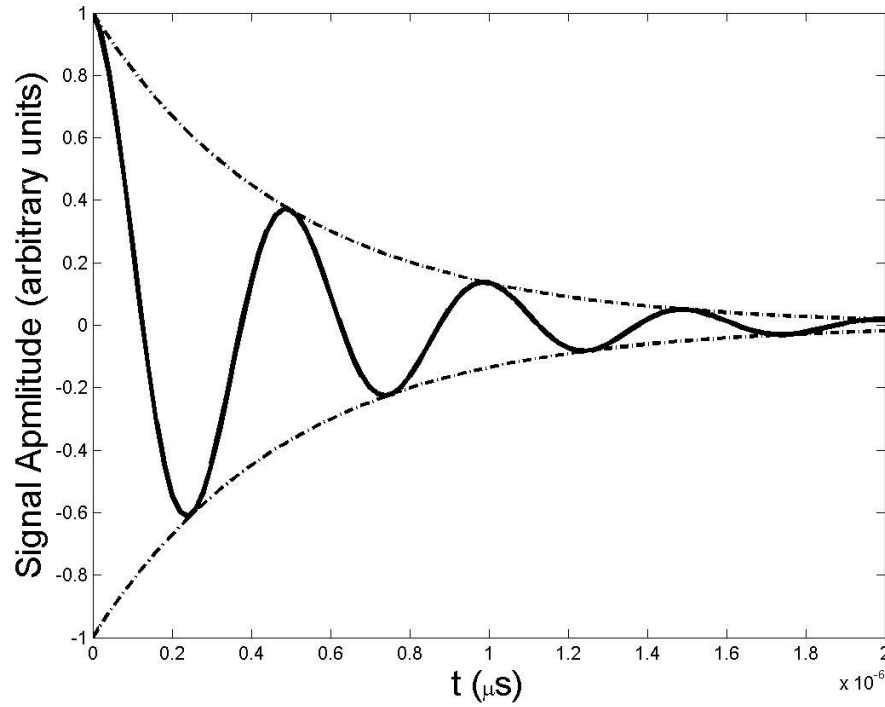


Figure 3.6 - Free induction decay (FID) signal.

Source: By the author.

The acquired oscillating and decaying tension is called the free induction decay (FID). The dotted line enveloping the signal is an exponential with a characteristic relaxation time $T_2^* < T_2$. The reason is the following: no matter how well a magnet is designed for generating \vec{B}_0 , it will never create a perfectly homogeneous magnetic field. This situation is even worse for logging acquisitions where the sample (rock formation) is located outside of the NMR tool, hence the static field is most generally a decaying function on the distance of the tool. Therefore, the additional local field experienced by the spins is a spatial varying function $\Delta B_0(\vec{r})$, which gives for total transverse magnetization from equation (3.24):

$$M_T(t) = M_0 e^{-t/T_2} \langle e^{-i\gamma \Delta B_0(\vec{r})t} \rangle \quad (3.25)$$

The term in brackets represents an average through all the spins, which are distributed spatially. Each one of them hence feels a slightly different static field, yielding different

Larmor frequencies and different accumulated phases. When summed up through all the nuclei, most complex exponentials will interfere destructively accelerating relaxation.

Before discussing the traditional way of getting rid of inhomogeneity effects, let's consider another important phenomenon. Throughout measurement, the nuclei do not stand still in the same position, but instead molecules diffuse through the sample carrying magnetization to different places. As they do so, each nucleus accumulates a phase that is also dependent on the specific trajectory that molecule went through. This effect can be taken into account by adding a diffusion term on the transverse part of equations (3.24):

$$\frac{\partial m_T}{\partial t} = D_0 \nabla^2 m_T - i\gamma \Delta B_0(\vec{r}, t) m_T - \frac{m_T}{T_2} \quad (3.26)$$

This is the Bloch-Torrey (14) equation, which sums up all relaxation and diffusion effects discussed throughout this Chapter, and is extremely important in understanding acquisition techniques, as well as magnetization behavior for fluid saturated rocks.

Its solution for the FID experiment on a bulk fluid sample, considering a constant gradient \vec{G} for field variation ($\Delta B_0(\vec{r}, t) = \vec{G} \cdot \vec{r}$), is:

$$M_T(t) = M_0 e^{-t/T_2} e^{-\frac{D(\gamma G)^2 t^3}{3}} \langle e^{-i\gamma \Delta B_0(\vec{r})t} \rangle \quad (3.27)$$

This solution shows the intuitive result that transverse relaxation is increased even more when diffusion is taken into account.

3.2 Laboratory acquisition techniques

In this section we will present the standard techniques for measuring T_1 , T_2 and D .

Transverse relaxation time (T_2) acquisition, the CPMG pulse sequence

After the application of a $\pi/2$ pulse on a sample thermalized with \vec{B}_0 , magnetization will tilt to the transversal plane and evolve accordingly to equation (3.27), generating a FID in the coil. The signal decays faster than T_2 because of inhomogeneity in the static field and diffusion.

Carr, Purcell, Meiboom and Gill (15-16) proposed that a time τ after the $\pi/2$ pulse, one should apply a sequence of π pulses in the transverse plane, spaced in an interval of 2τ , as shown schematically in Figure 3.7 (CPMG pulse sequence). The rectangular shapes represent the rf pulses.

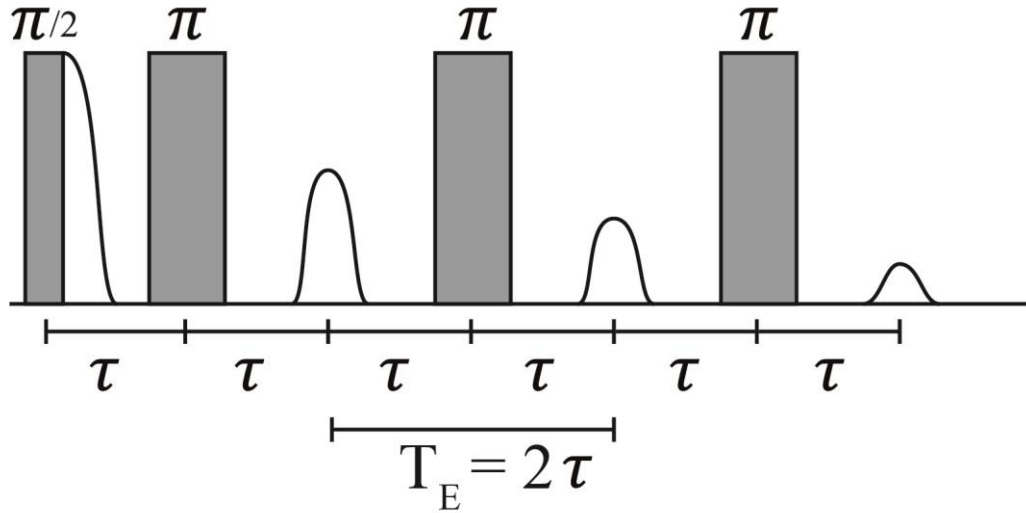


Figure 3.7 - CPMG pulse sequence.
Source: By the author.

After the first pulse, signal will oscillate and decay and, immediately before the first π pulse it will have the form:

$$M_T(\tau) = M_0 e^{-\tau/T_2} e^{-\frac{D(\gamma G)^2 \tau^3}{3}} \langle e^{-i\gamma \Delta B_0(\vec{r})\tau} \rangle \quad (3.28)$$

If the π pulse is applied for instance in the x' (rotating frame) direction, then it will have the effect of turning $m_{y'}$ into $-m_{y'}$, or simply $i \rightarrow -i$ in m_T . Transverse magnetization evolution will then be:

$$M_T(\tau + \Delta t) = M_0 e^{-\tau/T_2} e^{-\Delta t/T_2} e^{-\frac{D(\gamma G)^2 \tau^3}{3}} e^{-\frac{D(\gamma G)^2 \Delta t^3}{3}} \langle e^{i\gamma \Delta B_0(\vec{r})\tau} e^{-i\gamma \Delta B_0(\vec{r})\Delta t} \rangle \quad (3.29)$$

It can be seen that as time evolves, the terms into brackets tend to be equal to 1 as another time τ passes, making an *echo* signal appear. Transverse π pulses have the ability of re-focalize magnetization, as it dephases the spins among each other in such a way that the losses of phase during de-coherence are recovered after the pulse. If the process is repeated continuously, at each interval $T_E = 2\tau$, the inhomogeneous term disappears and the enveloping exponential is recovered. T_E , the time between π pulses is known as *echo-time*, and can be seen as a sampling time for T_2 relaxation curve. The collection of points acquired is also called in oil industry as *echo-train*. Acquired signal then becomes:

$$M_T(t) = M_0 e^{-t/T_2} e^{-\frac{D(\gamma G T_E)^2}{12} t} \quad (3.30)$$

If T_E is chosen small enough, diffusion term is suppressed and equation (3.30) becomes a measurement of transverse relaxation time.

Longitudinal relaxation time (T_1) acquisition

For T_1 to be measured, one has to be able to sample the exponential solution of equation (3.20). That is traditionally done in two ways.

Inversion recovery

A π pulse is applied to the sample initially in equilibrium with the static field, tilting the magnetization into direction $-z$. After a time T_I , longitudinal magnetization will have evolved and a $\pi/2$ pulse is applied. The resulting FID will have the amplitude given by:

$$M_z(t) = M_0 \left(1 - 2e^{-\frac{T_I}{T_1}} \right), \quad (3.31)$$

Which stands for a measurement of T_1 . The pulse sequence is shown in Figure 3.8.

Saturation recovery

The π pulse in Inversion Recovery is substituted by a fast train of $\pi/2$ pulses that destroys magnetization completely. After a time T_S a detection $\pi/2$ pulse is applied and resulting FID amplitude behaves as:

$$M_z(t) = M_0 \left(1 - e^{-\frac{T_S}{T_1}} \right) \quad (3.32)$$

Saturation recovery is preferred for well logging applications because it is twice faster than Inversion Recovery, as one only needs to acquire half of the exponential build up. On the other hand, measuring amplitudes around zero is always less precise, hence Saturation Recovery is more noisy for small T_1 s.

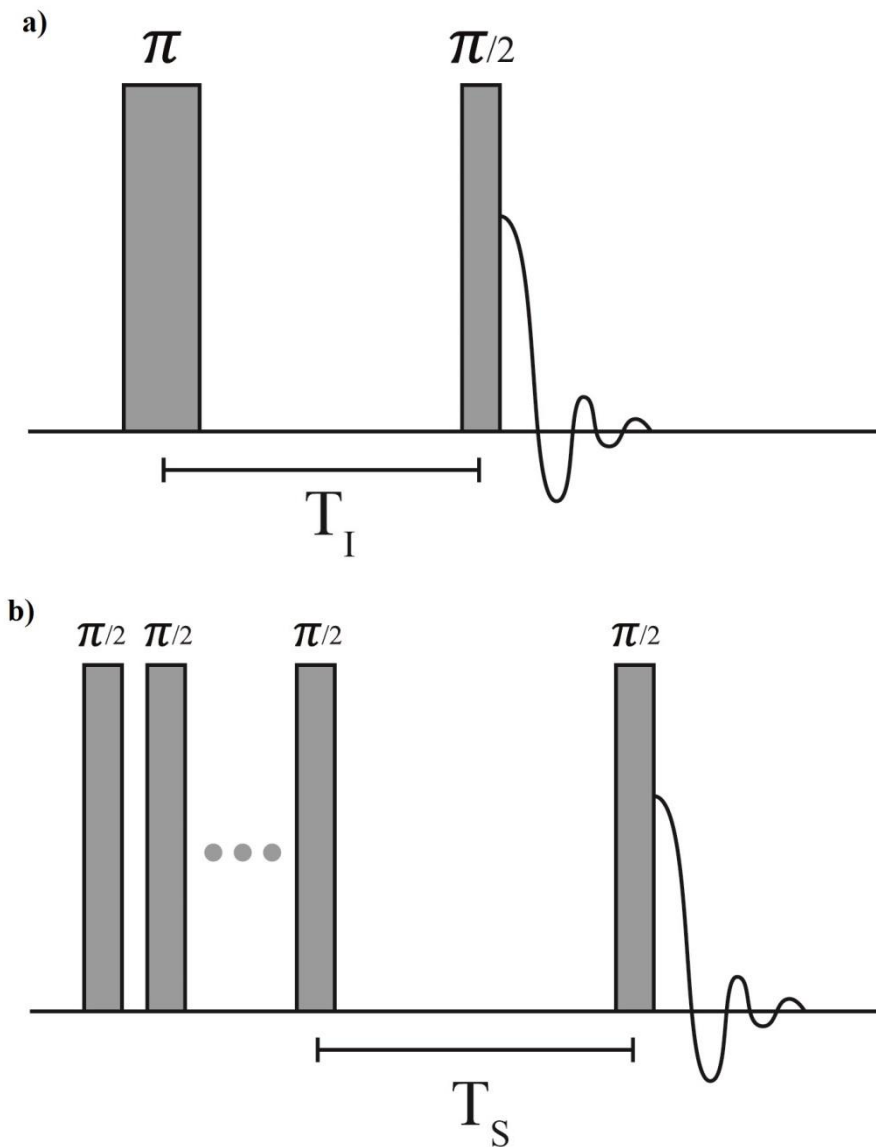


Figure 3.8 - Pulse sequence for a) Inversion Recovery and b) Saturation Recovery.
 Source: By the author.

Pulsed Field Gradient (PFG) sequence for diffusion (D) acquisition

Stejskal and Tanner (17-18) proposed the following pulse sequence for diffusion coefficient acquisition, shown in Figure 3.9.

After the application of a $\pi/2$ pulse over the equilibrium initial magnetization, and before the re-focusing π pulse, an artificial field gradient is imposed over \vec{B}_0 by flowing electric current through gradient coils, during a time δ . During the application of this extra current, the additional field term of Bloch-Torrey's equation (3.26) will be $\Delta B_0(\vec{r}, t) = \vec{G}(t) \cdot \vec{r}$. What the gradient pulse does is include an additional controlled dephasing which depends on D , encoding diffusion into the signal. The nuclei are then let to diffuse, and a time Δ after the beginning of the first gradient pulse (and after the rf re-focusing π), an identical gradient

pulse decodes diffusion. The echo amplitude is given by (solution of Bloch Torrey's equation for rectangular gradient pulses):

$$M_T = M_0 e^{-D(\gamma G)^2 \delta^2 (\Delta - \delta/3)} \quad (3.33)$$

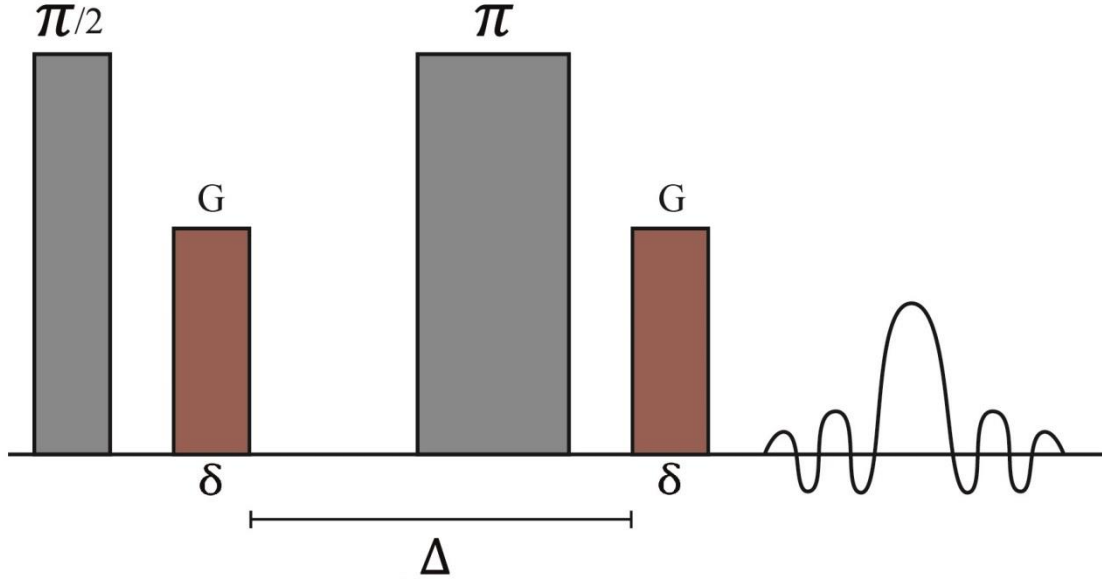


Figure 3.9 - Pulsed Field Gradient acquisition.
Source: By the author.

Combined Measurements

If instead of using a $\pi/2$ detection pulse at the end of Inversion Recovery, Saturation Recovery or Stejskal-Tanner, one uses a CPMG pulse sequence, that is a $\pi/2$ followed by equally spaced π train, one gets a combined measurement of $T_1 - T_2$ or $D - T_2$. Equations (3.31), (3.32) and (3.33) then become, respectively:

$$M_T(t) = M_0 \left(1 - 2e^{-\frac{T_I}{T_1}}\right) e^{-\frac{t}{T_2}} \quad (3.34)$$

$$M_T(t) = M_0 \left(1 - e^{-\frac{T_S}{T_1}}\right) e^{-\frac{t}{T_2}} \quad (3.35)$$

$$M_T = M_0 e^{-D(\gamma G)^2 \delta^2 (\Delta - \delta/3)} e^{-\frac{t}{T_2}} \quad (3.36)$$

3.3 NMR in porous media – Petrophysical Interpretations

Up to this point we presented basic NMR relaxation and diffusion principles, as well as acquisition techniques, though these principles were only applied to bulk fluids, that is, fluids that are not saturating porous media. Now we will discuss how the presence of pore

walls and tight spaces modify relaxation times and diffusion coefficients, allowing these quantities to carry information about pores themselves.

Relaxation processes inside porous media

A single nucleus inside a fluid sample feels as an NMR experiment goes on, a fluctuating local field from the environment around it. This induces a relaxation process expressed by relaxation time in the Bloch-Torrey equation (3.26), which also includes diffusion and gradient effects. Consider now that the fluid is confined inside a small rock pore. Although all those processes described by equation (3.26) still persist inside the pore, an additional local field fluctuation source comes into play, that is, the pore walls. As a molecule gets closer to a wall, their interaction has the effect of restricting the molecule's movements, that is, its translation and diffusion get slowed down by surface forces. The results are local field fluctuations that are 'less random' near the walls, increasing correlation time τ_c and as consequence relaxation times. Studies (19-23) correlate this additional surface relaxation process to the presence of paramagnetic elements at the pore walls, yielding interactions that should be restricted to few nanometers, which indicates that this additional process can be modeled by an additional contour condition to equation (3.26), valid only at the pore surface (equation 3 – 40). Figure 3.10 shows schematics the action of the pore wall over a molecule.

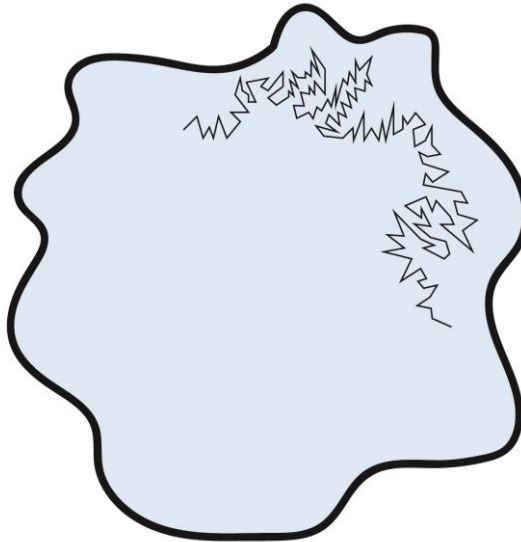


Figure 3.10 - Molecule's thumbling and diffusion restricted by interface interactions.

Source: By the author.

Consider a magnetization density function valid inside the pore, $m(\vec{r}, t)$, which stands either for longitudinal (m_z) or transversal (m_T) magnetization. Fick's Law of diffusion then states that the amount of magnetization that flows by an unit transverse area and unity time,

that is the current density, is given by the vector $\vec{J} = D_0 \vec{\nabla} m$. If $\hat{n}(\vec{r}_S)$ is a unit vector perpendicular to the pore wall at a point \vec{r}_S in the surface, pointing outwards the pore volume, then the total magnetization per unit time lost through the walls (through additional relaxation) is given by $(\vec{J} \cdot \hat{n})_S$, where the subscript S states that the quantities are calculated at the surface. In this mechanistic view of diffusion, if a magnetization carrier gets to the wall, it has a probability of leaving the system. It is reasonable to suppose that the higher is the quantity of carriers, higher is the probability of one of them to leave the system, which implies $(\vec{J} \cdot \hat{n})_S = -\rho_{1,2} m(\vec{r}_S)$. The proportionality constant $\rho_{1,2}$ is called surface relaxivity (subscript 1 and 2 stand respectively for longitudinal and transverse relaxivities).

Surface relaxivity indicates how much of magnetization can be lost at the interface due to relaxation processes at the pore walls. From the discussion presented up to this point, it measures how strong the interaction between the wall and the fluid molecules are. In some sense, it measures the affinity between the fluid and the pore walls. Therefore, surface relaxivity depends on fluid type and pore interface mineralogy. Typical values for relaxivities reported in literature are greater than $10 \mu m/s$ for sandstones (24), and it is usually assumed that they are one order of magnitude lower for carbonates. We will comment briefly in following sections the standard way these values are obtained and their limitations.

Considering that equation (3.26) is still valid for a fluid saturated pore, that static field inhomogeneity is corrected by CPMG like pulse sequences, and that diffusion through \vec{B}_0 gradients is reasonably well described by free fluid solution $e^{-\frac{(\gamma G T_E)^2 D_0 t}{12}}$ (CPMG, transverse magnetization), magnetization density inside a single pore is given by:

$$m_z(t) = m_0 - (m_0 - m_{z0}) e^{-\frac{t}{T_{1B}}} \sum_n C_n \psi_n(\vec{r}) e^{-\lambda_n t} \quad (3.37)$$

$$m_T(t) = m_0 e^{-\frac{t}{T_{2B}}} e^{-\frac{(\gamma G T_E)^2 D_0 t}{12}} \sum_n C_n \psi_n(\vec{r}) e^{-\lambda_n t} \quad (3.38)$$

We added subscript B for relaxation times, indicating those are bulk fluid values, coming from free relaxation. Spatial eigenfunctions $\psi_n(\vec{r})$ and eigenvalues λ_n are solutions of the Bloch-Torrey equation with relaxivity contour condition:

$$D_0 \nabla^2 \psi_n + \lambda_n \psi_n = 0 \quad (3.39)$$

$$(D_0 \vec{\nabla} \psi_n \cdot \hat{n} + \rho_{1,2} \psi_n)_S = 0 \quad (3.40)$$

It can be seen then that, for a single pore, total magnetization has in general a multi-exponential decay induced by interaction with pore walls. All surface relaxation times $1/\lambda_n$

depend on the specific pore geometry, and roughly on the characteristic pore size. Brownstein and Tarr (25) calculated the exact solutions (equation 3 – 38) for simple geometries (spherical, cylindrical and plate shaped pores) and defined the diffusion limits explained in the next topic.

Time scales and diffusion limits

There are two coupled processes governing the surface relaxation rates λ_n of solutions (3.37) and (3.38): relaxation at the interface and diffusion through the pore space. In order to see why diffusion is important for surface relaxation times, consider an extreme (imaginary) example where surface relaxation occurs in a characteristic time τ_s , but the molecules don't diffuse at all. No matter how strong is the surface relaxation process (that is, how small is τ_s meaning fast relaxation), once the molecules near the walls have relaxed, the rest of the fluid will continue to follow the slower bulk process, surface relaxation hence remaining virtually undetected. Diffusion has the important role of 'refilling' pore walls with new nuclei that have not relaxed yet. The time at which a molecule diffuses through a pore of characteristic length r is $\tau_D = r^2/D_0$, and is the matching between this time scale, τ_s , and the more or less accessible areas of the pore geometry by each eigenmode ψ_n , that gives rise to several decaying rates in solution (3.37) and (3.38).

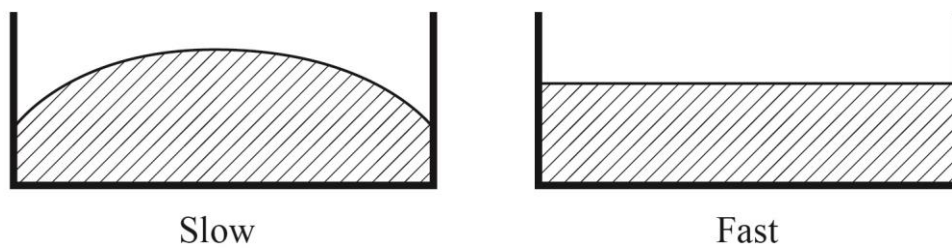


Figure 3.11 - Magnetization profile in a "1D pore" for Slow and Fast diffusion limits.

Source: Adapted from DUNN et al. (8)

One particular important scenario is when diffusion dominates over surface relaxation, known as the fast diffusion limit ($\tau_D \ll \tau_s$). In this case, diffusion rapidly redistributes all nuclei that yet carry magnetization through the whole pore, resulting in an magnetization density that is approximately uniform all times (Figure 3.11). Hence, the solution of Bloch-Torrey's equation in this case should be dominated by the eigenmode that satisfies $\psi(\vec{r}) \cong \text{constant}$. By integrating equation (3.40) through the entire pore surface, using the result $\oint_S \vec{\nabla}\psi \cdot \hat{n} da = \int_V \nabla^2\psi dV$ (Gauss' Theorem), and combining with equation (3.39), comes:

$$-\lambda \int_V \psi dV + \rho_{1,2} \oint_S \psi da = 0 \quad (3.41)$$

Using the fact that ψ should be approximately constant, equation (3.41) yields:

$$\lambda \approx \rho_{1,2} \frac{S}{V} \quad (3.42)$$

In the fast diffusion limit, magnetization decay is again mono exponential even for a fluid saturated pore, and surface relaxation time depends on the volume per surface ratio of the pore, that is $\tau_S = \frac{1}{\rho_{1,2}} V/S \sim r/\rho_{1,2}$.

Fast diffusion condition can be rephrased as $\frac{\tau_D}{\tau_S} \ll 1 \Rightarrow \frac{\rho_{1,2}r}{D_0} \ll 1$. On the other hand, if $\frac{\rho_{1,2}r}{D_0} \geq 1$, the system is in the intermediate to slow limit, yielding multiexponential decay for a single pore.

Considering water diffusion coefficient at room temperature as $2.4 \cdot 10^{-9} m^2/s$, a typical $10 \mu m$ pore and relaxivity as big as $10 \mu m/s$, one has $\frac{\tau_D}{\tau_S} \sim 0.1$, which is still in the fast diffusion limit. In this case, relaxation rates for a fluid saturated pore are:

$$\frac{1}{T_1} = \frac{1}{T_{1B}} + \rho_1 \frac{S}{V} \quad (3.43)$$

$$\frac{1}{T_2} = \frac{1}{T_{2B}} + \rho_2 \frac{S}{V} + \frac{D_0(\gamma G T_E)^2}{12} \quad (3.44)$$

Summing up, the decay rate for relaxation processes in a single pore has three distinct origins for transverse relaxation: bulk interaction between other molecules of the fluid, diffusion through field gradients and interaction with the pore wall (hence dependent of rock mineralogy and minerals distribution). In the fast diffusion limit surface relaxation time is then proportional to the pore size.

Relaxation time distribution and petrophysics

As explained in Chapter 2, rock structure generates a composition of several pores and throats, with different sizes and shapes. Therefore, even in the fast diffusion limit, NMR relaxation signal (transverse or longitudinal) will have a multiexponential behavior, as the ratio V/S changes from pore to pore. This information is extremely important for petrophysics, as it allows to correlate relaxation times to pore sizes. If total pore space can be subdivided in smaller volumes, each one with its defined size $\left(\frac{V}{S}\right)_i$, then each fluid volume

will contribute to transverse magnetization decay (from an CPMG measurement) accordingly to equation (3.44), yielding (26):

$$M_T(t) = \sum_i f_i e^{-t/T_{2i}} \quad (3.45)$$

Amplitude f_i is proportional to the amount of magnetization (hence fluid volume) that relaxes with that specific T_{2i} . The total sum $\sum_i f_i$ is then proportional to total fluid volume and can be easily converted to total porosity. If we consider the proportions f_i as a continuous function of relaxation time, then the CPMG result can be written as:

$$M_T(t) = \int_0^{\infty} f(T_2) e^{-\frac{t}{T_2}} dT_2 \quad (3.46)$$

Function $f(T_2)$ is the T_2 distribution and has the property that the area underneath it between two relaxation time values, is equal to the amount of fluid (or fluid fraction) that relaxes in that relaxation time range. Total area can then be expressed in terms of total porosity. $f(T_2)$ can be obtained from CPMG measurements through an inversion process described in Chapter 4.

If the time between echoes T_E is chosen small enough and considering that surface dominates over bulk relaxation, then equation (3.44) becomes:

$$T_2 \approx \frac{1}{\rho_2} \frac{V}{S} \quad (3.47)$$

Under these conditions, and considering that the rock is saturated with a single fluid, $f(T_2)$ is proportional to the pore size distribution introduced in Chapter 2. This allows some important petrophysical interpretations.

Porosity fractions

Considering that as the pores become smaller, capillary forces tend to increase, it is customary to define a limiting pore length that separates fluids that are still movable from those that are irreducible. Consequently, there should be a relaxation time cutoff (T_{2c}) that separates those two fluid fractions. T_{2c} can be obtained in laboratory by extracting movable fluids (FF) from a rock core and solving:

$$\int_{T_{2c}}^{\infty} f(T_2) dT_2 = FF \quad (3.48)$$

Justification for a T_2 cutoff depends on the assumption of a strong correlation between pore sizes and pore throat sizes, because capillary forces are essentially ruled by the throat system. Therefore, it is expected that interpretations based on cutoffs should give better

results for sandstones. On the other hand, throat sizes do not always correlate with pore sizes for carbonates, misleading interpretations. Nevertheless, standard literature values for T_{2c} are $33ms$ for sandstones (27) and $100ms$ for carbonates.

Another cutoff value stands for clay bound water (CBW), which relaxes at fast rates because of little molecule mobility, and is standardly defined as fluids relaxing below $3ms$.

In Figure 3.12, a well log result is shown with the standard T_2 distribution interpretation. Second track brings the distributions at each depth, and the first one brings Free Fluid (FF) in blue, Bound Volume Capillary (BVC) in light brown and Clay Bound Water (CBW) in dark brown, all adding up to total porosity.

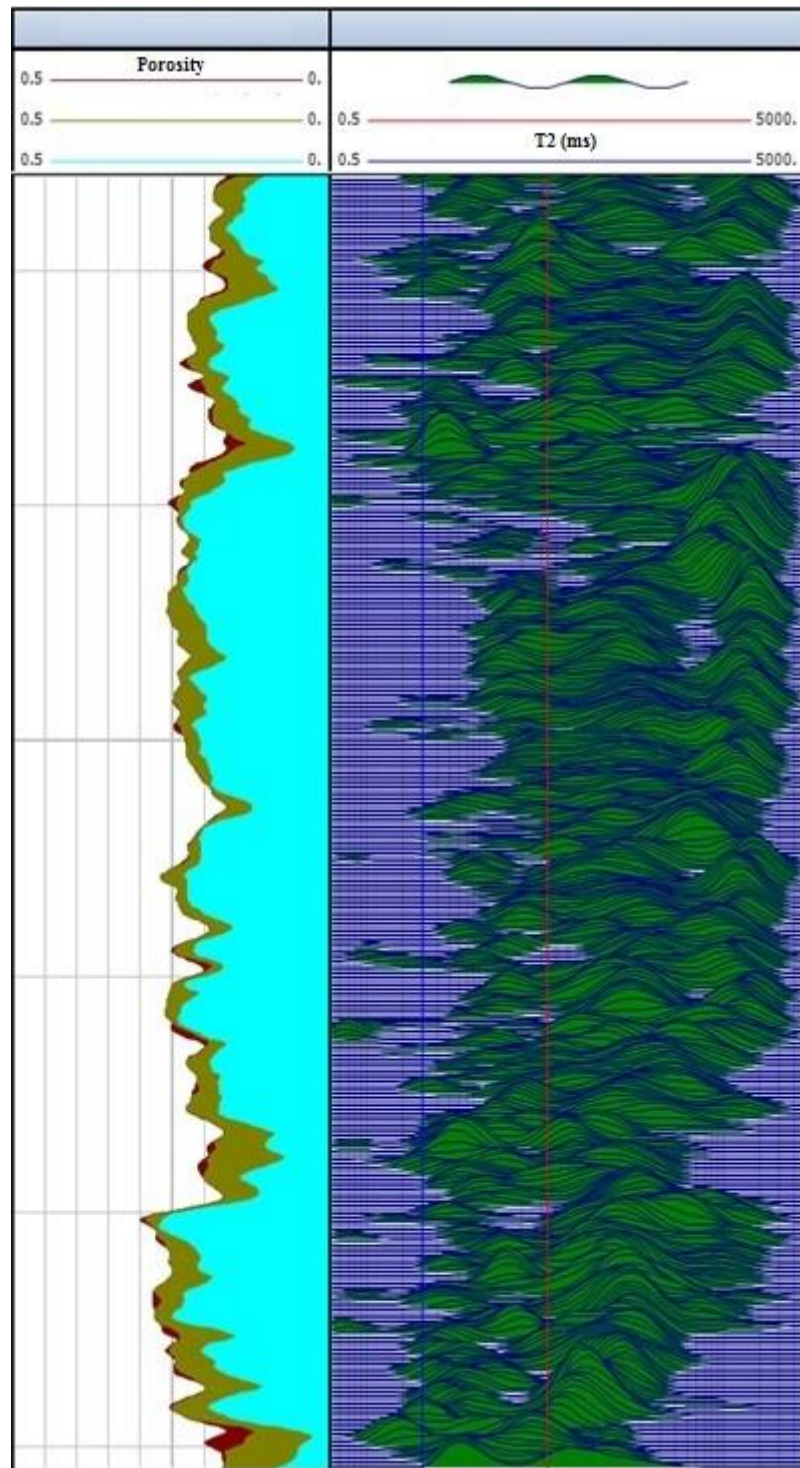


Figure 3.12 - Example of well log result with NMR standard petrophysical interpretation.
Source: Provided by Petrobras.

Figure 3.13 shows a schematic diagram relating portions of a T_2 distribution with fluid fractions and porosity. For formations saturated with water and oil, if the rocks remain water wet, then oil does not experience surface relaxation. For this reason light oils may be detected in T_2 distributions as they relax with more than 1s. If the rock is mixed to oil wet, or if the oil

has high viscosity, then bulk oil T_2 will overlap with water distribution, making interpretations harder.

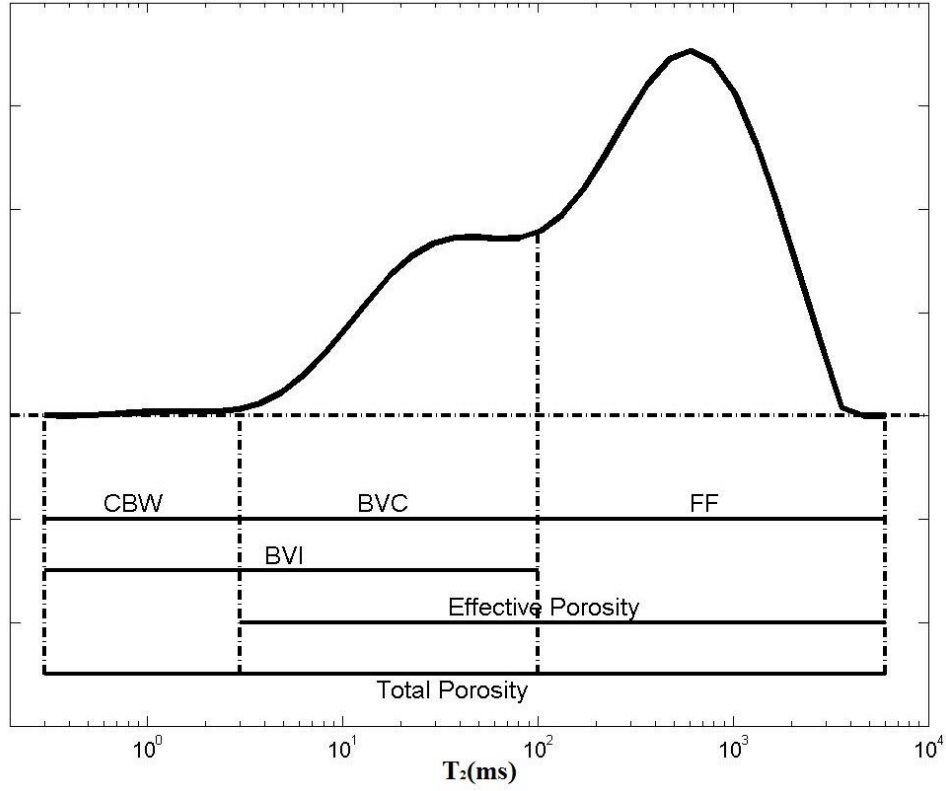


Figure 3.13 - Fluid fractions in a standard T_2 distribution.
Source: By the author.

For fluid typing, it might be more useful to look at diffusion coefficient distribution, as D_0 can be much smaller for oils than for water. Diffusion distribution ($f(D)$), joint diffusion-relaxation or relaxation-relaxation distributions ($f(D, T_2)$ and $f(T_1, T_2)$, respectively), can also be obtained through an inversion process from measurement styles described in Chapter 4, and correlate with petrophysical properties (28), including wettability (29):

$$M_T = \int dT_1 dT_2 f(T_1, T_2) \left(1 - e^{-\frac{T_S}{T_1}}\right) e^{-\frac{t}{T_2}} \quad (3.49)$$

$$M_T = \int dD dT_2 f(D, T_2) e^{-D(\gamma G)^2 \delta^2 (\Delta - \delta/3)} e^{-\frac{t}{T_2}} \quad (3.50)$$

Permeability

Permeability relates fluid flow rate with pressure difference through a rock path. For a simple model consisting of interconnected tubes, permeability is given by equation (2.5), hence has a strong correlation with the square of a characteristic length of the pore/throat

system. Based on the proportionality between T_2 and pore size, and on empirical correlations from experiments, Kenyon et al. (26) obtained the following permeability expression:

$$k_{SDR} = A\phi^4 T_{2LM}^2 \quad (3.51)$$

T_{2LM} is the logarithmic mean of $f(T_2)$, and A a scaling constant. Again, this method will have a better performance when pore sizes correlate well with pore throats, which is expected for sandstones. Another drawback is that k_{SDR} assumes that all pores are interconnected, in a way that permeability is mostly ruled by pore sizes, in spite of pore connectivity.

If surface relaxivity is known equation (3.51) can be corrected yielding:

$$k_\rho = A\phi^4 (\rho_2 T_{2LM})^2, \quad (3.52)$$

as not only T_2 , but ρT_2 equates to pore size. This correction has proved to have a good performance in predicting permeability for complex pore systems like carbonates (30-31), as it puts $f(T_2)$ in the correct length scale when one has large heterogeneity on relaxivities. (32)

Timur and Coates (33) proposed a different permeability predictor that takes into account the proportion of free fluid over irreducible:

$$k_{TC} = A\phi^4 \left(\frac{FF}{BVI} \right)^2 \quad (3.53)$$

As it is dependent of a T_2 cutoff reasoning it suffers from the same drawbacks of K_{SDR} , although it is also useful. Applications of NMR data for permeability and also bulk fluid properties have been extensively studied. (4, 34-35)

Diffusion processes inside porous media

If one could follow a single fluid molecule diffusing through the fluid in a Brownian motion fashion during a time Δ , they would see an erratic motion as depicted in Figure 3.14.

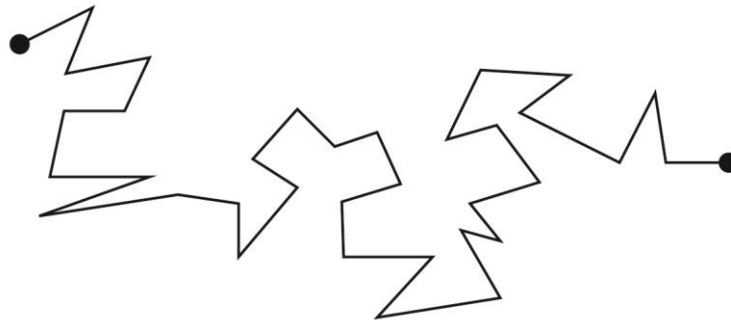


Figure 3.14 - Erratic motion of a molecule inside a fluid.

Source: By the author.

As diffusion time Δ increases, it becomes more likely for the particle to be found farther from its original position. In these kinds of motion, mean square distance increases linearly with diffusion time, in such a way that one can define the constant D_0 as:

$$D_0 = \frac{\langle \|\vec{r}(\Delta) - \vec{r}(0)\|^2 \rangle}{6\Delta} \quad (3.54)$$

If one attempts to use equation (3.54) as an operational definition of fluid diffusion coefficient inside a pore, they would find the following results (36): for small diffusion times, a particle inside the bulk pore space would still behave similar to a molecule in a free fluid, as it would not have time to feel the restriction imposed by pore walls. However, as Δ increases, numerator of equation (3.54) can only get as high as the square of the pore length, while the denominator increases indefinitely. Restricted diffusion coefficient is then a monotonic decreasing function of diffusion time Δ . For an isolated pore, $D(\Delta)$ will tend to zero as Δ increases. In the case of interconnected pores, when Δ is big enough for the particle to travel to several pores, the whole pore system will be seen as a macroscopic homogeneous medium, with an effective constant diffusion coefficient dependent on tortuosity (remind F is the electric formation factor).

$$D_\infty = \frac{1}{F\phi} \quad (3.55)$$

For small Δ , only the fraction of molecules that are close enough to the pore walls will contribute to the reduction of D , which are those as far as about $\sqrt{D_0\Delta}$ of the walls. The total amount of particles contributing for restrictions in D is then proportional to the volume $S\sqrt{D_0\Delta}$, S being total pore surface area. Then, at first order, restriction should depend on the ratio $\frac{S}{V}\sqrt{D_0\Delta}$. In fact, Mitra *et al* (37) showed analytically that when $\sqrt{D_0\Delta} \ll (V/S)$,

$$D(\Delta) = D_0 \left(1 - \frac{4}{9\sqrt{\pi}} \frac{S}{V} \sqrt{D_0\Delta} \right) \quad (3.56)$$

The concept of restricted diffusion along with equation 3 – 56 has been used to obtain petrophysical properties such as connectivity between pores and fluid saturation corrections (38), (39).

LaTour *et al.* proposed an insightful method for determining surface relaxivity from restricted diffusion measurements. (40-41) By using relation (3.56), $D(\Delta)$ can also be seen as a function of T_2 :

$$D(\Delta, T_2) = D_0 \left(1 - \frac{4}{9\sqrt{\pi}} \frac{\sqrt{D_0\Delta}}{\rho_2 T_2} \right) \quad (3.57)$$

By measuring tortuosity through electric formation factor (equation (2.6)), diffusion coefficients for short Δ , and interpolating both limits using a mathematical method called Padé fitting, one can solve equation (3.57) to obtain ρ_2 as a fitting parameter.

This method has been used to determine relaxivities for sandstones and carbonates, yielding good permeability estimations from equation (3.52). (30-31)

In Chapter 5 we discuss and develop a way to extend this methodology for determining surface relaxivity to data acquired in well logging.

Other diffusion techniques

NMR techniques can also be used to map internal magnetic field gradients arising at the interface between rock and fluids. (42-43)

3.4 NMR Well logging: general tool's characteristics and acquisition protocols

In order to fit into a wellbore that typically has 8 to 12 inches, NMR apparatus (magnet, antenna and spectrometer) are arranged into a case with cylindrical symmetry, that goes down into the well coupled with other logging tools. The magnet section is usually one meter long, with an antenna filling about 30cm in the middle, for generating rf pulses and detecting transverse magnetization. Combination of magnet and antenna design generates inside the formation a sensitive volume schematized in Figure 3.15.

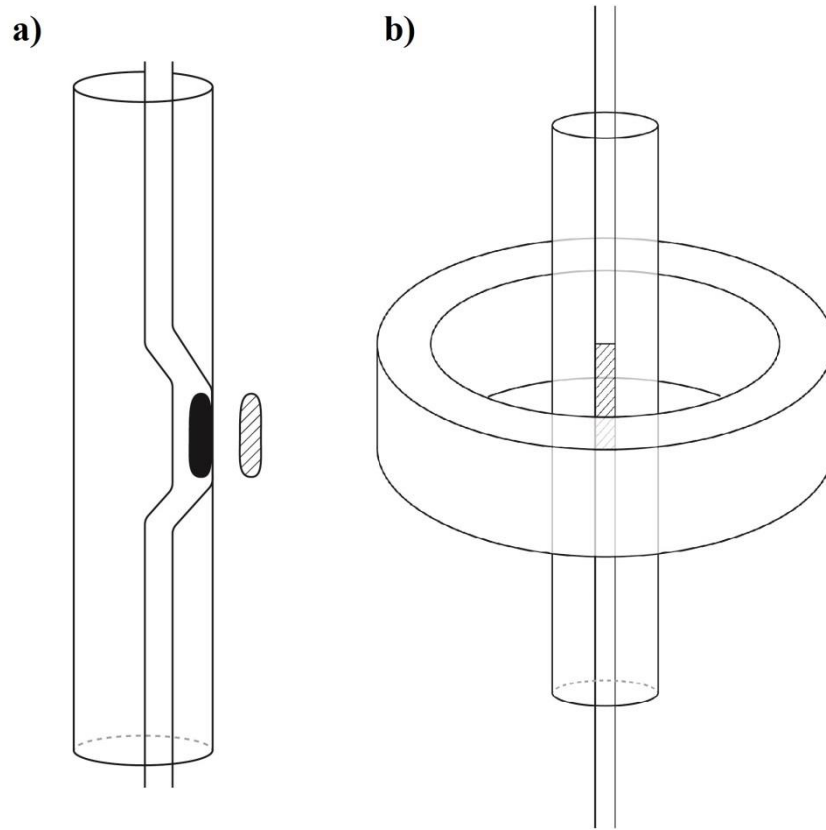


Figure 3.15 - Two common types of sensitive volumes: a) one sided or b) ring shaped.
Source: By the author.

For centralized tools such as Halliburton's MRIL Prime, Baker Hughes' Magtrak or Schlumberger's Provision, the static field \vec{B}_0 is axially symmetric, and the resulting sensitive volume forms a ring around tool's axis, inside formation, as in Figure 3.15a. A different magnet configuration can focus the static field to a preferably longitude of the wellbore (the tool then runs 'pressed' against the pore wall as in Figure 3.15b), which is the case for Halliburton's MRIL XL, Baker Hughes' MREX and Schlumberger's MRScanner. Either way, sensitive volume is actually composed of several shells, because of pulse tuning and selectivity in a field gradient. As one walks away from the tool (towards the formation), B_0 decreases as a function of the distance r from the tool, hence so does the Larmor Frequency. Therefore, by tuning the rf pulse at different frequencies f_p , one can excite just the spins located at a distance correspondent to that frequency. Due to the fact that finite pulses will always have a band of frequencies Δf (refer to Figure 3.16), all spins with Larmor frequencies between $f_p - \Delta f$ and $f_p + \Delta f$ will be excited, hence an excitation slice is generated in the formation.

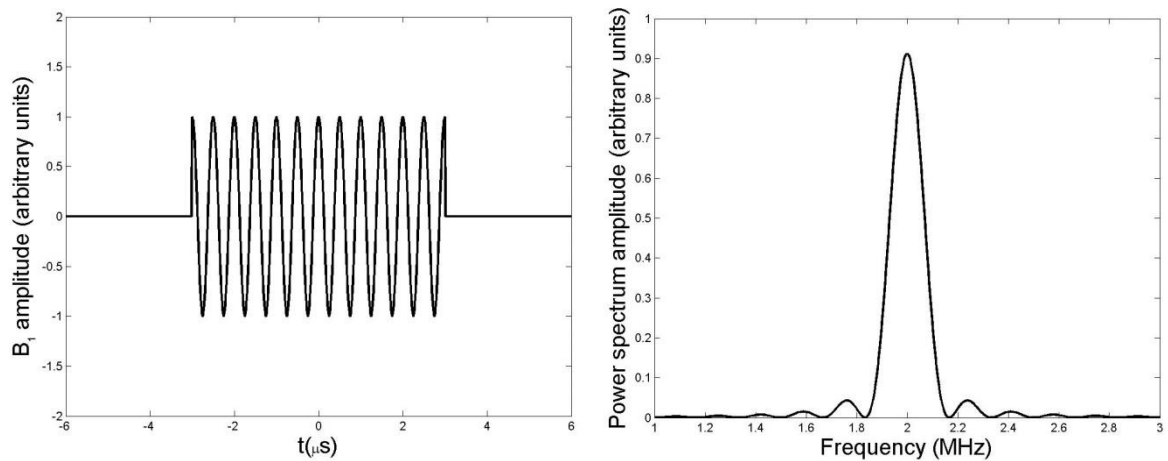


Figure 3.16 - A simple \vec{B}_1 rf pulse and its corresponding Fourier Transform. Even if the pulse is tuned to a single frequency, its limited duration carries a band of frequencies around the predominant one.

Source: By the author.

Typical B_0 fields through the slices range from 350 to 500 Gauss (Larmor frequencies between 0.8 to 2 MHz), and field gradient in each slice with values of 10 – 30 Gauss/cm. The depth of investigation (from wellbore interface towards the formation) typically ranges from 2 to 4 inches, and shells' thickness are of the order of millimeters, extending to about 10 cm the direction parallel to the well.

Well logging uses the existence of different shells to optimize the trade of between logging speed and signal to noise ratio (SNR), as the tool is always sliding through the well during acquisition, so that the measurement can be made as fast as possible for economic reasons. While the signal is being detected from spins in one of the slices, the static magnetic field is already polarizing the other shells. Therefore, as soon as the first CPMG is acquired, one can immediately start the acquisition of the other one in a different shell. During this second acquisition, magnetization of the first one is repolarized, and so on. Resultant CPMGs can be averaged to increase SNR or processed simultaneously, as will be described in Chapter 4. Figure 3.17 shows how such an acquisition diagram looks like.

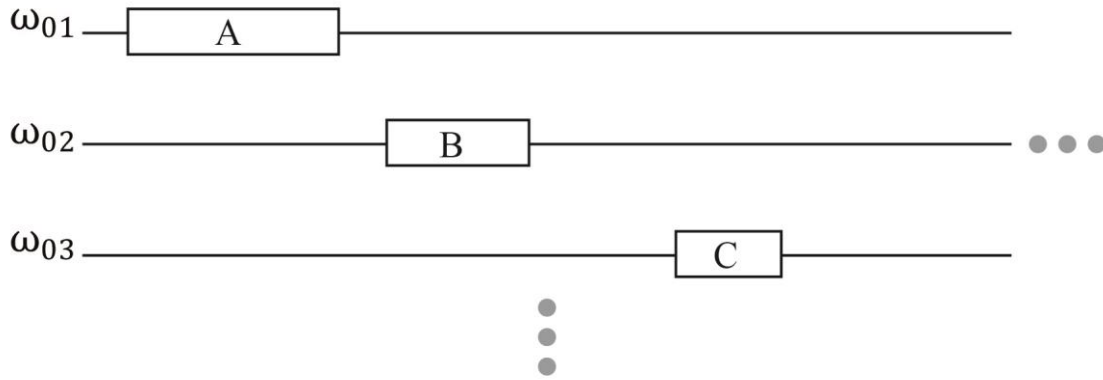


Figure 3.17 - CPMG blocks at several different frequencies (shells) through acquisition time (time increases to the right). Each acquired echotrain can have different waiting times (T_W), echo times (T_E), number of echoes (N_E) and repetition number (N_{rep}).

Source: By the author.

Table 3.1 - T_2 distribution acquisition scheme

<i>CPMG ID</i>	T_W (ms)	T_E (ms)	N_E	N_{rep}
<i>A</i>	∞	0.2	5000	1
<i>B</i>	∞	0.6	600	1
<i>C</i>	20	0.2	30	20
\vdots	\vdots	\vdots	\vdots	\vdots

Source: By the author.

Table 3.1 shows a typical acquisition scheme for T_2 distribution. Waiting times (T_W), that is, the time one should wait for magnetization build up in the static field before starting the acquisition, are predominantly long (virtually infinity considering prepolarization in different shells). Time between echoes (T_E) are short, reducing diffusion effects. Number of echoes (N_E) is simply the total number of points acquired in one CPMG, and repetition number (N_{rep}) refers to the amount of times the same CPMG is acquired in sequence (then averaged). For this specific acquisition scheme, one small echotrain is acquired 20 times using short T_W , which guarantees a good SNR for fast decaying signals. This short CPMG can be incorporated during inversion.

For acquiring joint T_1T_2 distribution, one can vary the wait time T_W from slice to slice, as in Table 3.2.

Table 3.2 - T_1T_2 distribution acquisition scheme

CPMG ID	T_W (ms)	T_E (ms)	N_E	N_{rep}
<i>A</i>	12000	0.4	2500	1
<i>B</i>	500	0.4	2500	1
<i>C</i>	100	0.4	2500	10
<i>D</i>	10	0.4	2500	10
\vdots	\vdots	\vdots	\vdots	\vdots

Source: By the author.

Each CPMG will then work as one step of an Saturation Recovery experiment.

For diffusion measurements, one cannot vary gradient intensity as easily as can be done in a PFG experiment, as gradient in each shell is fixed. What can then be done is vary echo time (T_E) from slice to slice, as in Table 3.3.

Table 3.3 - DT_2 acquisition scheme

CPMG ID	T_W (ms)	T_E (ms)	N_E	N_{rep}
<i>A</i>	∞	0.4	2500	1
<i>B</i>	∞	1	1000	1
<i>C</i>	∞	5	200	1
<i>D</i>	∞	12	100	1
\vdots	\vdots	\vdots	\vdots	\vdots

Source: By the author.

For all well logging acquisition schemes presented until now, each echotrain can be written in general as:

$$M_T(T_{W\eta}, T_{E\eta}, t) = \int dDdT_1dT_2f(D, T_1, T_2)(1 - e^{-T_{W\eta}/T_1})e^{-\frac{D(\gamma GT_{E\eta})^2}{12}t}e^{-t/T_2} \quad (3.58)$$

Index $\eta = A, B, C, \dots$ represents each CPMG block from different shells. All CPMG blocks acquired in one acquisition cycle can be composed together in an inversion method described in Chapter 4, in order to obtain desired distributions.

Besides the ones described in this section, another tool design is available, which is Schlumberger's CMR tool. Instead of generating a series of sensitive shells, the magnets are arranged in a way that a sweet spot of low gradient is generated inside the formation. The sensitive volume is big enough to achieve good SNR with less CPMG acquisitions. This

configuration is less amenable to diffusion effects, although high gradients can be found at the edges of the sensitive volume.

For diffusion measurements under highly inhomogeneous fields, net magnetization arises from the sum of several different coherence pathways, altering relaxation times and diffusion modulation of the echotrain. (44-45) However, the sensitive volume can in general be mathematically subdivided in smaller sections of constant gradient, defining a gradient distribution function $g(G)$ (46). Signal processing can be held in this case by writing any function $F(G)$ appearing in expressions such as (3.58) and (3.60) as:

$$F(G) \rightarrow \int_0^\infty g(G)F(G)dG \quad (3.59)$$

Gradient distribution function $g(G)$ is tool specific and can be measured by mapping its field distribution or estimated with an adequate inversion processing of a diffusion measurement. Figure 3.18 shows an example of how such a gradient distribution could look like. It is predominantly low gradient, but has values as high as 20Gauss/cm .

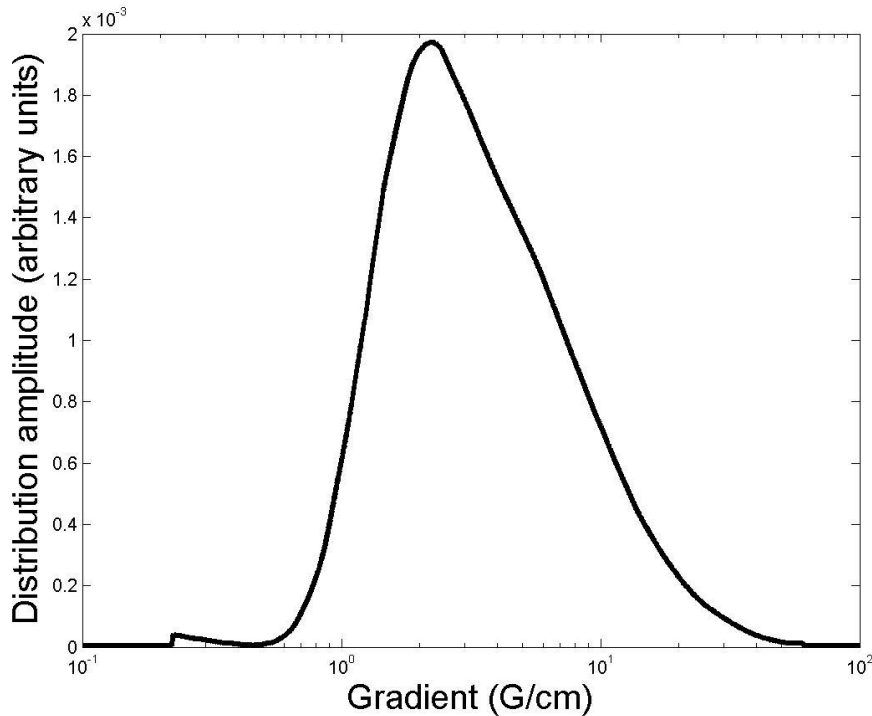


Figure 3.18 - Example of gradient distribution.
Source: Adapted from HURLIMANN et al. (46)

Diffusion editing

For DT_2 example presented in previous section, diffusion relaxation rate will affect T_2 as shown in equation (3.44), which means that acquired signal will suffer from diffusion losses throughout all CPMG duration. This reduces signal considerably, making CPMG's

with long T_E 's very poor regarding SNR. In order to overcome this effect, HURLIMANN et al (47) proposed the diffusion editing technique, shown in Figure 3.19.

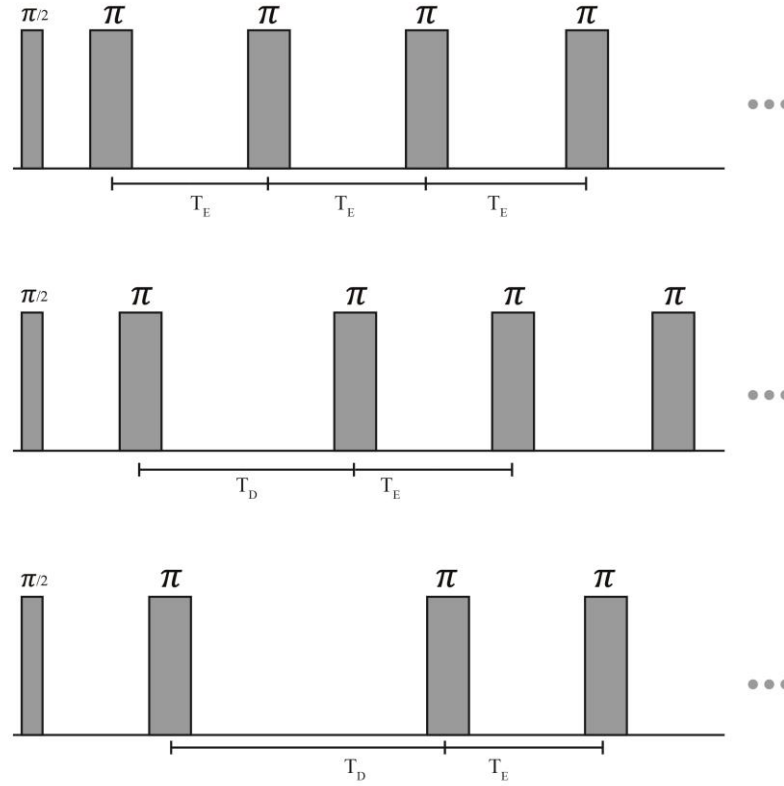


Figure 3.19 - Diffusion Editing pulse sequence.
Source: By the author.

A main CPMG is acquired with small T_E to suppress diffusion losses, except for the first one or two echoes. In this way, a diffusion-free CPMG is acquired, but modulated by a diffusion term:

$$M_T(T_D, t) = \int dD dT_2 f(D, T_2) e^{-\frac{D(\gamma G)^2 T_D^3}{12}} e^{-\frac{t}{T_2}} \quad (3.60)$$

T_D is the long echo time for first echoes, and equals twice the diffusion time Δ introduced in previous sections. By varying T_D one gets a resulting set of CPMGs that can be inverted for DT_2 distribution.

In Chapter 5 we show how diffusion editing like sequences can be used to allow relaxivity estimation downhole.

4 DATA PROCESSING

In Chapter 3 we showed that the basic NMR magnetization signal obtained from a CPMG pulse sequence can be mathematically described at an instant t_i after the $\pi/2$ pulse as:

$$M_T(t_i) = \int_0^{\infty} f(T_2) e^{-\frac{t_i}{T_2}} dT_2 \quad (4.1)$$

Index i ranges from 1 to N_E (number of echoes = number of π pulses), and consecutive t_i are spaced by an interval T_E , the echo time, resulting in a multiexponential decay sampled with N_E points. $f(T_2)$ is the T_2 distribution, which we are interested in obtaining from acquired signal. By writing the distribution over a predetermined discrete set of relaxation times $T_{2,1}, T_{2,2}, T_{2,3} \dots$, of size $N_{bins}T_2$, equation (4.1) becomes:

$$M_T(t_i) = \sum_j e^{-\frac{t_i}{T_{2,j}}} f(T_{2,j}) \quad (4.2)$$

In matrix form it can be written as:

$$\mathbf{d} = \mathbf{A}\mathbf{f} \quad (4.3)$$

With:

$$\left\{ \begin{array}{l} \mathbf{d} = \begin{pmatrix} M_T(t_1) \\ M_T(t_2) \\ \vdots \\ M_T(t_m) \end{pmatrix} \\ \mathbf{f} = \begin{pmatrix} f(T_{2,1}) \\ f(T_{2,2}) \\ \vdots \\ f(T_{2,n}) \end{pmatrix} \\ A_{ij} = e^{-\frac{t_i}{T_{2,j}}} \end{array} \right. \quad (4.4)$$

\mathbf{d} is the collection of all acquired points (data vector) and has in general size m , which for a simple CPMG sequence equals number of echoes N_E . \mathbf{f} is the collection of all parameters used to model the data (parameter vector), which in above example is simply the T_2 discrete distribution with total number of points $n = N_{bins}T_2$, logarithmic spaced. Consequently, \mathbf{A} is a $m \times n$ matrix (model matrix) that connects model parameters with the theoretical description of acquired data, through equation (4.3). All acquisition schemes described in Chapter 3 can be put in the form of equation (4.3), as we will show in next section.

Equation (4.3) is often called the direct problem, as it allows a straightforward calculation of expected output from a measurement, once the fluid/formation characteristics are known, and an appropriated model is given. In real life we are interested in the inverse problem, where data \mathbf{d} and model \mathbf{A} are known but system properties \mathbf{f} are to be determined. This chapter is devoted on explaining basic inversion techniques developed in this work based on literature algorithms, that can be used for downhole applications. Through this chapter we will adopt the convention that vectors are represented by bold short letters and matrices by bold capital letters.

4.1 Determining model matrix \mathbf{A}

1D distributions

In the introductory section we defined model matrix \mathbf{A} , data vector \mathbf{d} and parameter vector \mathbf{f} for an 1D T_2 distribution, acquired through a simple CPMG pulse sequence. For other 1D distributions the process is straightforward. Consider for example the results of an Saturation Recovery T_1 acquisition. The magnetization amplitude for a certain wait time T_{wi} is given by:

$$M_T(T_{w,i}) = \int dT_1 f(T_1)(1 - e^{-T_{w,i}/T_1}) \quad (4.5)$$

Data vector will then be the collection of all magnetization amplitudes at different wait times:

$$\mathbf{d} = \begin{pmatrix} M_T(T_{w,1}) \\ M_T(T_{w,2}) \\ \vdots \\ M_T(T_{w,m}) \end{pmatrix} \quad (4.6)$$

Similarly to T_2 , T_1 distribution will be the collection of all amplitudes at pre-defined T_1 values $T_{1,1}, T_{1,2}, \dots, T_{1,n}, n = NbinsT_1$:

$$\mathbf{f} = \begin{pmatrix} f(T_{1,1}) \\ f(T_{1,2}) \\ \vdots \\ f(T_{1,n}) \end{pmatrix} \quad (4.7)$$

Model matrix \mathbf{A} will then be written as:

$$A_{ij} = 1 - e^{-\frac{T_{w,i}}{T_{1,j}}} \quad (4.8)$$

For a PFG diffusion measurement, diffusion distribution will be written for predefined diffusion values $D_1, D_2, \dots, D_n, n = NbinsD$, data vector will be the collection of

magnetization amplitudes for different gradients, and matrix \mathbf{A} will be given from equation (3.33) as:

$$A_{ij} = e^{-D_j(\gamma G_i)^2 \delta^2 (\Delta - \delta/3)} \quad (4.9)$$

T₁T₂ distributions

Consider the well logging T_1T_2 acquisition described by table 2, where several CPMG echotraines are measured and labeled as A, B, C, \dots . Each one of them has essentially a different wait time, and assuming that echo time $T_{E\eta}$ is small enough so that diffusion can be neglected, or that diffusion effects are implicitly included in T_2 distribution, a single CPMG result at a time t_i will be given from equation (3.58) as:

$$M_T(T_{W\eta}, t_i) = \int dT_1 dT_2 f(T_1, T_2) (1 - e^{-T_{W\eta}/T_1}) e^{-t_i/T_2} \quad (4.10)$$

Besides the differences in wait times and possibly echo times, repetition numbers can also change from one CPMG to another. That means that each echotrain was acquired $N_{rep,\eta}$ times and averaged into a single response, which will consequently have a smaller noise level than those acquired a single time. Each echotrain will then have a different standard deviation σ_η measured from the noise channel.

A single CPMG decay data can be written as:

$$\mathbf{d}_\eta = \begin{pmatrix} M_T(T_{W,\eta} t_1) \\ M_T(T_{W,\eta} t_2) \\ \vdots \\ M_T(T_{W,\eta} t_{N_{E,\eta}}) \end{pmatrix} \quad (4.11)$$

The whole data vector \mathbf{d} will then be given by the collection of all acquired points:

$$\mathbf{d} = \begin{pmatrix} \mathbf{d}_A/\sigma_A \\ \mathbf{d}_B/\sigma_B \\ \mathbf{d}_C/\sigma_C \\ \vdots \end{pmatrix} \quad (4.12)$$

Each result is divided by its standard deviation so that the inversion algorithm can give a bigger weight to data acquired at smaller noise levels, as will be explained in following sections. \mathbf{d} has size $m = \sum_\eta N_{E,\eta}$.

Acquired data is represented by a bi dimensional distribution $F(T_1, T_2)$, that gives the amount of fluid relaxing at each (T_1, T_2) pair inside the rock sample or formation. By writing the distribution over a predefined discrete set of relaxation times $T_{1,1}, T_{1,2}, \dots, T_{1,NbinsT_1}$, and $T_{2,1}, T_{2,2}, \dots, T_{2,NbinsT_2}$, distribution F will have the following natural matrix form:

$$\mathbf{F} = \begin{pmatrix} F(T_{1,NbinsT_1}, T_{2,1}) & F(T_{1,NbinsT_1}, T_{2,2}) & \cdots & F(T_{1,NbinsT_1}, T_{2,NbinsT_2}) \\ \vdots & \vdots & \ddots & \vdots \\ F(T_{1,2}, T_{2,1}) & F(T_{1,2}, T_{2,2}) & \cdots & F(T_{1,2}, T_{2,NbinsT_2}) \\ F(T_{1,1}, T_{2,1}) & F(T_{1,1}, T_{2,2}) & \cdots & F(T_{1,1}, T_{2,NbinsT_2}) \end{pmatrix} \quad (4.13)$$

In order to pose the inversion problem in the form of equation 3, matrix \mathbf{F} needs to be “unfolded” into a vector \mathbf{f} , which can be done in the following way (48). Consider the T_2 distribution $\mathbf{f}_{T_{1,k}}$ given by all elements of \mathbf{F} that have a fixed T_1 value, say $T_{1,k}$:

$$\mathbf{f}_{T_{1,k}} = \begin{pmatrix} f(T_{1,k}, T_{2,1}) \\ f(T_{1,k}, T_{2,2}) \\ \vdots \\ f(T_{1,k}, T_{2,NbinsT_2}) \end{pmatrix} \quad (4.14)$$

In terms of the sub distributions $\mathbf{f}_{T_{1,k}}$, whole matrix \mathbf{F} is given by:

$$\mathbf{F} = \begin{pmatrix} \mathbf{f}_{T_{1,NbinsT_1}}^T \\ \vdots \\ \mathbf{f}_{T_{1,2}}^T \\ \mathbf{f}_{T_{1,1}}^T \end{pmatrix} \quad (4.15)$$

Unfolded vector \mathbf{f} has length $n = NbinsT_1 \times NbinsT_2$ and writes:

$$\mathbf{f} = \begin{pmatrix} \mathbf{f}_{T_{1,1}} \\ \mathbf{f}_{T_{1,2}} \\ \vdots \\ \mathbf{f}_{T_{1,NbinsT_1}} \end{pmatrix} \quad (4.16)$$

Equation (4.10) can then be used to relate \mathbf{d} and \mathbf{f} as in (4.3) through the following construction of model matrix \mathbf{A} :

$$\begin{pmatrix} \mathbf{d}_A/\sigma_A \\ \mathbf{d}_B/\sigma_B \\ \mathbf{d}_C/\sigma_C \\ \vdots \end{pmatrix} = \begin{pmatrix} \frac{1}{\sigma_A} \mathbf{A}(T_{W,A}, T_{1,1}) & \frac{1}{\sigma_A} \mathbf{A}(T_{W,A}, T_{1,2}) & \cdots \\ \frac{1}{\sigma_B} \mathbf{A}(T_{W,B}, T_{1,1}) & \frac{1}{\sigma_B} \mathbf{A}(T_{W,B}, T_{1,2}) & \cdots \\ \vdots & \vdots & \ddots \end{pmatrix} \begin{pmatrix} \mathbf{f}_{T_{1,1}} \\ \mathbf{f}_{T_{1,2}} \\ \vdots \end{pmatrix} \quad (4.17)$$

With:

$$[\mathbf{A}(T_{W,\eta}, T_{1,k})]_{ij} = (1 - e^{-T_{W,\eta}/T_{1,k}}) e^{-t_i/T_{2,j}} \quad (4.18)$$

Standard deviations σ_η were included for the same reason as in equation (4.12).

DT₂ distributions

Depending on the acquisition scheme, transverse magnetization decay for each acquired echotrain can be written from equation (3.58) (for an acquisition such as described in table 3) or from equation (3.60) (for diffusion editing), yielding:

$$M_T(T_{D,\eta}, t_i) = \begin{cases} \int dDdT_2 f(D, T_2) e^{-\frac{D(\gamma GT_{D,\eta})^2}{12} t_i} e^{-\frac{t_i}{T_2}} \\ \int dDdT_2 f(D, T_2) e^{-\frac{D(\gamma G)^2 T_{D,\eta}^3}{12}} e^{-\frac{t_i}{T_2}} \end{cases} \quad (4.19)$$

Acquired points are then:

$$\mathbf{d}_\eta = \begin{pmatrix} M_T(T_{D,\eta}, t_1) \\ M_T(T_{D,\eta}, t_2) \\ \vdots \\ M_T(T_{D,\eta}, t_{N_{E,\eta}}) \end{pmatrix} \quad (4.20)$$

With definitions above data vector \mathbf{d} is written in the exact same way as described in equation (4.12).

For bi dimensional distribution $F(D, T_2)$, matrix distribution \mathbf{F} and its correspondent unfolded vector \mathbf{f} are defined in analogy to equations (4.13) to (4.16) as (48):

$$\mathbf{F} = \begin{pmatrix} F(D_{NbinsD}, T_{2,1}) & F(D_{NbinsD}, T_{2,2}) & \cdots & F(D_{NbinsD}, T_{2,NbinsT_2}) \\ \vdots & \vdots & \ddots & \vdots \\ F(D_2, T_{2,1}) & F(D_2, T_{2,2}) & \cdots & F(D_2, T_{2,NbinsT_2}) \\ F(D_1, T_{2,1}) & F(D_1, T_{2,2}) & \cdots & F(D_1, T_{2,NbinsT_2}) \end{pmatrix} \quad (4.21)$$

$$\mathbf{f} = \begin{pmatrix} F(D_1, T_{2,1}) \\ \vdots \\ F(D_1, T_{2,NbinsT_2}) \\ F(D_2, T_{2,1}) \\ \vdots \\ F(D_2, T_{2,NbinsT_2}) \\ \vdots \end{pmatrix} \quad (4.22)$$

Matrix \mathbf{A} then becomes:

$$\mathbf{A} = \begin{pmatrix} \frac{1}{\sigma_A} \mathbf{A}(T_{D,A}, T_{1,1}) & \frac{1}{\sigma_A} \mathbf{A}(T_{D,A}, T_{1,2}) & \cdots \\ \frac{1}{\sigma_B} \mathbf{A}(T_{D,B}, T_{1,1}) & \frac{1}{\sigma_B} \mathbf{A}(T_{D,B}, T_{1,2}) & \cdots \\ \vdots & \vdots & \ddots \end{pmatrix} \quad (4.23)$$

With:

$$[\mathbf{A}(T_{D,\eta}, D_k)]_{ij} = \begin{cases} e^{-\frac{D_k(\gamma GT_{D,\eta})^2}{12} t_i} e^{-\frac{t_i}{T_{2,j}}} \\ e^{-\frac{D_k(\gamma G)^2 T_{D,\eta}^3}{12}} e^{-\frac{t_i}{T_{2,j}}} \end{cases} \quad (4.24)$$

The same reasoning can be applied to higher dimensional distributions coming from general measurements such as described by equation (3.58), through concatenation of data points, unfolding of the multidimensional distribution, and building up of an appropriate model matrix \mathbf{A} that correctly connects model parameters \mathbf{f} with data \mathbf{d} . The same logic is

used if the unknowns compose the gradient distribution $g(G)$ (49) instead of relaxation times or diffusion distributions, as will be exemplified in the following sections. One can also use concatenation and unfolding for one dimensional inversions coming from data acquired with different parameters, generally used in well logging to increase signal to noise of fast decaying short components of echotrails.

Other formulations are available in literature that allow a faster solution of the inversion problem. Venkataramanan et al. (50-51) decomposes matrix \mathbf{A} into a tensor product of smaller matrices, which speed up inversion computation. However, the method requires that the Kernels in integrals such as equation (3.58) are separable, which does not happen for sequences as diffusion editing, for example. We instead choose to use the method described in this Chapter that in principle can always be applied, with computational issues being overcome by the choice of smaller distribution matrices \mathbf{F} or compaction techniques mentioned in following sections. For the problems approached in this work, this method behaved goodly enough.

4.2 Ill posed nature of the inversion problem

Matrix expression (4.3) is actually a set of m equations that must be solved for n model parameters f_i organized in vector \mathbf{f} . In general, this constitutes an overdetermined system with $m > n$, with no possible solution. Instead, we search for a vector \mathbf{f}^* that best approximates all m equations accordingly to some predefined error measurement. The traditional functional to be minimized is the squared error sum defined as:

$$\phi_{MQ} = \|\mathbf{d} - \mathbf{A}\mathbf{f}\|^2 \quad (4.25)$$

The function \mathbf{f}^* that minimizes functional ϕ_{MSQ} is given by:

$$\mathbf{f}^* = (\mathbf{A}^T \mathbf{A})^{-1} \mathbf{A}^T \mathbf{d} \quad (4.26)$$

Equation (4.26) is known as the minimum squared solution of equation (4.3). Inversion problems that arise from Helmholtz Integrals of the first kind such as equations (3.58) and (3.60) are essentially ill posed (52), in the sense that there are virtually infinite solutions that reasonably minimize functional (4.25). What we mean by “virtually” is that although numerically one could always find a solution \mathbf{f}^* through equation (4.26), that solution would be so affected by the initial data that the smallest practical variations (even computer rounding in a noisyless signal!) would lead to a complete different solution, equally

acceptable mathematically. This can be understood in terms of the Singular Value Decomposition (SVD) of matrix \mathbf{A} .

SVD theorem states that any rectangular matrix \mathbf{A} can be written in terms of simpler matrices as:

$$\mathbf{A} = \mathbf{U}\mathbf{S}\mathbf{V}^T \quad (4.27)$$

\mathbf{V} is a square $n \times n$ matrix satisfying orthogonality relation $\mathbf{V}^T\mathbf{V} = \mathbf{V}\mathbf{V}^T = \mathbf{1}_{n \times n}$, $\mathbf{1}$ being the identity matrix. That means that the columns $\mathbf{v}_i, i = 1, \dots, n$ of \mathbf{V} are linearly independent vectors forming a basis for parameter space, that is, any parameter vector \mathbf{f} can be written as $\mathbf{f} = \sum_{i=1}^n \beta_i \mathbf{v}_i$. The \mathbf{v}_i are eigenvectors of $\mathbf{A}^T\mathbf{A}$.

Likewise, \mathbf{U} is a square $m \times m$ matrix satisfying orthogonality relation $\mathbf{U}^T\mathbf{U} = \mathbf{U}\mathbf{U}^T = \mathbf{1}_{m \times m}$. The columns $\mathbf{u}_i, i = 1, \dots, m$ of \mathbf{U} are linearly independent vectors forming a basis for data space, that is, any data vector \mathbf{d} can be written as $\mathbf{d} = \sum_{i=1}^m \alpha_i \mathbf{u}_i$. The \mathbf{u}_i are eigenvectors of $\mathbf{A}\mathbf{A}^T$.

\mathbf{S} is a rectangular $m \times n$ matrix that connects parameter space to data space, and is given by:

$$\mathbf{S} = \begin{pmatrix} s_1 & 0 & 0 & 0 \\ 0 & s_2 & 0 & 0 \\ \vdots & \vdots & \ddots & \vdots \\ 0 & 0 & 0 & s_n \\ 0 & 0 & 0 & 0 \\ \vdots & \vdots & \vdots & \vdots \\ 0 & 0 & 0 & 0 \end{pmatrix} \quad (4.28)$$

The $s_i, i = 1 \dots n$ are eigenvalues of $\mathbf{A}\mathbf{A}^T$, and are also called singular values of \mathbf{A} . They are all non-negative and are organized in descending order in \mathbf{S} . Action of model matrix \mathbf{A} on any parameter space basis vector \mathbf{v}_i is given by:

$$\mathbf{A}\mathbf{v}_k = s_k \mathbf{u}_k \quad (4.29)$$

The central role of equation (4.29) in understanding the ill posed nature of inverse problem (4.3) happens when at least one of the singular values is zero, yielding $\mathbf{A}\mathbf{v}_i = \mathbf{0}$ for the corresponding i . Suppose that the first q singular values are positive, remaining $n - q$ are null, and that \mathbf{f}^* is the minimum squared solution, that is, $\phi_{MSQ}^* = \|\mathbf{d} - \mathbf{A}\mathbf{f}^*\|^2$ is the smallest possible value for the error. Consider the new parameter vector $\mathbf{f}^{**} = \mathbf{f}^* + \sum_{i=q+1}^n \beta_i \mathbf{v}_i$, with arbitrary β_i . From equation (4.29) one has:

$$\begin{aligned}\Phi_{MQ}^{**} &= \|\mathbf{d} - \mathbf{A}\mathbf{f}^{**}\|^2 = \left\| \mathbf{d} - \mathbf{A}\mathbf{f}^* - \sum_{i=q+1}^n \beta_i \mathbf{A}\mathbf{v}_i \right\|^2 = \\ &= \|\mathbf{d} - \mathbf{A}\mathbf{f}^*\|^2 \Rightarrow \Phi_{MQ}^{**} = \Phi_{MQ}^*\end{aligned}\quad (4.30)$$

Therefore, \mathbf{f}^{**} is an equally valid minimum squared error solution for the same problem. As the β_i are arbitrary, there is an infinite number of such solutions. The condition for existence of at least one null singular value, hence infinite solutions, is the appearance of linearly dependent lines or columns in matrix \mathbf{A} . Although NMR problems do not generate any null s_i , due to the exponential nature of matrices' elements the singular values cover several orders of magnitude from the largest to the smallest. Relative change in \mathbf{f}^* due to small changes in \mathbf{d} is governed by relation $\frac{\|\Delta\mathbf{f}^*\|}{\|\mathbf{f}^*\|} \leq \frac{s_1}{s_n} \frac{\|\Delta\mathbf{d}\|}{\|\mathbf{d}\|}$, so that even fluctuations of the order of 10^{-13} (typical computer precision) will lead to relative changes in the distribution of more than 10^3 .

Indeed, minimum squared error solution (4.26) can be written in terms of SVD as:

$$\mathbf{f}^* = \sum_{i=1}^n \frac{(\mathbf{U}^T \mathbf{d})_i}{s_i} \mathbf{v}_i \quad (4.31)$$

Again, small variations in the input data will lead to big changes in the solution as the singular values (including the smallest) appear in the denominator of (4.31).

Tikhonov's Regularization

Due to the ill posed nature of inversion problem stated by equation (4.3), one is forced to face the challenging task of choosing among an infinite number of solutions, the one that is most physical reasonable or acceptable. Fortunately, mathematician Andrey Tikhonov developed a systematic way of choosing such distribution. (53) He proposed that instead of looking for the minimum of the error ϕ_{MSQ} , one should minimize the following functional:

$$\Phi_{TK} = \|\mathbf{d} - \mathbf{A}\mathbf{f}\|^2 + \alpha \|\mathbf{R}\mathbf{f}\|^2 \quad (4.32)$$

α is a free parameter known as regularization constant, and \mathbf{R} is a regularization matrix. If α is small, ϕ_{TK} approaches the error and inversion tends to reproduce the same results as minimum squared method. For big α on the other hand, inversion process imposes the minimization of $\|\mathbf{R}\mathbf{f}\|$, which has nothing to do with the modeled system and only poses restrictions over the resulting distribution. Therefore, minimizing ϕ_{TK} is a way of searching for a distribution that best reproduces data \mathbf{d} , while restricting features of \mathbf{f} , reducing the infinite space of possible solutions to a few that are physically acceptable. One can impose

smoothness over \mathbf{f} by making \mathbf{R} equal to the identity matrix, which is called zeroth order regularization. If \mathbf{R} is the difference or second difference operator, one is then imposing smoothness over the derivative or curvature of \mathbf{f} , respectively (first and second order regularization). (54-55)

Regularization parameter is chosen through the following tradeoff. For $\alpha = 0$, the error expressed by minimum squared functional ϕ_{MSQ} is the smallest possible one. As α increases, the error does not change too much as a result of an infinitude of solutions. However, when α values keep going up the results tend to differ from the original data, increasing the error until it reaches a maximum for when \mathbf{f} approaches a constant. This is expressed in Figure 4.1. α should be chosen as the bigger value for which the error had still not increased too much from its minimum. There are several ways to automatically determine the regularization parameter overcoming the vagueness of that expression (56), although they are all based on the search of the highlighted area in Figure 4.1. Even a visual inspection of the error as function of α will lead to consistent results as the distribution's shape is more sensitive to changes in the order of magnitude of the regularization parameter.

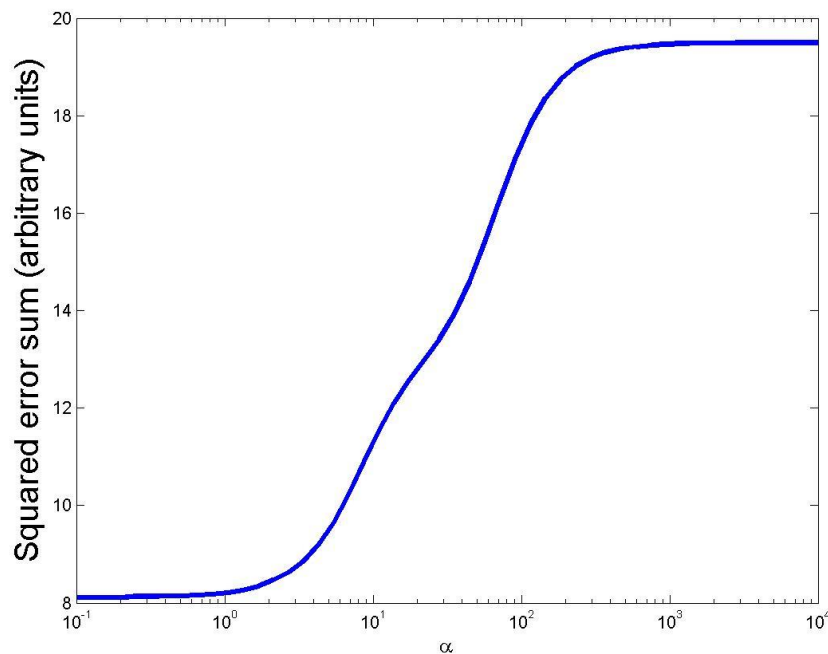


Figure 4.1 - Error ϕ_{MSQ} as a function of regularization parameter α .
Source: By the author.

When $\mathbf{R} = \mathbf{1}$, minimization of ϕ_{TK} leads to:

$$\mathbf{f}^* = \sum_{i=1}^n \frac{s_i}{s_i^2 + \alpha} (\mathbf{U}^T \mathbf{d})_i \mathbf{v}_i \quad (4.33)$$

$\mathbf{U}^T \mathbf{d}$ is a vector with the projections of data \mathbf{d} over each one of the basis' vectors \mathbf{u}_i . Therefore, zeroth order Tikhonov's regularization has the effect of filtering out parts of the data corresponding to small singular values, as $\frac{s_i}{s_i^2 + \alpha} \approx \frac{1}{s_i}$, for $\alpha \ll s_i$ and $\frac{s_i}{s_i^2 + \alpha} \approx 0$, for $\alpha \gg s_i$. It smoothly peaks the solution less influenced by small singular values, stabilizing it under small changes in \mathbf{d} .

In general, for $\mathbf{R} \neq \mathbf{1}$:

$$\mathbf{f}^* = \sum_{i=1}^n C_i(s_1, \dots, s_n, \alpha, \mathbf{R}) (\mathbf{U}^T \mathbf{d})_i \mathbf{v}_i \quad (4.34)$$

The C_i are obtained from the direct solution of:

$$\mathbf{f}^* = (\mathbf{A}^T \mathbf{A} + \alpha \mathbf{R}^T \mathbf{R})^{-1} \mathbf{A}^T \mathbf{d} \quad (4.35)$$

4.3 Inversion algorithm description

The inversion method described up to this point takes care of the infinitude of minimum squared solutions and numeric stability, however, it does not impose any restriction over the sign of elements in \mathbf{f} . Physically, as \mathbf{f} represents a probability distribution function or fluid volume fractions, one has also to demand that any acceptable solution should be strictly non-negative. BUTLER et al. (54) (BRD method) achieve this goal by simultaneously solving the pair of equations:

$$\begin{cases} \mathbf{f}^* = (\mathbf{A}^T \mathbf{A} + \alpha \mathbf{1})^{-1} \mathbf{A}^T \mathbf{d} \\ \mathbf{f}^* \geq \mathbf{0} \end{cases} \quad (4.36)$$

The analytic solution allows for an algorithm to iteratively search for the solution through the minimization of a functional that comprehends both of equations (4.36). Although the BRD method has a robust analytic solution, it is applicable only for $\mathbf{R} = \mathbf{1}$. We then choose to use the following algorithm instead:

1 – For a given α , equation (4.35) is directly solved for a first estimate of \mathbf{f}^* .

2 – The indices i for which $f_i^* < 0$ are found and regularization matrix is changed in such a way that $(\mathbf{R}^T \mathbf{R})_{ii} \rightarrow (\mathbf{R}^T \mathbf{R})_{ii} + N$, N being a large number. (57-58) This forces f_i^* to approach zero at each iteration. As only the regularization matrix is modified, the original inversion problem does not change and the solution converges to a reasonable representation of \mathbf{d} .

3 – Steps 1 and 2 are repeated until the difference between two consecutive solutions is smaller than a selected precision threshold.

Solution of equation (4.35) is achieved by using Matlab function *tikhonov* from a library made available by van HANSEN. (59)

Before initializing inversion an additional data compression step can be done, for reducing model matrix and data sizes. (48) Solution (4.31) for minimum squared inversion states that the projection $(\mathbf{U}^T \mathbf{d})_i$ of original data \mathbf{d} over each basis vector \mathbf{u}_i is amplified in the final solution by a factor $1/s_i$. A typical plot of the projections (in absolute value) as a function of the singular value position is shown in Figure 4.2.

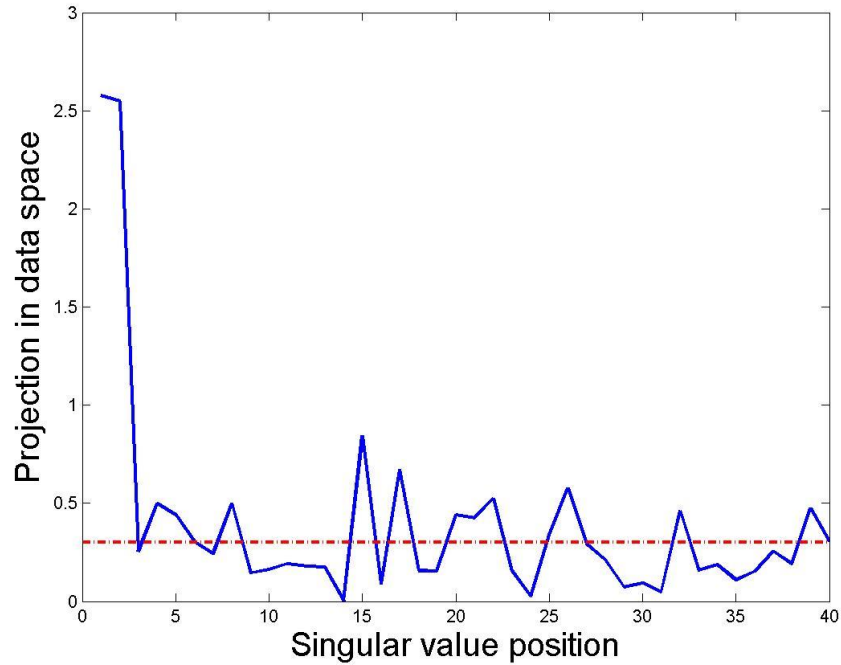


Figure 4.2 - Data projection for each eigenvector \mathbf{u}_i . The red dotted line represents the noise level of the data.

Source: By the author.

Constant red line in Figure 4.2 represents the noise level of original data, the standard deviation of the noise channel. If the projection $(\mathbf{U}^T \mathbf{d})_i$ is below the noise level of the data, there is no point in trusting in that component for inversion, as the correspondent singular value would essentially amplify noise. Assuming the projections cross the noise level before the q th singular value, one can build truncated versions $\tilde{\mathbf{U}}$ and $\tilde{\mathbf{S}}$ of the original matrices by eliminating the last $m - q$ columns of \mathbf{U} and the last $n - q$ lines of \mathbf{S} . By defining $\tilde{\mathbf{d}} = \mathbf{U}^T \mathbf{d}$, $\tilde{\mathbf{A}} = \tilde{\mathbf{S}} \mathbf{V}^T$, and noticing that orthogonality relation $\tilde{\mathbf{U}}^T \tilde{\mathbf{U}} = \mathbf{1}$ still holds, equation (4.3) becomes $\tilde{\mathbf{d}} = \tilde{\mathbf{A}} \mathbf{f}$. Vector $\tilde{\mathbf{d}}$ and matrix $\tilde{\mathbf{A}}$ are much smaller than the original ones and can be used in the inversion algorithm as the new data and model.

We pointed out earlier that in the definitions of data vector \mathbf{d} and model matrix \mathbf{A} , standard deviations were included in order to give bigger weights to best acquired data. That happens because minimum squared error functional is then written as:

$$\phi_{MSQ} = \sum_{\eta} \frac{\phi_{MSQ,\eta}}{\sigma_{\eta}^2} \quad (4.37)$$

Where $\phi_{MSQ,\eta}$ represents the error for each echotrain η . Therefore, terms with smaller standard deviations will give higher contributions to the total error, forcing the algorithm to privilege parameters that reduce them.

4.4 Application for DT_2 well logging acquisition: fluid typing

In this section we show an example of diffusion and relaxation data acquired in a Petrobras well with carbonate reservoirs, in a section comprehending sandstone reservoirs. Figure 4.3 shows a plot of density and neutron porosity logs throughout reservoirs' section.

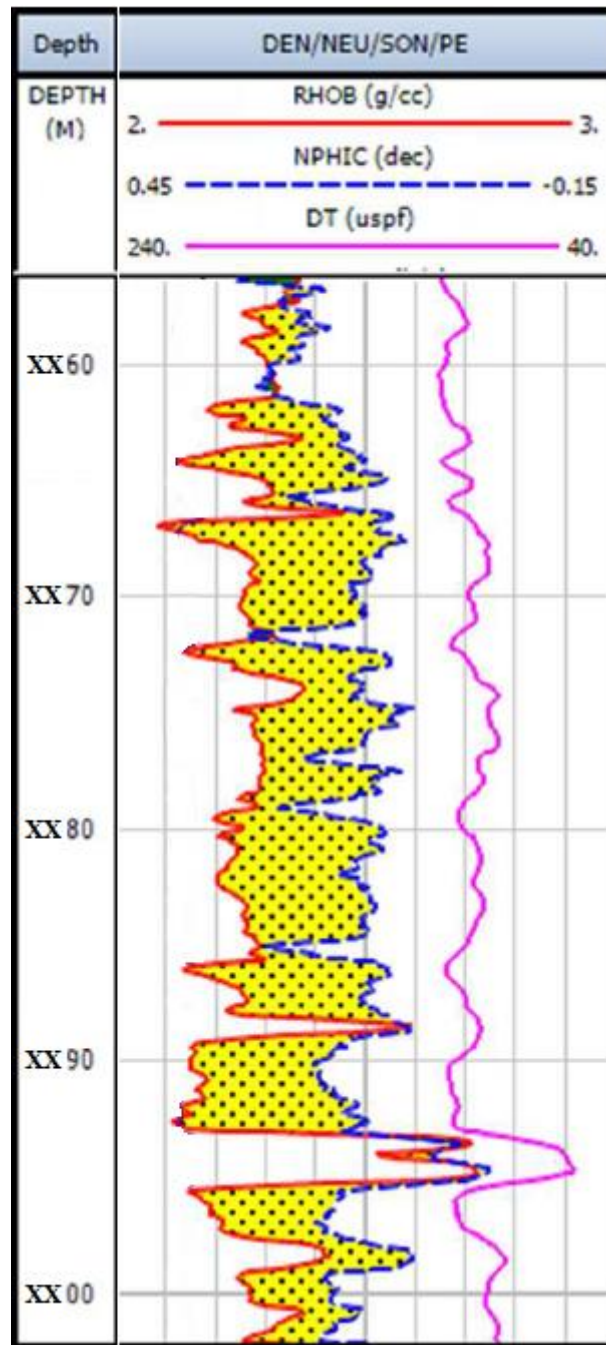


Figure 4.3 - Density (red), neutron (blue), and sonic (pink) logs for well in a sandstone field.
Source: Provided by Petrobras.

As explained in Chapter 2, density is measured indirectly by counting the amount of electrons existing in the formation, through scattering of incident gamma ray (Compton effect) emitted by the tool. It measures an average density from both rock matrix and fluid. Therefore, as fluid density becomes smaller, porosity calculation through equation (2.7) with fixed parameters for matrix and fluid densities tends to overestimate results. On the other hand, as neutron porosity depends on the presence of hydrogen atoms, hence measuring only fluids, lighter oils or gas tend to underestimate porosities because of lower hydrogen indexes.

This leads to the separation between porosities estimated from density and neutron logs in Figure 4.3, and are an indicative of fluid filled sandstones. As the fluid becomes lighter, separation tends to increase.

Table 4.1 - Well logging DT_2 distribution acquisition

<i>CPMG ID</i>	T_W (ms)	T_E (ms)	N_E	G (Gauss/cm)
<i>A</i>	12000	1.2	800	5.5
<i>B</i>	12000	3.6	266	5.5
<i>C</i>	12000	7.2	133	6.9
<i>D</i>	12000	12	80	6.9

Source: By the author.

In order to characterize the fluids present in each sandstone pack identified in Figure 4.3, a DT_2 NMR acquisition was made through the interval, with parametrization of Table 4.1, and the averaged resultant echotrails (averaged through the whole interval) are shown in Figure 4.4:

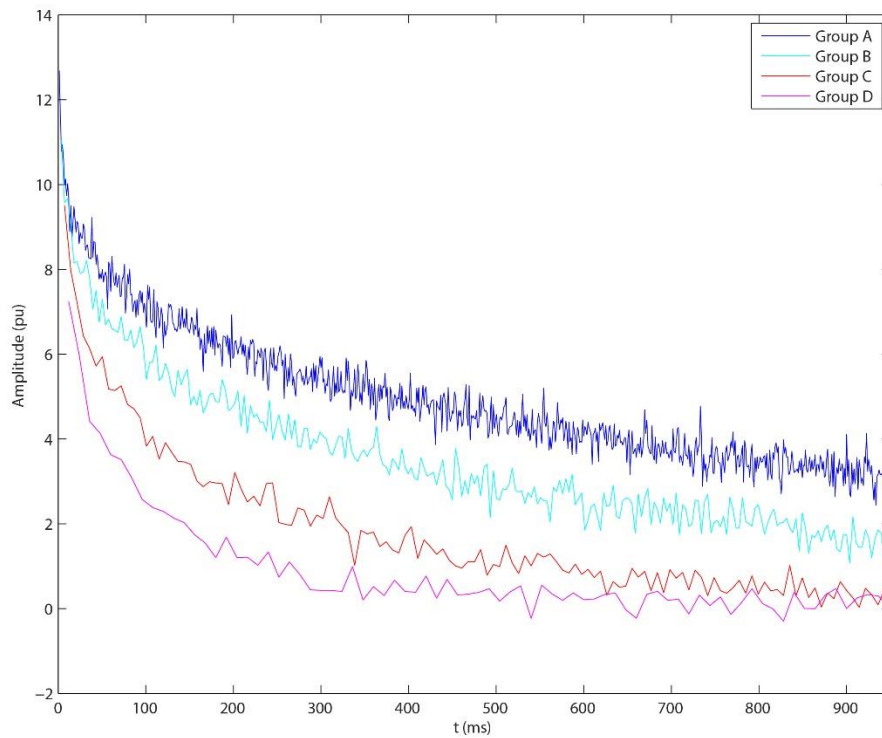


Figure 4.4 - Averaged echotrails from DT_2 acquisition.
Source: By the author.

For inversion bi dimensional distribution \mathbf{F} (equation (4.21)) was built considering 30 bins for diffusion dimension, with diffusion coefficient values ranging logarithmicly from 10^{-11} to $10^{-6}m^2/s$, and also 30 bins in the relaxation dimension, with T_2 values ranging logarithmicly from 0.5 to 3000ms. Data vector \mathbf{d} was built as in equation (4.20) and matrix \mathbf{A} using equation (4.23) and the first of (4.24).

A data compaction step was made using singular values decomposition of \mathbf{A} , and the projections of data \mathbf{d} over data space basis as function of singular values position is shown in Figure 4.5.

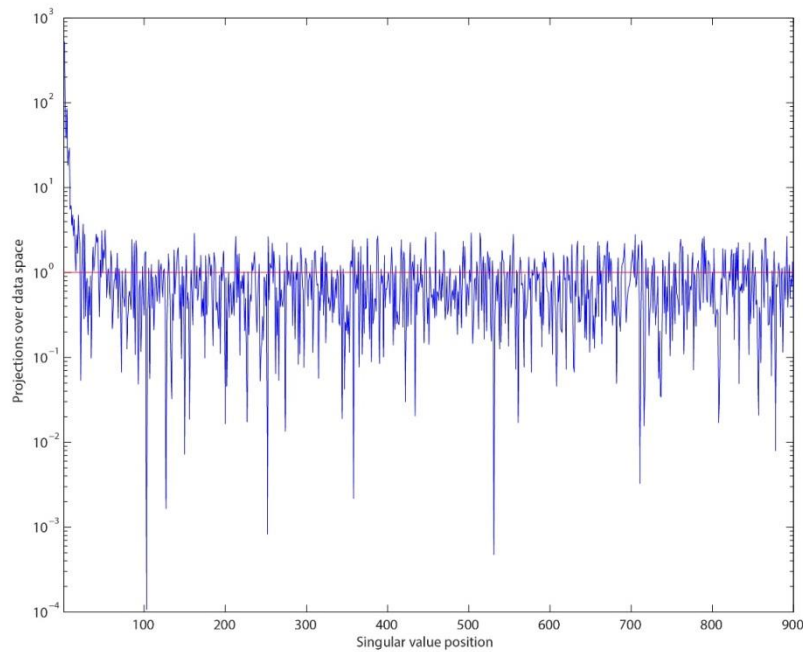


Figure 4.5 - Data projection for each eigenvector \mathbf{u}_i in a \mathbf{DT}_2 well data.
Source: By the author.

It can be seen that the majority part of the projected data follows a constant trend that lies below the normalized noise level shown in red (as each echotrain is divided by its own standard deviation in equation (4.20), the noise level of \mathbf{d} is then equal to 1). Truncated vector $\tilde{\mathbf{d}}$ and matrix $\tilde{\mathbf{A}}$ were then built by retaining the first 100 singular values. The resultant error curve as function of regularization parameter is presented in Figure 4.6.

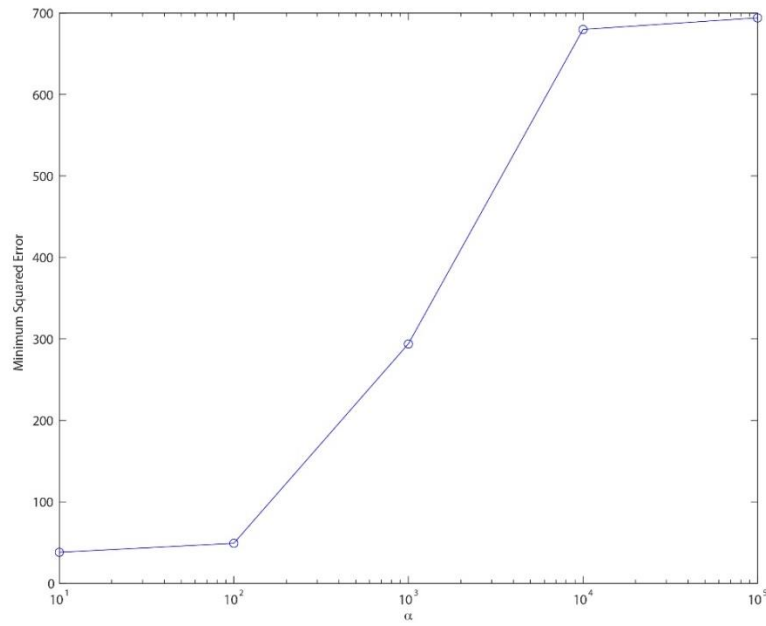


Figure 4.6 - Error as a function of regularization parameter α in a DT_2 well data.
Source: By the author.

By choosing $\alpha = 10$, the following fit is obtained:

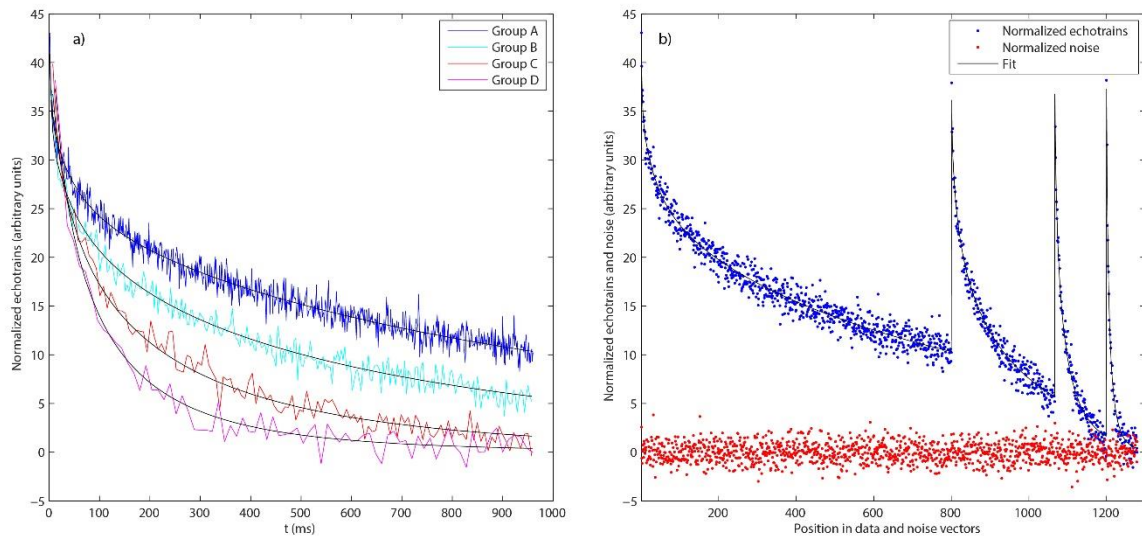


Figure 4.7 - Data fit for a) echotrails as function of time and b) echotrails and noise as function of the position in the data vector \mathbf{d} .

Source: By the author.

Inverted DT_2 distribution is shown in Figure 4.8 below:

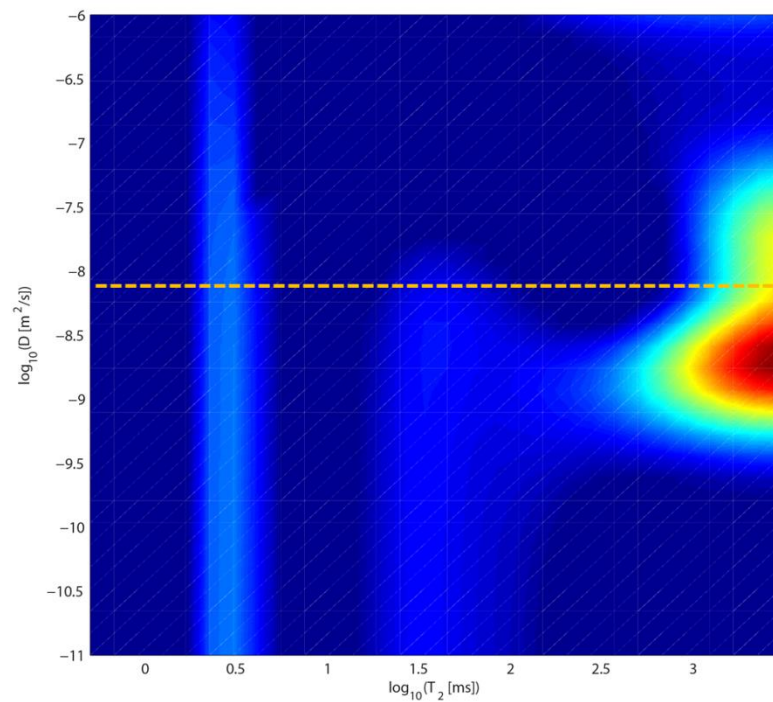


Figure 4.8 - Diffusion-relaxation distribution for the whole averaged interval shown in Figure 4.3. The dotted reference line corresponds to water diffusion coefficient at room temperature.

Source: By the author.

There can be identified in Figure 4.8 two main fluid portions, one located below the water line and another with higher diffusion coefficients. The main peak is identified with either light oil or drilling mud filtrate, both having similar properties as water, regarding viscosity and diffusion coefficient. The other portion has higher diffusion coefficient, indicating an even lighter oil, which can be resultant of dissolved gas.

Other low intensity signals can be seen around 0.5 and 20ms. The slower component is likely to be associated with microporous regions of the rock, or even water associated with clay filled pores. The signal around 20ms can be even from irreducible water or a heavier oil. However the resolution in diffusion dimension achieved in this particular acquisition cannot separate diffusion coefficients associated with relaxation times lower than 200ms. An acquisition with higher gradients would be necessary.

The sandstones packs were divided in two main reservoirs (labeled as 1 and 2 in the following figures), and DT_2 acquisition was used to identify differences between both reservoirs, and specially between the upper and lower intervals within each one of them.

Figure 4.9 to Figure 4.12 show the decaying data for each interval (reservoirs 1 and 2 top and bottom zones), resulting fit, singular value decomposition and error curve as function of regularization parameter.

Resulting DT_2 distributions are shown Figure 4.13. They show an increase in diffusion coefficient as one moves to upper parts of the reservoir. That is a result of an expected gravitational segregation, where gas tends to move up due to buoyance forces acting through geological times. As a consequence, the upper part of those reservoirs are composed of condensed gas, while oil remains in the lower parts.

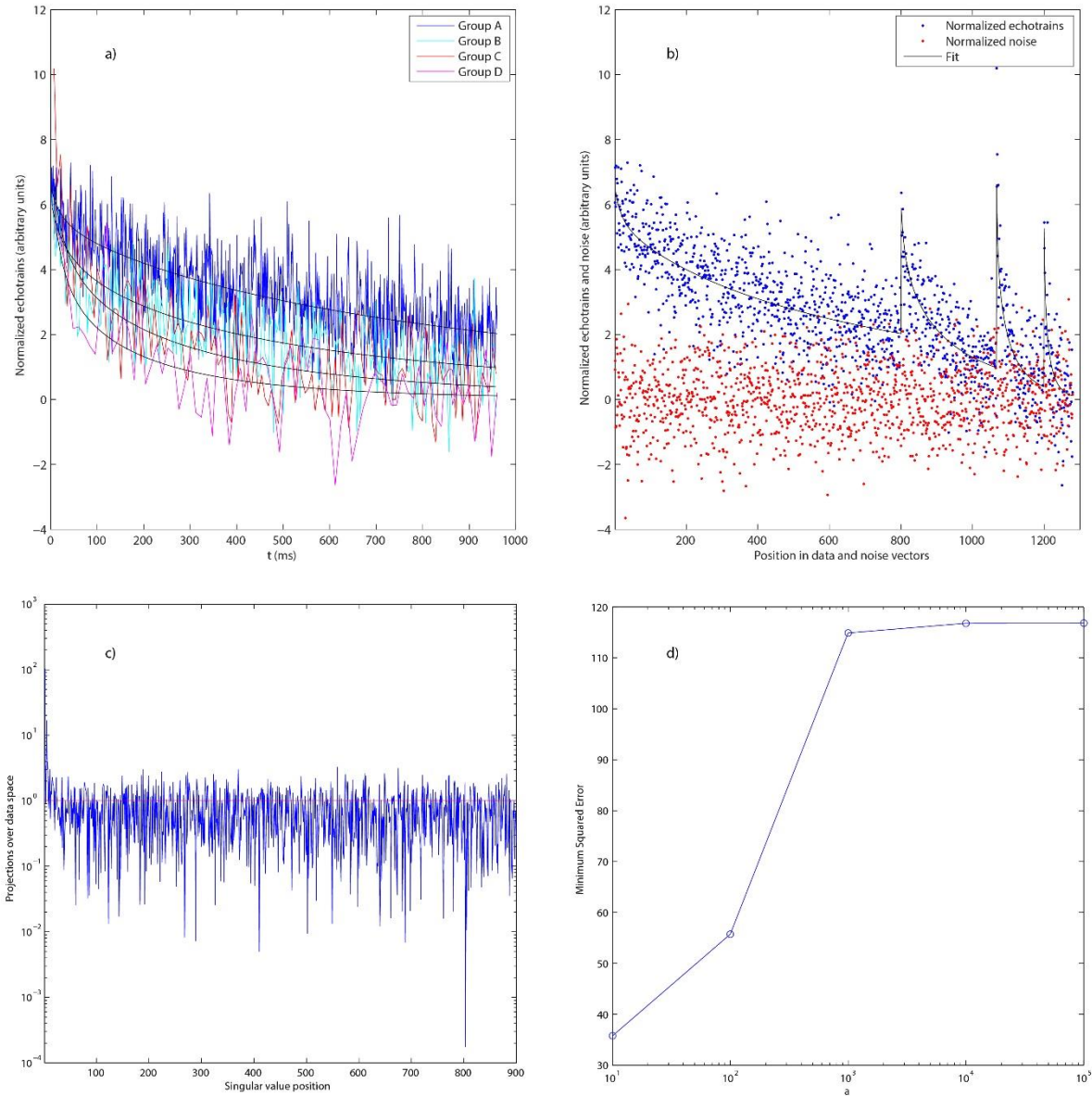


Figure 4.9 - Reservoir 1 top zone. a) acquired data and fit as function of time b) normalized data, normalized noise and fit as function of position in data vector c) data projection over data space basis (SVD) d) fit error as function of regularization parameter α . For final inversion there were used 100 singular values and $\alpha = 2$, based on fit curve.

Source: By the author.

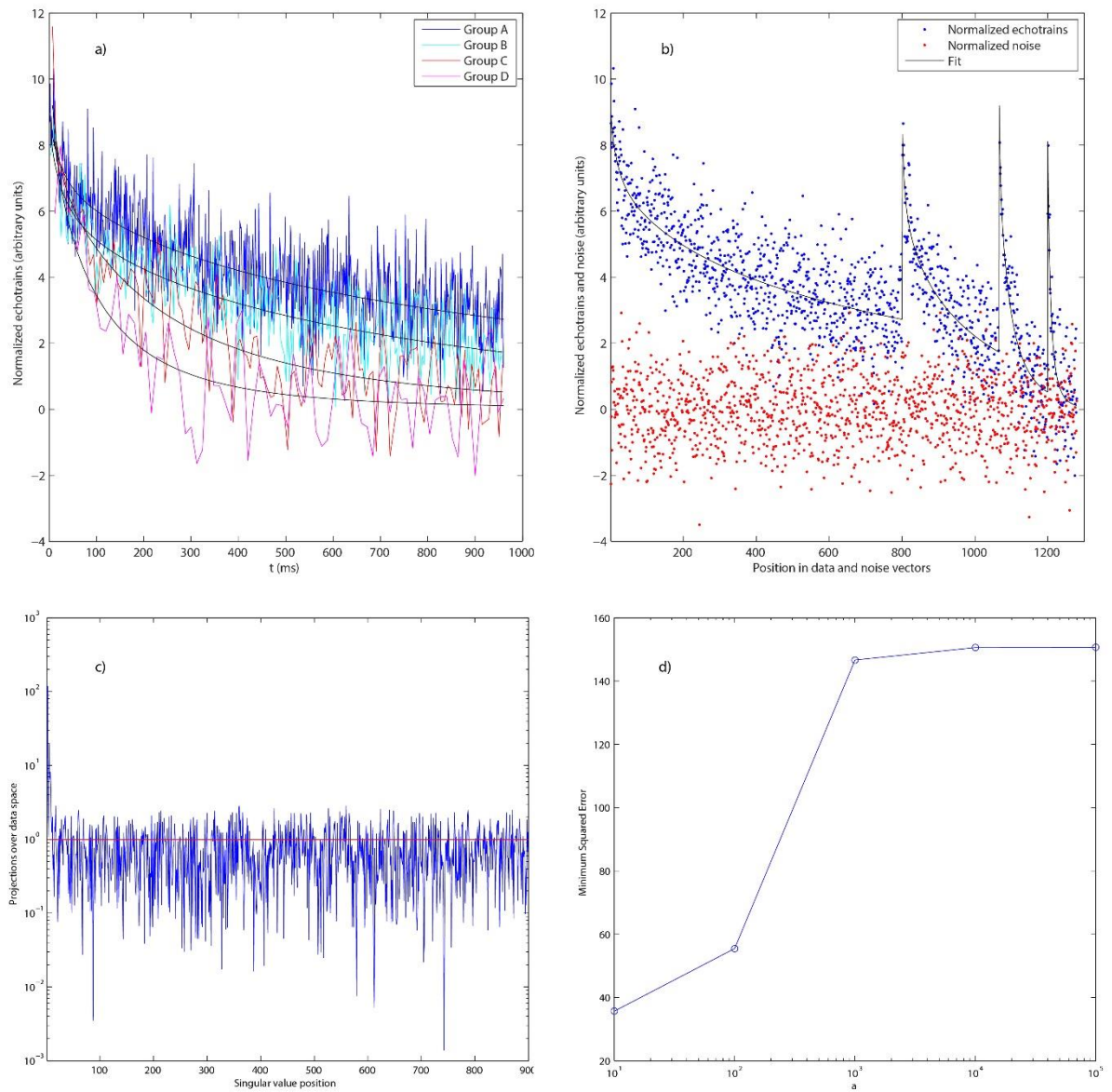


Figure 4.10 - Reservoir 1 bottom zone. a) acquired data and fit as function of time b) normalized data, normalized noise and fit as function of position in data vector c) data projection over data space basis (SVD) d) fit error as function of regularization parameter α . For final inversion there were used 100 singular values and $\alpha = 2$, based on fit curve.

Source: By the author.

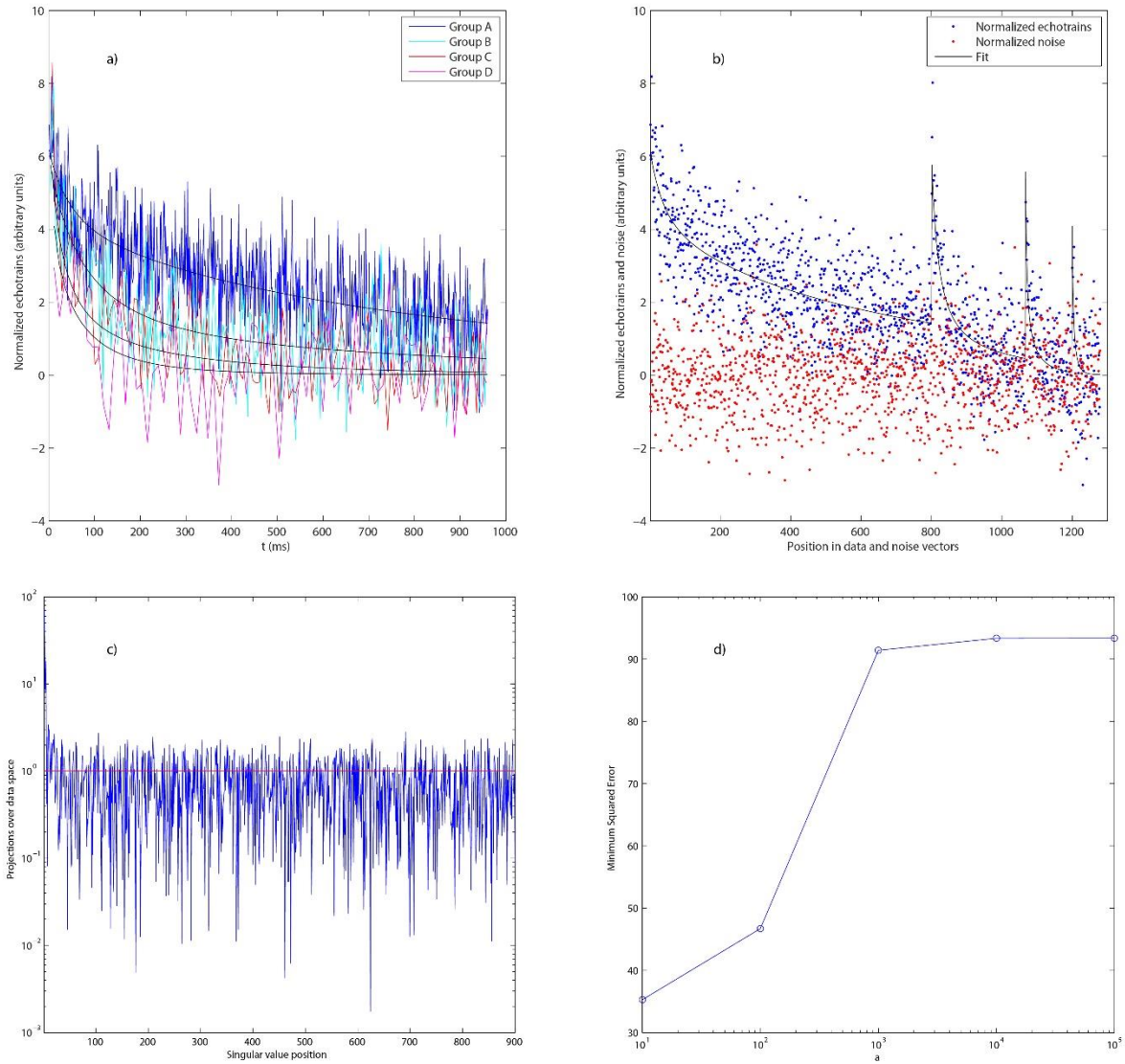


Figure 4.11 - Reservoir 2 top zone. a) acquired data and fit as function of time b) normalized data, normalized noise and fit as function of position in data vector c) data projection over data space basis (SVD) d) fit error as function of regularization parameter α . For final inversion there were used 100 singular values and $\alpha = 2$, based on fit curve.

Source: By the author.

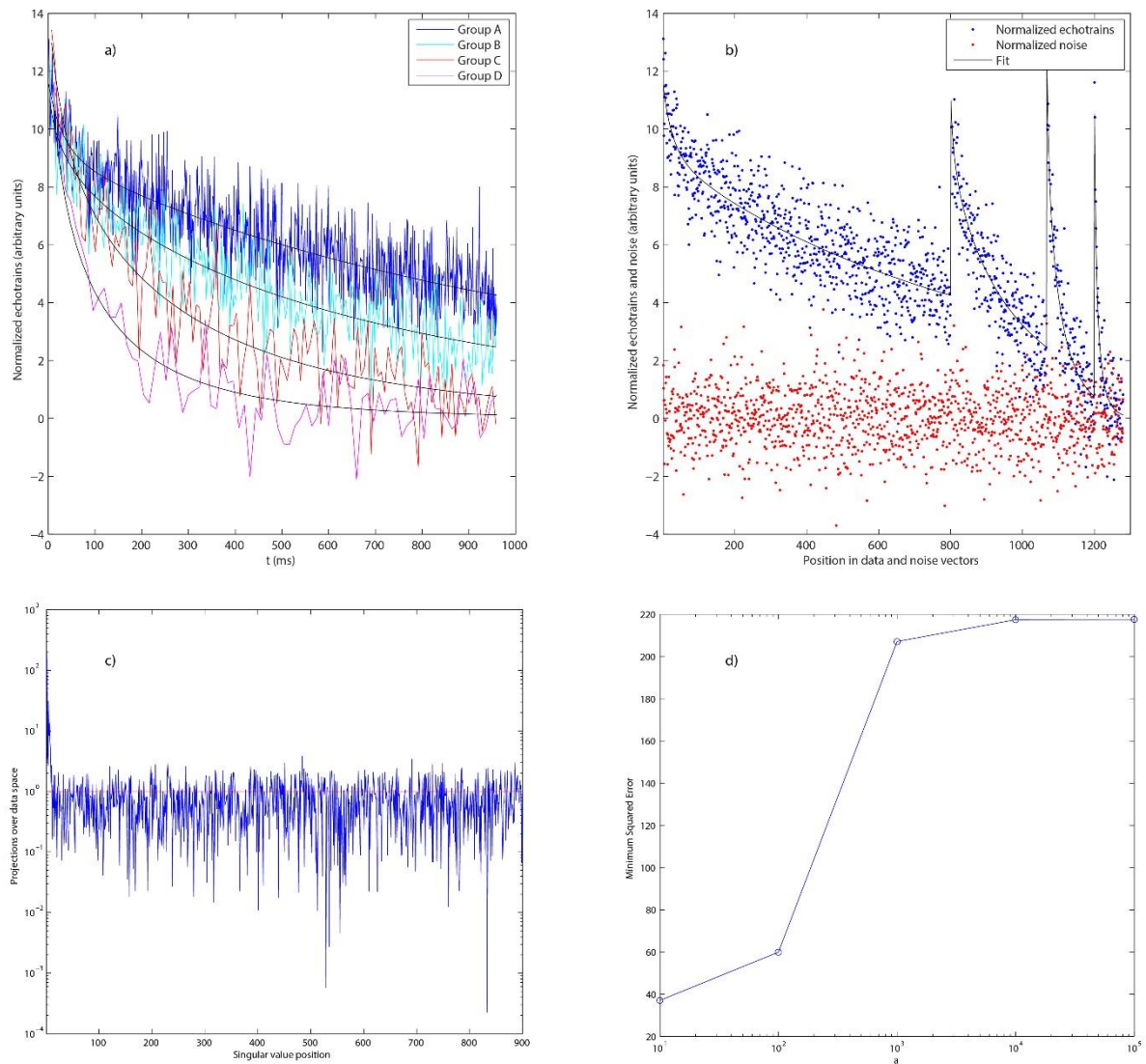


Figure 4.12 - Reservoir 2 bottom zone. a) acquired data and fit as function of time b) normalized data, normalized noise and fit as function of position in data vector c) data projection over data space basis (SVD) d) fit error as function of regularization parameter α . For final inversion there were used 100 singular values and $\alpha = 2$, based on fit curve.

Source: By the author.

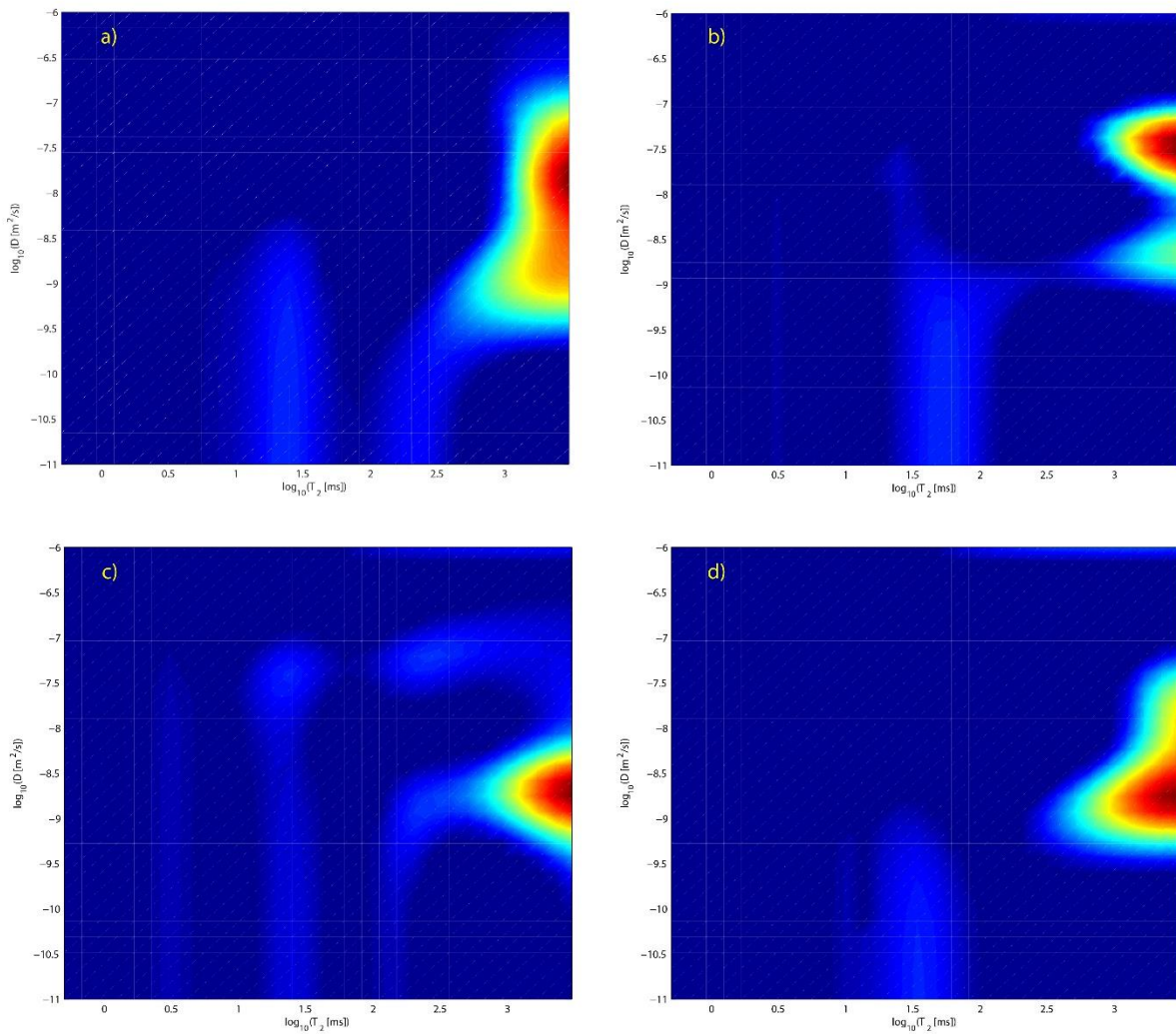


Figure 4.13 - DT_2 distributions for a) reservoir 1 top zone b) reservoir 2 top zone c) reservoir 1 bottom zone d) reservoir 2 bottom zone.

Source: By the author.

4.5 One dimensional T_2 distributions and T_1/T_2 ratio estimation

It is common that even for one dimensional log acquisitions, such as for T_2 distribution, more than one echotrain is acquired (with different parametrization) at each depth, as exemplified in Table 4.2 below.

Table 4.2 - Well logging T_2 distribution acquisition

<i>CPMG ID</i>	<i>T_W (ms)</i>	<i>T_E (ms)</i>	<i>N_E</i>
<i>A</i>	17000	0.2	3000
<i>B</i>	32	0.2	30

Source: By the author.

In this example a long and a short echotrain are acquired, the later using a much smaller wait time. As mentioned before this allows enough time for the same short echotrain to be acquired several times approximately in the same depth (remember the logging tool is always moving even during acquisition). Repeated signals are averaged resulting in one decay with less noise, which improves precision for shorter relaxation times, hence porosity estimation.

This sort of acquisition poses an additional problem to the inversion process. Wait times enter in matrix \mathbf{A} through a factor $(1 - e^{-T_w/T_1})$, however neither do we have a value for T_1 nor enough resolution to determine an accurate $T_1 T_2$ distribution based on only two echotrains. Assuming that the rock is saturated with only one fluid, and that diffusion and bulk effects can be neglected, both T_1 and T_2 become proportional to pore size, yielding a constant ratio $R = T_1/T_2$. With this assumption, inverted distribution remains one dimensional and an additional parameter R to be determined is included, as the polarization factor becomes $(1 - e^{-T_w/(RT_2)})$.

In the following paragraphs we describe a way to determine R for an actual log data acquired with parameters described in Table 4.2, for a Petrobras well in a sandstone interval. We illustrate the method applying it to the averaged signal through all the logging interval, shown in Figure 4.14.

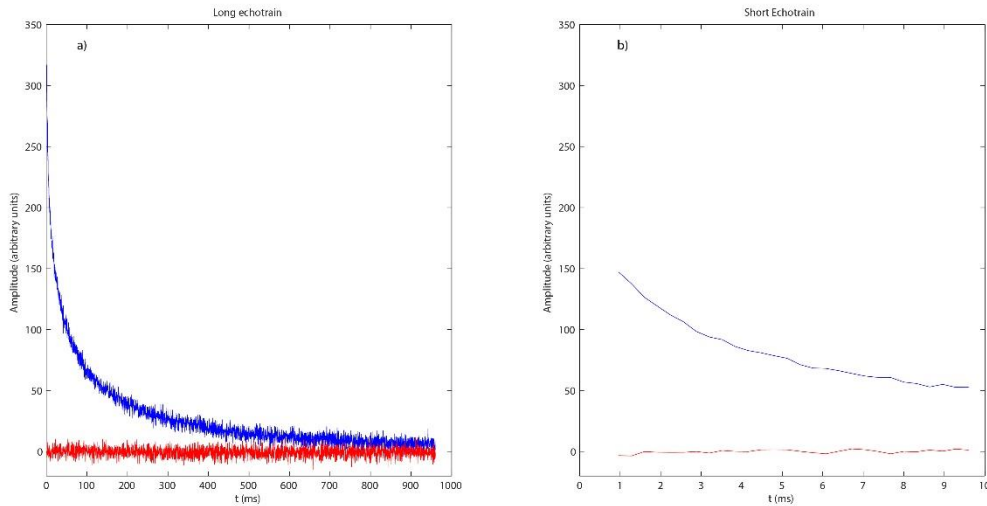


Figure 4.14 - Averaged log data acquired with parametrization of Table 4.2.

Source: By the author.

By choosing 30 T_2 values logarithmicly spaced from 0.3 to 3000ms, and building matrix \mathbf{A}_{Long} with the exact same prescription described in equation (4.4), the long echotrain

can be inverted yielding a T_2 distribution shown in Figure 4.15. Zeroth order regularization with $\alpha = 1$ was used.

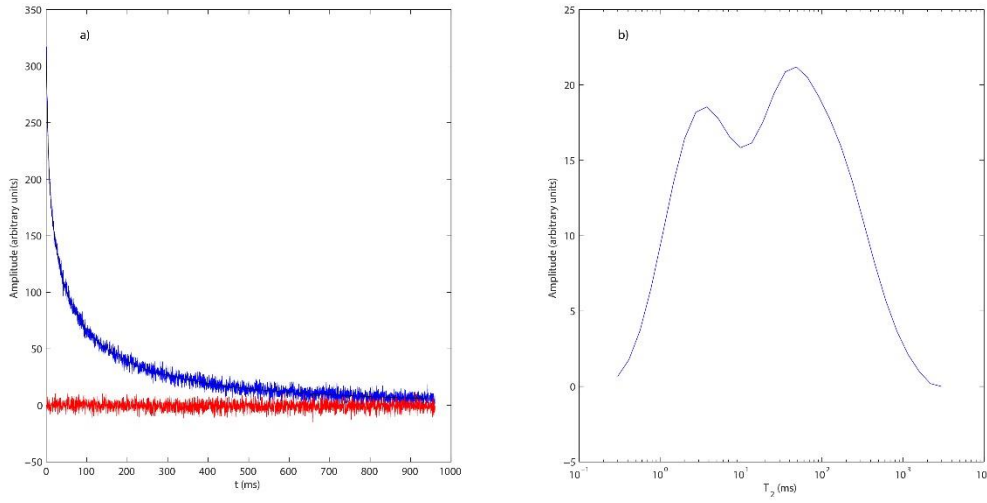


Figure 4.15 - T_2 distribution and data fit for long echotrain.
Source: By the author.

In order to include the short echotrain, one can follow the ideas described in previous sections and the introduction of ratio R , writing:

$$\left\{ \begin{array}{l} \mathbf{d} = \begin{pmatrix} \mathbf{d}/\sigma_A \\ \mathbf{d}/\sigma_B \end{pmatrix} \\ \mathbf{A} = \begin{pmatrix} \mathbf{A}_{\text{Long}}/\sigma_A \\ \mathbf{A}_{\text{Short}}/\sigma_B \end{pmatrix} \\ [\mathbf{A}_{\text{Short}}]_{ij} = \left(1 - e^{-\frac{T_{WB}}{RT_{2,j}}} \right) e^{-\frac{t_i}{T_{2,j}}} \end{array} \right. \quad (4.38)$$

The inversion can be quickly performed for several different values of ratio R . The error between the acquired echotrain and resultant fit, for the short signal only, is shown in Figure 4.16.

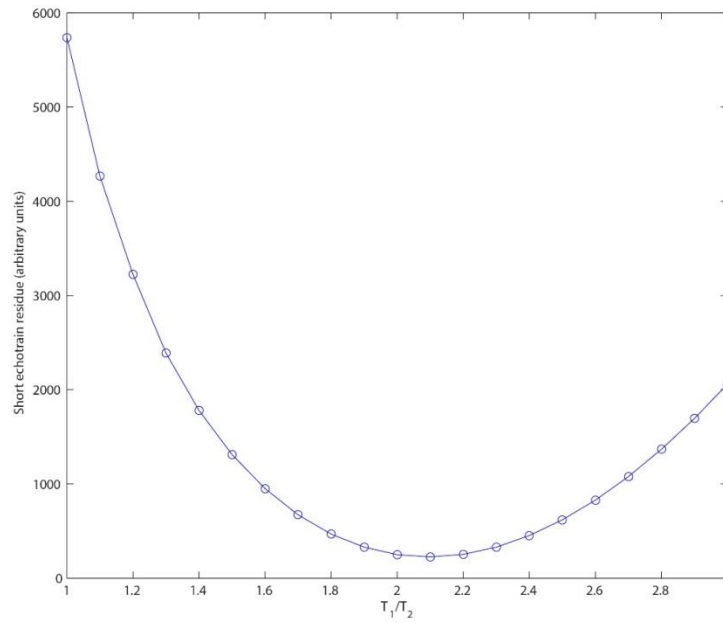


Figure 4.16 - Error between fit and acquired data for short echotrain, as a function of $R = T_1/T_2$.
Source: By the author.

The minimum shown in Figure 4.16 happens for the best ratio $R = 2.1$. Corresponding fit and T_2 distribution are shown respectively in Figure 4.17 and Figure 4.18.

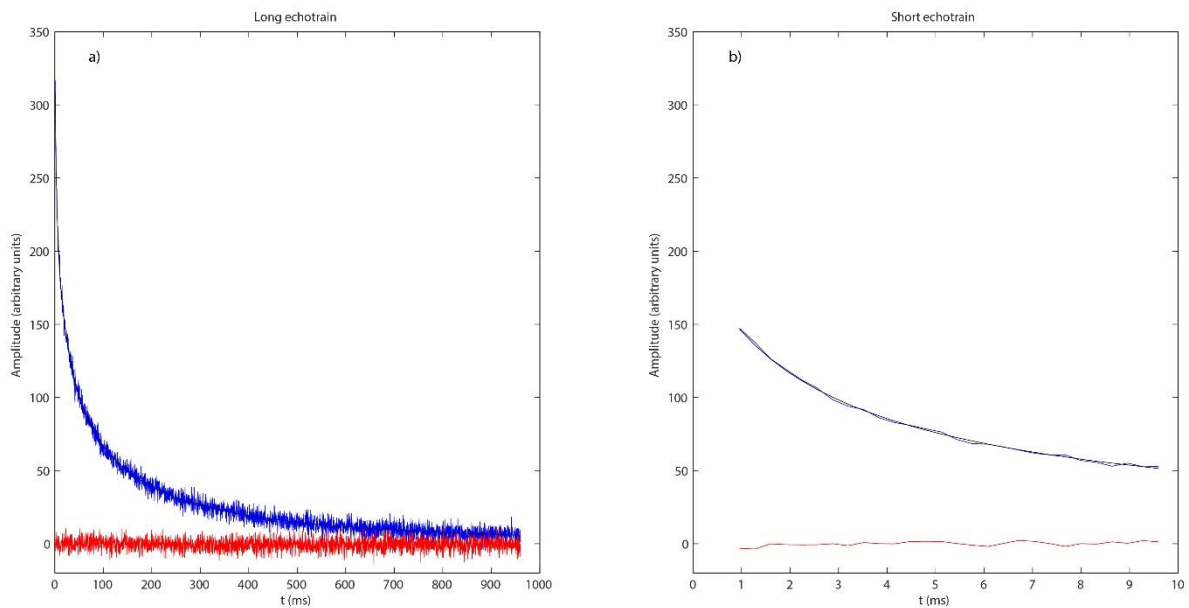


Figure 4.17 - Fit for long and short echotrain using $R = 2.1$ and full inversion described by matrix A of equation (4.38).

Source: By the author.

The two resulting distributions agree for long times, but the complete one resolves better lower relaxation times, showing that the lower peak is centered in $2ms$. By looking at the inversion through all the well shown in Figure 4.20, this peak corresponds to non-reservoir intervals, that present only short relaxation times ranging from 1 to $3ms$.

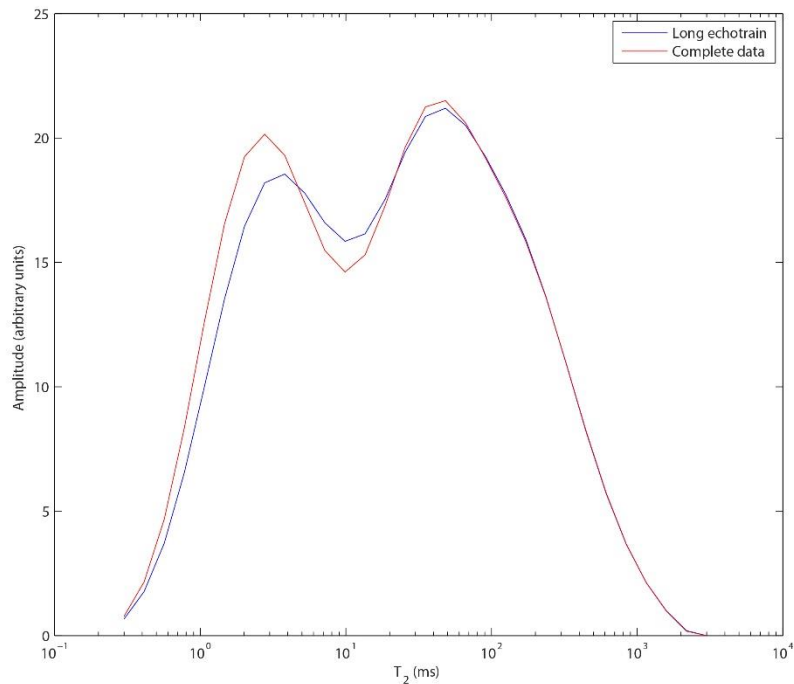


Figure 4.18 - Comparison between distributions obtained from inversion of long echotrain only, and from complete data.

Source: By the author.

This method for determining relaxation times ratio is fast enough so that it can be applied to the entire log, resulting in the traditional T_2 distribution and an extra logging curve, the T_1/T_2 log. It can be used as an indicative of heavy oil presence, or unconventional reservoir identification in shale intervals. (60) Figure 4.19 shows the resulting fit for long and short echotrain in a small section of the well. In Figure 4.20 is shown a comparison between the inverted distribution and T_1/T_2 curve from our processing and the one commercially delivered by the logging company.

Both T_2 distributions show the same features, identifying the reservoir zones with longer times. T_1/T_2 ratios also agree on average.

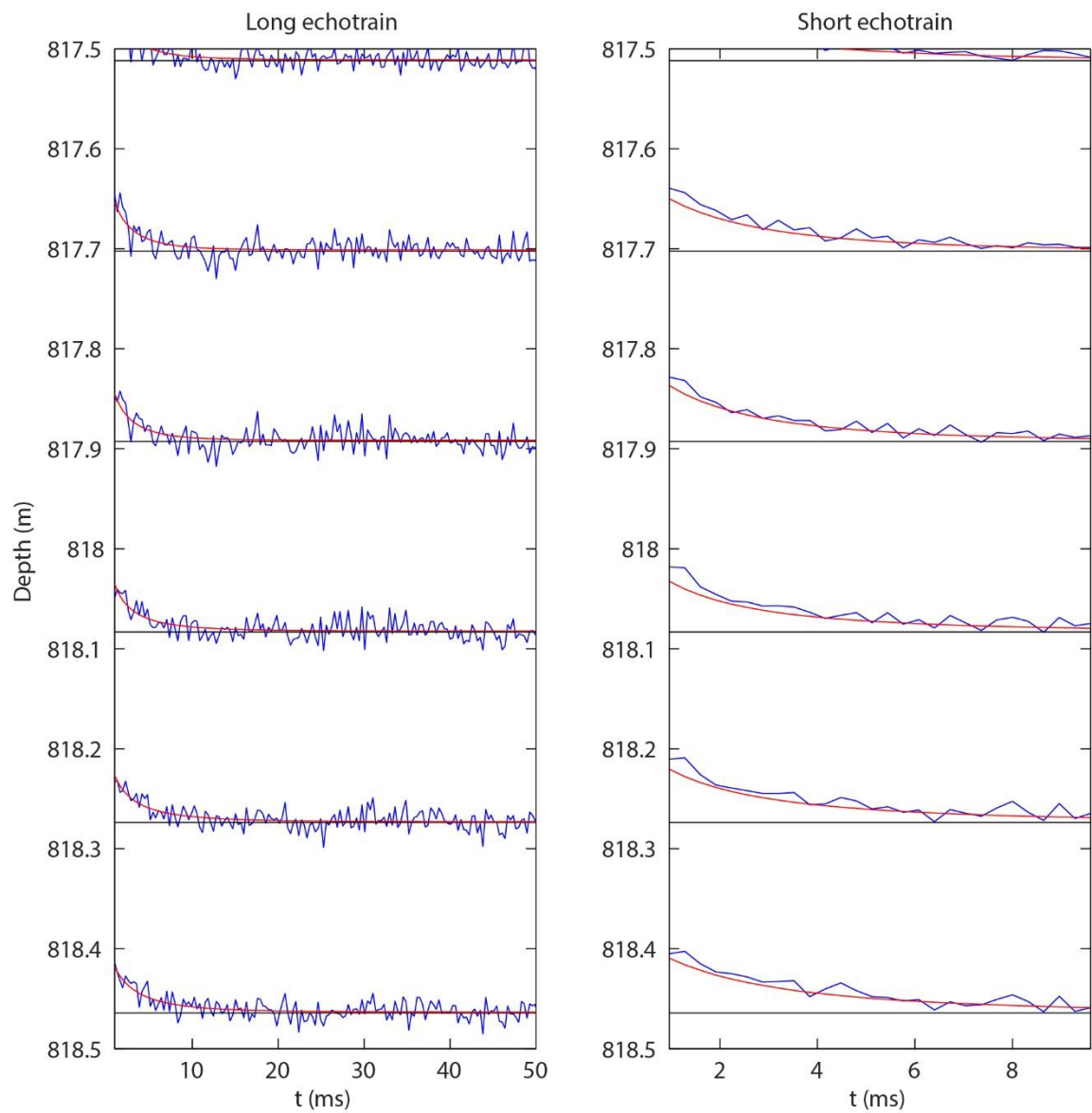


Figure 4.19 - Data fit for long and short echotrain in a well section.
Source: By the author.

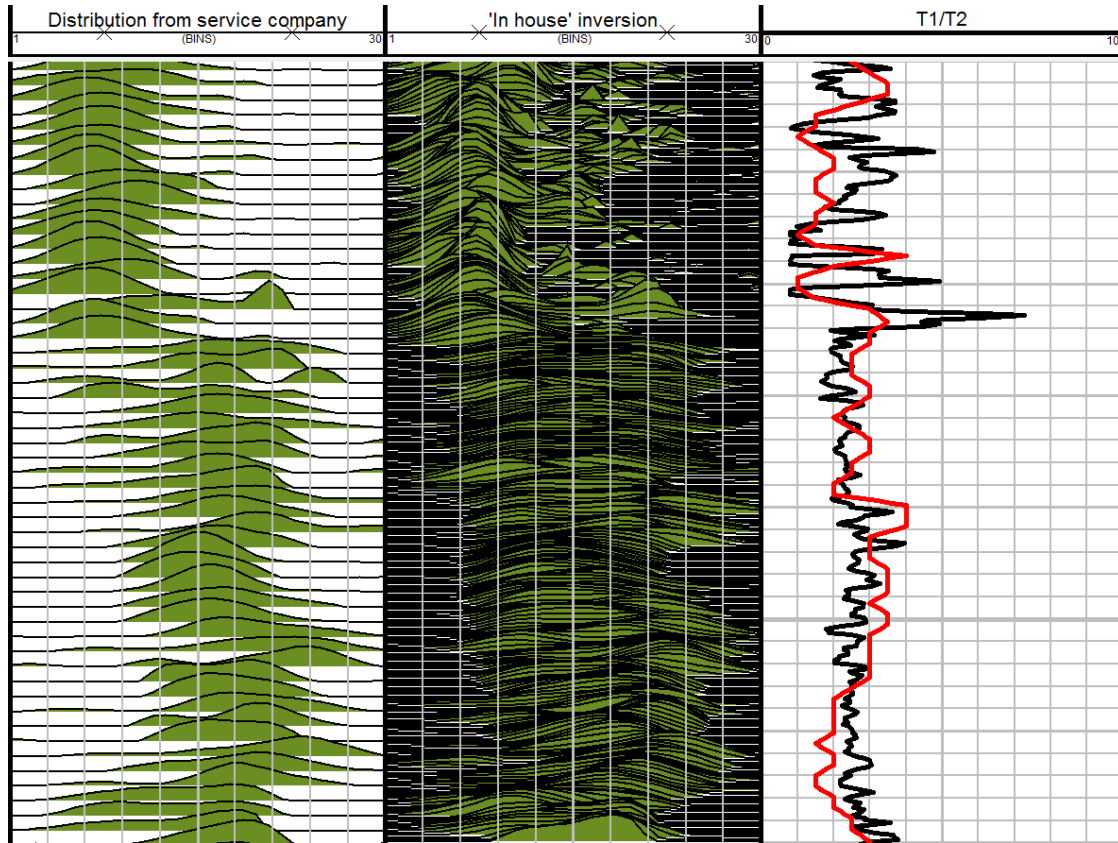


Figure 4.20 - Comparison with the commercially delivered distribution and T1/T2 curve (black – service company and red – in house processing).

Source: By the author.

4.6 Determining gradient distribution for inhomogeneous magnetic fields

In Chapter 3 we mentioned that the static magnetic field generated by NMR logging tools is inhomogeneous, with field gradients present through the sensitive volume or shell. Some tool designs generate well defined gradient value, while others have a broad gradient distribution $g(G)$ in the sensitive volume. Specially in the latter case, inversion processing for diffusion measurements will have better resolution if $g(G)$ is known and incorporated in matrix \mathbf{A} . In this section we show some results based on laboratory NMR experiments done with a single sided apparatus, emulating the field geometry that one would expect in a logging environment. We show how the gradient distribution can be obtained from diffusion acquisitions (similar to reported by d'Eurydice (49)) and how it can be incorporated in processing of diffusion editing measurements.

We used a commercial magnet (61) (Figure 4.21) which consists internally of two parallel polar plates with inverted polarities with respect to each other. This configuration generates a \vec{B}_0 field that is parallel to the device's surface (at its center), and it decays as one

moves away from the apparatus. Magnetic field intensity as a function of the distance to the magnet is shown in Figure 4.22.

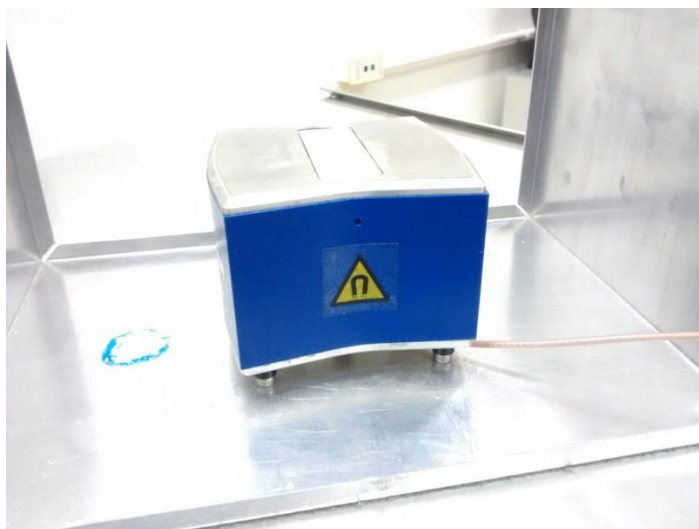


Figure 4.21 - Single sided magnet.
Source: By the author.

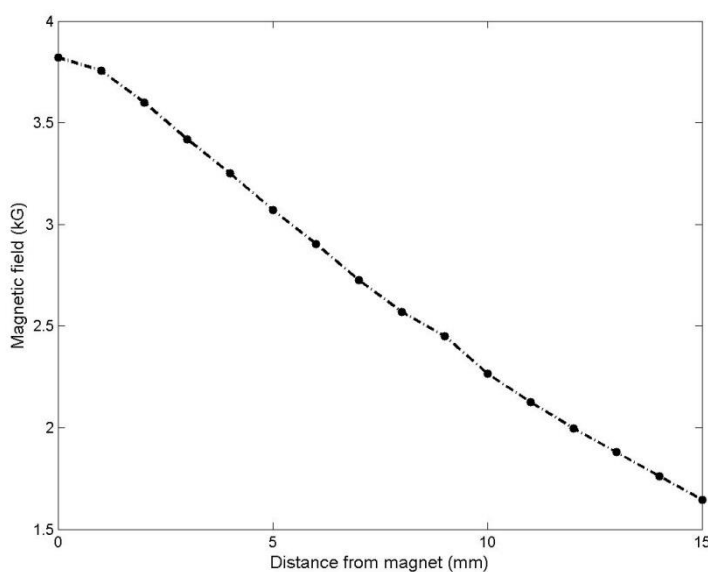


Figure 4.22 - Field intensity as a function of the distance from the magnet.
Source: By the author.

It can be seen from the simple profile of Figure 4.22 that field gradients tend to be smaller near magnet surface, increasing as one moves away from it up to a value of about 1500 Gauss/cm . Using a probe tuned in 16 MHz , one can excite spins that feel a magnetic field of 4000 Gauss at the surface. These values are far off the ones used for well logging, but the concepts involved in the inversion are the same.

Initially simple CPMG decays were measured with interecho spacing of 0.1 ms and radio frequency pulses of $0.6 \mu\text{s}$. Solutions with 0.01 , 0.1 and 1 M of CuSO_4 concentration

were used to vary water's transverse relaxation time. π pulses were generated by doubling $\pi/2$'s intensity, and their durations were held fixed in order to guarantee that all the pulses would act in the same volume. Because of high selectivity of short pulses in the presence of gradients Figure 3.16, a pulse duration of $0.6\mu\text{s}$ in this setup corresponds to a sensitive shell of about 0.2mm width from the probe surface. If the pulses duration is decreased to $0.2\mu\text{s}$, the shell extends to 1mm from the surface. Because of the field profile in Figure 4.22, it is expected that the larger sensitive shell would experience higher gradients than the smaller one.

Results for T_2 distributions (Figure 4.23) show that the three solutions tested (0.01, 0.1 and 1M respectively) have relaxation times of 100, 10 and 1ms , as the dissolved ions interact magnetically with Hydrogen nuclei in water, enhancing relaxation proportionally with ions concentration.

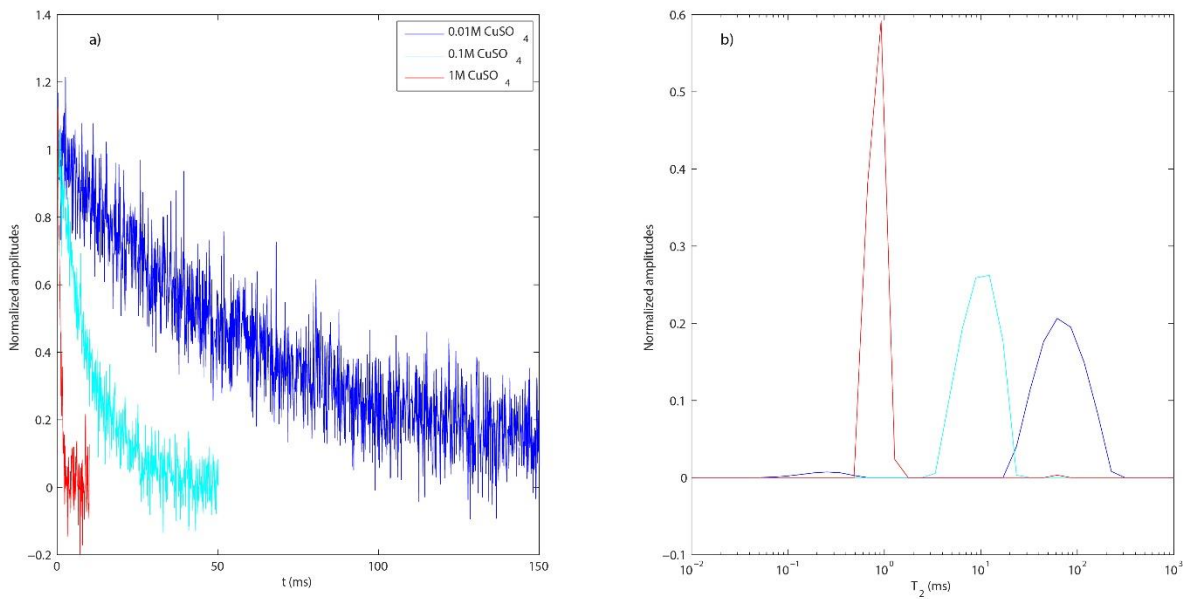


Figure 4.23 - a) CPMGs and b) T_2 distributions for solutions with **0.01**, **0.1** and **1M** of **CuSO_4** measured using a single sided magnet.

Source: By the author.

In order to investigate gradient distributions and inversion for diffusion, a diffusion editing sequence was measured for the three water samples. Echotime T_D for the first echo (equation (3.60) and Figure 3.19) was varied from 0.1 to 2.5ms , totalizing 37 echotrains acquired. Figure 4.24 shows all the echotrains for the sample with 0.1M , for illustration.

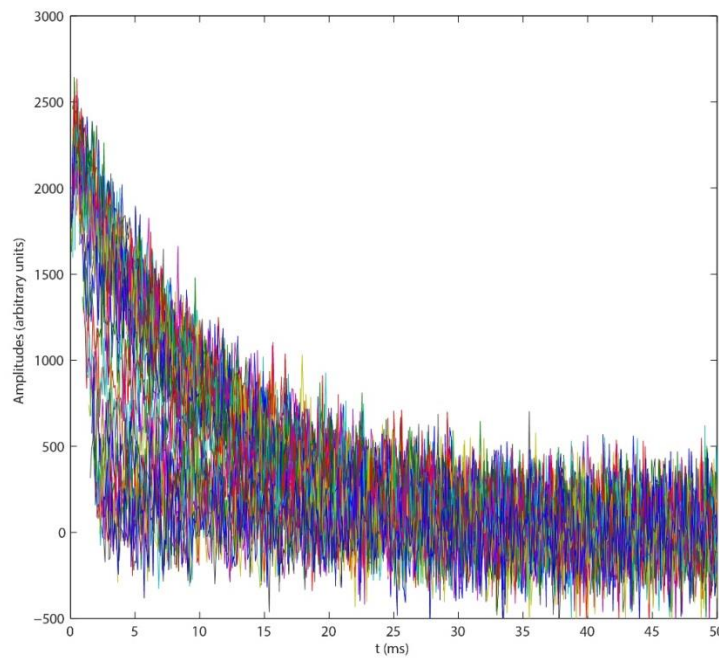


Figure 4.24 - Echotrails acquired for solution with **0.1M CuSO_4** in a diffusion editing experiment.
Source: By the author.

In Figure 4.25 we show the first echo amplitude for each one of the echotrails acquired in the diffusion editing experiment, as a function of first echotime T_D .

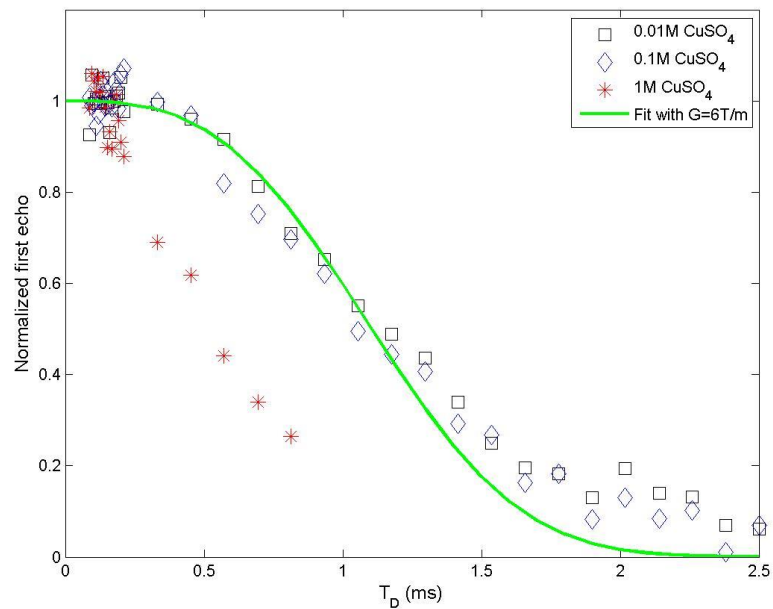


Figure 4.25 - First echo amplitude as function of T_D in diffusion editing sequences, for solutions with different concentrations of **CuSO_4** .
Source: By the author.

Accordingly to equation (3.60), the amplitude for first echotrain should follow the relation:

$$M_T(T_D) \propto e^{-\frac{D(\gamma G)^2 T_D^3}{12}} \quad (4.39)$$

This expression is plotted in green considering self-diffusion coefficient of water at room temperature ($D = 2.4 \cdot 10^{-9} \text{ m}^2/\text{s}$) and a gradient value of $G = 6 \text{ T/m}$. It follows the same trend as samples with 0.1 and 0.01 M concentrations, although it doesn't match experimental results completely. This is an indication that the sensitive shell actually feels a gradient distribution that is broader than a single well defined value. Sample with 1 M concentration falls completely off this trend because its relaxation time is much smaller, about 1 ms , and relaxation process e^{-t/T_2} competes with expression (4.39), obliterating diffusion.

In order to obtain the gradient distribution $g(G)$, one can think of the collection of data points shown in Figure 4.25 as the new data vector \mathbf{d} , and the distribution to be obtained as $\mathbf{f} = (g(G_1), g(G_2), g(G_3), \dots)^T$. Then, our standard inversion problem posed by equation 3 remains valid with the following definition for matrix \mathbf{A} :

$$A_{ij} = e^{-\frac{D(\gamma G_j)^2 T_{D,i}^3}{12}} \quad (4.40)$$

Inversion is then done in the exact same way described in previous sections. By choosing $D = 2.4 \cdot 10^{-9} \text{ m}^2/\text{s}$, and the data from 0.1 M concentration sample, resulting gradient distribution is shown in Figure 4.26.

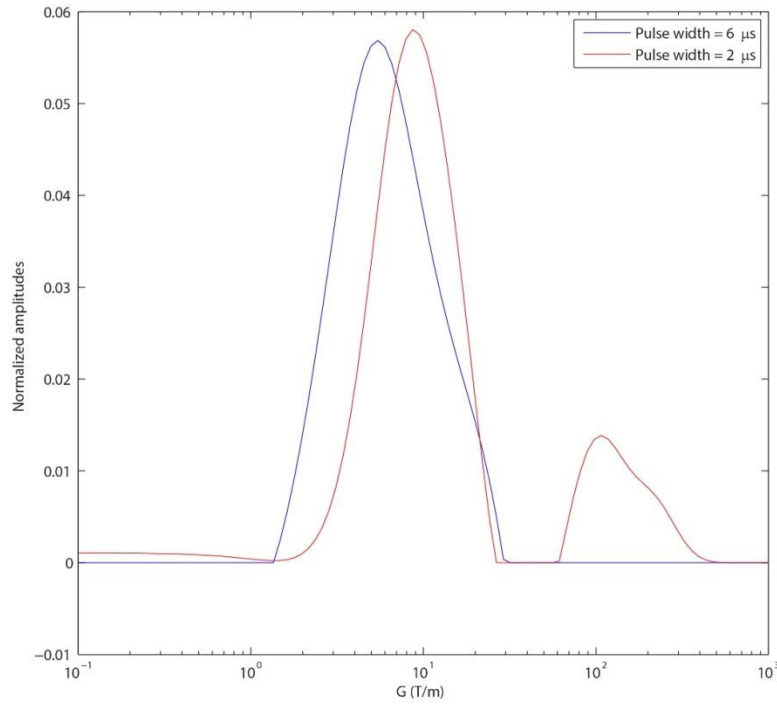


Figure 4.26 - Gradient distributions calculated from data acquired with **0.1 M** concentration sample, using **6** and **2 μs** for radiofrequency pulses.

Source: By the author.

For data acquired using radiofrequency pulses of $6\mu s$ duration, the gradients are predominantly of $4T/m$, but can reach values as high as 10 to $20T/m$. When data is acquired using pulses with $2\mu s$, hence with larger excited shells, gradient distribution tends to move towards $10T/m$, confirming the expected tendency of increasing gradients towards the upper limit of $15T/m$.

DT_2 inversion of the whole diffusion editing data (such as the one shown in Figure 4.24) can be done incorporating the calculated gradient distribution into the processing by using equations from (4.20) to (4.24) to build the problem, but substituting matrix \mathbf{A} by:

$$[\mathbf{A}(T_{D,\eta}, D)]_{ij} = \sum_k g(G_k) e^{-\frac{D(\gamma G_k)^2 T_{D,\eta}^3}{12}} e^{-\frac{t_i}{T_{2,j}}} \quad (4.41)$$

The results for three samples are shown in Figure 4.27.

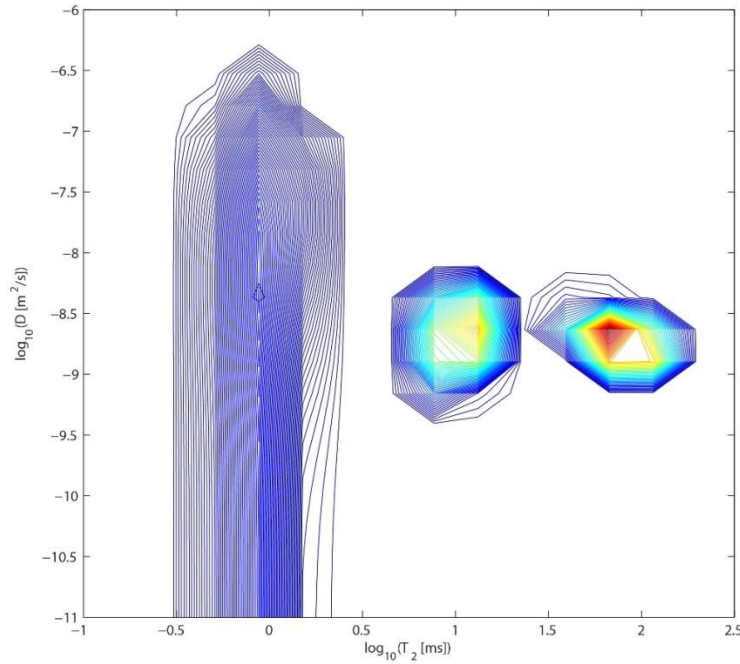


Figure 4.27 - DT_2 maps for samples with **0.01**, **0.1** and **1M $CuSO_4$** concentrations, obtained from diffusion editing acquisition, and incorporating gradient distribution in the inversion.

Source: By the author.

Distributions have a well defined value for relaxation time T_2 (matching with the one dimensional data of Figure 4.23) and diffusion coefficient, except for the one with 1M concentration that, as mentioned before, doesn't have enough resolution as bulk relaxation dominates over diffusion.

If the data were inverted without the complete gradient distribution, DT_2 map would lose resolution in the diffusion dimension, as shown in the result for sample with 0.1M in Figure 4.28, where we considered a single gradient of $6T/m$.

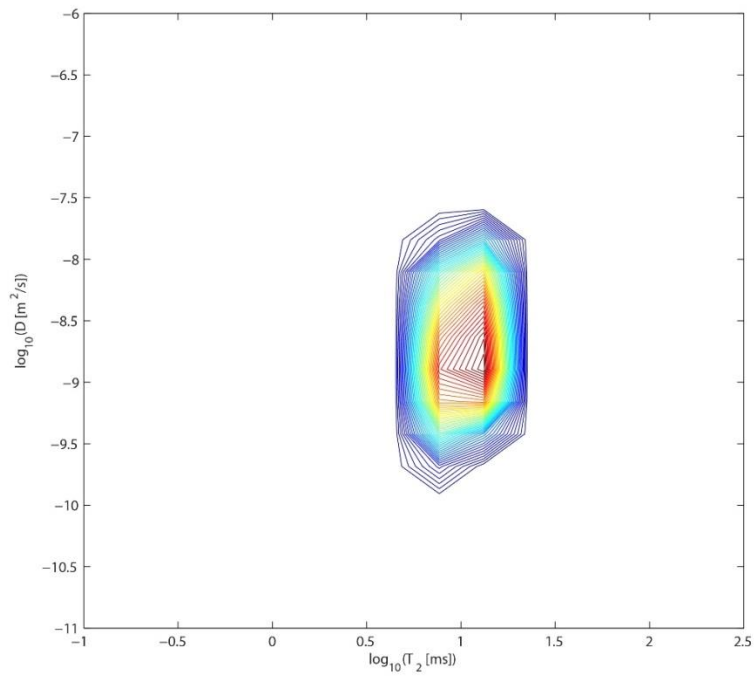


Figure 4.28 - DT_2 map for samples with **0.1M $CuSO_4$** concentration, obtained from diffusion editing acquisition, and considering a single gradient in the inversion.

Source: By the author.

5 SURFACE RELAXIVITY FOR WELL LOGGING

In Chapter 3 it was shown that when a spin is subject to an external magnetic field, its average angular momentum executes precession movement with frequency dependent on the field. As the molecule diffuses through the medium, variations in the field locally enhance and diminish this frequency, inducing losses in coherence between spins, hence relaxation. When these variations are resultant of local fields produced by the pore walls, relaxation carries information on pore geometry, expressed approximately as (equation (3.47)):

$$1/T_{1,2} \approx \rho_{1,2} S/V \quad (5.1)$$

Surface relaxivity ρ can then be seen as a measure of the strength of interaction between molecules and walls, as relaxation enhancement results from restrictions in molecular tumbling, increasing correlation times τ_c (refer to equations (3.23)). Equation (5.1) stresses that surface relaxivity makes the connection between relaxation times and pore size properties. As this connection is the key property that allows permeability models to be made, its determination brings improvements in permeability predictors' performance. (30-31)

There are laboratory approaches to determine relaxivity, as mercury injection (62) and DT_2 analysis. However, these methods do not easily extend to well logs, where the applications would be most beneficial. In this chapter, we briefly review DT_2 relaxivity determination with Padè fitting (introduced in Chapter 3), and then propose a new method that could extend its applications to well logging.

5.1 Laboratory determination of surface relaxivity and challenges for well logging

In laboratory conditions, fluid diffusivity (D) and transverse relaxation times (T_2) can be measured using a Pulsed Field Gradient (PFG) technique, where transverse magnetization behaves as:

$$M_T = \int dDdT_2 f(D, T_2) e^{-D(\gamma G)^2 \delta^2 (\Delta - \delta/3)} e^{-\frac{t}{T_2}} \quad (5.2)$$

Transverse magnetization is measured as a function of acquisition time t for several different field gradient amplitudes G . This allows for an inversion process (discussed in Chapter 4) to obtain the diffusion and relaxation distribution $f(D, T_2)$. One example of such an inversion map for a water saturated rock core is shown in Figure 5.1:

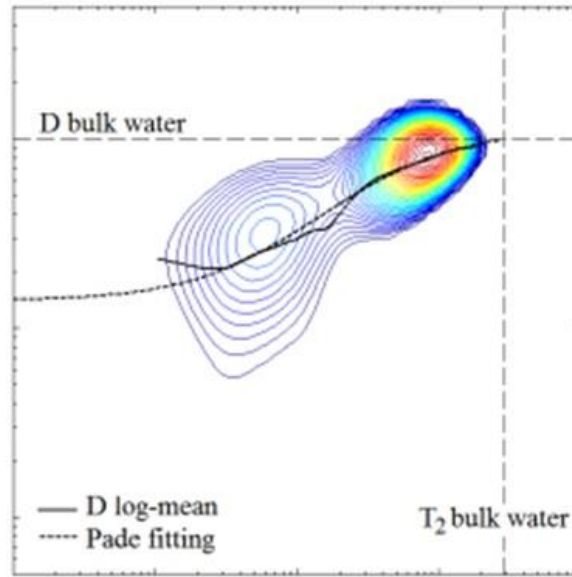


Figure 5.1 - DT_2 map obtained from a PFG experiment on water saturated rock core
Source: Adapted from SOUZA et al. (31)

As the rock is saturated with only one fluid, it would be expected that one would detect only water's diffusion coefficient in the map. However, it can be seen a continuum of values below the expected one. This is a result of restricted diffusion, introduced in Chapter 3, forcing the diffusion coefficient D to behave as:

$$D(\Delta, T_2) = D_0 \left(1 - \frac{4}{9\sqrt{\pi}} \frac{\sqrt{D_0 \Delta}}{\rho_2 T_2} \right), \text{ for } \frac{\sqrt{D_0 \Delta}}{\rho_2 T_2} \ll 1 \text{ (big pores)} \quad (5.3)$$

$$D(\Delta, T_2) = \frac{D_0}{F\phi}, \text{ for } \frac{\sqrt{D_0 \Delta}}{\rho_2 T_2} \gg 1 \text{ (small pores)} \quad (5.4)$$

If the diffusion length is smaller than pore sizes, restricted diffusion coefficient depends on surface relaxivity, as in equation (5.3), the big pores regime. On the other hand, if diffusion length is much bigger than the pore sizes, restricted diffusion will tend to a constant value (small pores regime) that depends on electrical properties (the formation factor F). An important feature of DT_2 measurement and restricted diffusion modelling is the diffusion time Δ . This is the time between gradient pulses during which the spins are allowed to diffuse, and is responsible for encoding restricted diffusion information. It can be seen as a fixed parameter in the PFG acquisition scheme.

No relaxation signals that decay faster than Δ can be measured in a PFG experiment, which implies that the small pores regime (equation (5.4)) is effectively never measured in such an experiment. However, if one can obtain the correspondent diffusion coefficient through other methods (say through resistivity measurements), equations (5.3) and (5.4) can

be interpolated through a mathematical process known as Pade fitting. D_0 and ρ are then obtained as fitting parameters.

Souza et al. (31) showed that surface relaxivities obtained from this method can vary from $1 - 5\mu\text{m/s}$ up to $30\mu\text{m/s}$. They also showed that the permeability prediction performance through SDR model (equations (3.51) and (3.52)) can be increased when one uses the correct values of ρ , instead of treating it as a constant. Figure 5.2 shows the improvement on permeability.

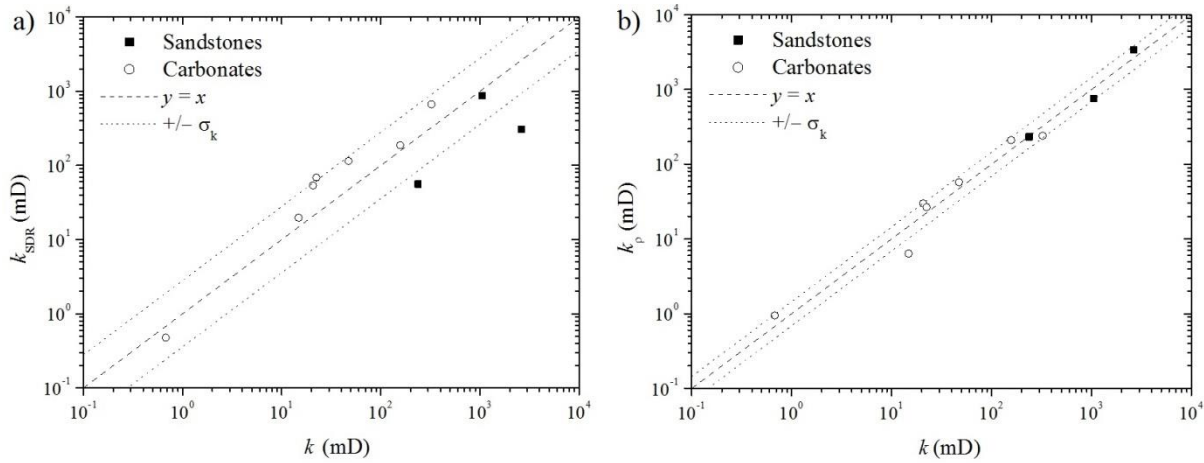


Figure 5.2 - Permeability prediction improvement by introducing surface relaxivity ρ in the model. a) standard k_{SDR} model (equation 3 – 51) and b) k_ρ model (equation 3 – 52), compared with core permeability.

Source: Adapted from SOUZA et al. (31)

As the permeability models assume that relaxation times relate to pore sizes, their performances are enhanced as surface relaxivity gives the correct correspondence between T_2 and geometry.

For well logging techniques, magnetic field gradients are fixed and are determined by geometrical characteristics of tools' magnet. Therefore, diffusion measurements are made through variation of diffusion times, yielding for transverse magnetization:

$$M_T(T_E, t) = \int dD dT_2 f(D, T_2) e^{-\frac{D(\gamma G T_E)^2}{12} t} e^{-t/T_2}, \quad (5.5)$$

for standard acquisition where interecho times are varied, or:

$$M_T(T_D, t) = \int dD dT_2 f(D, T_2) e^{-\frac{D(\gamma G)^2 T_D^3}{12}} e^{-\frac{t}{T_2}}, \quad (5.6)$$

for Diffusion Editing.

In both cases, interecho intervals equal twice the diffusion time Δ . Considering well logging acquisition schemes, we enumerate three challenges that must be overcome in extending the surface relaxivity method to the well site:

1) In well logging diffusion acquisitions, there is not a well defined diffusion time Δ . Consequently, the tendency expressed by continuous line in figure 1 cannot be exactly described by expressions such as (5.3) and (5.4), but by some sort of average expression on Δ .

2) The second challenge lies on the fact that, in general, electrical measurements used for determining the small pores regime (equation (5.4)), are either not available in the same depth of investigation of NMR acquisitions, or are not precise enough for complex carbonate reservoirs. Therefore, extending the ρ determination method to well logs should consider the case where one has only NMR measurements, which means dealing only with information on the big pores limit.

3) Finally, we should take into account that logging measurements are much noisier than laboratory ones, implying that whatever method is developed, it should be able to perform well at low Signal to Noise Ratios (SNR).

5.2 Developing ρ logging method – forward simulations and DT_2 inversions

In the next two sections we will consider simulated acquired diffusion editing data, contaminated with random noise at different SNR levels, to develop a method that can address the three challenges presented before, and determine at which noise extent one can still trust that method. At first, we will mostly show the implications of naively trying to use inverted DT_2 maps to fit the expression described by regime (5.3), addressing mainly challenges 2 and 3. Then, in the following section, we show how one can take advantage of challenge 1 to develop a more robust method that performs better at smaller SNR. We finish the Chapter by showing laboratory and well logging data that work as a proof of concept for the developed method.

Consider a water saturated reservoir, with corresponding T_2 distribution $f(T_2)$ showed in Figure 5.3 below:

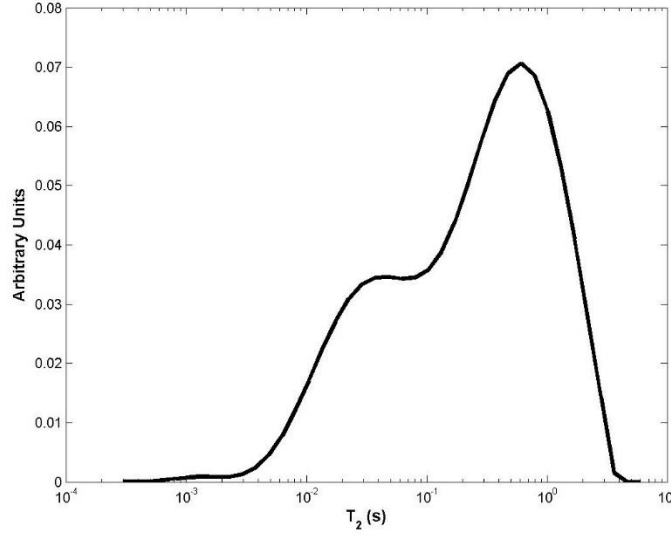


Figure 5.3 - T_2 distribution for a water saturated reservoir.
Source: By the author.

The magnetization decay for a diffusion editing echotrain obtained with first echo spacing T_D can then be forward modeled as:

$$M_T(T_D, t) = \int dT_2 f(T_2) \exp \left\{ -\frac{(\gamma G)^2 T_D^3}{12} D_{rest}(T_D/2, T_2) \right\} e^{-\frac{t}{T_2}} \quad (5.7)$$

Function $D_{rest}(\Delta, T_2)$ describes the restricted diffusion effect. In expression 6, each bin in the T_2 distribution represents a group of spins located in a pore with given size (proportional to T_2), which are consequently subject to a restriction in diffusion correspondent to that pore size. Instead of describing the whole diffusion-relaxation phenomena with a bi dimensional distribution, we treat it as a forward effect on the pore sizes represented by a single relaxation distribution. Modeled $D_{rest}(\Delta, T_2)$ must roughly capture the key features of restricted diffusion such as the existence of big/small pore limits, and a smooth transition interpolating both. We choose that function to be:

$$\ln D_{rest}(\Delta, T_2) = \begin{cases} \ln \left\{ D_0 \left(1 - \frac{4}{9\sqrt{\pi}} \frac{\sqrt{D_0 \Delta}}{\rho T_2} \right) \right\}, & \text{for } T_2 > T_{2c} \equiv \sqrt{D_0 \Delta} / \rho \\ \ln(RD_0) + A(\ln T_2 - \ln T_{min})^2 + B(\ln T_2 - \ln T_{min})^3, & \text{for } T_2 < T_{2c} \equiv \sqrt{D_0 \Delta} / \rho \end{cases} \quad (5.8)$$

The first part of equation (5.8) ensures the big pore limit when $\frac{\sqrt{D_0 \Delta}}{\rho T_2} < 1$. The second part is the simplest polynomial function (on $\ln T_2$) with enough degrees of freedom to ensure that when $T_2 \rightarrow T_{min}$, $D_{rest} \rightarrow RD_0$, with $0 \leq R < 1$ (small pore limit), and that it has continuous values and first derivative everywhere, including the transition point $T_c = \sqrt{D_0 \Delta} / \rho$. This last constraint allows parameters A and B to be calculated by solving:

$$\begin{pmatrix} A \\ B \end{pmatrix} = \begin{pmatrix} (\ln T_{2C} - \ln T_{min})^2 & (\ln T_{2C} - \ln T_{min})^3 \\ 2(\ln T_{2C} - \ln T_{min})/T_{2C} & 3(\ln T_{2C} - \ln T_{min})^2/T_{2C} \end{pmatrix}^{-1} \begin{pmatrix} \ln D_{rest}(\Delta, T_{2C}) - \ln RD_0 \\ D'_{rest}(\Delta, T_{2C})/D_{rest}(\Delta, T_{2C}) \end{pmatrix} \quad (5.9)$$

In our simulations we chose $T_{min} = 10^{-3}s$, $R = 0.01$ and $D_0 = 2.3 \cdot 10^{-9}m^2/s$. Specifics of the small pore limit behavior are not determinant for the method developed here, as NMR acquisitions will be most sensitive to the other limit, where we will apply approaches using equation (5.3). Figure 5.4 and Figure 5.5 show examples of D_{rest} for different values of ρ and Δ .

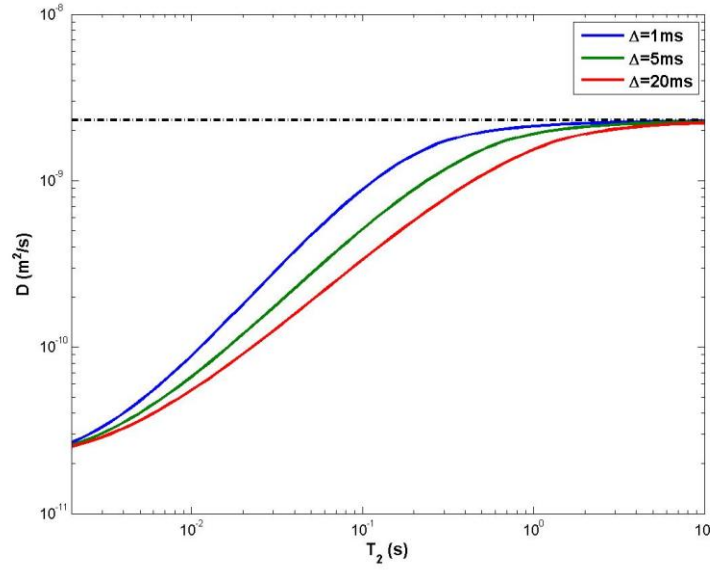


Figure 5.4 - Modeled restricted diffusion coefficient using function $D_{rest}(\Delta, T_2)$, with $\rho = 5\mu m/s$ and $\Delta = 1, 5$ and $10\mu m/s$. As diffusion time increases, long pore limit shrinks as more spins are subject to stronger restriction.

Source: By the author.

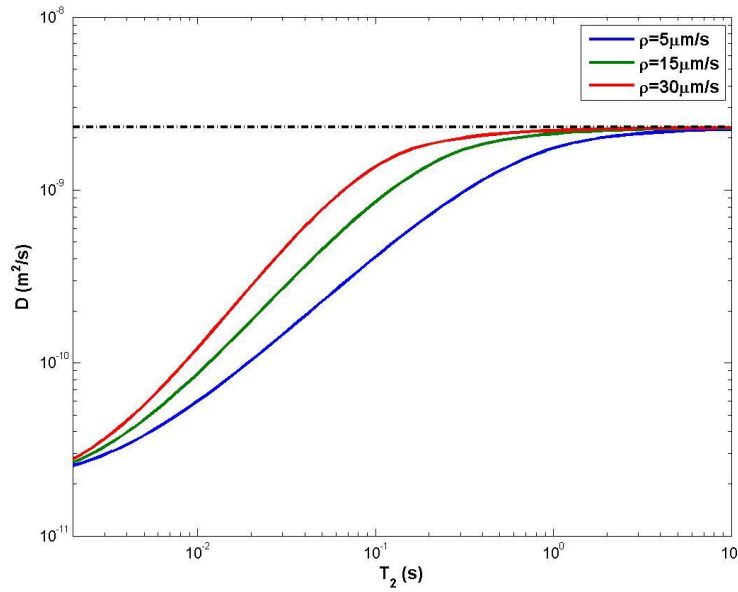


Figure 5.5 - Modeled restricted diffusion coefficient using function $D_{rest}(\Delta, T_2)$, with $\Delta = 5ms$ and $\rho = 5, 15$ and $30\mu m/s$. An increase of ρ makes the restriction for big pores less severe, making it difficult to detect.

Source: By the author.

As surface relaxivity increases, spins that reach the walls tend to rapidly lose coherence in relation to the other ones. Therefore, less “survivor” molecules (those who still contribute to net magnetization) will feel the movement restrictions imposed by the grain/pore interface, leading to smaller restriction in diffusion coefficients. In these cases, as measured restricted diffusion coefficients tend to be closer to the bulk value D_0 , determining surface relaxivity should be a difficult task. Likewise, an increase in diffusion times Δ will also be a limiting factor as measured data will tend to drift away from the big pores limit.

We modeled a series of well logging diffusion editing data assuming the reservoir is filled with water with T_2 distribution as in Figure 5.3, using equations (5.7) and (5.8) with the following parameters: $D_0 = 2.3 \cdot 10^{-9} m^2/s$, $R = 0.01$, $T_{min} = 1ms$ and echo time $T_E = 0.6ms$. We assumed at first a single gradient tool with $G = 30G/cm$. In each “experiment”, ten T_D values were used, varying logarithmically from 0.6 to 15ms. Reservoir surface relaxivities were varied from 5 to 35 $\mu m/s$, in steps of 5 $\mu m/s$. SNR was also varied from 100 to 10, in steps of 10. We defined SNR as the ratio between the total amount of signal (set to 1 through normalization of T_2 distribution amplitudes) and the standard deviation of the random noise. Figure 5.6 shows the modeled data at $SNR = 100$, for varying relaxivities. Similarly, Figure 5.7 shows an example of varying SNR at fixed surface relaxivity.

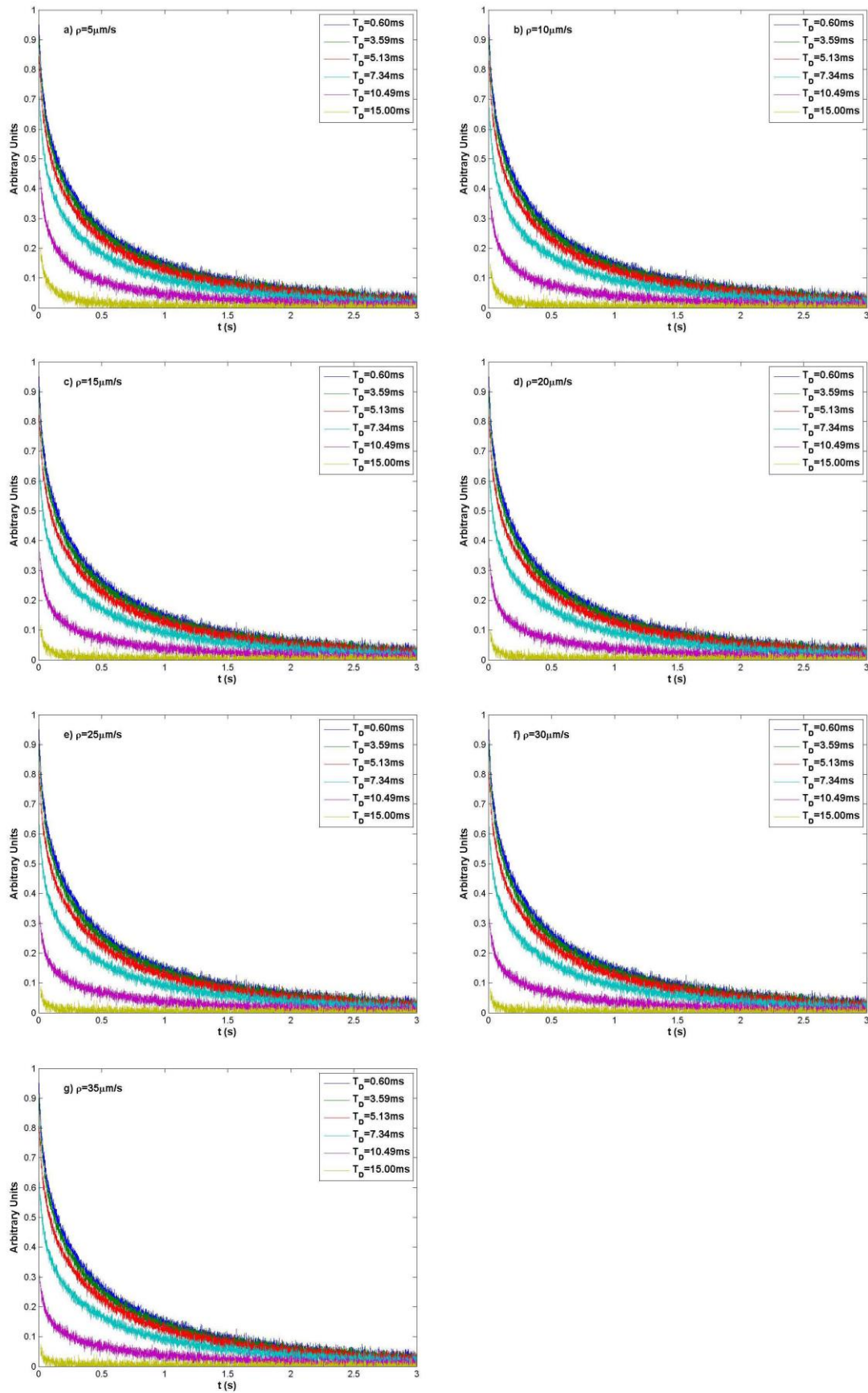
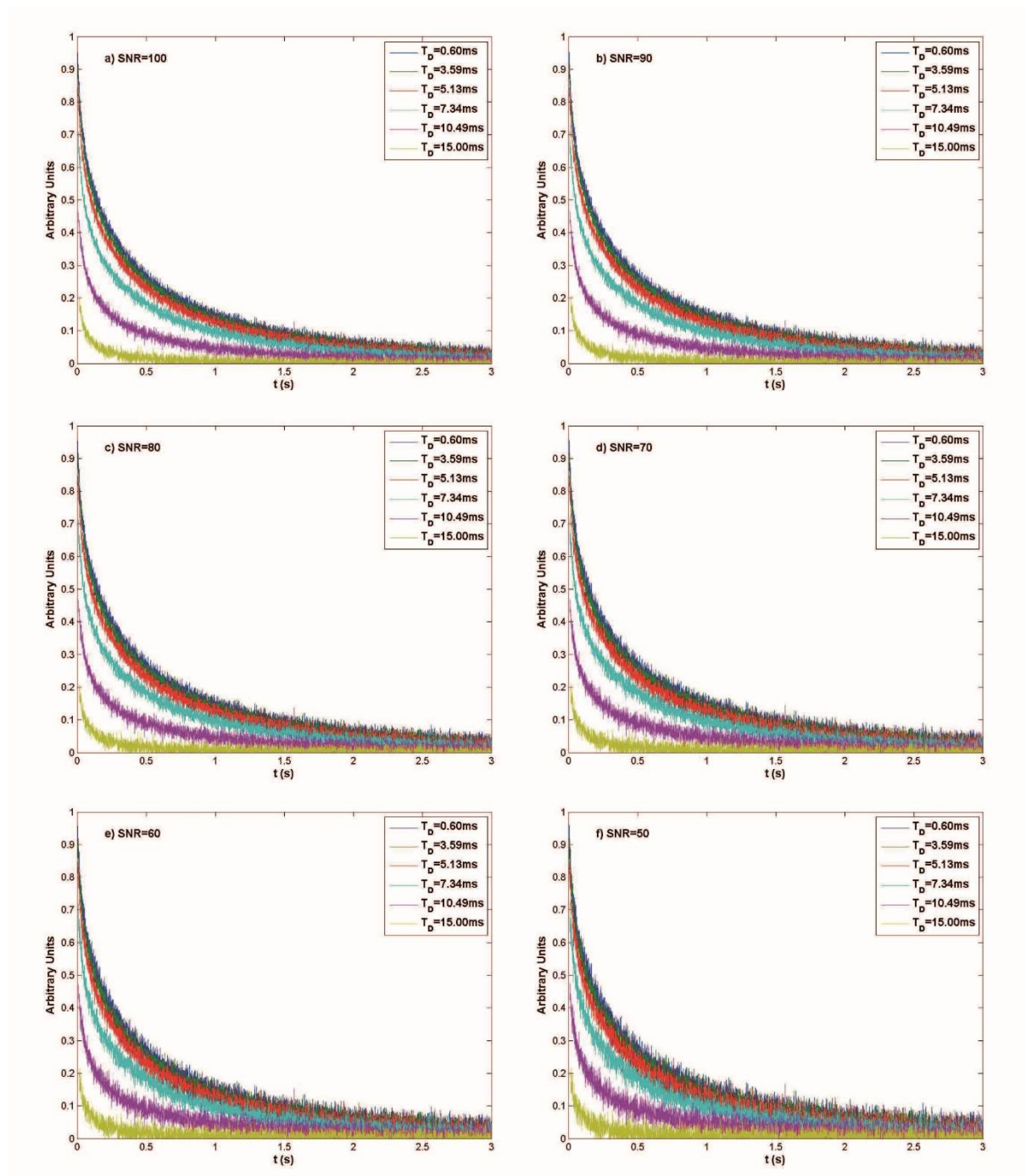


Figure 5.6 - Modeled well logging diffusion editing data for various reservoir surface relaxivities.
Source: By the author.



(continued)

(continuation)

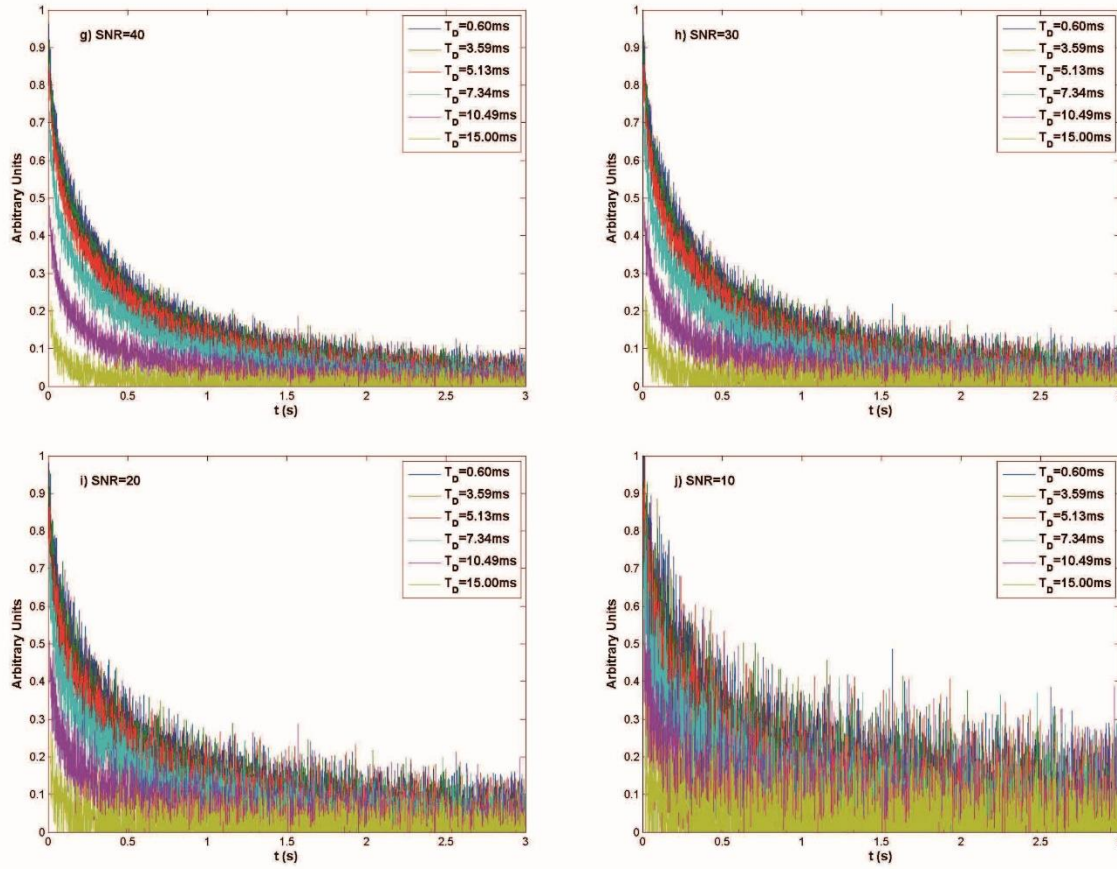


Figure 5.7 - Modeled well logging diffusion editing data for various SNR and $\rho = 5\mu\text{m/s}$.
Source: By the author.

It is worth noticing the DT_2 map behavior for such an acquired data. Figure 5.8 shows the bidimensional distribution for data expressed in Figure 5.6a. Superimposed to the distribution are the restricted diffusion coefficients as a function of T_2 (accordingly to equation (5.7)) for each one of the T_D 's used in the “acquisition”. As pointed out before, diffusion editing techniques do not have a well defined diffusion time, consequently the bidimensional DT_2 map will have a width governed by the distribution of restricted coefficients as a function of T_D . However, it has been shown that the logarithmic mean of the restricted diffusion coefficient as function of T_2 , $D_{LM}(T_2)$, follows reasonably well the trend defined by equation (5.8), when Δ is substituted by its root mean square value $\Delta_{RMS} = \sqrt{\frac{1}{N} \sum_{i=1}^N (T_{Di}/2)^2}$. Figure 5.9 shows $D_{LM}(T_2)$ obtained from the maps in Figure 5.6 (star dots), along with $D_{rest}(\Delta_{RMS}, T_2)$ (continuous black line).

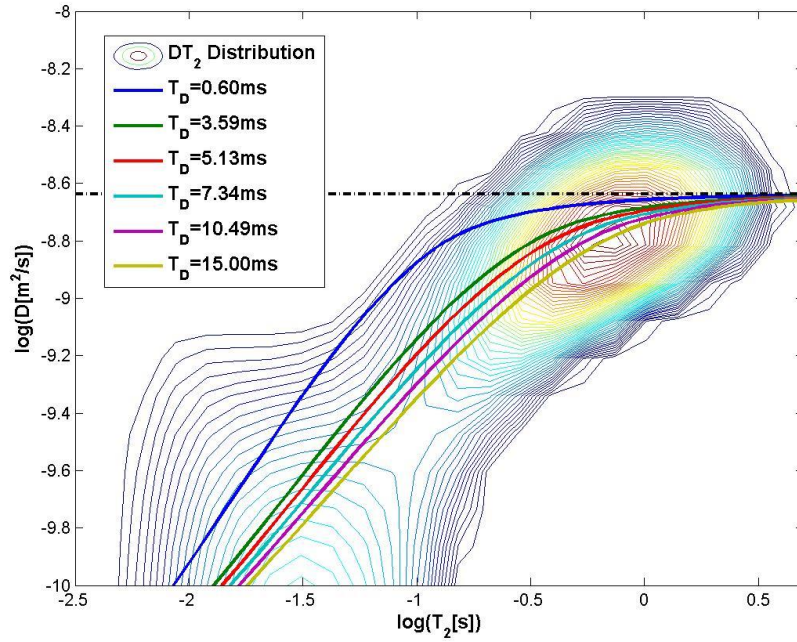


Figure 5.8 - Inversion of diffusion editing data showed in Figure 5.6a. Continuous lines represent restricted diffusion coefficients $D_{rest}(T_D, T_2)$, for each one of the diffusion times used in the modeling.

Source: By the author.

Considering that the use of Δ_{RMS} and measurement of $D_{LM}(T_2)$ solves challenge 1, one would have to take into account the lack of information NMR Diffusion Editing data has on the small pores limit (challenge 2). There is no use working with detailed information on smaller T_2 values (such as in equation (5.8)) in the bidimensional map, as those are generally not available. The simplest way to proceed would be to consider a simplified version of D_{rest} , with information only on the big pores limit:

$$D_{simp}(\Delta, T_2) = D_0 \left(1 - \frac{4}{9\sqrt{\pi}} \frac{\sqrt{D_0 \Delta}}{\rho_2 T_2} \right) \quad (5.10)$$

By choosing $\Delta = \Delta_{RMS}$, free parameters D_0 and ρ would then be obtained as fitting constants when expression (5.11) was compared to $D_{LM}(T_2)$ from the map, in a region where T_2 was greater than some T_{2C} , as exemplified in by the blue lines in Figure 5.9. The question that remains to be answered is: is there a way to determine a limiting T_{2C} , such as the fitting parameters remain close to the real ones, in a wide range of relaxivities? The answer is, unfortunately: only for a very limited range of SNR, in an even more limited tool scenario, as explained next.

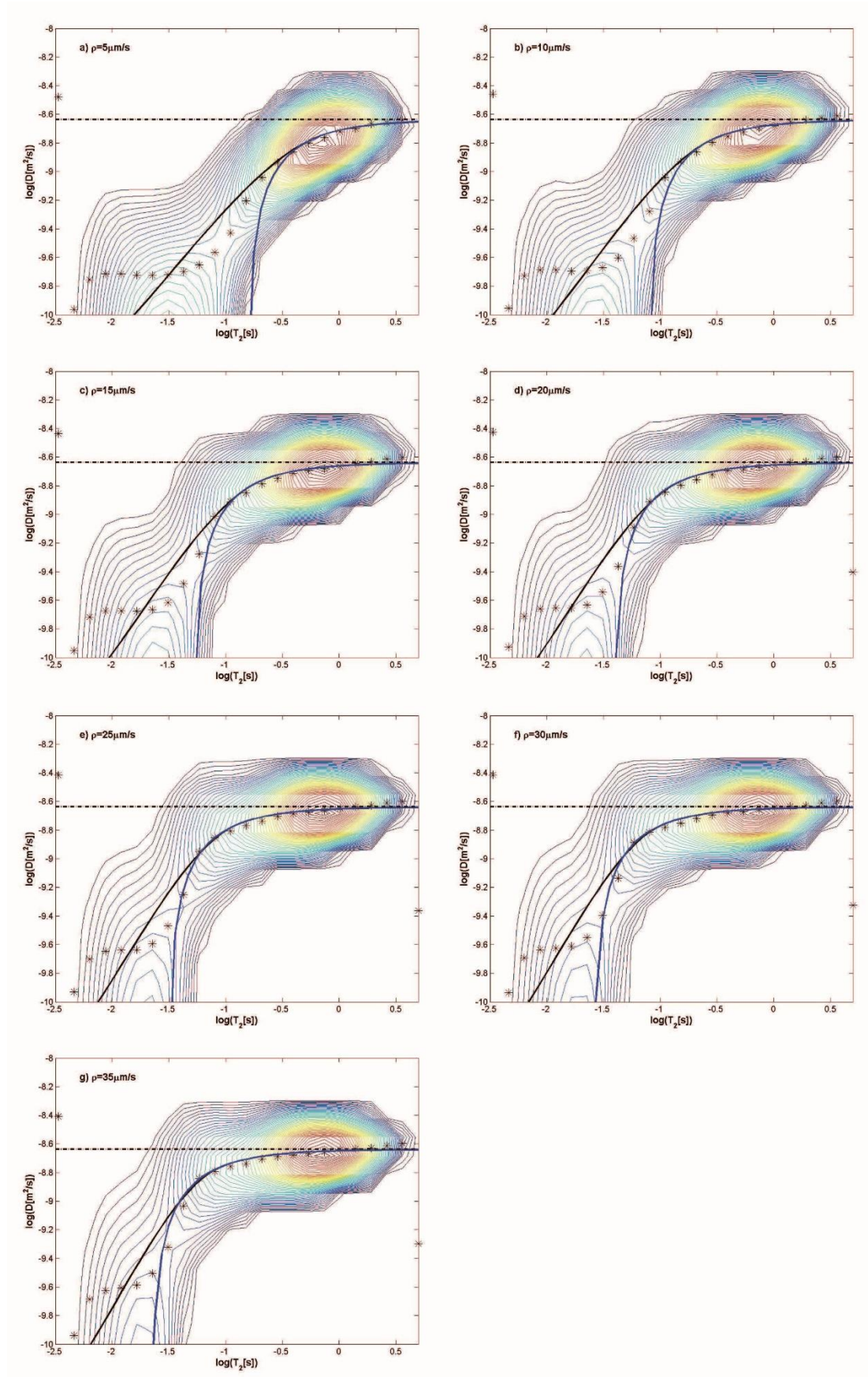


Figure 5.9 - Restricted diffusion coefficient logarithmic mean $D_{LM}(T_2)$ (star dots) compared with $D_{rest}(\Delta_{RMS}, T_2)$ (continuous line).

Source: By the author.

Average surface relaxivities were obtained from the maps in Figure 5.9 as fitting constants based on equation (5.11), for several different T_{2C} . The fitting procedure was made through the Levenberg-Marquadt algorithm, implemented in Matlab's built in function *nlinfit*. Figure 5.10 shows the relative difference between fitted parameters ρ_{fit} and real ones, as a function of T_{2C} .

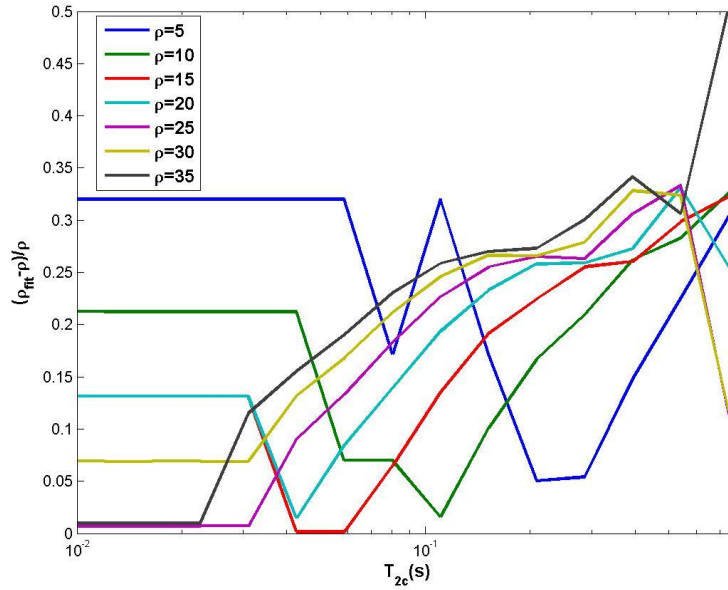


Figure 5.10 - Fitting results as a function of T_{2C} , for all surface relaxivity simulated data.
Source: By the author.

As it is expected, there is no special value for T_{2C} that minimizes all relative errors, as the limiting value $T_{2C} \sim \sqrt{D_0 \Delta} / \rho$ depends on D_0 and ρ themselves. It can be seen that for $T_{2C} \sim 0.1s$, smaller relaxivities are privileged, as the opposite is true for $T_{2C} \sim 0.05s$. If we choose the latter one, the biggest error will be of about 30% for the smallest relaxivity, $\rho = 5 \mu m/s$, but rapidly diminishes as ρ increases. Allowing ourselves to tolerate such disparity for the sake of analyzing noise behavior, fitted values for other SNR's with fixed $T_{2C} = 0.05s$ are shown in Figure 5.11a. As each SNR experiment was repeated 30 times with different realizations of noise, Figure 5.11b shows the average fitted ρ values with errorbars corresponding to twice the standard deviation.

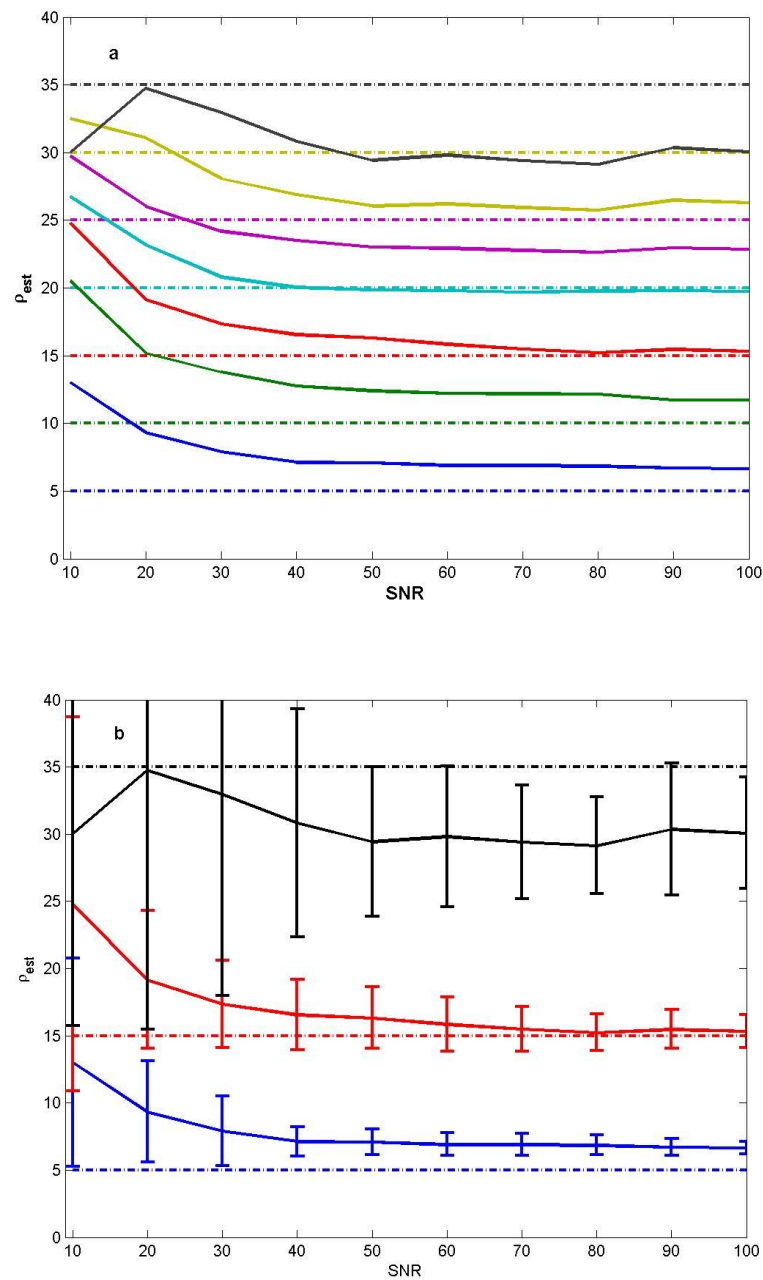


Figure 5.11 - a) Average fitted surface relaxivities as function of SNR and b) Average fitted surface relaxivities and standard deviations. Each noise level was repeated 30 times for calculating statistics. Dotted lines correspond to the real values used in the forward modeling.

Source: By the author.

Despite the superestimation of very low relaxivities, this naive approach can separate low, intermediate and high ρ 's until SNR's as low as 40. Below this value, small and intermediate relaxivities become superestimated and their ranges start to mix as the errorbars rapidly increase. For reference, logging data have typical SNR of 10 to 20.

If we model the data using a logging tool that has a distributed gradient, such as Schlumberger's CMR, the situation is even more dramatic. Data can be modeled by substituting $\exp\left\{-\frac{(\gamma G)^2 T_D^3}{12} D_{rest}(T_D/2, T_2)\right\} \rightarrow \sum_i g(G_i) \exp\left\{-\frac{(\gamma G_i)^2 T_D^3}{12} D_{rest}(T_D/2, T_2)\right\}$ in equation 5 – 6, with gradient distribution $g(G)$ given in Figure 3.18. The results are then shown in Figure 5.12.

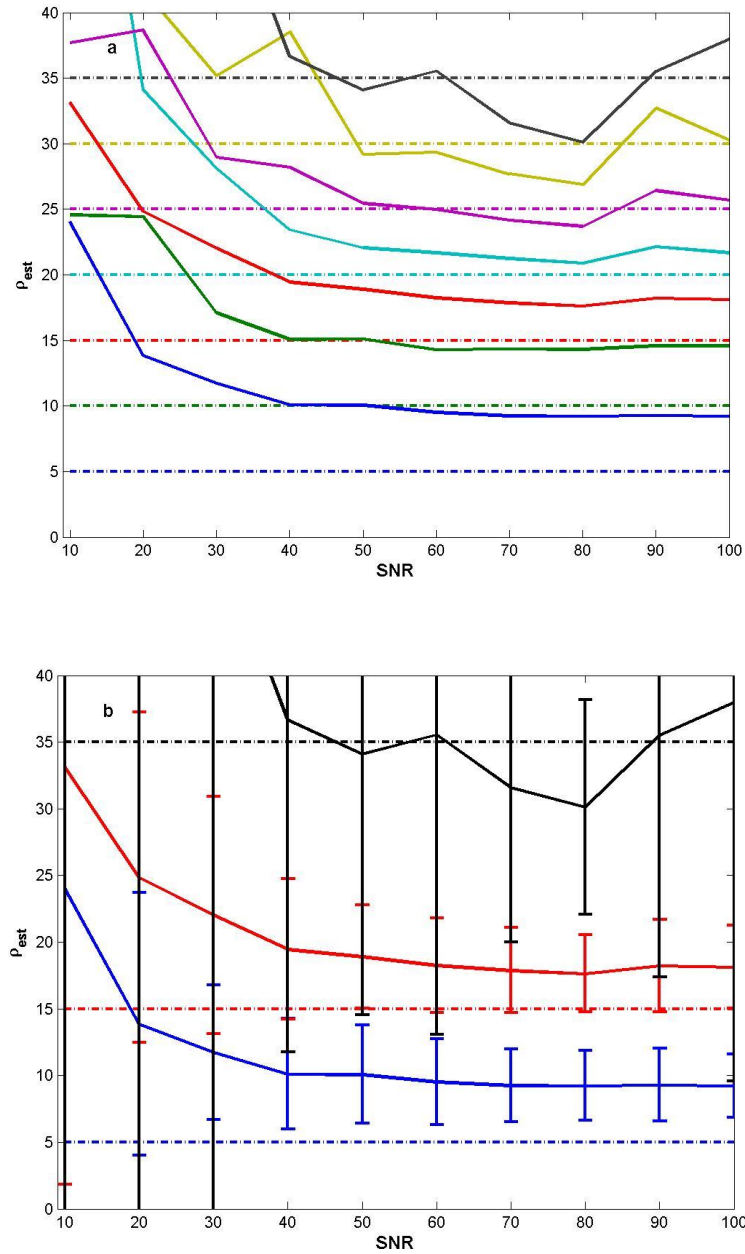


Figure 5.12 - a) Average fitted surface relaxivities as function of SNR for data modeled from a distributed gradient tool, and b) Average fitted surface relaxivities and standard deviations. Each noise level was repeated 30 times for calculating statistics. Dotted lines correspond to the real values used in the forward modeling.

Source: By the author.

In the case of distributed gradient logging tools differentiation of relaxivities is virtually impossible through this method, because every broadening in the gradient distribution implies (through equation (5.7)) in a loss of resolution in the diffusion dimension. This effect is much more dramatic for high relaxivities, as the consequently smaller restriction in D demands higher resolution.

5.3 ρ logging method – raw data non-linear regression

In dealing with surface relaxivity extraction from DT_2 maps, different diffusion times (coming either from diffusion editing or standard acquisition) end up mixing restricted diffusion regimes yielding a sort of averaged bidimensional distribution. Although distorted, relaxivity information is still present in the long T_2 portion of the map, and can be decoded by means of Δ_{RMS} . However, this solution to Challenge 1 ended up being not feasible for well logging, as it behaves poorly as SNR decreases. In this section, we propose a different solution that uses directly the raw data, skipping the 2D inversion procedure. Indeed, restricted diffusion information coded by different T_D 's is already present in the magnetization decays and, as far as it concerns to ρ extraction, there is no point in mixing and distorting it in an average DT_2 map.

Considering that equation (5.7) fairly represents magnetization decays, it can be turned into a function of D_0 and ρ by making the approximation $D_{rest} \approx D_{simp}$. That eliminates the necessity of knowing detailed information on the small pores limit, and takes advantage of variations in T_D , which directly encode the slope of equation (5.11), hence relaxivity. However, this alone does not solve Challenge 2 completely, as this approximation for the echotrails remains good only for longer times, where $\frac{\sqrt{D_0(T_D/2)}}{\rho T_2} < 1$. We propose an iterative procedure that, at each step, calculates an approximation for D_0 and ρ , and then uses them to determine a cutoff value $T_{2C} = \sqrt{D_0(T_D/2)}/\rho$. There will be one cutoff value for each echotrain, as they were acquired at different T_D 's. In the next iteration only the portions of echotrails greater than their respective T_{2C} are used. The algorithm is detailed below:

- 1) The acquisition corresponds of a set of magnetization decays $M_T(T_D^\eta, t)$, each one acquired with a different T_D^η . A simple T_2 inversion is made using solely the echotrain corresponding to the smaller diffusion time, which usually equals the

echotime ($T_D^1 = T_E$). If T_E was chosen small enough to suppress diffusion effects, resulting T_2 distribution $f(T_2)$ can be considered diffusion free.

- 2) Raw data is then expressed by the following function:

$$M_T^\eta = \begin{cases} \int dT_2 f(T_2) \exp \left\{ -\frac{(\gamma G)^2 (T_D^\eta)^3}{12} D_{simp}(T_D^\eta/2, T_2) \right\} e^{-\frac{t}{T_2}} \\ D_{simp}(T_D^\eta/2, T_2) = D_0 \left(1 - \frac{4}{9\sqrt{\pi}} \frac{\sqrt{D_0(T_D^\eta/2)}}{\rho_2 T_2} \right) \end{cases} \quad (5.11)$$

All parameters above are known, except for bulk diffusion coefficient and surface relaxivity, which makes M_T^η a function of D_0 and ρ . Equation (5.11) is implemented in a Levenberg-Marquadt non-linear regression algorithm, by means of Matlab's built in function *nlinfit*, where the free parameters can be determined by minimizing the squared error sum relative to the data. In this procedure, we limit possible relaxivities by demanding $0 < \rho < 100 \mu\text{m/s}$. *nlinfit* takes as input a vector with the acquisition times t , the corresponding data vector M_T^η (all echotrains), and an initial guess for the free parameters. A scaling step helps convergence with the substitution $D_0 \rightarrow D_0 \cdot 10^{10}$ and $\rho \rightarrow \rho \cdot 10^6$. Only for the first iteration, $D_{simp} \equiv D_0$, and an average bulk diffusion coefficient D_0^1 is determined as first approximation. First approximation for ρ is then manually set as $\rho^1 = 90 \mu\text{m/s}$. This procedure pushes the algorithm away from an infinitude of local minima located at high ρ 's and arbitrary D_0 's.

- 3) For each echotrain, a cutoff value is determined as $(T_{2c}^\eta)^i = \left(\sqrt{D_0^i \left(\frac{T_D^\eta}{2} \right)} \right) / \rho^i$. All

data corresponding to $t < (T_{2c}^\eta)^i$, for each decay, are discarded.

- 4) D_0^i and ρ^i are used as initial values in step 2, and the non-linear regression returns D_0^{i+1} and ρ^{i+1} .
- 5) Steps 3 and 4 are repeated until $|\rho^{i+1} - \rho^i| < \epsilon$, or the number of iterations reaches a predefined maximum. No more than 10 iterations were needed for convergence in all tested cases. A good stopping rule is $\epsilon = 1 - 3 \mu\text{m/s}$.

Figure 5.13 shows the iteration steps for example data of Figure 5.6 a to c.

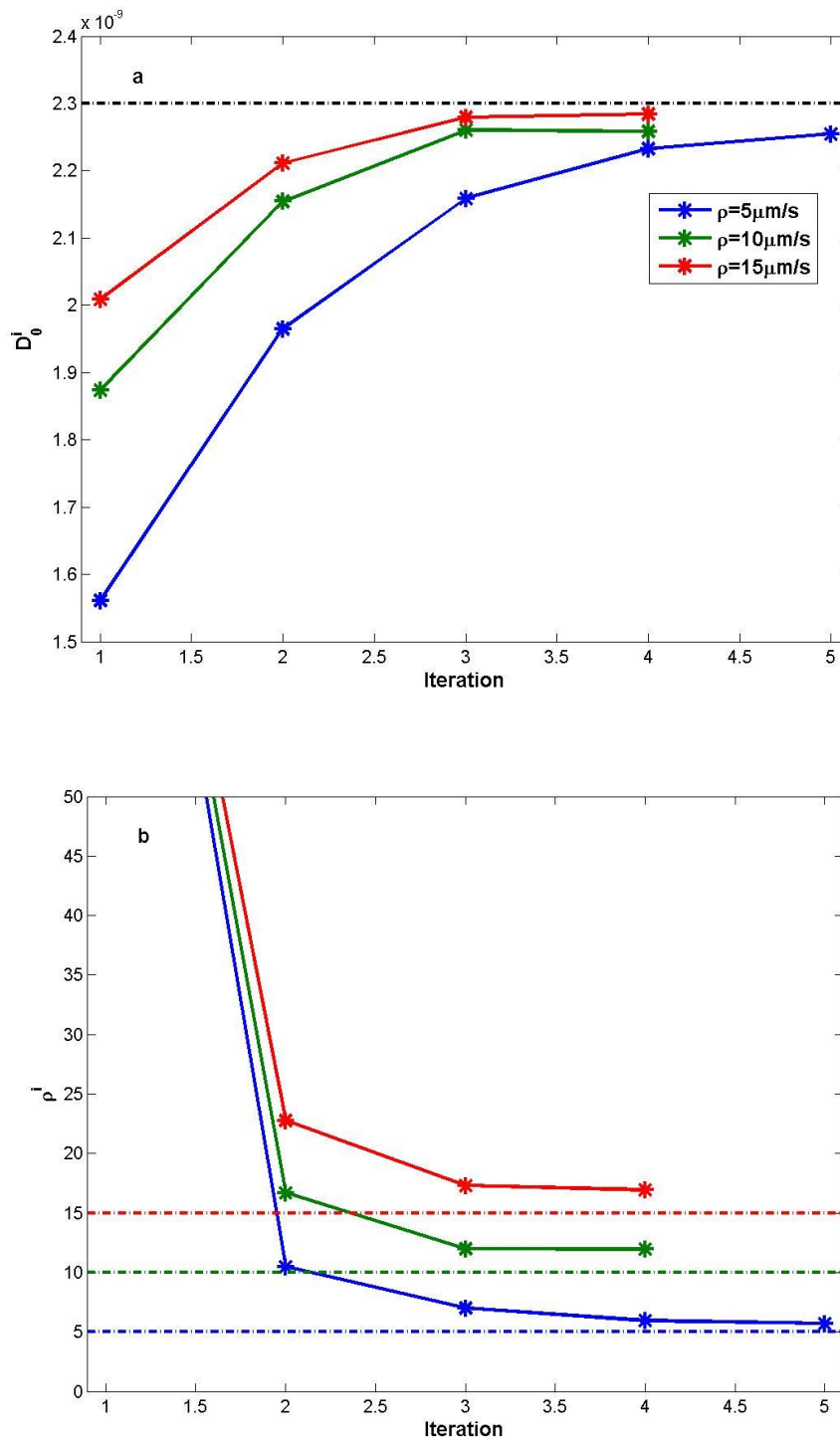


Figure 5.13 - a) D_0 and b) ρ determined at each iteration, for example cases where data was simulated with $\rho = 5, 10$ and $15 \mu\text{m/s}$.

Source: By the author.

Figure 5.14 shows the fit produced by equation 5 – 11 and parameter pair $D_0^{est} = 2.25 \cdot 10^{-9} \text{m}^2/\text{s}$, $\rho^{est} = 5.70 \mu\text{m/s}$, estimated from the algorithm, real values been $D_0 = 2.3 \cdot 10^{-9} \text{m}^2/\text{s}$ and $\rho = 5 \mu\text{m/s}$. As pointed out before, the fitting procedure commits only with the part of the data greater than cutoff values determined recursively.

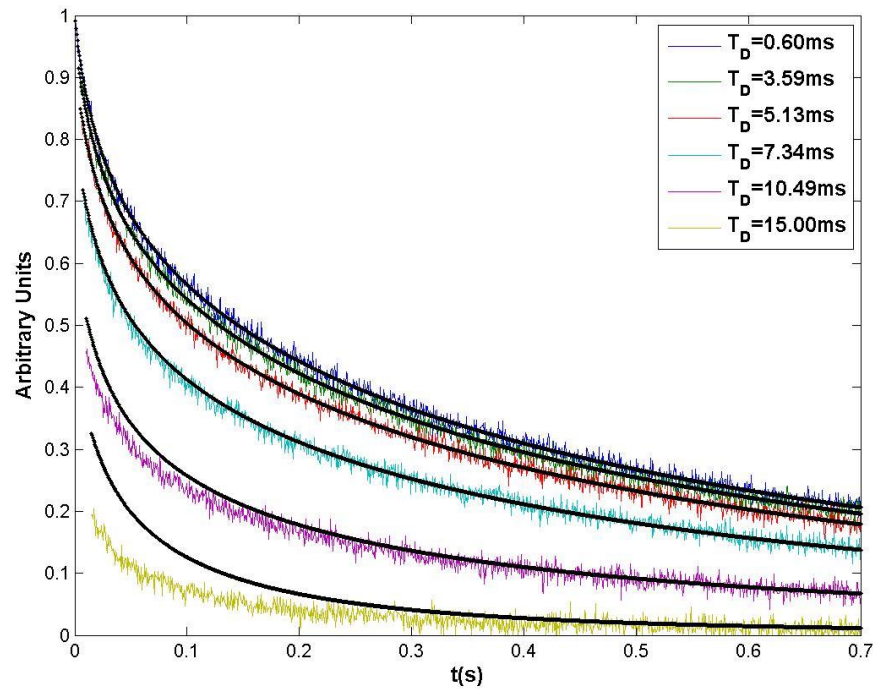
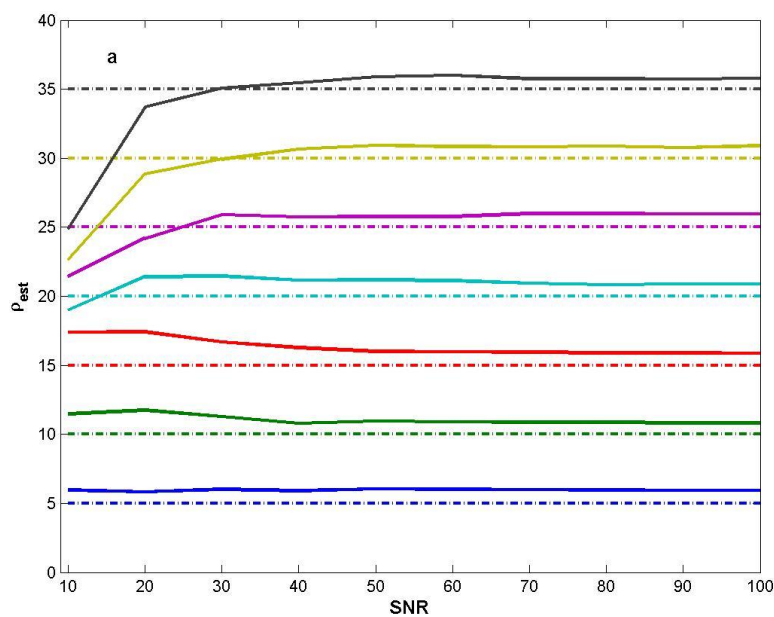


Figure 5.14 - Example of data fit (continuous black lines) generated by the non-linear regression algorithm. Data was simulated with $\rho = 5\mu\text{m/s}$, and estimated parameters were $\rho^{est} = 5.70\mu\text{m/s}$ and $D_0^{est} = 2.25 \cdot 10^{-9} \text{m}^2/\text{s}$.

Source: By the author.

The method was tested for all simulated examples represented by Figure 5.6 (30 different realizations of each one of the 10 SNR levels, with 7 values of ρ) and results are summarized in Figure 5.15.



(continued)

(continuation)

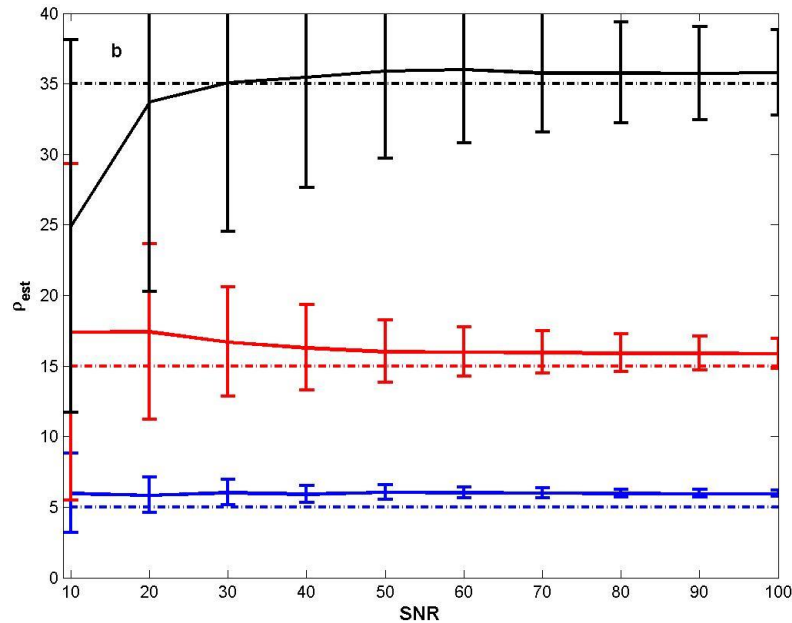


Figure 5.15 - a) Average fitted surface relaxivities (using the non linear regression algorithm) as function of SNR and b) Average fitted surface relaxivities and standard deviations. Each noise level was repeated 30 times for calculating statistics. Dotted lines correspond to the real values used in the forward modeling.

Source: By the author.

Comparison with Figure 5.11 shows a great improvement in determination of relaxivities as a function of SNR. In the present case, low and intermediate parameters can be found with fairly good precision (although with some overestimation), and higher values (more rare) can be at least separated from smaller ones up to an SNR level of about 25. Usually a DT_2 acquisition can be made slow enough to reach SNR's of about 20, even in the well bore. If that is not possible, some stacking of the data (about four levels) would be necessary in order to reach the desired noise level.

When the method is applied to distributed gradient tools (making use of gradient distributions) the results are much better than the ones shown in Figure 5.12, as shown in figure Figure 5.16. Separation of relaxivities is now possible in a similar fashion as with single gradient tools, to a SNR level as low as 30.

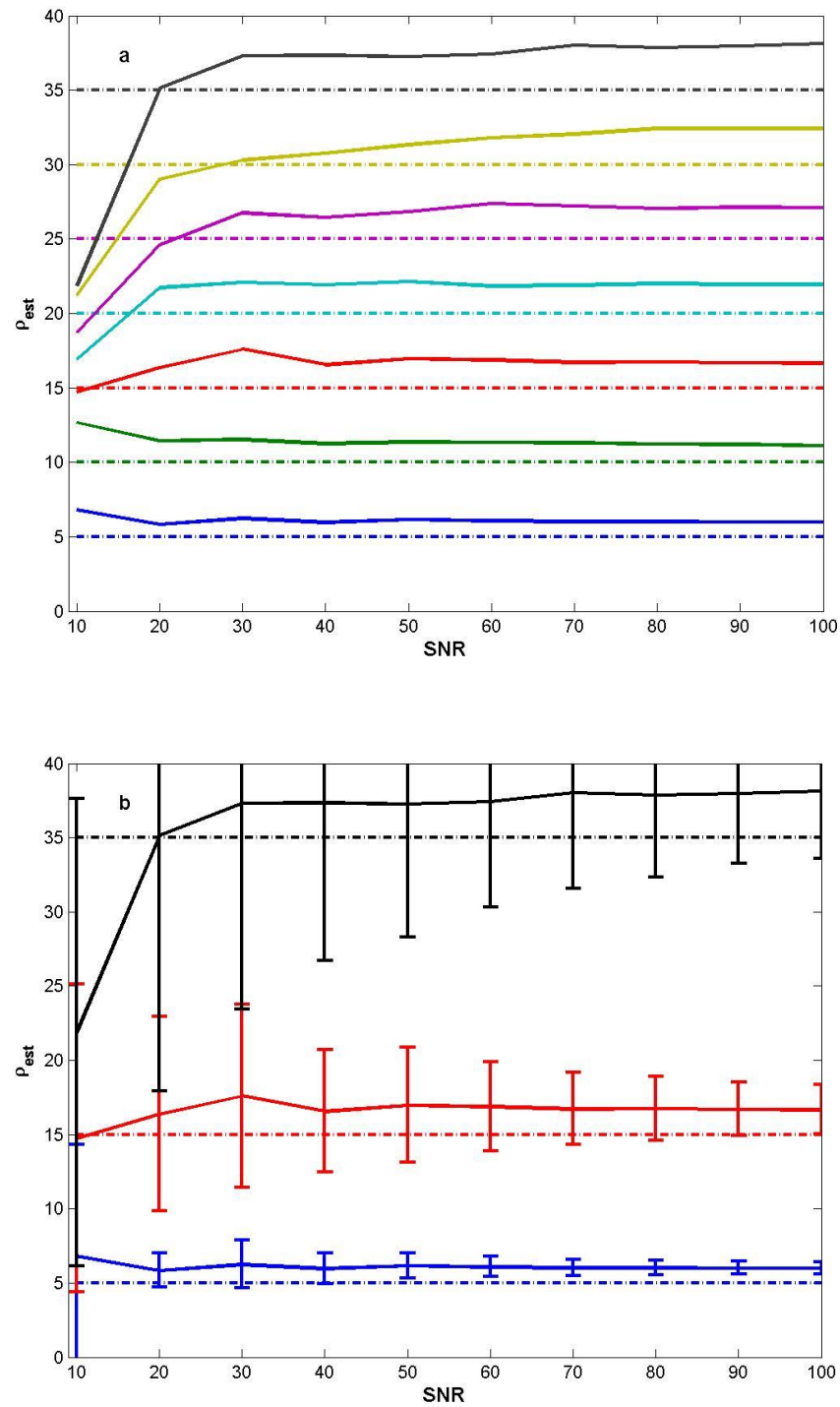


Figure 5.16 - a) Average fitted surface relaxivities (using the non linear regression algorithm) as function of SNR for data modeled from a distributed gradient tool, and b) Average fitted surface relaxivities and standard deviations. Each noise level was repeated 30 times for calculating statistics. Dotted lines correspond to the real values used in the forward modeling.

Source: By the author.

5.4 Laboratory Experimental Results

The ideas presented in previous sections for the relaxivity non-linear regression method were tested in the laboratory with a 9 sample set of carbonate reservoir rock cores. The core plugs are 1.5in diameter cylinders, with lengths ranging between 3 and 4cm. Their petrophysical properties (from routine core analysis) and surface relaxivity are described in Table 5.1.

Table 5.1 - Routine core analysis (porosity and permeability) and surface relaxivity, for the core samples studied.

<i>Sample</i>	<i>Porosity ϕ</i> <i>(pu)</i>	<i>Permeability k</i> <i>(mD)</i>	<i>Relaxivity ρ</i> <i>($\mu\text{m/s}$)</i>
1	15.4	17.50	7.2
2	13.7	66.10	5.1
3	5.6	0.44	16.9
4	8.8	3.40	28.9
5	4.7	0.04	5.9
6	8.6	36.10	26.6
7	11.8	556.00	11.4
8	10.3	0.65	5.6
9	10.9	11.30	3.9

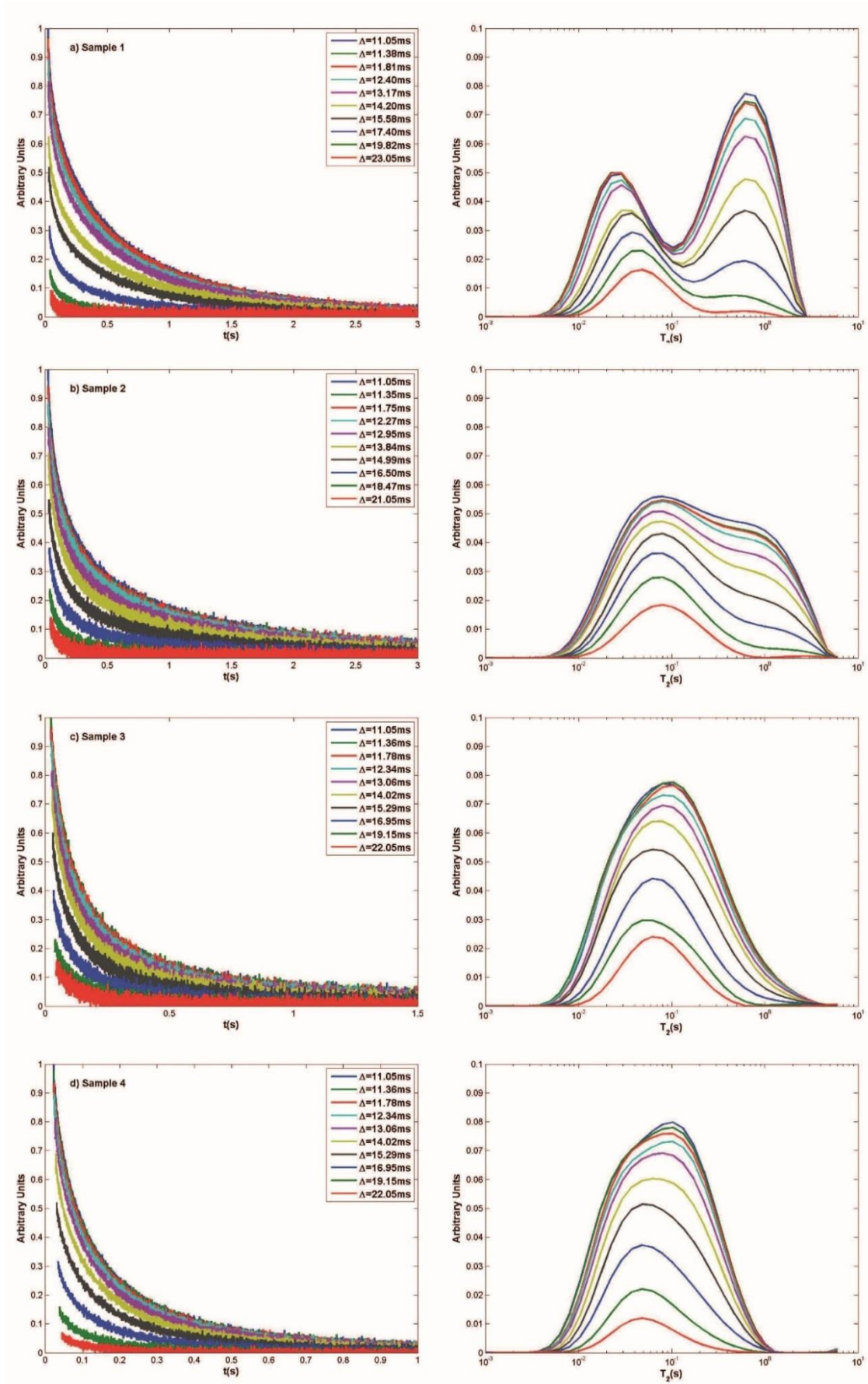
Source: By the author.

Surface relaxivities were obtained through Padé interpolation between NMR and electric limits in the DT_2 maps, described in the beginning of the Chapter.

For the following NMR experiments, samples were saturated with brine at a salinity of 20000ppm, prepared with deionized water and NaCl. They were performed in a magnetic field corresponding to a Larmor frequency of 1.8MHz for Hydrogen, with 50ppm in a 5mm sphere of homogeneity in the middle of a 40cm bore cylindrical magnet. Both magnet and spectrometer were acquired from Tecmag. Rock core NMR probes and gradient coils were built by the NMR group (LEAR – Laboratório de Espectroscopia de Alta Resolução por Ressonância Magnética Nuclear) of São Carlos Institute of Physics, University of São Paulo (IFSC/USP).

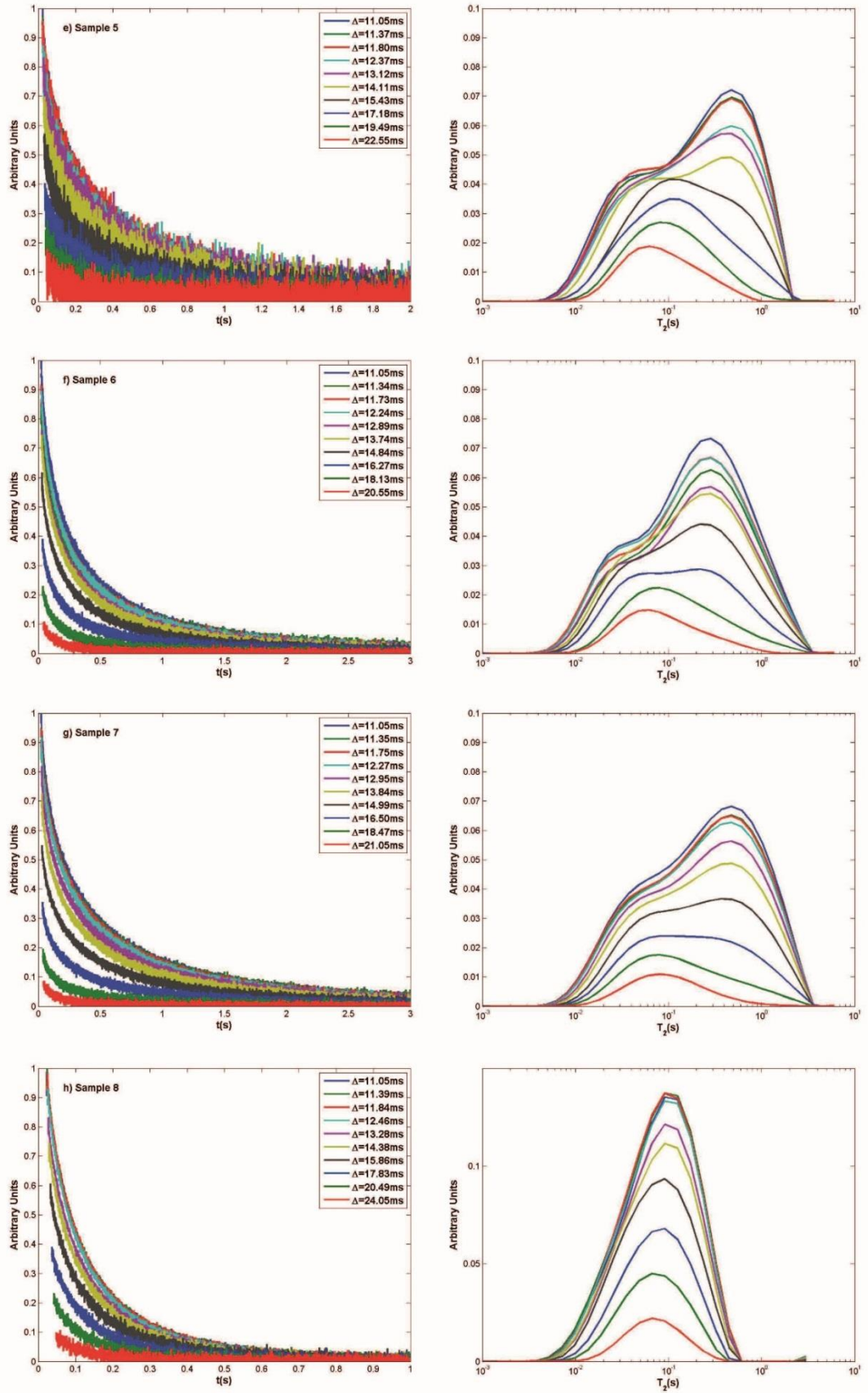
The ideal scenario for reproducing well log acquisitions in the lab would be to continuously apply a background linear magnetic field, imposing over the initial homogeneous field a controlled gradient. Due to limitations in the power amplifier circuits feeding the gradient coils, gradients as high as $10 - 30\text{G/cm}$ (covering the typical ranges for logging tools) cannot be sustained during the whole echotrain acquisition time. In fact, we could safely have a maximum gradient of about 2G/cm in this setup. Considering a diffusion editing experiment, the diffusion time needed for reducing magnetization to about 35% ($1/e$) of its initial value is (equation (5.6)), due only to diffusion effects is $\Delta = \sqrt[3]{\frac{3}{2(\gamma G)^2 D}}$, which gives in this case $\Delta \sim 30\text{ms}$, for water bulk diffusion coefficient at 25°C . For the smallest relaxivities the only T_2 values for which we would remain in the NMR sensitive region $\sqrt{D_0 \Delta} / \rho T_2 < 1$ would be those greater than 1.6s. In order to be able to detect surface relaxivity effects, we should have enough NMR signals decaying with such long times, which would be difficult for water saturated rock samples. In addition, radiofrequency pulses applied in an inhomogeneous field become selective, exciting a smaller part of the sample and diminishing SNR. We then opted for emulating diffusion editing acquisitions through an adaptation of the pulse field gradient sequence (Figure 3.9), proposed by MITCHELL et al. (63) Instead varying the gradient strengths, one can change their durations δ , which implies in changing diffusion times Δ , hence encoding information on ρ . The downside is when gradient coils are turned off, variations in magnetic fields inside the bore induces eddy currents within the magnet, which in turn generate more distortions in the fields. Therefore, a time delay δ_G is needed after the gradient pulse for B_0 to stabilize. In our experiments we were able to increase gradient strength up to 10G/cm , with a delay of $\delta_G = 10\text{ms}$. Consequently, diffusion times are of at least $\Delta \sim 10\text{ms}$, which allows detection of ρ for relaxation times greater than or of order of 0.9s (smaller relaxivities) of 0.1s (bigger relaxivities). This constitutes a better scenario than the one with constant background gradients, but is still near the limits of validity of equation (5.10), for samples studied.

Figure 5.17 sums up acquired data for the carbonate samples, along with corresponding T_2 distributions (inverted for each echotrain).



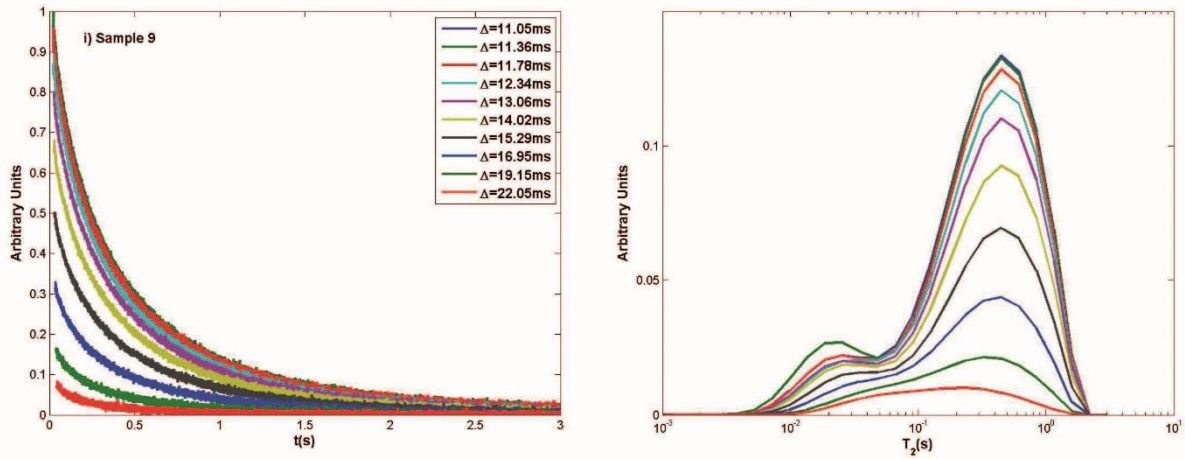
(continued)

(continuation)



(continued)

(conclusion)

Figure 5.17 - PFG data for brine saturated carbonate samples, along with corresponding T_2 distributions.

Source: By the author.

In order to apply the non-linear regression method for ρ , the kernel in equation (5.11) must be modified to take into account the PFG data acquisition scheme. This can be done through the modification $\exp\left\{-\frac{(\gamma G)^2 (T_D^\eta)^3}{12} D_{simp}(T_D^\eta/2, T_2)\right\} \rightarrow \exp\left\{-(\gamma G \Delta^\eta)^2 \left(\Delta^\eta - \frac{\delta^\eta}{3}\right) D_{simp}(\Delta^\eta, T_2)\right\}$. Another modification was made regarding the definition of limiting T_{2c} . Approximation $D_{rest}(\Delta, T_2) \approx D_{simp}(\Delta, T_2)$ is valid only when $\sqrt{D_0 \Delta}/(\rho T_2)$ is smaller than 1. In the simulations, we set the cutoff value T_{2c} above which that condition is valid by demanding that ratio to be precisely 1. For real samples, one should expect that $\sqrt{D_0 \Delta}/(\rho T_{2c}) = r$, where r is some number around 1. Fitted ρ values for the studied rock cores were obtained for several different values of r . For those above 1, results tend to severely overestimate the relaxivities. On the opposite direction, the algorithm diverges for some samples, as T_{2c} becomes too big consequently discarding most of the data. We found out $r = 0.8$ to give the best estimations for ρ . These results are shown in Figure 5.18.

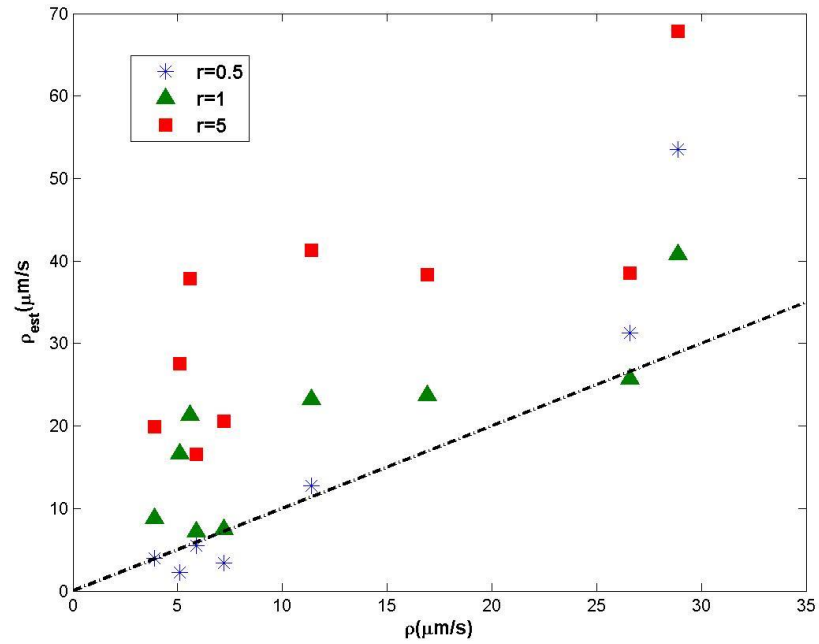


Figure 5.18 - Relaxivities from non-linear regression as function of expected ones, for several r values.
Source: By the author.

Results corresponding to $r = 0.8$ are shown in Figure 5.19.

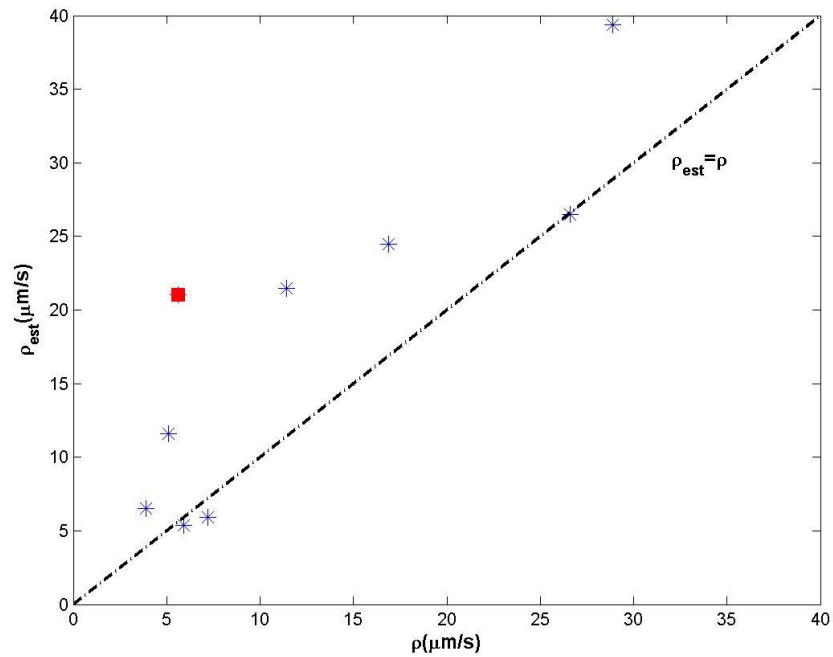


Figure 5.19 - Relaxivities from non-linear regression as function of expected ones, for $r = 0.8$.
Source: By the author.

Similar to what was observed in the simulations, this procedure in general overestimates relaxivities. The reason can be twofold: 1) as already discussed, this data is acquired near the limit of applicability of approximation $D_{rest} \approx D_{simp}$. Therefore, during the fit, D_{simp} will try to reproduce the transition from small to big pores limit. In Figure 5.9, this is analogous to trying to use the blue curve (D_{simp}) to reproduce the black one (D_{rest}), in a region where they are not alike. The least mean squared error solution is then to increase both D_0 and the steepness of the curve, by increasing ρ . 2) The algorithm might stop at a local minimum before reaching the correct parameter values.

For sample 8, marked as a red square in Figure 5.19, estimated relaxivity was four times bigger than the expected value, more than any other sample. However, for this sample, $T_{2c} = \sqrt{D_0^{expected} \Delta_{RMS} / (r \rho^{expected})} \sim 1s$, and observation of T_2 distributions in figure 18h shows that all its relaxation times are way below this value. Therefore an abnormal overestimation is expected. In fact, Figure 5.20 shows a correlation between $\rho^{estimated} / \rho^{expected}$, and the ratio T_{2max} / T_{2c} , T_{2max} being the point of maximum of the T_2 distribution. As most of the data becomes smaller than T_{2c} , overestimation tends to increase.

Ignoring sample 8, Figure 5.19 shows that the estimated relaxivities are compatible with the expected ones, and can even separate the samples into groups of small and high values. In the well site, this information can solve some pitfalls in the formation evaluation based only on T_2 distributions, as distributions with long times can correspond to low permeability reservoirs, if relaxivity is small, for example.

Although we cannot translate the results of this section directly to the well because of the differences in acquisition scheme and validity region (regard $\sqrt{D_0 \Delta} / (\rho T_2) \sim 1$ in our acquisitions), the laboratory showed that this approach is indeed sensitive to rock core relaxivities.

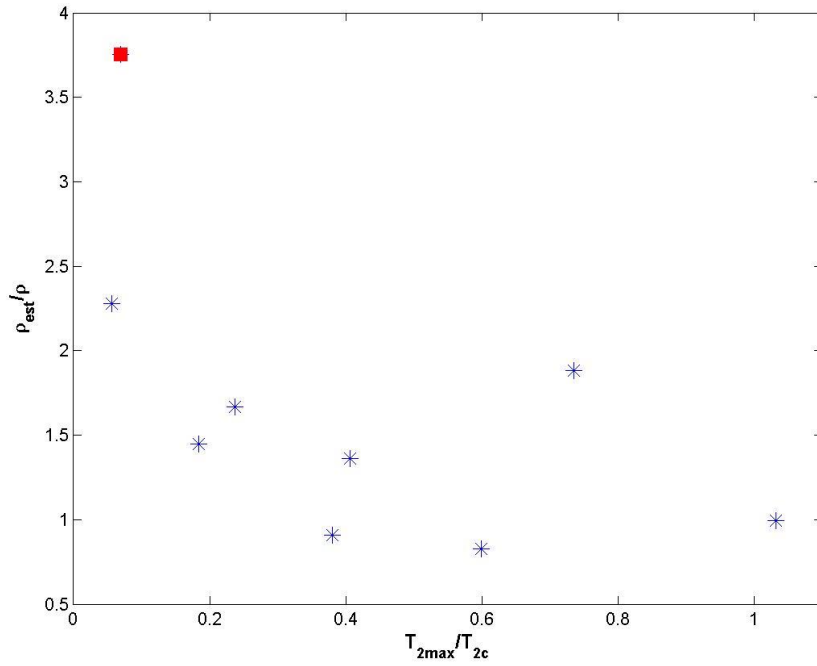


Figure 5.20 - $\rho^{estimated}/\rho^{expected}$ as a function of T_{2max}/T_{2c} , for all samples.
Source: By the author.

5.5 Well Logging Experimental Results

In this section we show the application of the relaxivity non-linear regression method to a well log acquired data. Data corresponds to a diffusion editing experiment made downhole in a sandstone reservoir from Petrobras, using a tool with broad gradient distribution represented by Figure 3.18. The well was drilled using water based mud, which implies that the tool should read a region in the formation saturated with original water/oil, and invaded water. As we are dealing with a sandstone reservoir (which tends to be water wet), it is expected that invaded water occupies the bigger pores, remaining oil being in the smaller ones.

Four echotrails were acquired, with first interecho time $T_D = 2, 4, 8$ and $10ms$, and small interecho time T_E being equal to $0.2ms$. In this specific acquisition, the tool stopped at the target area and acquired the data for about 30 minutes, to guarantee good SNR. For well logging, diffusion editing sequence acquires two first echoes with longer time interval between π pulses, yielding two consecutive applications of the diffusion exponential part of the inversion kernel in equation (5.11). Therefore, the kernel must be modified with the substitution

$$\exp\left\{-\frac{(\gamma G)^2(T_D^\eta)^3}{12}D_{simp}(T_D^\eta/2, T_2)\right\} \rightarrow \int dG g(G) \exp\left\{-\frac{(\gamma G)^2(T_D^\eta)^3}{6}D_{simp}(T_D^\eta/$$

$2, T_2\}$, $g(G)$ taking into account the broad gradient distribution of Figure 3.18. Data is shown in Figure 5.21, along with T_2 distributions.

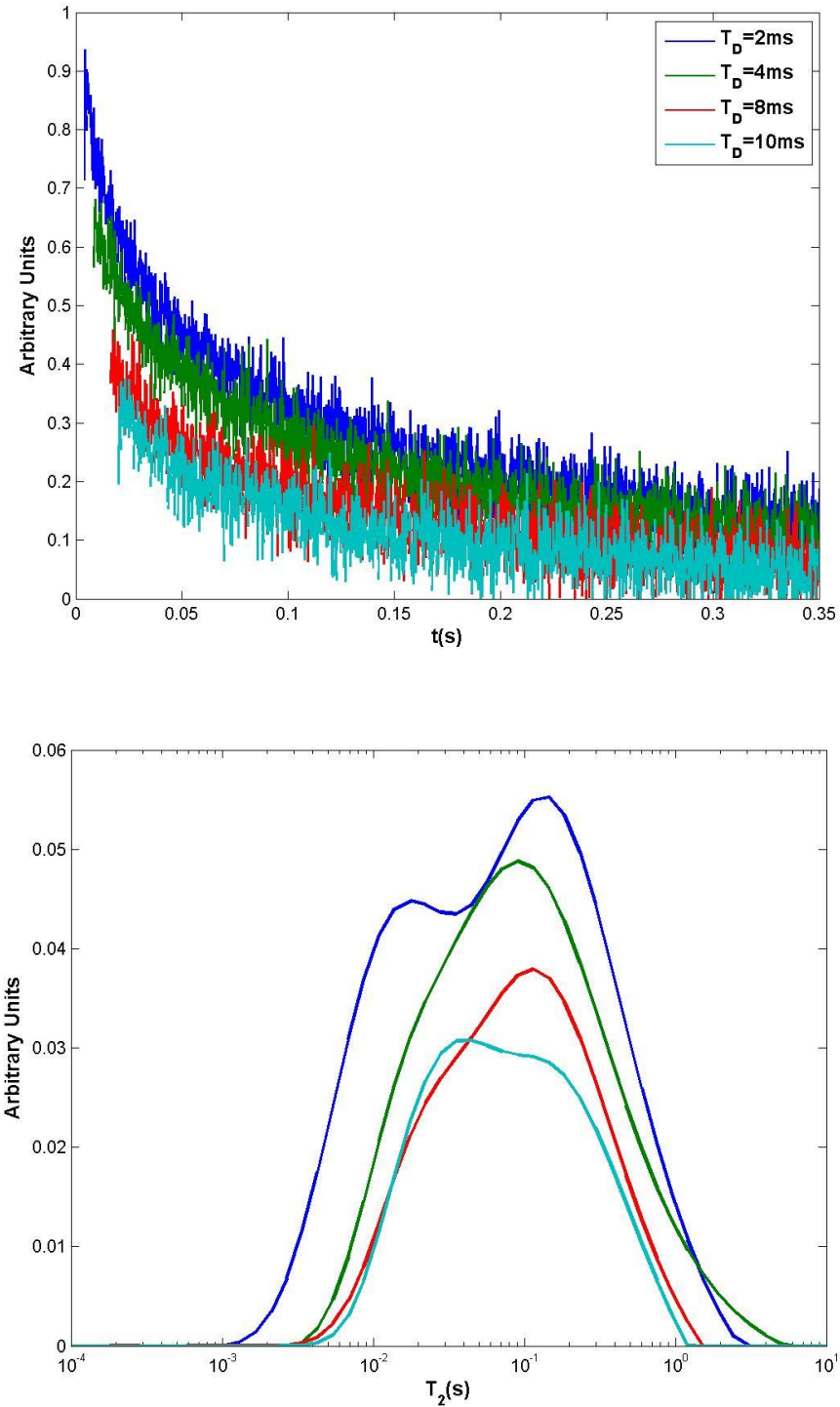


Figure 5.21 - a) Well logging diffusion editing acquisition and b) corresponding T_2 distributions.
Source: By the author.

The standard interpretation using the DT_2 inversion is reproduced from an internal Petrobras report in Figure 5.22.

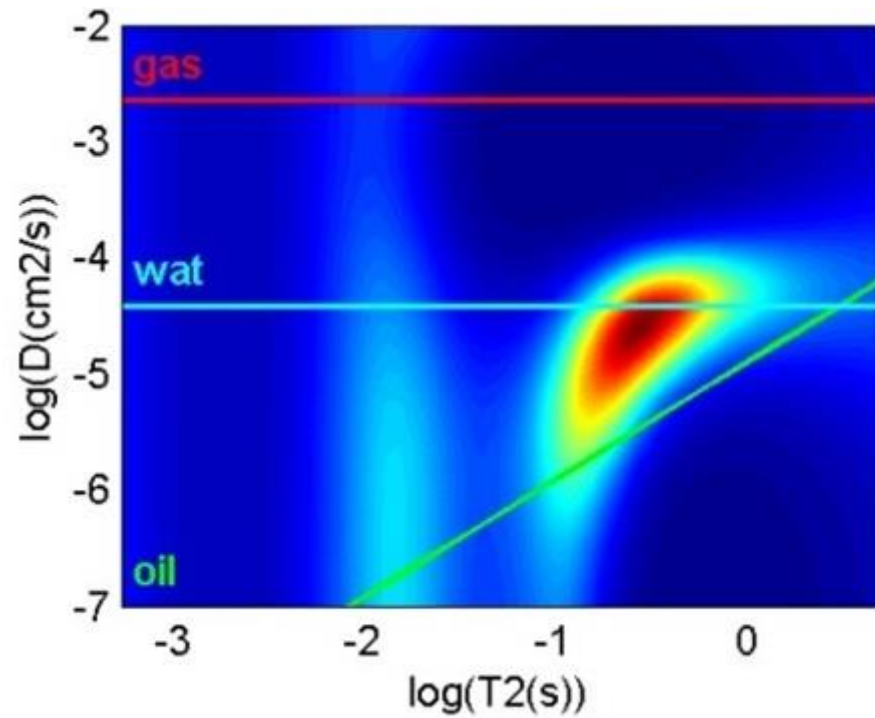


Figure 5.22 - DT_2 map for well logging diffusion editing data.
Source: Provided by Petrobras.

The peak near $10^{-2}s$ reveals a fluid with diffusion coefficient one to two orders of magnitude smaller than water's, corresponding to a heavy oil. Consequently, the signal appearing from 0.1 to 1s should correspond to water in the bigger pores.

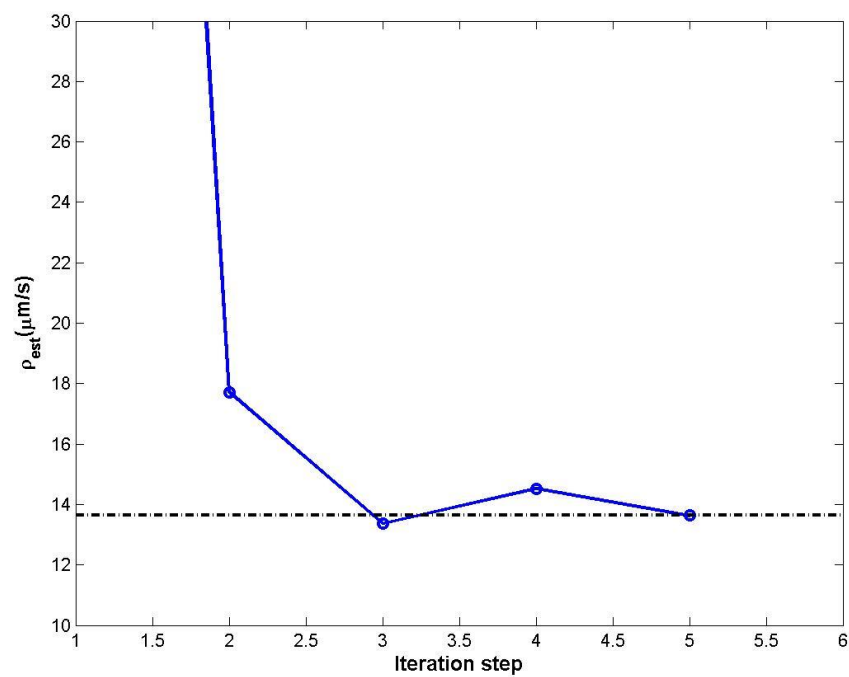


Figure 5.23 - Relaxivity iteration steps for well logging diffusion editing data.
Source: By the author.

Application of the non-linear regression yields after few iterations (shown in Figure 5.23) a relaxivity value of $\rho \approx 14\mu m/s$, which is a reasonable value for this kind of rock. Sandstones are expected to have higher surface relaxivities ($> 10\mu m/s$), specially because of clay minerals that might accumulate at the grain surfaces. The estimated limiting value for validity of D_{simp} is then $\sim 0.13s$, meaning that the algorithm automatically discarded any data below this time value in computing relaxivity. From the diffusion map in Figure 5.22, one can see that the oil signal was ignored, as well as the steepest part of water signal. This result shows that the method has potential to be applied even if the reservoir is saturated with multiple fluids, as long as oil and water signals are resolved in the T_2 dimension. This is not true for oil base muds, as the oil filtrate is usually extremely light with diffusion coefficient and bulk T_2 close to water values.

6 ANALYTICAL APPROXIMATIONS FOR DIFFUSION IN POROUS MEDIA – DIGITAL ROCK

The main objective in analyzing a porous medium, regardless the physical technique used (NMR, resistivity, acoustic velocities), is to obtain or relate the measurements with its petrophysical properties, mainly porosity, permeability, or features that correlate with multiphase flow such as wettability. For this matter, a discussion on the time and space scales at which each phenomenon takes place is necessary.

Regarding NMR, from competition between diffusion time through a characteristic dimension a of a pore (a^2/D), and the surface relaxation time (ρ/a), emerges the correlation between magnetization decay times and pore geometry. If the ratio $\rho a/D$ is greater than one (slow diffusion limit where surface relaxation is dominant), magnetization carriers that reach the pore walls are “whipped out” of the system, and magnetization density $m(\vec{r}, t)$ assumes a spatial distribution much governed by the pore borders. In this scenario, total magnetization is expressed in terms of diffusional normal modes expressed in equation 3 – 38, with correspondent relaxation times carrying a detailed information of the pore geometry. On the other hand, in the fast diffusion limit each molecule has enough time to travel throughout all the pore space before losing coherence relative to the others. Therefore, relaxation times do not carry geometry information more detailed than the average surface per volume ratio.

Another example present in this work up to this point is the observation of restricted diffusion. In Chapter 5 we saw that the effects could be observed if the particles were allowed to move through diffusion no more than the characteristic pore length. Also, the time at which this displacement takes place should be compatible to the surface relaxation in such a way that there were still coherent spins to be measured. For much longer times one particle could be able to travel through several different small pores, in a way that diffusion could be represented by a single restricted diffusion coefficient that does not depend on relaxivity anymore.

Consider the following scheme of a pore system, that could come from a rock’s thin section, a detailed micro tomography scan or another conceivable imaging technique.

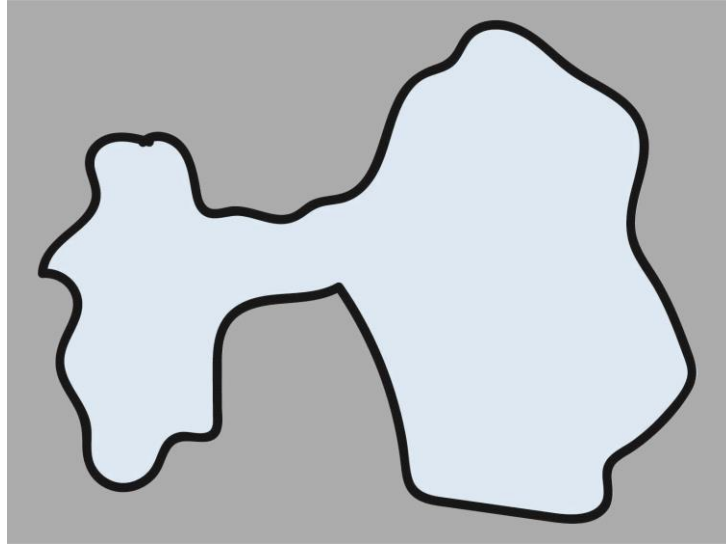


Figure 6.1 - Schematics of a pore system.
Source: By the author.

It is natural for the human eye to identify and subdivide this image in three important regions. A big pore, a small one and a throat connecting both. Any model based on this subdivision will only succeed in explaining a physical property, if the latter scales in the same way as the image. Flow properties, for example, are mainly controlled by capillary forces, which vary with the transverse area of the system. Therefore a permeability model coming from Figure 6.1 with this natural segmentation might obtain consistent results, as the subdivision directly enhances the region that dominates the flow capacity (throat).

However, that same porous medium might generate an NMR signal that brings a different classification for the system, even if always in the fast diffusion limit. If the two pores are poorly connected, one would see a clear division of two peaks in the T_2 distribution, with relaxation times corresponding to the pore sizes. In this scenario one sees the two pore classification in the NMR data, but does not have information on the throat. As the connection becomes stronger (even by increasing diffusion coefficient, throat size or decreasing relaxivity) the peaks will come closer to each other due to diffusional coupling (64-65), that is, a spin relaxing in one pore changes its relaxation time as it moves to another one. In this case one starts to lose information on the pores, but gains information on their connectivity. In the extreme scenario of even faster diffusion, the whole system will be seen as a single pore, with one relaxation time. On the other direction (towards slow diffusion limit) the system will also be seen as a single pore, but with an extremely detailed information on pore geometry encoded in complex diffusion-relaxation normal modes.

The following question emerges: how to treat the image data in a way that the dynamical processes are described with time and spatial scales compatible with NMR

relaxation? This question is part of a larger discipline that has been called by the petroleum industry as “Digital Rock”, and consists of obtaining all the physical or petrophysical properties based on images from rock cores (mainly micro tomography). This is an important matter as such images offer complementary geological description of the rocks, as well as detailed spatial information that allow in principle physical information to be obtained.

In this Chapter we develop one possible solution for this question, describing the system in terms of a rate equation between almost arbitrary subdivisions (cells) of the pores. This formulation is compatible with the diffusion equation, therefore reproducing NMR data. Also, the obtained rate expressions (equation (6.21)) give an insightful way on how to create the cells themselves. We compare the approximation with analytical solutions.

6.1 Rate equations and transition rates

Consider the description of the pore system in terms of an arbitrary grid, as the one represented in Figure 6.2.

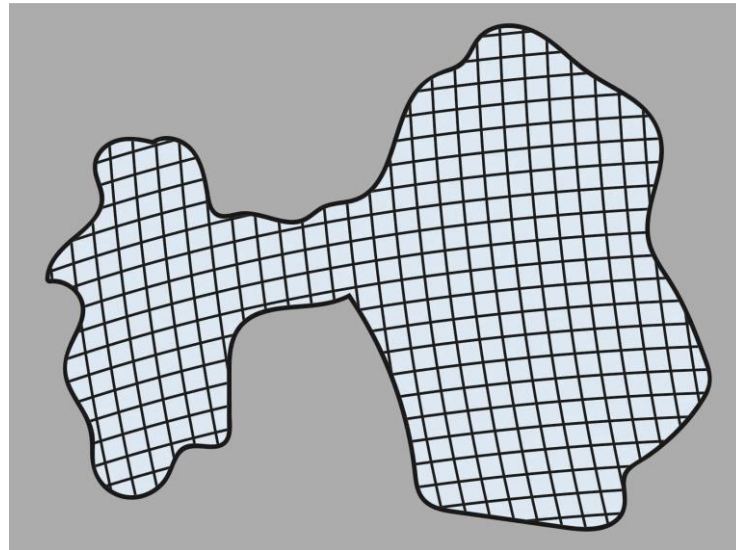


Figure 6.2 - Grid subdivision of a schematic pore system.
Source: By the author.

The dynamics of diffusion can be described in a random walk fashion of particles carrying magnetization from cell to cell. Let p_n be the total number of “magnetization particles” within the n th cell. Its variation in time can be described by a rate equation below:

$$\frac{dp_n}{dt} = \sum_k \lambda_{kn} p_k - \sum_k \lambda_{nk} p_n \quad (6.1)$$

The rates λ_{nm} have a precise interpretation in the master equation formulation (or microscopically in a Markov random walk process). $\lambda_{nm} \Delta t$ is the probability that within a

time interval Δt , one particle randomly placed within any part of cell n , jumps to a neighbor cell m . The total number of particles that make this transition from t to $t + \Delta t$ is then $\lambda_{nm}p_n(t)\Delta t$. Consequently, the first sum in equation (6.1) represents the total particle flow towards cell n , and the second sum the total particle flow outwards that cell. Writing equation (6.1) in vector form yields

$$\frac{d}{dt}\vec{p} = \mathbf{\Lambda}\vec{p} \quad (6.2)$$

Matrix $\mathbf{\Lambda}$ is composed by all transition rates. With the initial condition that magnetization is created uniformly through all space at $t = 0$, that is, $p_n(0) = (M_0/V)V_n$ (V_n is the volume of cell n and V is the total volume of the system), the solution of (6.2) becomes:

$$\vec{p}(t) = M_0 e^{\mathbf{\Lambda}t} (\vec{V}/V) \quad (6.3)$$

\vec{V} is the vector of cell volumes. If $\mathbf{\Lambda}$ can be diagonalized, then exists a matrix \mathbf{B} which columns are eigenvectors of $\mathbf{\Lambda}$, and a diagonal matrix \mathbf{D} of their eigenvalues such as $\mathbf{\Lambda} = \mathbf{B}\mathbf{D}\mathbf{B}^{-1}$. Total magnetization $M(t) = \sum_n p_n(t)$ then becomes:

$$M(t) = M_0 \sum_n C_n e^{-\beta_n t}, \quad C_n = \left(\sum_m B_{mn} \right) \left(\frac{\mathbf{B}^{-1}\vec{V}}{V} \right)_n \quad (6.4)$$

In expression (6.4) β_n is the n th eigenvalue of $\mathbf{\Lambda}$. This solution is formally identical to equation 3 – 38, which is the exact solution of the Bloch-Torrey equation (3 – 39 and 3 – 40) describing the NMR system. Therefore, the rate equation approach can in principle approximate the exact solution.

The only question that remains is how to calculate the rates λ_{nm} for the cells, in a manner that solution (6.4) approximates the exact one. More technically, we are searching for rate expressions that, when the dimension of cells tends to zero and their number tends to infinity, then equation (6.1) or (6.2) tends to the diffusion equation for the particle density $f(\vec{r}, t)$:

$$\begin{aligned} \frac{\partial f}{\partial t} &= D \nabla^2 f \\ (D \vec{\nabla} f + \rho f)_s &= 0 \end{aligned} \quad (6.5)$$

Another expected property for the rates is that they should depend on geometric features of the corresponding cell, specially their surface areas. Consider one cell from Figure 6.2:

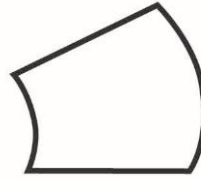


Figure 6.3 - Representation of a single cell in the pore system.
Source: By the author.

If a particle is randomly placed at any point within that cell, it is more likely that it jumps after a time Δt to a neighbor cell to the right, rather than each one of the neighbors in the other directions, for its surface area is the biggest one. Therefore rates must have an explicit dependence on cell areas.

Rate equation in a cubic grid

Starting with the simplest system, consider a cubic subdivision of the porous space in cells with volumes $\Delta V = \Delta x \Delta y \Delta z$, that are naturally described by the Cartesian coordinates (x, y, z) . We will omit two dimensions and consider only the x axis, as allowed by the symmetry of the coordinate system. Figure 6.4 shows the n th cell located at $x = n\Delta x$. It connects along the x dimension with two other cells, $n + 1$ to its right at $x + \Delta x$, and $n - 1$ to its left at $x - \Delta x$. Each particle located at this cell (between $x - \Delta x/2$ and $x + \Delta x/2$) has a probability per unit time $\lambda^+(x)$ to jump to the right, and $\lambda^-(x)$ to jump to the left.

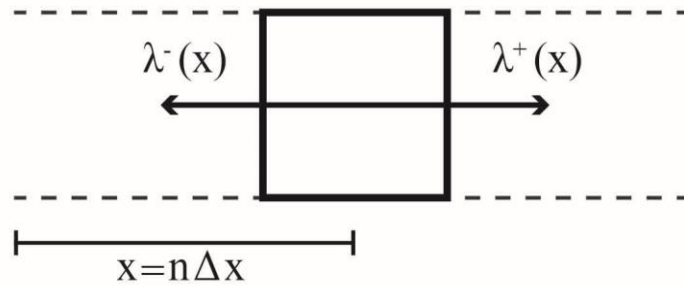


Figure 6.4 - Cubic cell represented along the x axis, located at $x = n\Delta x$.
Source: By the author.

Equation (6.1) then becomes:

$$\frac{dp_x}{dt} = \lambda^-(x + \Delta x)p_{x+\Delta x} - (\lambda^-(x) + \lambda^+(x))p_x + \lambda^+(x - \Delta x)p_{x-\Delta x} \quad (6.6)$$

The discreet nature of (6.6) is implicit in x , as $x = n\Delta x$. In terms of the particle density $f_x(t)$, defined as $p_x = f_x \Delta x \Delta y \Delta z$, one has simply:

$$\frac{df_x}{dt} = \lambda^-(x + \Delta x)f_{x+\Delta x} - (\lambda^-(x) + \lambda^+(x))f_x + \lambda^+(x - \Delta x)f_{x-\Delta x} \quad (6.7)$$

There is no geometrical reason to assume that the rates to the right and to the left should be different. In fact, by making $\lambda^+(x) = \lambda^-(x) = D/(\Delta x)^2$, one promptly gets:

$$\frac{df_x}{dt} = D \left(\frac{f_{x+\Delta x} - 2f_x + f_{x-\Delta x}}{(\Delta x)^2} \right) \quad (6.8)$$

In the continuum limit, as $\Delta x \rightarrow 0$ and $n \rightarrow \infty$, with $n\Delta x \rightarrow x$, equation (6.8) reproduces the diffusion equation.

$$\frac{\partial f}{\partial t} = D \frac{\partial^2 f}{\partial x^2} \quad (6.9)$$

From this simplest case, we can learn that the time scale for the rates is given by the ratio between diffusion coefficient and the square of a characteristic length throughout the cell, which is already expected for a diffusion process. However, nothing can be said about the dependence on surface areas for the cells, as in this example they are all the same.

Rate equation in a spherical grid

In order to extract a surface dependency on the rates, we will proceed to a more complex subdivision of cells, in which each one of them has some inner structure. Consider a subdivision of the pore space in a grid that matches the spherical coordinate system, where each cell is located by the radial, azimuthal and polar coordinates (r, θ, ϕ) , and has a volume $\Delta V = r^2 \sin(\theta) \Delta r \Delta \theta \Delta \phi$.

In this scenario, whatever rate expressions we find, at the continuum limit the master equation (6.1) must lead to:

$$\frac{\partial f}{\partial t} = D \left(\frac{\partial^2 f}{\partial r^2} + \frac{2}{r} \frac{\partial f}{\partial r} \right) + \frac{D}{r^2} \left(\frac{\partial^2 f}{\partial \theta^2} + \frac{\cos(\theta)}{\sin(\theta)} \frac{\partial f}{\partial \theta} \right) + \frac{D}{r^2 \sin^2(\theta)} \frac{\partial^2 f}{\partial \phi^2} \quad (6.10)$$

Figure 6.5 shows the scheme of one cell (focused on the r coordinate).

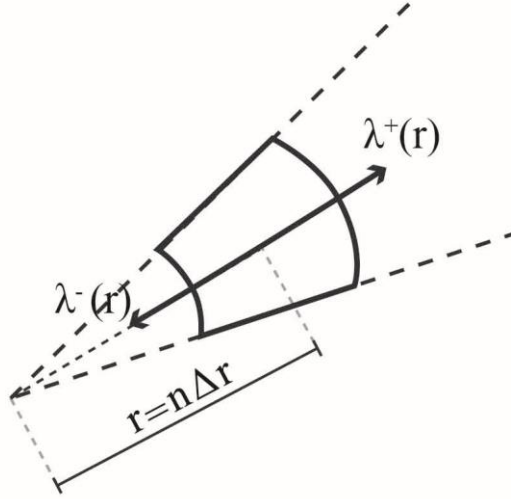


Figure 6.5 - Spherical cell located at $\mathbf{r} = n\Delta\mathbf{r}$, $\theta = m\Delta\theta$ and $\phi = l\Delta\phi$, focused mainly on the r dimension.
Source: By the author.

From Figure 6.5 representation, it can be seen that the most external area (along the r axis) is bigger than the inner one. Therefore we should expect that the rates $\lambda^\pm(r)$ must have a general time dependence governed by $D/(\Delta r)^2$, along with some correction dependent on the areas. Considering only the r coordinate, the rate equation is written similarly to (6.6):

$$\frac{dp_r}{dt} = \lambda^-(r + \Delta r)p_{r+\Delta r} - (\lambda^-(r) + \lambda^+(r))p_r + \lambda^+(r - \Delta r)p_{r-\Delta r} \quad (6.11)$$

Particle density is now given by $p_r = f_r r^2 \sin(\theta) \Delta r \Delta \theta \Delta \phi$, so that equation (6.11) leads to:

$$\begin{aligned} \frac{df_r}{dt} = & \lambda^-(r + \Delta r) \frac{(r + \Delta r)^2}{r^2} f_{r+\Delta r} + \lambda^+(r - \Delta r) \frac{(r - \Delta r)^2}{r^2} f_{r-\Delta r} \\ & - (\lambda^-(r) + \lambda^+(r)) f_r \end{aligned} \quad (6.12)$$

If we chose the rates the same way it worked out for the cubic grid, then we should have $\lambda^\pm(r) = D/(\Delta r)^2$, yielding in the continuum limit to:

$$\frac{\partial f}{\partial t} = \frac{D}{r^2} \frac{\partial^2}{\partial r^2} (r^2 f(r)) = D \frac{\partial^2 f}{\partial r^2} + \frac{4D}{r} \frac{\partial f}{\partial r} + \frac{2D}{r^2} f(r) \quad (6.13)$$

Equation (6.13) does not reproduce the radial part of the diffusion equation (6.10), as it was expected. Therefore, some modifications should be made on the rates. First, we will show that any expressions in the rates that are independent of Δr , or dependent on powers equal to or higher than Δr^1 , will make no contributions to the diffusion equation. In fact, by choosing $\lambda^\pm(r) = \lambda_0^\pm(r) + O(\Delta r)$, plugging it in equation (6.12) and expanding all the terms in powers of Δr , one would get:

$$\frac{df_r}{dt} = (\lambda_0^-(r) - \lambda_0^+(r))(f_r - f_r) + O(\Delta r) \quad (6.14)$$

The first term of (6.14) is already zero, and the other one tends to zero in the continuum limit. Therefore, the rates must have the following form:

$$\lambda^\pm(r) = \frac{D}{(\Delta r)^2} + D \frac{\lambda_1^\pm(r)}{\Delta r} \quad (6.15)$$

Solution (6.15) is not unique, as any other function independent of Δr that is added to that one, or expandable on positive powers of Δr , will produce the same results in the continuum limit.

By plugging in equation (6.15) into expression (6.12) one finally gets as $\Delta r \rightarrow 0$ and $n \rightarrow \infty$ with $n\Delta r \rightarrow r$:

$$\frac{\partial f}{\partial t} = D \frac{\partial^2 f}{\partial r^2} + \frac{2D}{r} \frac{\partial f}{\partial r} \left(2 - \frac{r}{2} (\lambda_1^+ - \lambda_1^-) \right) + \frac{Df(r)}{r^2} \left(2 - \frac{\partial}{\partial r} \{ r^2 (\lambda_1^+ - \lambda_1^-) \} \right) \quad (6.16)$$

The choice $\lambda_1^+(r) - \lambda_1^-(r) = 2/r$ turns equation (6.16) directly into the radial part of the diffusion equation (6.10).

The final information needed to determine expression (6.15) completely, lies within the following question. If one asked for the probability that a particle initially in cell n , was found outside of it, regardless of which wall it had gone through, the answer should be dependent only on the time scale defined by $D/(\Delta r)^2$, and not on the details of the walls.

Therefore, $\lambda^+ + \lambda^- = \frac{2D}{\Delta r} \Rightarrow \lambda_1^+ + \lambda_1^- = 0$.

These two equations combine to give $\lambda_1^\pm(r) = \pm 1/r$, which yields:

$$\lambda^\pm(r) = \frac{D}{(\Delta r)^2} \left(1 \pm \frac{\Delta r}{r} \right) \quad (6.17)$$

As expected, the rates are mainly controlled by the time scale of diffusion, corrected by a geometrical factor which is greater than one for the bigger surface, and smaller than one for the other.

The external surface of Figure 6.5 (in the radial direction) has an area of $A^+ = \left(r + \frac{\Delta r}{2} \right)^2 \sin(\theta) \Delta\theta \Delta\phi$, while the internal one has area $A^- = \left(r - \frac{\Delta r}{2} \right)^2 \sin(\theta) \Delta\theta \Delta\phi$.

Therefore, the following relation holds:

$$\frac{A^+ - A^-}{A^+ + A^-} = \frac{(r + \Delta r/2)^2 - (r - \Delta r/2)^2}{(r + \Delta r/2)^2 + (r - \Delta r/2)^2} = \frac{\Delta r}{r} + O(\Delta r^2) \quad (6.18)$$

Therefore, correction $\Delta r/r$ equals the ratio between areas despite an additive term of order Δr^2 , that would generate on the rates expression a term independent of Δr , which as

discussed does not change the diffusion equation. It is then safe to replace $\frac{\Delta r}{r} \rightarrow \frac{A^+ - A^-}{A^+ + A^-}$ in expression (6.17):

$$\lambda^\pm(r) = \frac{D}{(\Delta r)^2} \frac{A^\pm}{\bar{A}}, \quad \bar{A} = \frac{A^+ + A^-}{2} \quad (6.19)$$

Expression (6.19) makes explicit the correction on the rates based on surface areas information. Adaptation of this equation to θ or ϕ coordinates could be made by replacing $\Delta r \rightarrow r\Delta\theta$ for the former, or $\Delta r \rightarrow r\sin(\theta)\Delta\phi$ for the latter. However, in order to make the rates completely independent of the coordinate system, consider the ratio $\bar{A}/\Delta V$:

$$\left(\frac{\bar{A}}{\Delta V}\right)^2 = \left\{ \frac{\left(r + \frac{\Delta r}{2}\right)^2 + \left(r - \frac{\Delta r}{2}\right)^2}{2} \cdot \frac{1}{r^2 \Delta r} \right\}^2 = \frac{1}{(\Delta r)^2} (1 + O(\Delta r^2)) \quad (6.20)$$

Again, the diffusion equation does not change by replacing $1/\Delta r \rightarrow \bar{A}/\Delta V$, and the rate expression finally becomes dependent only on the geometrical features of the cell:

$$\lambda^\pm = D \frac{\bar{A}}{\Delta V^2} A^\pm \quad (6.21)$$

We can check expression (6.21) for the other coordinates, θ and ϕ . Consider the cell in Figure 6.5, but now from the point of view of the azimuthal coordinate, ignoring r and ϕ .

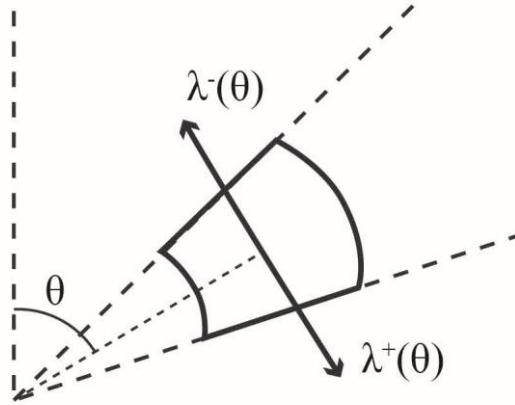


Figure 6.6 - Spherical cell located at $r=n\Delta r$, $\theta=m\Delta\theta$ and $\phi=l\Delta\phi$, focused mainly on the θ dimension.
Source: By the author.

The surface areas can now be written as $A^\pm = r\sin(\theta \pm \Delta\theta/2)\Delta r\Delta\phi$. The master equation for particle densities now becomes (analogous to expression (6.12) for the r part):

$$\begin{aligned} \frac{df_\theta}{dt} = & \lambda^-(\theta + \Delta\theta) \frac{\sin(\theta + \Delta\theta)}{\sin(\theta)} f_{\theta+\Delta\theta} + \lambda^+(\theta - \Delta\theta) \frac{\sin(\theta - \Delta\theta)}{\sin(\theta)} f_{\theta-\Delta\theta} \\ & - (\lambda^-(\theta) + \lambda^+(\theta)) f_\theta \end{aligned} \quad (6.22)$$

Expanding expression (6.21) up to the appropriated power of $\Delta\theta$ yields:

$$\lambda^\pm(\theta) = \frac{D}{r^2 \Delta\theta^2} \left(1 \pm \frac{\cos(\theta)}{2\sin(\theta)} \Delta\theta \right) \quad (6.23)$$

By substituting expression (6.23) into equation (6.22) and taking the continuum limit one gets:

$$\begin{aligned} \frac{\partial f}{\partial t} &= \frac{D}{r^2 \sin(\theta)} \left\{ \frac{\partial^2}{\partial \theta^2} (\sin(\theta) f(\theta)) - \frac{\partial}{\partial \theta} (\cos(\theta) f(\theta)) \right\} \\ &= \frac{D}{r^2} \left(\frac{\partial^2 f}{\partial \theta^2} + \frac{\cos(\theta)}{\sin(\theta)} \frac{\partial f}{\partial \theta} \right), \end{aligned} \quad (6.24)$$

which is exactly the θ part of the diffusion equation (6.10).

For the polar ϕ coordinate verification is much simpler, as $A^\pm = r\Delta r\Delta\theta$, and the continuum limit goes similarly as the cubic grid, yielding $\frac{\partial f}{\partial t} = \frac{D}{r^2 \sin^2(\theta)} \frac{\partial^2 f}{\partial \phi^2}$.

Detailed Balance

Expression (6.21) for the rates only guarantees that the correct diffusion equation is obtained when the physical dimensions of the cells approach zero. It does not ensure that the error in the macroscopic approach with the master equation will remain tolerable whatever cell size one has. However, one can always build the cells in accordance with the detailed balance principle, in order to obtain physical correct answers.

When the diffusional system is in equilibrium, the particle density in each cell is the same for the whole pore, and cannot vary in time anymore (ignoring losses at the walls through surface relaxativity). As a consequence, any particle flux outwards a cell must be compensated by an equal influx coming from the neighboring cells. The detailed balance principle states that this compensation must happen for each pair of cells, throughout all pairs. It is reasonable to assume that this holds for our system as there is an infinite number of possible arbitrary subdivision of space.

Considering two neighbor cells, 1 and 2, connected by a common surface of area A , detailed balance implies that:

$$\Delta V_1 \frac{D\bar{A}_1}{\Delta V_1^2} A = \Delta V_2 \frac{D\bar{A}_2}{\Delta V_2^2} A \Rightarrow \frac{\bar{A}_1}{\Delta V_1} = \frac{\bar{A}_2}{\Delta V_2} \quad (6.25)$$

Therefore, the “characteristic length” (more precisely the volume per mean surface) must be the same throughout all the cells. One is not obliged to follow this constraint in building the grid, as they can always make the cells small enough so that expression (6.21)

holds. However, there are some cases shown further in this chapter in which detailed balance proved to be advantageous.

Surface losses

In order to complete the master equation approach (6.1) to the NMR diffusion within a pore, one must calculate the magnetization loss rate when a cell is in contact with a pore wall. From diffusion theory, the amount of magnetization per unit time that hits a transverse unit area is given by the density current vector $\vec{J} = D\vec{\nabla}f$, f being the magnetization density. However, at the pore wall vector \vec{J} is promptly determined by the contour condition of equation (6.5). Therefore, magnetization rate loss through a pore wall of area S_n , in a cell n is given by $\frac{dp_n}{dt} = \int_{S_n} \vec{J} \cdot \hat{n} da = -\rho \int_{S_n} f_n da = -\rho S_n f_n = -\rho \frac{S_n}{\Delta V_n} p_n$. Loss rate through a pore wall in cell n is then given by:

$$\lambda_n^S = \rho \frac{S_n}{\Delta V_n} \quad (6.26)$$

Master equation can then be rewritten to make the losses explicit:

$$\frac{dp_n}{dt} = \sum_k \lambda_{kn} p_k - \sum_k \lambda_{nk} p_n - \lambda_n^S p_n, \quad (6.27)$$

where the λ_{ij} are given by expression (6.21) and λ_n^S by (6.26).

If one sums equation (6.27) through all cells, total magnetization $M(t) = \sum_n p_n(t)$ evolution becomes:

$$\frac{dM}{dt} = - \sum_n \lambda_n^S p_n \quad (6.28)$$

If the system is in the fast diffusion limit, the density becomes uniform throughout all pore space. In that condition, $\lambda_n^S p_n = \rho S_n (p_n / \Delta V_n) = \rho S_n (M / V)$, V being the total pore volume. Equation (6.28) then becomes $\frac{dM}{dt} = -\rho \frac{(\sum_n S_n)}{V} M = -\rho \frac{S}{V} M$, giving as solution:

$$M(t) = M_0 e^{-\rho \frac{S}{V} t}, \text{ which is the exact solution in the fast diffusion limit.}$$

Therefore, the master equation approach (6.27) not only gives the correct solution in general (expression (6.4)), but also the fast diffusion approximation.

6.2 Comparison with exact solutions

Master equation approach in a sphere

Consider a spherical pore of radius a . The exact solution of (6.5) for total magnetization is then given by:

$$M(t) = \sum_n I_n e^{-\frac{t}{T_{2n}}}$$

$$\frac{1}{T_{2n}} = \frac{D}{a^2} \xi_n^2 \quad (6.29)$$

$$I_n = 3 \frac{\left(\int_0^1 u^2 \psi_n(u) du \right)^2}{\int_0^1 u^2 \psi_n^2(u) du}$$

The eigenfunctions ψ_n are given by $\psi_n(u) = \frac{\sin(\xi_n u)}{\xi_n u}$, and the ξ_n are roots of:

$$\cos(\xi_n) + \left(\frac{\rho a}{D} - 1 \right) \sin(\xi_n) = 0 \quad (6.30)$$

The master equation approach can be applied by dividing the pore in terms of N spherical surfaces of radii r_i , with the last one being $r_N = a$, as represented in Figure 6.7. They can be calculated in a way that the resulting cells (spherical shells) respect the detailed balance principle.

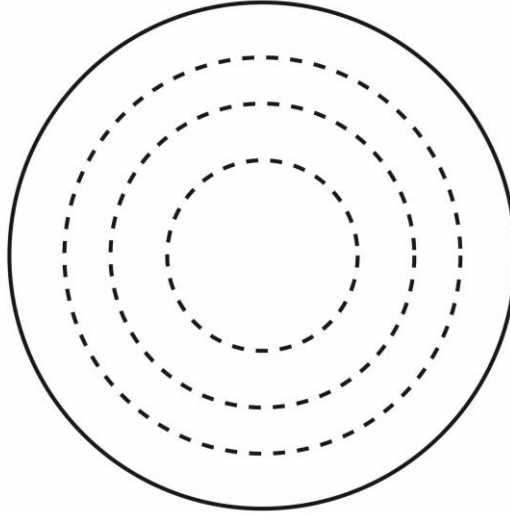


Figure 6.7 - Example of cell subdivision in a spherical pore.
Source: By the author.

The surface areas are given by $A_i = 4\pi r_i^2$, cell volumes being $\Delta V_i = \frac{4\pi}{3} (r_i^3 - r_{i-1}^3)$, except for the first one which is just $\Delta V_1 = \frac{4\pi}{3} r_1^3$. For the 2nd up to the $(N - 1)th$ shell, the rates can be calculated as:

$$\begin{aligned}\bar{A}_i &= \frac{A_i + A_{i-1}}{2} \\ \lambda_i^+ &= \frac{D\bar{A}_i A_i}{\Delta V_i^2}, \quad \lambda_i^- = \frac{D\bar{A}_i A_{i-1}}{\Delta V_i^2}\end{aligned}\tag{6.31}$$

The extremal ones are:

$$\begin{aligned}\lambda_1^+ &= \frac{DA_1^2}{\Delta V_1^2}, \quad \lambda_1^- = 0 \\ \lambda_N^+ &= \lambda_N^S = \frac{\rho A_N}{\Delta V_N}, \quad \lambda_N^- = \frac{DA_N^2}{\Delta V_N^2}\end{aligned}\tag{6.32}$$

Matrix $\mathbf{\Lambda}$ in expression (6.2) can then be calculated as:

$$\mathbf{\Lambda} = \begin{pmatrix} -(\lambda_1^+ + \lambda_1^-) & \lambda_2^- & 0 & & & \\ \lambda_1^+ & -(\lambda_2^+ + \lambda_2^-) & \lambda_3^- & & & 0 \\ 0 & \lambda_2^+ & \ddots & & & \\ & & \ddots & \lambda_{N-1}^- & 0 & \\ & 0 & \lambda_{N-2}^+ & -(\lambda_{N-1}^+ + \lambda_{N-1}^-) & \lambda_N^- & \\ & & 0 & \lambda_{N-1}^+ & -(\lambda_N^+ + \lambda_N^-) & \end{pmatrix}\tag{6.33}$$

Solution through the master equation approach can then be calculated as in expression (6.4).

Considering a sphere of radius $a = 10\mu m$, $D = 2.3 \cdot 10^{-9} m^2/s$, the fast diffusion limit with $\rho a/D = 0.1$, using $N = 4$ cells, the resulting amplitudes of the normal modes and corresponding relaxation times are shown by the red star dots in Figure 6.8. The black circles correspond to the exact solution (6.29).

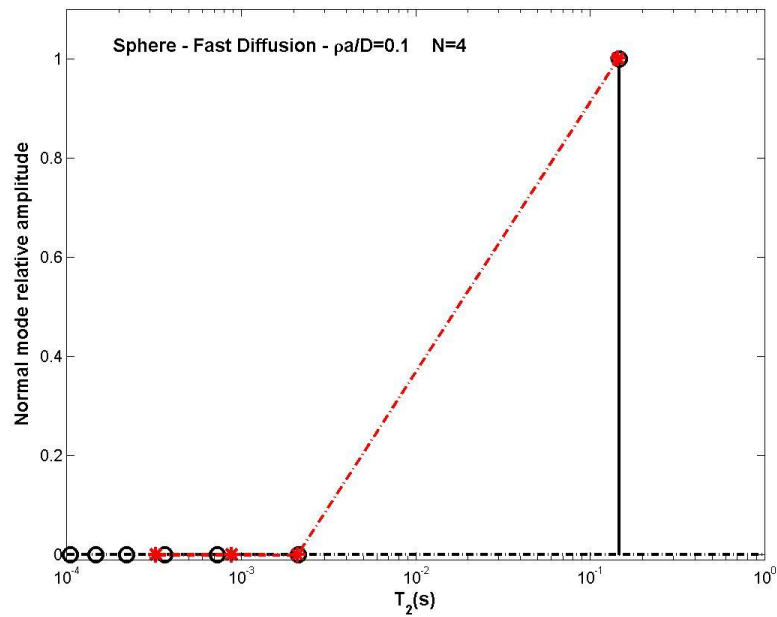


Figure 6.8 - Comparison between exact solution (black circles) and master equation approach (red star dots) for normal modes and relaxation rates in a sphere of radius $a = 10\mu\text{m}$ in the fast diffusion limit, using 4 cells.

Source: By the author.

Figure 6.8 shows that the master equation solution correctly reproduces the exact one. If detailed balance were not used in building the cells, the same level of accuracy would be achieved using about 15 cells. The results for the slow diffusion limit with $\rho a/D = 10$ are shown in Figure 6.9.

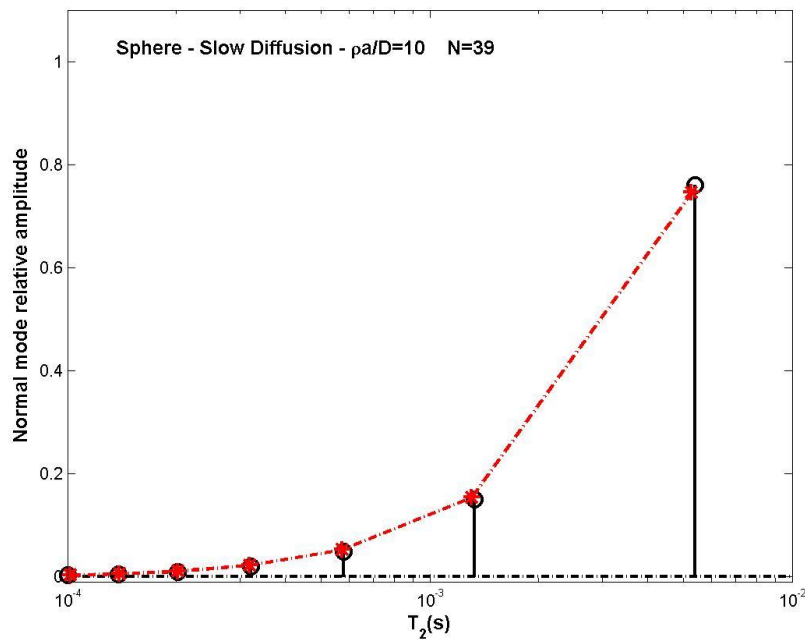


Figure 6.9 - Comparison between exact solution (black circles) and master equation approach (red star dots) for normal modes and relaxation rates in a sphere of radius $a = 10\mu\text{m}$ in the slow diffusion limit, using 39 cells.

Source: By the author.

Master equation approach in a cube

As a second example of application, consider a cubic pore of side $a = 10\mu m$. In this case, the exact solution for magnetization is given by (analogous to expressions (6.29) and (6.30)):

$$M(t) = \sum_{nml} I_n I_m I_l e^{-\frac{t}{T_{nml}}}$$

$$\frac{1}{T_{nml}} = \frac{D}{a^2} (\xi_n^2 + \xi_m^2 + \xi_l^2)$$

$$I_n = \frac{\left(\int_0^1 \psi_n(u) du \right)^2}{\int_0^1 \psi_n^2(u) du}$$
(6.34)

The eigenfunctions ψ_n are given by $\psi_n(u) = \cos(\xi_n u) + \frac{\rho a}{D} \frac{\sin(\xi_n u)}{\xi_n}$, and the ξ_n are roots of:

$$\left(\left(\frac{\rho a}{D} \right)^2 - \xi_n^2 \right) \sin(\xi_n) + 2 \frac{\rho a}{D} \xi_n \cos(\xi_n) = 0$$
(6.35)

It is natural to try following the pore symmetry by building the cells in this case using N concentric cubes of side L_i , with $L_N = a$, as shown in Figure 6.10. Again the lengths L_i can be calculated in a way that respects detailed balance principle.

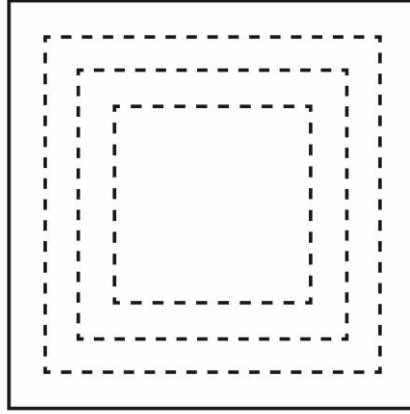


Figure 6.10 - Attempt of cell subdivision in a cubic pore.
Source: By the author.

The rates and rate matrix $\mathbf{\Lambda}$ have the exact same expressions as (6.31), (6.32) and (6.33), except that the areas and volumes are now calculated as $A_i = 6L_i^2$ and $\Delta V_i = L_i^3 - L_{i-1}^3$, with $\Delta V_1 = L_1^3$. The results for fast and slow diffusion limits are shown in Figure 6.11.

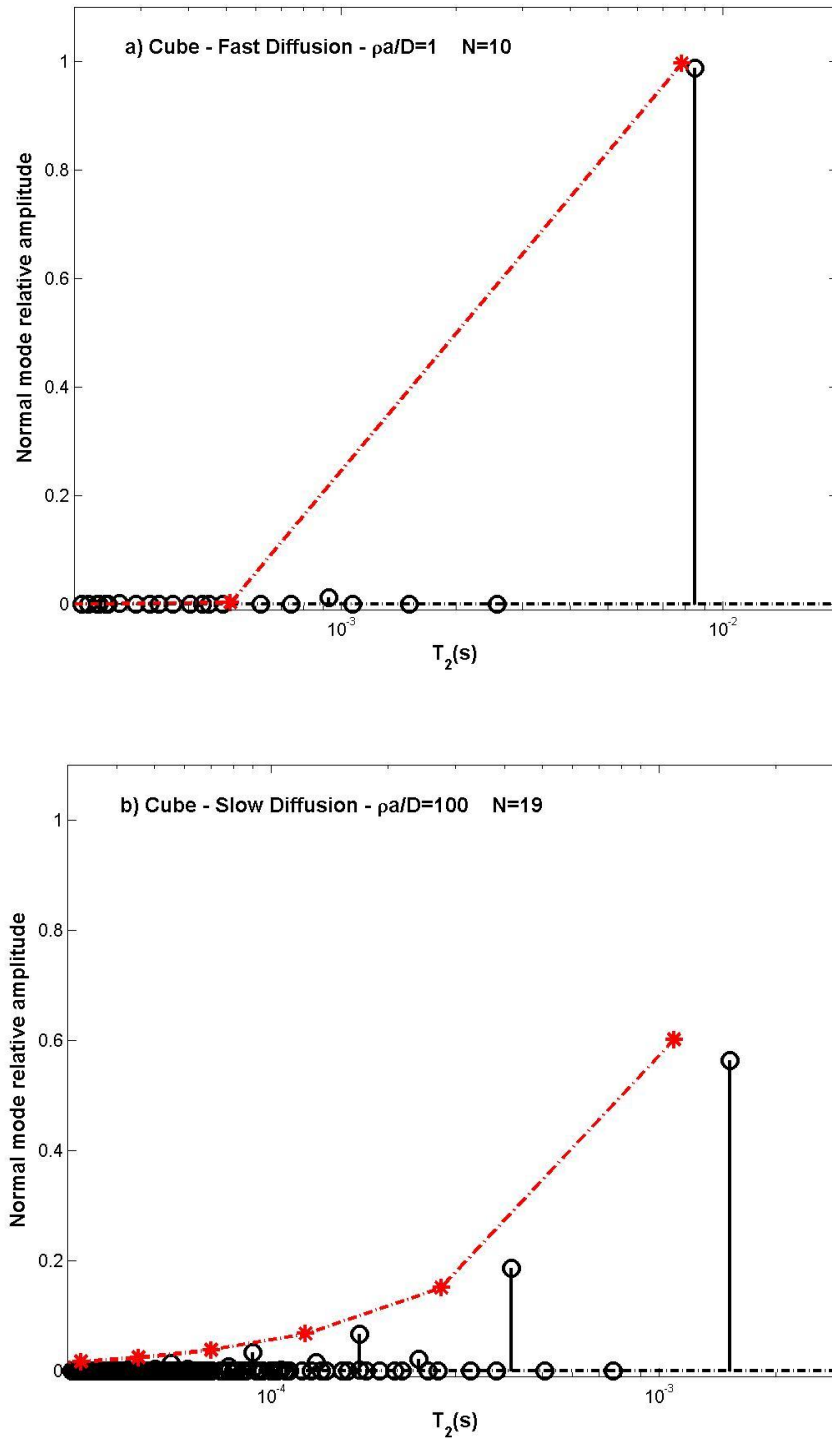


Figure 6.11 - Comparison between exact solution (black circles) and master equation approach (red star dots) for normal modes and relaxation rates in a cube of side $a = 10\mu\text{m}$ in the a) fast diffusion limit with 10 cells and b) slow diffusion limit with 19 cells.

Source: By the author.

Although the fast diffusion limit can be reproduced reasonably well, in the slow diffusion case the relaxation times are all severely underestimated. When we subdivided the pore space in a set of cubic concentric shells, we implicitly imposed over the system a

symmetry constraint that is not completely natural to it. In fact, like it was discussed in the introduction of this Chapter, magnetization density spatial distribution will be much governed by the shape of the pore, a cube in this case. It is then expected that magnetization density would follow a cubic spatial distribution nearby the pore walls. However, as one moves away from every wall (towards the center in this geometry), it is expected that physically the pore effects become less and less important, and magnetization spatial distribution becomes closer to that of free space, that is, a sphere. It is precisely this symmetry (near the center) that is not been respected by the cell scheme of Figure 6.10. A much more natural subdivision would be like the one represented in Figure 6.12, where the shells start cubic like near the walls, and smoothly change to sphere like as one moves to the center. In the next section we present an algorithm to determine these cells for, in principle, any pore shape.

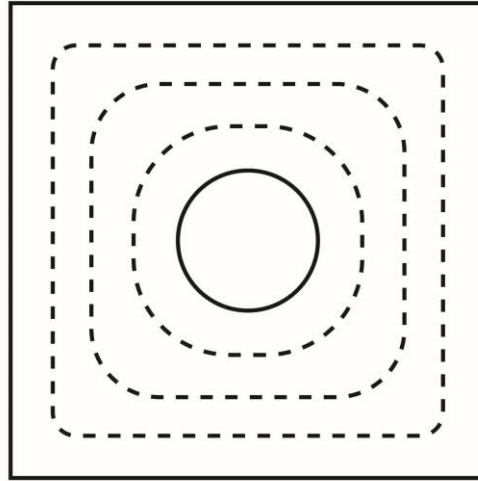


Figure 6.12 - Natural shell subdivision for a cubic pore, respecting pore geometry and free diffusion symmetries.
Source: By the author.

The symmetry argument is highlighted when we look at the normal modes eigenfunction $\psi_n(x)\psi_m(y)\psi_l(z)$ of solution (6.34) and (6.35). The dominant mode (with highest amplitude in Figure 6.11b is mode 111, whose slice at $z = 0$ is shown in Figure 6.13.

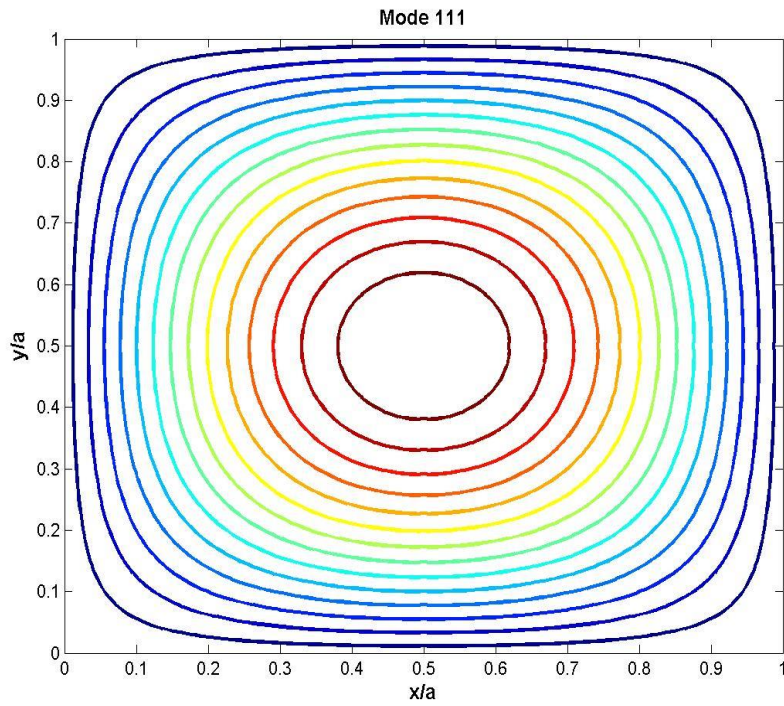
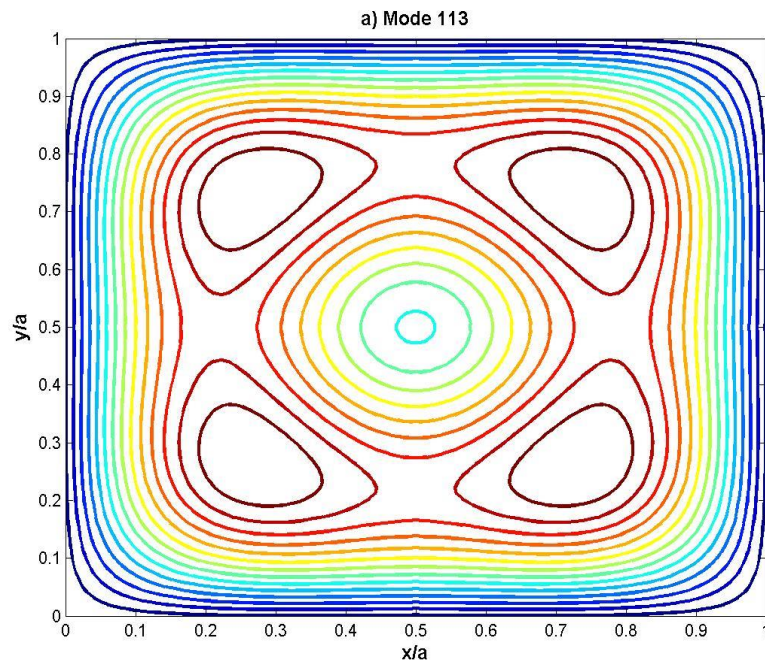


Figure 6.13 - Diffusion-relaxation eigenmode 111 contour plot for a cubic pore.
Source: By the author.

The dominant mode follows exactly the physically intuitive spatial distribution discussed in the paragraph that leads to Figure 6.12. The higher order modes, although not exactly, also hold a resemblance to this symmetry. Figure 6.14 shows the two other dominant modes of Figure 6.11b, which are 113 and 115.



(continued)

(continuation)

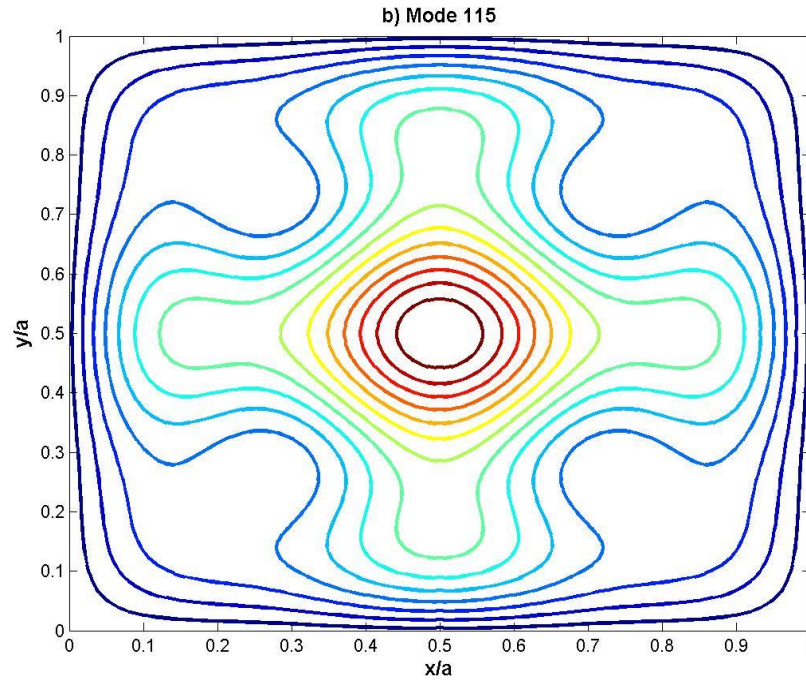


Figure 6.14 - Diffusion-relaxation eigenmodes a) 113 and b) 115 contour plots for a cubic pore.
Source: By the author.

Higher order modes allow for a more complex magnetization distribution in the intermediate pore space, but still generate surfaces that are sphere like away from the walls, and cubic like nearby them.

6.3 Generating diffusional and geometrical symmetric cells for an arbitrary pore

In this section we propose an algorithm that generates cells symmetric in the sense that they resemble the pore shape near the pore walls, and smoothly tend to a sphere away from every wall, as the ones represented in Figure 6.12. They also respect the detailed balance principle.

Consider N surfaces in Figure 6.12, with areas A_i and inner volumes V_i . These are not to be confused with the cell volumes ΔV_i , which in turn are determined as $\Delta V_i = V_i - V_{i-1}$, $\Delta V_1 = V_1$. The most external surface (N), has area $A_N = S$ (the pore surface area) and encloses a volume $V_N = V$ (the pore volume). Let the characteristic length r_i of each surface be defined as $r_i = V_i/A_i$. Once all the A_i and ΔV_i are known, the rates and rate matrix are determined in the exact same way as expressions (6.31), (6.32) and (6.33).

The first step is to determine the point that is most distant from every wall, which in the case of a cubic pore is its center. At this point, let a small sphere of volume V_{sph} , area A_{sph} , and characteristic length $r_{sph} = V_{sph}/A_{sph}$ be placed, as in Figure 6.15.

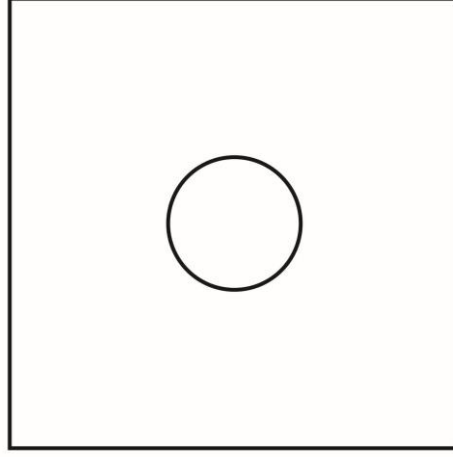


Figure 6.15 - Building symmetrical surfaces for a cubic pore.
Source: By the author.

At each step one should generate a surface that resembles its external neighbor, but smoothly turns into that small sphere. Assuming one has surfaces $i+1$ and $i+2$, the question is how to generate surface i . If surface i were simply a scaled down version of surface $i+1$, then it would have a characteristic length $r_i = \alpha r_{i+1}$, with $\alpha < 1$ to be determined. In this case, its surface area would simply equal $\alpha^2 A_{i+1}$. On the other hand, if surface i were a scaled up version of the small sphere, then its area would equal $\left(\frac{\alpha r_{i+1}}{r_{sph}}\right)^2 A_{sph}$. The desired surface is located somewhere in between these former two, therefore we will assume that it has an area given by:

$$A_i(\alpha) = \frac{\alpha^2}{2} \left\{ A_{i+1} + \left(\frac{r_{i+1}}{r_{sph}} \right)^2 A_{sph} \right\} \quad (6.36)$$

Following the same reasoning for volumes, one has:

$$V_i(\alpha) = \frac{\alpha^3}{2} \left\{ V_{i+1} + \left(\frac{r_{i+1}}{r_{sph}} \right)^3 V_{sph} \right\} \quad (6.37)$$

Finally, detailed balance principle requires that:

$$\frac{V_{i+1} - V_i(\alpha)}{A_{i+1} + A_i(\alpha)} = \frac{V_{i+2} - V_{i+1}}{A_{i+2} + A_{i+1}} \quad (6.38)$$

Once (6.38) is solved for α , equations (6.36) and (6.37) give the desired properties for the surface. The algorithm can be initiated assuming that surface $N - 1$ is a slightly scaled down version of the pore.

We applied this method for the cube in the slow diffusion limit (the same condition as in Figure 6.11b) and results are shown below, for $N = 30$ cells.

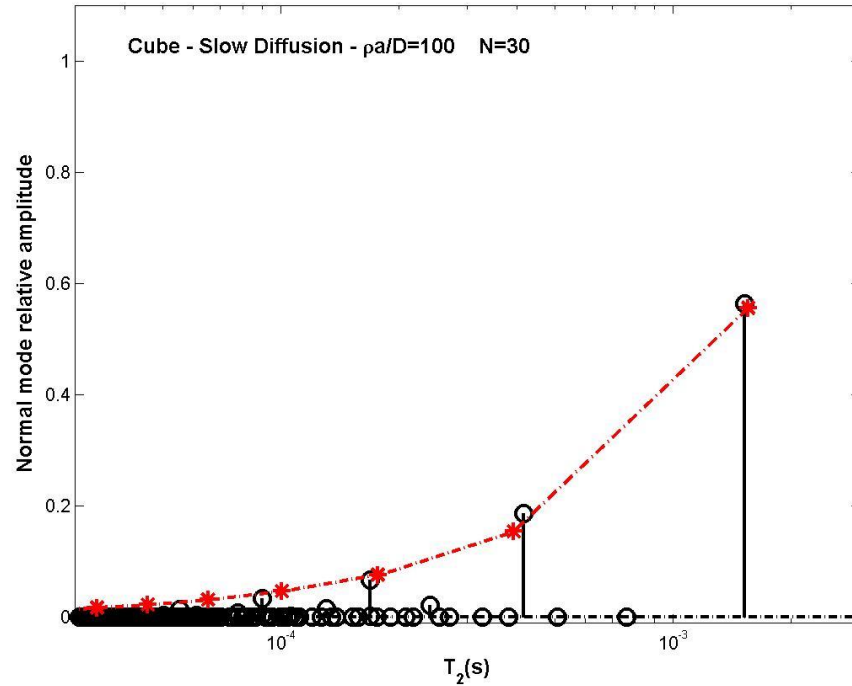


Figure 6.16 - Comparison between exact solution (black circles) and master equation approach (red star dots) for normal modes and relaxation rates in a cube of side $a = 10\mu\text{m}$ in the slow diffusion limit with 30 cells. The cells were made symmetrical with respect to the pore shape and free diffusion.

Source: By the author.

Comparison with Figure 6.11 shows that this method successfully corrects the decay rates for the most relevant diffusion modes. The main advantage of the method is that expressions (6.36) to (6.38) do not make any reference to the detailed shape of the pore, or to the ability one has to analytically describe (or draw) each one of the surfaces. The only information needed is the total volume and area of the pore, to allow a recursive determination of surfaces' areas and volumes. The details of pore geometry are of course implicit in the method. Specifically, for placing the small sphere in the pore, one must be able to determine the point that is the most farther away from every wall. This can be done in image analysis by means of a distance transform.

7 CONCLUSION AND PERSPECTIVES

The ideas exposed through Chapter 4 and developed in Chapter 5 indicate that a better calculation of actual pore size distributions are feasible downhole, through the continuous determination of surface relaxivity in the well logging operation. The key for obtaining relaxivity *in situ* using only NMR diffusion techniques lies on the understanding that downhole acquisition schemes and protocols encode diffusion and restricted diffusion by varying the diffusion times at which data are acquired (as in the diffusion editing technique for instance). The acknowledgement of this fact allows for the inversion machinery described in Chapter 4 to be adapted to decode relaxivity information, as described in Chapter 5. This compensates the lack of electrical information necessary for the Padé fitting approach (31) and allows restricted diffusion to be determined reasonably well.

Figures 5.15 and 5.16 show that noise level impacts differently the determination of higher and lower relaxivities. It can be seen that lower values of ρ such as $5\mu\text{m/s}$ are well estimated, almost independently of noise levels. For SNRs as low as 20, intermediate ρ values around 10 to $15\mu\text{m/s}$ can still be reasonably well estimated, especially for single gradient tools. Highest relaxivities (~ 20 to $30\mu\text{m/s}$) cannot be precisely determined, however, they can be separated from intermediate values. This separation alone can represent qualitative information of elevated value in formation evaluation discipline, as it may represent the difference between a good or poor reservoir, even if the exact value of pore size cannot be exactly determined.

Achieving an SNR of 20 downhole still requires some noise attenuation techniques. For well logging, that can be achieved by making several measurements at the same depth with the tool being held still, such as in the laboratory, or by stacking data from different depths. However, by trying to obtain relaxivities just by fitting a DT_2 map as shown in Figure 5.11 (for single gradient tools), a similar performance as obtained by the new method, able to separate high and intermediate relaxivity values, would be able with SNRs of about 40. Therefore, the method presented here reduces the required SNR by a factor of about 2, which reflects in an acquisition 4 times faster, or a smaller stacking, either reducing acquisition costs or improving vertical resolution. It also makes ρ determination possible for distributed gradient tools as shown by the comparison of Figures 5.12 and 5.16.

Experimental results with laboratory and well logging data indicate that the relaxivity information can be in fact “decoded” through the proposed method, although in principle it can be made more robust with more experimentation. As perspectives and next steps, new

logging runs can be made with the diffusion editing techniques. Also, the LEAR group in IFSC/USP is developing an experimental apparatus that emulates a logging acquisition, with a constant background field gradient produced by a single sided magnet, at the same typical values as the ones observed downhole. This apparatus can be used to obtain more data from rock samples without the limitations described in Chapter 5, regarding the laboratory restrictions in emulating data acquisition in a log like fashion.

In Chapter 6 we explored a deeper understanding of the dynamics governing the relaxation rates for the surface diffusion-relaxation process. The most important result is that the exact solution of diffusion equation inside the pore can be much simplified with rate equations, as long as equilibrium and symmetries information are correctly introduced in the solution. With the transition rates λ_{nm} introduced in the Chapter, the diffusional symmetry can be considered in a quite simple way, by using mainly the information of pore surface area and volume.

Although we restricted the applications of the calculated rates to the problem of obtaining NMR response based on pore imaging (Digital Rock), these results can be extended to other fields. For instance, the connection between transition rates and geometrical information can in principle be used for dealing with diffusional coupling between pores. Also, NMR techniques that measure directly the connection between pore sites, such as exchange techniques (66), can also benefit from such an approach. In other words, we saw that even for an arbitrary segmentation of space, transition rates between different cells depend only on the total volume of the cell and on the interface area between consecutive sites. Therefore, the theoretical link between cells' geometry and pore connectivity, for example, can be easily modeled or understood in exchange experiments.

As further applications on the digital rock front, we will validate the theoretical apparatus developed here, regarding transition rates and symmetries, by comparing experimental NMR relaxation data with calculated signal based on pore imaging.

REFERENCES

- 1 ALLEN, P.; ALLEN, J. **Basin analysis: principles and application to petroleum play assessment**. 2nd ed. Malden, MA: Willey-Blackwell, 2005
- 2 PETERS, E. J. **Advanced petrophysics**. Austin: Live Oak book Company, 2012. v. 1
- 3 PRESS, F. et al. **Understanding earth**. New York: W. H. Freeman, 2003.
- 4 DAIGLE, H.; DUGAN, B. Extending NMR data for permeability estimation in fine-grained sediments. **Marine and Petroleum Geology**, v. 26, n. 8, p. 1419-1427, 2009.
- 5 COATES, G.; XIAO, L.; PRAMMER, M. **NMR logging: principles and applications**. Houston: Halliburton Energy Services, 1999.
- 6 STEWART, S. A. Salt tectonics in the North Sea Basin: a structural style template for seismic interpreters. **Geological Society**, v. 272, p. 361-396, 2007. doi: 10.1144/GSL.SP.2007.272.01.19.
- 7 ARCHIE, G. E. The electrical resistivity log as an aid in determining some reservoir characteristics. **Transactions of the AIME**, v. 146, n. 1, 1942. doi: 10.2118/942054-G.
- 8 DUNN, K.-J.; BERGMAN, D. L.; LATORRACA, G. A. **Nuclear magnetic resonance: petrophysical and logging applications**. Amsterdam: Pergamon, 2002.
- 9 ABRAGAM, A. **Principles of nuclear magnetism**. Oxford: Oxford University Press, 1961.
- 10 COHEN-TANNOUDJI, C.; DIU, B.; LALOË, F. **Quantum mechanics**. Paris: Hermann, 1977.
- 11 SLICHTER, H. P. **Principles of magnetic resonance**. New York: Springer, 1990.
- 12 BLOCH, F. Nuclear induction. **Physical Review**, v. 70, n. 7-8, p. 460-474, 1946.
- 13 BLOEMBERGEN, N.; PURCELL, E. M.; POUND, R. V. Relaxation effects in nuclear magnetic resonance absorption. **Physical Review**, v. 73, n. 7, p. 679-712, 1948.
- 14 TORREY, H. C. Bloch equations with diffusion terms. **Physical Review**, v. 104, n. 3, p. 563-565, 1956.
- 15 CARR, H. Y.; PURCELL, E. M. Effects of diffusion on free precession in nuclear magnetic resonance experiments. **Physical Review**, v. 94, n. 3, p. 630-638, 1954.
- 16 MEIBOOM, S.; GILL, D. Modified spin-echo method for measuring nuclear relaxation times. **Review of Scientific Instruments**, v. 29, n. 8, p. 688-691, 1958.
- 17 STEJSKAL, E. O.; TANNER, J. E. Spin diffusion measurements: spin echoes in the presence of a time - dependent field gradient. **Journal of Chemical Physics**, v. 42, n. 1, p. 288-292, 1965. doi: 10.1063/1.1695690.
- 18 TANNER, J. E. Use of the stimulated echo in NMR diffusion studies. **Journal of Chemical Physics**, v. 52, n. 5, p. 2523-2526, 1970.

- 19 KORRINGA, J.; SEEVERS, D. O.; TORREY, H. C. Theory of spin pumping and relaxation in systems with a low concentration of electron spin resonance centers. **Physical Review**, v. 127, n. 4, p. 1143-1150, 1962.
- 20 KLEINBERG, R. L.; HORSFIELD, M. A. Transverse relaxation processes in porous sedimentary rock. **Journal of Magnetic Resonance**, v. 88, n. 1, p. 9-19, 1990.
- 21 KLEINBERG, R. L.; KENYON, W. E.; MITRA, P. P. Mechanism of NMR relaxation of fluids in rock. **Journal of Magnetic Resonance A**, v. 108, n. 2, p. 206-214, 1994.
- 22 FOLEY, I.; FAROOQUI, S. A.; KLEINBERG, R. L. Effect of paramagnetic ions on NMR\ relaxation of fluids at solid surfaces. **Journal of Magnetic Resonance A**, v. 123, n. 1, p. 95-104, 1996.
- 23 KEATING, K.; KNIGHT, R. A laboratory study to determine the effect of iron oxides on proton NMR measurements. **Geophysics**, v. 72, n. 1, p. E27-E32, 2007.
- 24 ROBERTS, S. P.; MCDONALD, P. J.; PRITCHARD, T. A bulk and spatially resolved NMR\ relaxation study of sandstone rock plugs. **Journal of Magnetic Resonance A**, v. 116, n. 2, p. 189-195, 1995.
- 25 BROWNSTEIN, K. R.; TARR, C. E. Importance of classical diffusion in NMR studies of water in biological cells. **Physical Review A**, v. 19, n. 6, p. 2446-2453, 1979.
- 26 KENYON, W. E. et al. A three-part study of NMR longitudinal relaxation properties of water-saturated sandstones. **SPE Formation Evaluation**, v. 3, n. 3, p. 622-636, 1988.
- 27 MORRISS, C. et al. Core analysis by low-field NMR. **The Log Analyst**, v. 38, n. 2, p. 84-94, 1997.
- 28 SUN, B.; DUNN, K.-J. Two-dimensional nuclear magnetic resonance petrophysics. **Magnetic Resonance Imaging**, v. 23, n. 2, p. 259-262, 2005.
- 29 FLAUM, M.; CHEN, J.; HIRASAKI, G. J. NMR diffusion editing for DT2 maps: application to recognition of wettability change. **Petrophysics**, v. 46, p. W02401, 2005. doi:10.1029/2006WR005635.
- 30 SOUZA, A. **Estudo de propriedades petrofísicas de rochas sedimentares por Ressonância Magnética Nuclear**. 2012. 236 p. Tese (Doutorado em Ciências) - Instituto de Física de São Carlos, Universidade de São Paulo, São Carlos, 2012.
- 31 SOUZA, A. et al. **Permeability prediction improvement using 2D NMR diffusion-T2 maps**. 2013. Available from: <<https://www.onepetro.org/download/conference-paper/SPWLA-2013-U?id=conference-paper%2FSPWLA-2013-U>>. Accessible at: 23 Jan. 2016.
- 32 ARNS, C. H. et al. **Prediction of permeability from NMR response: surface relaxivity heterogeneity**. 2006. Available from: <http://people.physics.anu.edu.au/~tjs110/2005-2008%20Papers/No.25_Prediction%20of%20Permeability%20from%20NMR%20Response.pdf>. Accessible at: 23 Jan. 2016.
- 33 TIMUR, A. **Effective porosity and permeability of sandstones investigated through nuclear magnetic resonance principles**. 1968. Available from: <

<https://www.onepetro.org/download/conference-paper/SPWLA-1968-K?id=conference-paper%2FSPWLA-1968-K>>. Accessible at: 23 Jan. 2016.

34 FREEDMAN, R. et al. Wettability, saturation, and viscosity using the magnetic resonance fluid characterization method and new diffusion-editing pulse sequences. In: SPE ANNUAL TECHNICAL CONFERENCE AND EXHIBITION, Sept. 29 - Oct.2 2002, San Antonio, Texas. **Proceedings...** San Antonio: SPE, 2002. paper 77397-MS.

35 DAIGLE, H.; DUGAN, B. An improved technique for computing permeability from NMR measurements in mudstones. **Journal of Geophysical Research: solid earth**, v. 116, n.B8, 2011. doi: 10.1029/2011JB008353.

36 WOESSNER, D. E. N.M.R. spin-echo self-diffusion measurements on fluids undergoing restricted diffusion. **Journal of Physical Chemistry**, v. 67, n. 6, p. 1365-1367, 1963.

37 MITRA, P. P. et al. Diffusion propagator as a probe of the structure of porous media. **Physical Review Letters**, v. 68, n. 24, p. 3555-3558, 1992.

38 SEN, P. N. Time-dependent diffusion coefficient as a probe of geometry. **Concepts in Magnetic Resonance A**, v. 23A, n.1, p. 1-21, 2004.

39 SONG, Y.-Q.; ZIELINSKI, L.; RYU, S. Two-dimensional NMR of diffusion systems. **Physical Review Letters**, v. 100, n. 24, p. 248002, 2008.

40 LATOUR, L. L. et al. Time-dependent diffusion coefficient of fluids in porous media as a probe of surface-to-volume ratio. **Journal of Magnetic Resonance A**, v. 101, n.3, p. 342-346, 1993.

41 HURLIMANN, M. D. et al. Restricted diffusion in sedimentary rocks. determination of surface-area-to-volume ratio and surface relaxivity. **Journal of Magnetic Resonance A**, v. 111, n.2, p. 169-178, 1994.

42 SONG, Y.-Q. Using internal magnetic fields to obtain pore size distributions of porous media. **Concepts in Magnetic Resonance A**, v. 18A, n.2, p. 97-110, 2003.

43 SONG, Y.-Q. Recent progress of nuclear magnetic resonance applications in sandstones and carbonate rocks. **Vadose Zone Journal**, v. 9, n.4, p. 828-834, 2010.

44 GOELMAN, G.; PRAMMER, M. G. The CPMG\ pulse sequence in strong magnetic field gradients with applications to oil-well logging. **Journal of Magnetic Resonance A**, v. 113, n.1, p. 11-18, 1995.

45 HÜRLIMANN, M. D. Diffusion and relaxation effects in general stray field NMR experiments. **Journal of Magnetic Resonance**, v. 148, n.2, p. 367-378, 2001.

46 HÜRLIMANN, M. D.; GRIFFIN, D. D. Spin dynamics of Carr–Purcell–Meiboom–Gill-like sequences in grossly inhomogeneous B₀ and B₁ fields and application to NMR well logging. **Journal of Magnetic Resonance**, v. 143, n.1, p. 120-135, 2000.

47 HURLIMANN, M. D. et al. Diffusion-editing: new nmr measurement of saturation and pore geometry. In: SPWLA ANNUAL LOGGING SYMPOSIUM, 43rd, 2-5 June 2002, Oiso, Japan. **Proceedings...** Oiso: 2002. paper SPWLA FFF.

- 48 MITCHELL, J.; CHANDRASEKERA, T. C.; GLADDEN, L. F. Numerical estimation of relaxation and diffusion distributions in two dimensions. **Progress in Nuclear Magnetic Resonance Spectroscopy**, v. 62, p. 34-50, 2012. doi:10.1016/j.pnmrs.2011.07.002.
- 49 D'EURYDICE, M. N.; GALVOSAS, P. Measuring diffusion–relaxation correlation maps using non-uniform field gradients of single-sided NMR devices. **Journal of Magnetic Resonance**, v. 248, p. 137-145, 2014. doi: 10.1016/j.jmr.2014.07.012.
- 50 VENKATARAMANAN, L.; SONG, Y.-Q.; HURLIMANN, M. D. Solving Fredholm integrals of the first kind with tensor product structure in 2 and 2.5 dimensions. **IEEE Transactions on Signal Processing**, v. 50, n.5, p. 1017-1026, 2002.
- 51 SONG, Y.-Q. et al. T1–T2 correlation spectra obtained using a fast two-dimensional Laplace inversion. **Journal of Magnetic Resonance**, v. 154,n.2, p. 261-268, 2002.
- 52 EPSTEIN, C. L.; SCHOTLAND, J. The Bad truth about Laplace's transform. **SIAM Review**, v. 50, n.3, p. 504-520, 2008.
- 53 HONERKAMP, J.; WEESE, J. Tikhonovs regularization method for ill-posed problems. **Continuum Mechanics and Thermodynamics**, v. 2, n.1, p. 17-30, 1990.
- 54 BUTLER, J. P.; REEDS, J. A.; DAWSON, S. V. Estimating solutions of first kind integral equations with nonnegative constraints and optimal smoothing. **SIAM Journal on Numerical Analysis**, v. 18, n.3, p. 381-397, 1981.
- 55 CHEN, S. et al. Optimization of NMR logging acquisition and processing. In: SPE ANNUAL TECHNICAL CONFERENCE AND EXHIBITION, 3-6 Oc. 1999, Houston, Texas. **Proceedings...** Houston: SPE, 1999. paper 56766-MS.
- 56 HANSEN, P. C. Analysis of discrete ill-posed problems by means of the l-curve. **SIAM Review**, v. 34, n.4, p. 561-580, 1992.
- 57 BORGIA, G. C.; BROWN, R. J. S.; FANTAZZINI, P. Uniform-penalty inversion of multiexponential decay data. **Journal of Magnetic Resonance**, v. 132,n.1, p. 65-77, 1998.
- 58 D'EURYDICE, M. N. **Desenvolvimento de metodologias para o estudo de meios porosos por ressonância magnética nuclear**.2011. 168p. Tese (Doutorado em Ciências) - Instituto de Física de São Carlos, Universidade de São Paulo, São Carlos, 2011.
- 59 HANSEN, P. C. Regularization tools: a Matlab package for analysis and solution of discrete ill-posed problems. **Numerical Algorithms**, v. 6, n.1, p. 1-35, 1994.
- 60 CHEN, S. et al. Qualitative and quantitative information nmr logging delivers for characterization of unconventional shale plays: case studies. In: SPWLA ANNUAL LOGGING SYMPOSIUM,54th, 22-26 June 2013, New Orleans, Louisiana. **Proceedings...** New Orleans: SPWLA, 2013.paper Z.
- 61 EIDMANN, G. et al. The NMR MOUSE, a mobile universal surface explorer. **Journal of Magnetic Resonance A**, v. 122, n.1, p. 104-109, 1996.
- 62 MARSCHALL, D. et al. Method for correlating NMR relaxometry and mercury injection data. **SCA Conference**, v.9511,p. 1-12, 1995.

63 MITCHELL, J.; FORDHAM, E. J. Emulation of petroleum well-logging D – T2 correlations on a standard benchtop spectrometer. **Journal of Magnetic Resonance** , v. 212, n.2, p. 394-401, 2011.

64 RAMAKRISHNAN, T. S. et al. Forward models for nuclear magnetic resonance in carbonate rocks. In: SPWLA ANNUAL LOGGING SYMPOSIUM, 39th, 26-28 May 1998, Keystone, Colorado. **Proceedings...** Keystone: SPWLA, 998. 12p.

65 ANAND, V.; HIRASAKI, G. J. Diffusional coupling between micro and macroporosity for nmr relaxation in sandstones and grainstones1. **Petrophysics**, v. 48, n.4, p.289-307,2007.

66 D'EURYDICE, M. N. et al. T2-filtered T2 – T2 exchange NMR. **Journal of Chemical Physics**, v. 144, n.20,p. 204201, 2016.